TECHNICAL REPORT STANDARD PAGE

1. Report No.	2. Government Accession No.	3. Recipient's Catalog No.
FHWA/LA.11/477		

4. Title and Subtitle	5. Report Date
Evaluation of Continuity Detail for Precast Prestressed Girders	**August 2011**
	6. Performing Organization Code

7. Author(s)	8. Performing Organization Report No.
Ayman M. Okeil, Ph.D., P.E. **Steve Cai, Ph.D., P.E.** **Veeravenkata Chebole and Tanvir Hossain, M.S.**	

9. Performing Organization Name and Address	10. Work Unit No.
Department of Civil and Environmental Engineering **Louisiana State University** **Baton Rouge, LA 70803**	11. Contract or Grant No. **LTRC Project Number: 08-1ST** **SIO Number: 30000150**

12. Sponsoring Agency Name and Address	13. Type of Report and Period Covered
Louisiana Department of Transportation and Development **P.O. Box 94245** **Baton Rouge, LA 70804-9245**	**Final Report** **March 2008 – December 2010**
	14. Sponsoring Agency Code

15. Supplementary Notes

16. Abstract

The construction of highway bridges using precast prestressed concrete (PSC) girders is considered one of the most economical construction alternatives because of the advantages they offer (e.g. reducing formwork and rapid construction). Constructing multi-simple span bridges is an easy alternative for precast PSC girder bridges. However, the existence of expansion joints often leads to a host of problems in their vicinity due to drainage leaks and debris accumulation. The maintenance of expansion joints is, therefore, an activity that bridge owners would rather avoid by eliminating these joints by building connections between precast elements that are capable of resisting the forces resulting from establishing continuity. Several continuity details have been used over the years for slab-on-girder bridges with the goal of avoiding the aforementioned maintenance issues and reaping the benefits of continuity without the drawbacks of introducing it in large structures such as bridges (e.g. thermal movements). A new continuity detail is adopted in the John James Audubon Bridge that differs from the current standard detail in Louisiana. The new detail is based on the recommendation of the National Cooperative Highway Research Program (NCHRP) Report 519 [*1*].

A 96-channel monitoring system was installed to provide information that can be used to assess the performance of the continuity detail. Embedded and surface-mounted sensors of different types were installed to measure strains, temperatures, rotations, and gap openings in critical locations in the monitored segment. Data from about 24 months of monitoring was collected. The data, its processing, and interpretation are presented in this report. Analyses based on NCHRP Report 519 model and finite element models were also conducted to further understand the behavior of the new detail. Results from the analyses were also used to recommend girder age at continuity to meet prespecified design criteria. A live load test was also conducted to assess the performance of the new detail.

Recommendations based on the findings of the project are drawn. It can be said that the continuity detail is capable of transferring forces between girder ends. However, girder ends may be subjected to high localized strains, especially due to thermal variation, which can cause cracking. Such cracks are detrimental to the shear strength of PSC girders. Therefore, thermal gradients need to be considered in the design of this detail.

17. Key Words	18. Distribution Statement
prestressed concrete; creep; continuous structures; bridges, live load	Unrestricted

19. Security Classification (of this report)	20. Security Classification (of this page)	21. No. of Pages	22. Price
N/A	N/A	206	N/A

Project Review Committee

Each research project will have an advisory committee appointed by the LTRC Director. The Project Review Committee is responsible for assisting the LTRC Administrator or Manager in the development of acceptable research problem statements, requests for proposals, review of research proposals, oversight of approved research projects, and implementation of findings.

LTRC appreciates the dedication of the following Project Review Committee Members in guiding this research study to fruition.

LTRC Manager

Walid Alaywan, Ph.D., P.E.
Senior Structures Research Engineer

Members

Paul Fossier
Gill Gautreau
Mike Boudreau
Arturo Aguirre

Directorate Implementation Sponsor

Richard D. Savoie
DOTD Chief Engineer

Evaluation of Continuity Detail for Precast Prestressed Girders

by

Ayman M. Okeil, Ph.D., P.E.
Associate Professor

Steve Cai, Ph.D., P.E.
Professor

Veeravenkata Chebole
Research Assistant

Tanvir Hossain, M.S.
Research Assistant

Department of Civil and Environmental Engineering
3513-D Patrick F. Taylor Hall
Louisiana State University
Baton Rouge, LA 70803

LTRC Project No. 08-1ST
State Project No. 736-99-1513

conducted for

Louisiana Department of Transportation and Development
Louisiana Transportation Research Center

August 2011

ABSTRACT

The construction of highway bridges using precast prestressed concrete (PSC) girders is considered one of the most economical construction alternatives because of the advantages they offer (e.g., reducing formwork and rapid construction). Constructing multi-simple span bridges is an easy alternative for precast PSC girder bridges. However, the existence of expansion joints often leads to a host of problems in their vicinity due to drainage leaks and debris accumulation. The maintenance of expansion joints is, therefore, an activity that bridge owners would rather avoid by eliminating these joints by building connections between precast elements that are capable of resisting the forces resulting from establishing continuity. Several continuity details have been used over the years for slab-on-girder bridges with the goal of avoiding the aforementioned maintenance issues and reaping the benefits of continuity without the drawbacks of introducing it in large structures such as bridges (e.g., thermal movements). A new continuity detail is adopted in the John James Audubon Bridge that differs from the current standard detail in Louisiana. The new detail is based on the recommendation of the National Cooperative Highway Research Program NCHR Report 519 [*1*].

A 96-channel monitoring system was installed to provide information that can be used to assess the performance of the continuity detail. Embedded and surface-mounted sensors of different types were installed to measure strains, temperatures, rotations, and gap openings in critical locations in the monitored segment. Data from about 24 months of monitoring was collected. The data, its processing, and interpretation are presented in this report. Analyses based on NCHRP Report 519 models and finite element models were also conducted to further understand the behavior of the new detail. Results from the analyses were also used to recommend the girder age at continuity to meet prespecified design criteria. A live load test was also conducted to assess the performance of the new detail.

Recommendations based on the findings of the project are drawn. It can be said that the continuity detail is capable of transferring forces between girder ends. However, girder ends may be subjected to high localized strains, especially due to thermal variation, which can cause cracking. Such cracks are detrimental to the shear strength of PSC girders. Therefore, thermal gradients need to be considered in the design of this detail.

ACKNOWLEDGMENTS

The authors gratefully acknowledged the financial support provided by the Louisiana Transportation Research Center (LTRC) (LTRC Project No. 08-1ST) and the Louisiana Department of Transportation and Development (DOTD) (State Project No. 736-99-1513).

The authors also acknowledge the assistance of the graduate students Tanvir Hossain and Veeravenkata Chebole who helped in some of the analysis reported herein. Many other graduate students who helped with the installation and live load testing included Yilmaz Bingol, Miao Xia, Xuan Kong, Archana Nair, and Fenghong Fan are also acknowledged.

The authors would also like to thank Paul Fossier (DOTD) for initiating the idea behind this project and for providing information pertinent to the project throughout its execution. The support from the DOTD's Structures and Facilities Maintenance Administration (Gill Gautreau and Steven Sibley) is greatly appreciated. Onsite support from Louisiana TIMED Managers (Jim Wiley and Wayne Marchand) was essential for the success of this project. Support from the LTRC Concrete Research Laboratory (Randy Young) with the testing of concrete specimens is greatly appreciated. Finally, the assistance from contractors of the bridge and the monitoring system (G.J Shexnayder and Zach Jopling – Boh Brothers, Jeremy Adkins and Eric Hebert – Dunham Price, Jeff Schultz, Scott Aschermann, and Jesse Grimson – Bridge Diagnostics, Inc.) is greatly acknowledged.

Special thanks are due to Walid Alaywan (LTRC), senior structures research engineer, for his support of this research.

IMPLEMENTATION STATEMENT

New bridges whether designed by DOTD engineers or consulting firms can directly and immediately benefit from this study. The results from this study provide engineers with essential information for a successful design using the new detail. These can be summarized as follows:

1. The study highlights the importance of considering the effect of thermal variations on bridges employing this detail. Most studies on this and similar continuity details focused on other factors and did not discuss or quantify the effects of thermal variations, which was shown to be a dominant factor for the new detail. Unlike creep and shrinkage effects, which can be reduced by establishing continuity after the girders have reached an age that ensures that a large portion of the creep has already taken place, thermal effects cannot be controlled by the designer. Hence, their effect should be considered at the design stage and superimposed to other straining actions.
2. It also brings to the attention of the designer that one girder age criterion such as the 90-day limit in NCHRP Report 519 may not be appropriate for all bridge configurations. Therefore, detailed analyses need to be conducted so appropriate girder ages are used to ensure the avoidance of adverse effects of high positive restraint moments, i.e., diaphragm or girder end cracking. The modified `RESTRAINT` program (`mRESTRAINT`) can be used to help in assessing the appropriate age for any bridge configuration after superimposing the thermal effects.
3. The effects of live loads on the detail are small when it comes to the positive moment action and, therefore, may be ignored. The effect of live loads on the negative moment action is considerable and needs to be considered.
4. Simpler details that eliminate expansion joints by keeping the deck continuous over simply-supported girders, i.e., partial integration, expedite the construction of bridges and reduce the potential for damage caused by leaks through expansion joints or high positive restraint moments. Therefore, such details should be the default continuity detail in DOTD projects. Several state DOTs adopt simpler details. For example, the state of Texas does not require the construction of continuity diaphragms, while decks are poured continuous over bridge bents.

TABLE OF CONTENTS

See attached CD for Appendixes

LIST OF TABLES

LIST OF FIGURES

See attached CD for Figures 43-206

INTRODUCTION

Continuity in Precast Prestressed Girder Bridges

The construction of highway bridges using precast PSC girders is considered one of the most economical construction alternatives. Not only does it eliminate the need for cumbersome formwork that is costly and may negatively impact daily activities around the construction site, but it also speeds up the construction time since the precast PSC girders are only erected after being cured in the casting yard. One of the challenges for precast construction has always been the development of connection details that achieve the design goals without affecting the ease of construction. By default, precast elements are not connected monolithically. Therefore, many of the existing precast PSC girder bridges are constructed as simply supported spans as can be seen in Figure 1(a). The existence of expansion joints between spans is known to cause serious maintenance problems due to the accumulation of debris in the joints and the deterioration of elements in their vicinity (e.g., girder ends) due to drainage water leaks. Several continuity details have been used over the years in the bridge industry for slab-on-girder bridges with the goal of avoiding the aforementioned maintenance issues and reaping the benefits of continuity without the drawbacks of introducing it in large structures such as bridges (e.g., thermal movements). The continuity details can be categorized into two types, namely *full integration* details and *partial integration* details. Full integration details [Figure 1(b)] result in a fully continuous structure (both deck and girders) that can resist the bending moments that develop at the supports due to long term, thermal, and live load effects. In bridges with partial integration details [Figure 1(c)], the expansion joints are eliminated by casting a continuous deck over the support, while allowing adjacent girders movement with respect to each other, thus relieving some of the continuity effects.

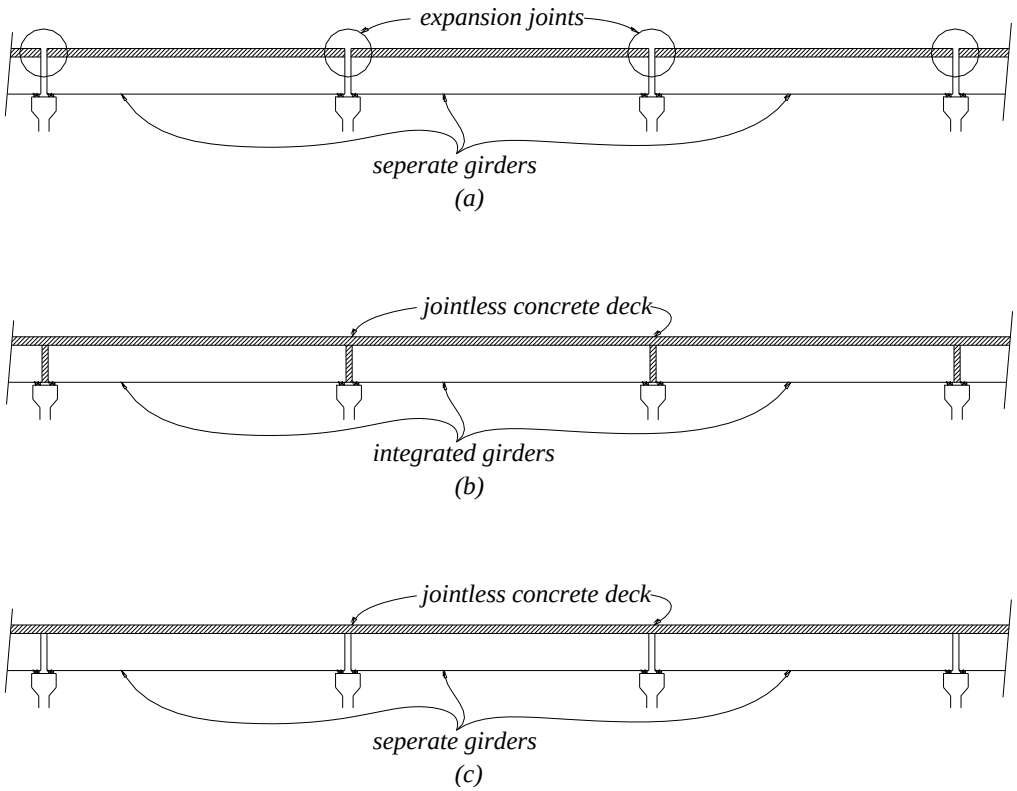

Figure 1
Typical continuity conditions in precast PSC girder bridges:
(a) simply-supported, (b) fully continuous, and (c) partially continuous [*2*]

Negative as well as positive moments develop over the continuous support once continuity is established in the system. Negative moments can be easily resisted by the abundance of tensile reinforcement in the deck and the ability of bottom flanges of precast PSC girders to transfer compression forces from one span to another through the diaphragm. The compression forces in the flanges of adjacent girders are transferred through the continuity diaphragm. Positive moments mainly develop in continuous bridge structures due to long term effects (e.g. creep) as can be seen in Figure 2. They cause compression in the deck over the support, which is not a problem because of the large deck area. However, the tensile forces developing in the girders' bottom flanges cannot be easily transferred from one span to the other. There are two solutions for the positive continuity moment problem. The first relies on providing additional bottom reinforcement at the girder ends that go through the continuity diaphragms to transfer the tensile forces between adjacent spans. This approach leads to *full integration* of the structure. Conversely, the designer may opt to relieve the tensile force by separating girder ends and allowing some movement between the girder bottoms while maintaining the deck continuity. This option leads to a *partially continuous* structure.

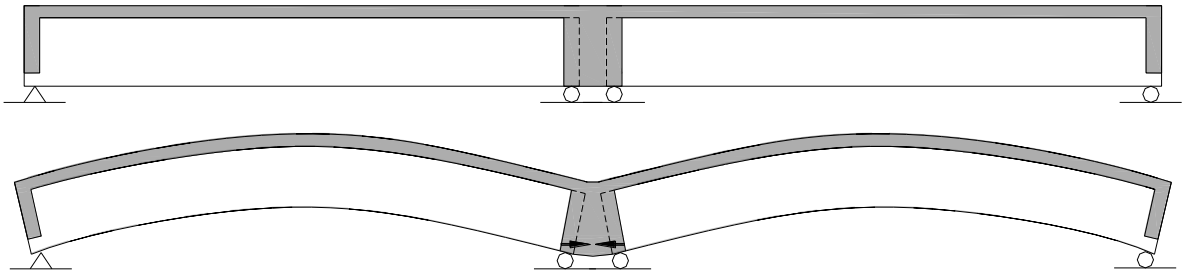

Figure 2
Development of positive moment in bridge connections with continuity diaphragm

DOTD uses a detail that can be categorized under *partial integration*. In the current detail, girder ends are debonded from the continuity diaphragm by providing an asphaltic material layer as can be seen in Figure 3. A continuous deck is cast over the support. The debonding allows some movement of the girder ends from adjacent spans with respect to each other. Because of the existence of the diaphragm and continuous deck, the relative movement becomes more restrained at the top of the girder in comparison with the bottom. Despite the ability of this detail to resist negative moments, spans are conservatively designed as simply supported spans without taking advantage of the continuity. This approach may be justified based on the fact that if both girders are cambered up due to creep or thermal gradients, a gap may develop between girder ends from adjacent spans and the diaphragm. A negative moment effect will first have to close this gap before a compression force can be transferred, i.e., the negative moment, or part of it, will be redistributed.

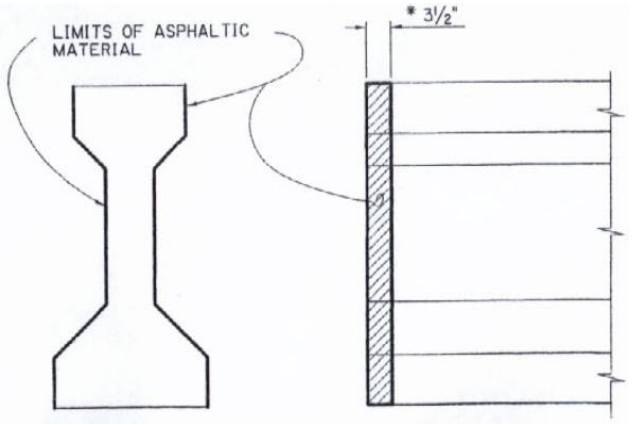

Figure 3
Bond breaker at girder ends

The new John James Audubon Bridge crossing the Mississippi River in Saint Francisville, LA, consists of eight bridges including the main cable-stayed span over the river. The designer of Bridge #2 (described later in detail) adopted a detail that is different than the current continuity diaphragm standard used in Louisiana. It is based on the recommendations of the National Cooperative Highway Research Program (NCHRP) Project 12-53 (Report 519) [*1*]. The adopted detail introduces positive reinforcement in the form of hairpin bars to the bottom at girder ends. Hairpin bars extend outside girders and into the continuity diaphragm. DOTD seized the unique opportunity by calling for an investigation into the performance of this new detail. LTRC is managing the project, which is conducted by a research team from Louisiana State University. This report summarizes the efforts and findings from the research project. The evaluation of the performance of the continuity detail is based on structural health monitoring and on analytical investigations that look into more details than what can be obtained from a single bridge.

Historic Background

The behavior of bridges' continuity detail has been studied by several researchers. The majority of the work is related to the full integration technique. For example, Loveall and Wasserman reported their experience with jointless bridge decks over continuous girders [*3, 4*]. Russell and Gerken wrote *Knowns and Unknowns* about jointless bridges [*5*]. Burke, Jr. [*6, 7*] discussed the attributes and limitations of integral bridges. He also demonstrated some of the adverse effects of full bridge integration due to the buildup of stresses in concrete pavements [*8*]. Alampalli and Yannotti surveyed the integral and jointless-deck bridge inventory in the state of New York, US, indicating that their performance is as designed [*9*]. They recommended new details for future projects to avoid and problems noted in the existing bridges. Thippeswamy et al. also evaluated the performance of in-service jointless bridges [*10*].

Documentation of bridges that have been constructed or rehabilitated using one of the mentioned approaches can also be found in the literature. Demartini and Haywood reported their work on the repair of the Story Bridge in Australia by eliminating contraction joints [*11*]. A redecking case study where joints were eliminated was reported by Pierce [*12*]. The construction of a demonstration bridge with jointless decks in North Carolina, US, was reported by Caner and Zia [*13*]. The positive performance of bridges with jointless decks in seismic zones is demonstrated by Caner et al. using existing bridges in Turkey [*14*]. More recently, Wing and Kowalsky reported the results obtained from monitoring an instrumented jointless bridge with debonded link slabs that was constructed as a pilot bridge in North Carolina, US [*15*]. Long-term effects were also investigated by several researchers [*7, 16*]. The results from these studies indicate that within certain limits, long-term effects may be

ignored. This finding simplifies the analysis considerably. Several methods for the analysis of jointless deck systems were proposed [*13, 17-20*]. Most of these methods are based on the finite element method, where researchers developed special computer code to incorporate the specifics of the jointless deck problem in the analysis. In a recent study by Okeil and El-Safty, a simplified analysis method was developed for jointless bridges [*2*]. In this study, two support configurations, an upper and a lower bound, were considered. Closed-form expressions were derived and used to develop design tables that eliminated the need for computationally intensive finite element analyses.

NCHRP Projects 12-29 (Report 322) and 12-53 (Report 519) and Related Research

In 1989, the National Cooperative Highway Research Program (NCHRP) published the findings from Project 12-29 in Report 322 titled *Design of Precast Prestressed Bridge Girders Made Continuous*, which is a comprehensive study on converting precast prestressed concrete girders into a continuous system [*21*]. The authors of the report presented analytical methods for estimating the moments introduced by positive moment continuity details due to long-term as well as live load effects. It was concluded in the report that the construction of the positive moment continuity details is "difficult, time consuming, and costly." The authors also concluded that "there is no structural advantage for providing positive moment reinforcement at the supports." It should be noted that thermal effects were not within the scope of the study.

Recently, NCHRP sponsored Project 12-53, (findings were published in Report 519), to survey current practices by different DOTs and to experimentally investigate the performance of positive moment continuity details [*1*]. Design methods and tools were also developed for the design of live loads on bridges with the recommended continuity detail. Six specimens were fabricated and tested under cyclic loads until failure. Continuity details where positive moment reinforcement extends from the bottom flange at girder ends were investigated. Additional hairpin/hooked bars or prestressing strands can be utilized as seen in Figure 4. The conclusion from the study is that positive moment continuity details are not costly ($200 per girder). It was recommended that positive moment connections should be designed for a capacity less than 1.2 M_{cr}, since connections with higher capacities are not efficient. To reduce the applied moments, and therefore reduce the possibility of a diaphragm cracking and leading to a loss of continuity, the report recommends that the continuity be introduced after 90 days or more after casting the PSC girders. The 90-day girder age limit was based on the response to the survey and analytical results. Experimental results showed that the loss of continuity was not seen until the connection was close to failure, and even then, the loss was about 30 percent. Furthermore, the authors of the report stated that positive moment continuity details also enhance the structural integrity of the bridge even if they do

not reduce the total design moment. The authors of NCHRP Report 519 recommended further research to study the performance of the recommended positive moment continuity details in full-size specimens since the tested specimens were single line AASHTO Type II girders. The effects of bridge skew and thermal changes were not investigated.

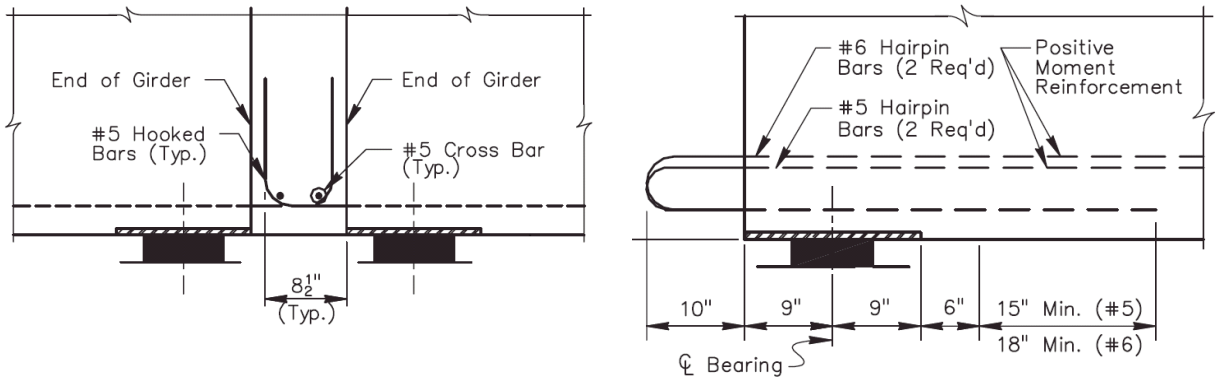

(a) hooked bars or prestressing strands **(b) hairpin bars**

Figure 4
Alternatives for positive moment reinforcement [*1*]

A thorough investigation of prestressed concrete Bulb-T (PCBT) girder bridges with positive moment continuity details as those recommended in NCHRP Report 519 was the subject of a Ph.D. dissertation in Virginia Polytechnic Institute and State University [*22*]. Experimental and analytical investigations were carried out on a 45-in. PCBT. It was concluded by the author that the restraint moments due to thermal influences measured during the study appear equally significant, or even more significant, than the restraint moments due to creep and shrinkage. Therefore, it was recommended that thermal restraint moments should be considered in the design. One specimen had the prestressing strands extend into the diaphragm to provide the positive moment reinforcement, while the other relied on 180º-bent (hairpin) bars. A third specimen was also tested where no continuity diaphragm was provided; however, the deck was cast continuous over the support. It was concluded that the hairpin detail results in a stiffer connection than the bent-up prestressing strand detail, and therefore it was recommended that the hairpin detail be used if a continuous deck is cast over the support. The conducted research only looked at single-line specimens and therefore did not study the effect of bridge skew. Furthermore, the size of the specific PCBT girders used in manufacturing the specimens is almost equal to an AASHTO Type IV. In other words, large Bulb-T sections (e.g., BT-72) have not been investigated.

Louisiana Research on Bridge Diaphragms

In Louisiana, several research projects that address bridge diaphragms were conducted through LTRC. The effectiveness of continuity diaphragms in skewed PSC girder bridges was investigated in LTRC Final Report No. 383 [*23*]. The necessity of providing a continuity diaphragm over skewed bents and its effects on the distribution of stress and deflections were investigated using an elastic finite element model. The parameters considered in the analysis were the skew angle of the bent, span length, girder spacing, girder types, and diaphragm conditions. The analytical results showed that the effect of a continuity diaphragm on the stress and deflection is limited and can be omitted. The authors finally concluded that the continuity diaphragms may improve the load distribution characteristics, but their effectiveness for skewed continuous bridges is limited. Since this effort was based on analytical results, the authors recommended that laboratory tests and field measurements be considered to verify the theoretical results. A field investigation was the focus of the second study on the performance of continuity diaphragms in skewed PSC girder bridges [LTRC Final Report No. 440 - *24*]. In this project, the Burlington Northern Santa Fe (BNSF) overpass was load tested using one truck with a gross vehicle weight (GVW) of 48.66 kips. The span length for the tested overpass was 79 ft. with a skew angle (defined as the angle between the centerline of a support and a line normal to the roadway centerline) of 48º. AASHTO Type III girders spaced at 8 ft. carried an 8-in. reinforced concrete deck. Strains and deflections were compared with those determined through theoretical analyses. The authors concluded that continuity diaphragms used in PSC girder bridges on skewed bents provided additional redundancy in the bridge, but their effects are negligible and caused difficulties in detailing and construction, especially for bridges with high skew angles and/or narrow girder spacing.

Intermediate diaphragms (ID) in PSC girder bridges were investigated by another LTRC project [LTRC Final Report No. 420 - *25*]. Analytical investigations were conducted to assess the need for IDs in precast PSC girder bridges. The results showed that several parameters such as skew, span length, spacing, stiffness of diaphragm, and girder influence the effectiveness of diaphragms in live load distribution for bridges. The research team also tested a bridge over Cypress Bayou on LA 408 East. The authors concluded that reinforced concrete IDs are beneficial in distributing lateral impact forces from over height trucks. Gravity live load distribution is also influenced by IDs, which can be addressed by modification factors to current AASHTO formulas. The stability of precast PSC girders during construction is an issue that can be addressed by steel intermediate diaphragms rather than the reinforced concrete diaphragms, which increase the cost and time of construction.

Calculation of Restraint Moment

Studies on precast/prestressed concrete bridges made continuous started in the early 1960s. Mattock in his fifth study reported an experimental and analytical investigation of the influence of creep of precast girders and of differential shrinkage between precast girders and cast-in-situ deck slab on continuity behavior [*26*]. In this early study, it was concluded that positive restraint moments may develop at the interior support sections of the continuous girders, which may result in cracking at the bottom of the diaphragm at these sections. The developed restraint moments and the resulting cracking, if any, will affect the behavior of girders at the service load level. Design recommendations are suggested for the critical girder sections, considering restraint moments due to long-term deformations.

Freyermuth used the results from Mattock's studies and presented a complete design procedure, popularly known as Portland Cement Association (PCA) method for calculating restraint moments [*27*]. In NCHRP Project 12-29 (Report 322), Oesterle et al. developed a computer program, `BRIDGERM`, to calculate time dependent restraint moments based on the PCA method, with several improvements including time-step analysis proposed by Construction Technology Laboratories (CTL) and is called the CTL method [*21*].

Peterman and Ramirez proposed a modification to the restraint moment calculations by PCA and CTL methods and named it *P*-method, intended for bridges with precast/prestressed concrete form panels [*28*]. McDonagh and Hinkley proposed a new computer program, `RMCalc`, to compute restraint moments using the Microsoft Windows Platform [*29*]. `RMCalc` is essentially a repackaging of `BRIDGERM` where a graphical user interface is added to convert it into a more user-friendly design tool.

The most recent analysis tool was developed as part of NCHRP Projects 12-53 (Report 519) [*1*]. The spreadsheet tool is a program called `RESTRAINT` that calculates restraint moments in continuous PSC bridges. `RESTRAINT` uses both PCA and CTL methods with some modifications. This method is described in detail in the Analytical Model section in the Methodology of this report.

Research Needs

As can be seen from the review of previous work, it is inconclusive whether the benefits of introducing continuity diaphragms justify the additional cost and time required for their construction or not. The performance of continuity diaphragms has also been the subject for debate. Some researchers concluded that the effect of continuity diaphragms on bridge design is of negligible or no structural benefit [*21, 23, 24*]. Other researchers concluded that they perform well if properly designed to avoid loss of continuity [*1, 22*]. Furthermore, the

performance of positive moment continuity details in full size bridges rather than single line laboratory specimens was not investigated to the best of the research team's knowledge, especially for skewed spans.

DOTD seized an opportunity from the construction of a design-build project in Louisiana where the designer adopted the NCHRP 519 positive moment continuity detail. The current study is a research project through LTRC initiated to assess the performance of the detail in a full-size bridge. A structural health monitoring (SHM) approach was adopted for the task. A SHM system was installed and was monitored for almost 24 months since the completion of the bridge in November 2008. A live load test was also conducted in August 2010. This report summarizes the findings from interpreting the SHM data and additional analytical results.

OBJECTIVE

The main objective of this project was to install a monitoring system for the purpose of investigating the performance of a continuity diaphragm detail that is newly introduced in Louisiana and is employed in Bridge #2 of the James Audubon Bridge Project. The investigation of the detail's performance under long-term (creep, shrinkage, and thermal) and live load effects is conducted to validate the performance of the NCHRP Report 519 continuity detail for a skewed span with Bulb-T girders.

The goals of the project were to:

1. Collect, analyze, and interpret field monitoring data to understand the behavior of Bridge #2 under long-term and live load effects.
2. Develop a robust analysis tool that accounts for continuity diaphragm properties and is capable of analyzing general bridge configurations (e.g., unsymmetric span lengths).
3. Provide DOTD with recommendations for the implementation of the NCHRP 519 continuity in future projects based on a full understanding of the behavior of the continuity diaphragm connection detail.

SCOPE

This study focused on the performance of an NCHRP Report 519 positive moment continuity detail in a skewed bridge segment that exists in Bridge #2 of the John James Audubon Project. Because of the nature of the adopted methodology (i.e., SHM) the project activities and findings were limited to the specifics of the monitored bridge (skewed segment with Bulb-T girders). The main focus of the project activities was to monitor long-term (creep, shrinkage, and thermal) effects on the continuity detail. The effects of live loads on the detail were also investigated.

Comparison between the performance of the monitored bridge segment and bridges with different continuity details was not possible because of the lack of monitoring data from similar bridges with different continuity details. Analytical investigations were therefore utilized to provide comparative information.

The results from this investigation were thoroughly documented to serve as a reference point for future projects that monitor similar and other continuity details.

METHODOLOGY

The assessment of the performance of positive moment continuity details was assessed using three different approaches. They are:

- SHM of a bridge in service that employs the detail from the beginning of construction.
- Assessment of the restraint moments that develop in continuous structures over a wide range of parameters using the computer program `RESTRAINT` after expanding its capabilities to include conditions specific to the bridge used in this study.
- Finite element (FE) analyses of global as well as local behavior of the monitored bridges.

The performance of the positive moment continuity detail was assessed for long-term and live load effects. The following sections describe the details of all three assessment methods and the live load test.

Structural Health Monitoring

A structural health monitoring plan was devised for the bridge chosen by DOTD to conduct the assessment study. This section describes the details of the monitored bridge, instrumentation plan, data processing, and interpretation.

Description of Monitored Bridge

Bridge #2 is one of eight bridges in the John James Audubon Project that will add a new transportation artery across the Mississippi River between the cities of New Roads and St. Francisville [see Figure 5 (a)]. The purpose of Bridge #2 is to cross an existing railway track. It was constructed by Boh Brothers, as the general contractor, using precast girders produced by Dunham Price in their casting yard in Lake Charles. The 52-span bridge has a total length of about 4000 ft., which is divided into 14 continuous segments. DOTD chose a 242-ft. segment for monitoring the performance of the adopted continuity detail. The segment is a three-span continuous superstructure with a skewed layout for its middle and longest span (102 ft.). The exterior spans were 70 ft. long and can be seen in Figure 5(b). Because of the 45^{o}-skew of the middle span, the girders supporting the exterior spans range in length from 51 ft. to 89 ft. as can be seen in Figure 6(a). The chosen segment was constructed using AASHTO Bulb–T girders (BT-72). Because of the antisymmetry of the bridge, only one of the identical intermediate bents (Bent 24 and Bent 25) was chosen for the investigation. This segment was chosen because of its configuration, which has not been covered by the tests

conducted and reported in NCHRP Report 519, namely skewed configuration and Bulb-T girders.

Figure 6(b) shows a cross section of the monitored bridge segment, which supports a clear roadway width of 38 ft. on five prestressed BT-72 girders spaced at 8.25 ft. The 7.5-in. reinforced concrete deck was monolithically cast with the continuity diaphragm joining adjacent girders over intermediate bents. Hairpin bars were embedded in the girders and extended 8 in. outside the girder ends to provide positive reinforcement. It should be noted that the girders are supported by rubber bearing pads over typical pile bents.

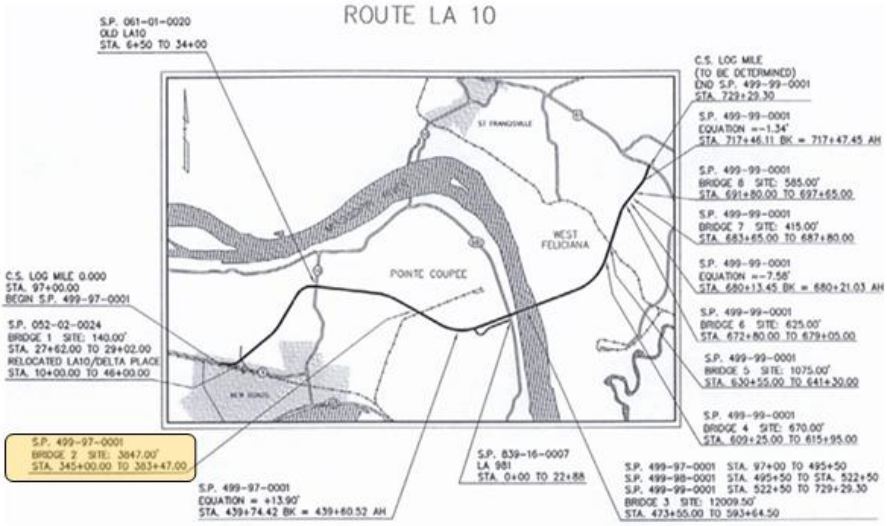

(a) Map of bridge site location

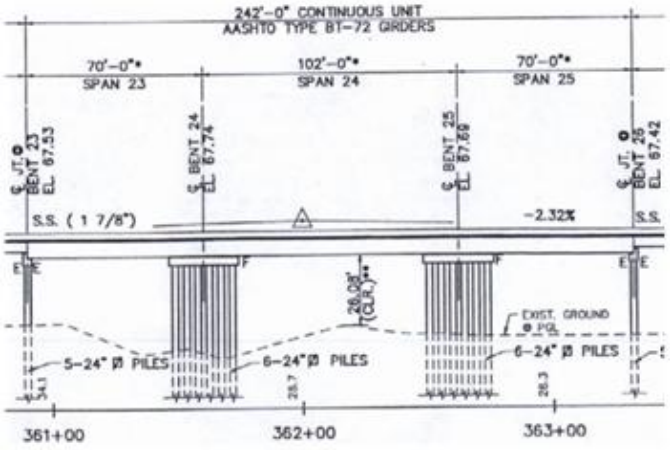

(b) Elevation of chosen segment

Figure 5
Bridge #2 chosen by DOTD for monitoring the continuity detail

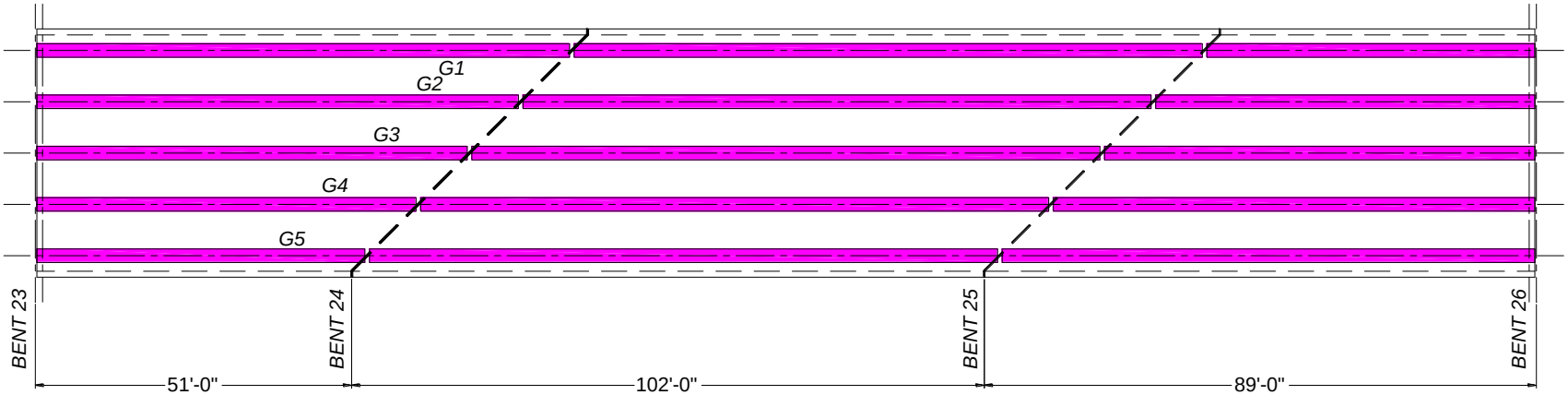

(a) Bridge layout

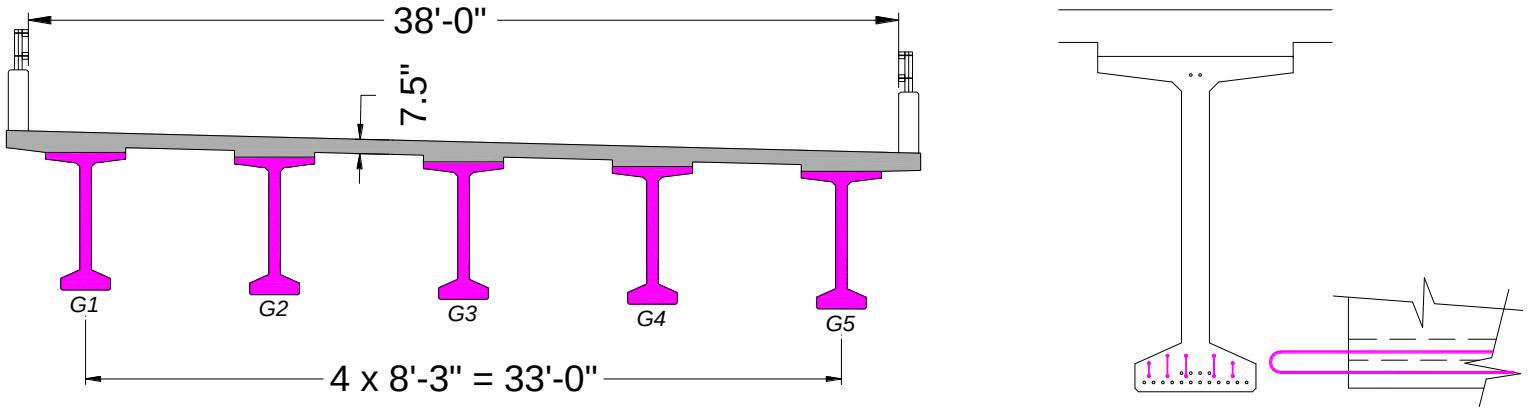

(b) Cross section and continuity detail (5#5 hairpin bars)

Figure 6
Main dimensions of monitored Bridge #2

Material Properties and Fabrication Details

The PSC girders were cast in June 2008. Three standard concrete cylinders and one prism were taken from the monitored beams and were tested in the Concrete Research Laboratory at LTRC. Two of the cyclinders were tested to determine the compressive strength after 28 days according to ASTM C 39 and the third cylinder was used to determined the concrete's modulus of elasticity, E_c, according to ASTM C 469 [*30, 31*]. The modulus of rupture was determined using the 6 in. x 6 in. x 20 in. three point bending according to ASTM C 78 [*32*]. The deck specimens from the deck pour were also collected and tested. Three cylinders were tested in compressive strength; one cylinder was tested for the modulus of elasticity, and a splitting tensile strength test was conducted instead of the modulus of rupture test (ASTM C496) [*33*].

The design compressive strength for the Bulb-T girders and bridge deck concretes were 8,000 psi and 4,000 psi, respectively.

Table 1
Mechanical properties for concrete

Test	Girder / Span							Deck
	G1 S23	**G3 S23**	**G1 S24**	**G3 S24**	**G4 S24**	**G5* S24**	**G5** S24**	
Date of Pour	6/13	6/13	6/18	6/18	6/18	6/18	8/9	11/18
Date of Test	7/11	7/11	7/16	7/16	7/16	7/16	9/9	12/16
Age (days)	28	28	28	28	28	28	31	28
ASTM C 39 (psi) (f_c' - Cylinder #1)	8864	9711	9420	10079	10555	10579	10766	—
ASTM C 39 (psi) (f_c' - Cylinder #2)	9101	9480	9266	9860	10429	10322	10912	—
Average (psi)	**8983**	**9596**	**9343**	**9970**	**10492**	**10451**	**10839**	**6591**
ASTM C 469 (ksi) (E_c - Cylinder #3)	**6450**	**6600**	**6100**	**6450**	**5850**	**6450**	**5850**	**6175**
ASTM C 78 (psi) (f_r - Prism)	**948**	**1082**	**1165**	**1150**	**1074**	**1171**	**1203**	—
ASTM C 496 (psi) (f_{sp} - Prism)	—	—	—	—	—	—	—	**372**

* Rejected girder ** Replacement girder

The stress strain relationship for the prestressing strands was obtained from the project's records and can be seen in Figure 7. The points that can be seen on the smooth relationship are digitized points on the plot to help establish a theoretical stress-strain relationship for future analyses.

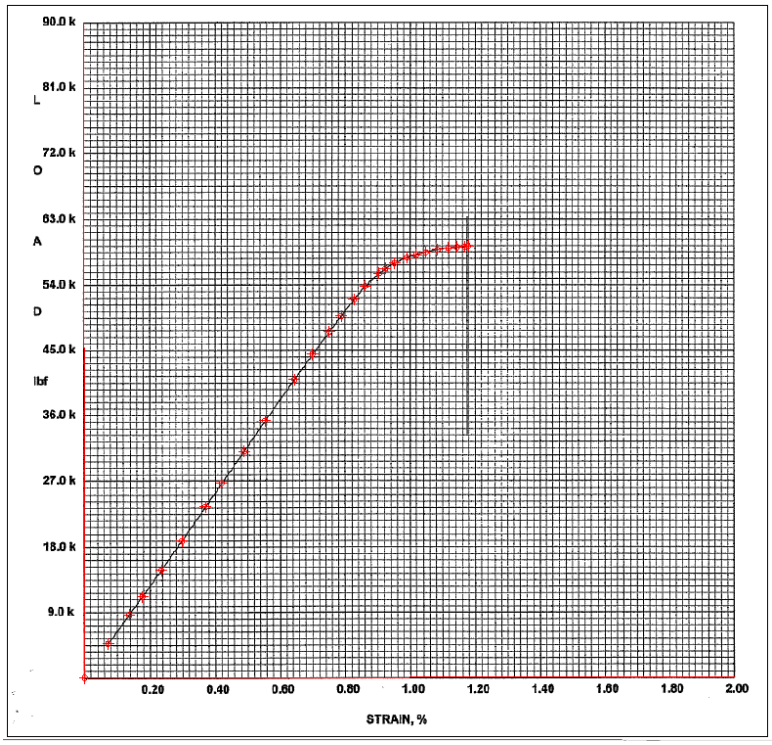

Figure 7
Stress-strain relationship for prestressing strands

Instrumentation Plan

The monitoring system was designed to capture: (1) the tensile force in the positive moment reinforcement, (2) the strain distribution at key locations (intermediate bent and midspan), (3) differential shrinkage between cast-in-place (CIP) deck and precast girders, (4) the degree of continuity between adjacent girders, (5) the development of cracks of gaps at the continuity diaphragm, and finally (6) the corresponding temperature for each of the recorded readings. In selecting the sensor locations, the research team identified the most critical locations that deliver the information required to assess the performance of the continuity detail. In most locations where embedded sensors were employed, two sensors were used to reduce the risk of losing sensors during the casting of girders. Furthermore, surge protection was provided to one of the two sensors at the same location in case lightning hit the bridge and replacing embedded sensors is not possible.

One of the major causes of the development of positive moment in continuous structures is long-term effects, namely, creep and thermal deformations. Therefore, all of the selected gages employed vibrating wire technology. Vibrating wire gages convert the change in resonant frequencies in an internal wire into an output reading that represents the relative movement between the wire ends. Gages that can measure strain, displacement, and slope are available and were employed in the system. Table 2 lists the type and number of each of the employed sensors. Both embedded and external (surface mounted) sensors were used. The technical specifications for the sensors used in this study are summarized in Table 3. The total number of sensors installed from each type is listed in Table 2. Reducing the number of sensors was possible by taking advantage of the bridge's antisymmetry shown in Figure 8 under symmetric loading conditions such as long-term effects, which is the focus of this study. Three positive moment connections were fully instrumented (connecting Griders G1, G3, and G5) at the support. Embedded sensors were installed in the deck over the support at the remaining two girders. At midspan, three girders (Girders G3, G4, and G5) were fully instrumented. Along the midspan line, Girder G1 is identical to Girder G5 and Girder G2 is identical to Girder G4. Therefore, information across the the midspan section is attainable.

Figure 9 shows the final instrumentation plan where the monitored girders, sensor types, locations, and numbers can be seen. It should be noted that this plan is almost identical to the approved instrumentation plan except for a few minor changes. For example, Girder G5 was not instrumented with embedded strandmeters because the research team was not informed by the precaster of its casting date. Another example is also related to Girder G5 in Span 24 where all sensors in the approved instrumentation plan were initially installed. However, due to circumstances beyond the research team's control, that girder was rejected by the contractor because of an error in dimensions. As a result, the research team had to install new sensors in the replacement girder with less than a 24-hour notice. It was only possible to install four of the six embedded sensors in the original plan, i.e., two strandmeters at the midspan were not installed in the replacement girder. The decision to install the available strandmeters at the support was based on prioritizing that location because of its vicinity to the continuity and because there were sisterbars at the midspan that would still yield useful information for that location.

Table 2
Types and number of sensors employed in this study

Sensor Type	Measurement	Location	Number
Sisterbars (VW4911)	Strain in concrete	Embedded	12
Strandmeters (VW4410)	Strain in reinforcement		16
Strain gages (VW4000)	Surface strains	Surface Mounted	29
Gapmeters (VW4420)	Gap width		3
Tiltmeter (VW6350)	Slope		6
Crackmeter*	Crack width		7
		Total:**	**66**

*Crackmeters were not installed due to lack of significant cracking.

**Excluding uninstalled crackmeters

Table 3
Technical specifications of employed sensors

Type	Frequency Range (Hz)		Gage Length	Measurement Range
	Low	High	Inches	
EC = Sisterbar	1200	2800	n/a	2500 (microstrain)
ES = Strandmeter	1500	2700	8.0	20000 (microstrain)
TM = Tiltmeter	1400	3500	n/a	+/- 10 degrees
VW = VW Strain Gage	500	1100	5.875	3000 (microstrain)
DM1 = (1 in.) Crackmeter	1400	3000	13.1	1.00
DM2 = (2 in.) Gapmeter	1400	3000	14.9	2.00

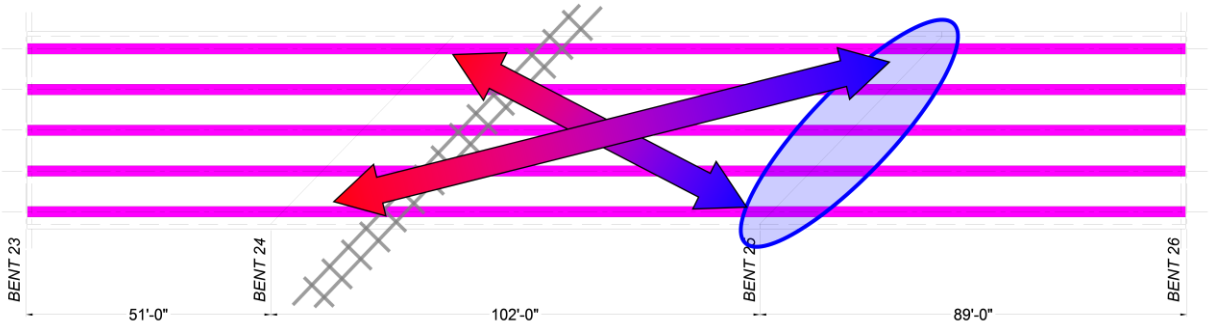

(a) General Layout

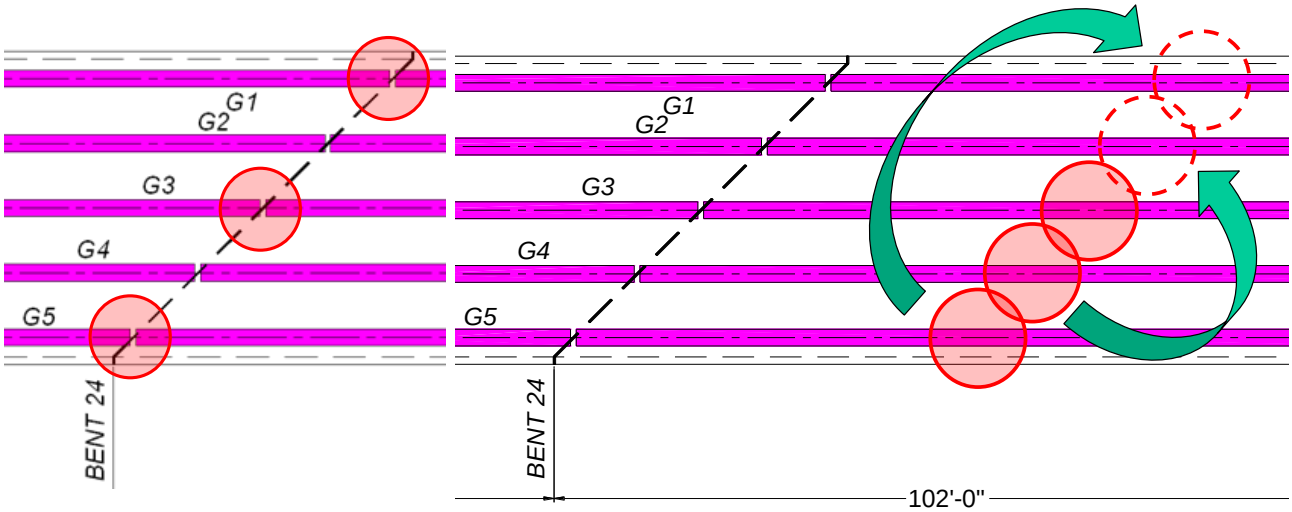

(b) At Continuity **(c) At Midspan**

Figure 8
Antisymmetry of Bridge #2 allowed monitoring only one of the continuity details

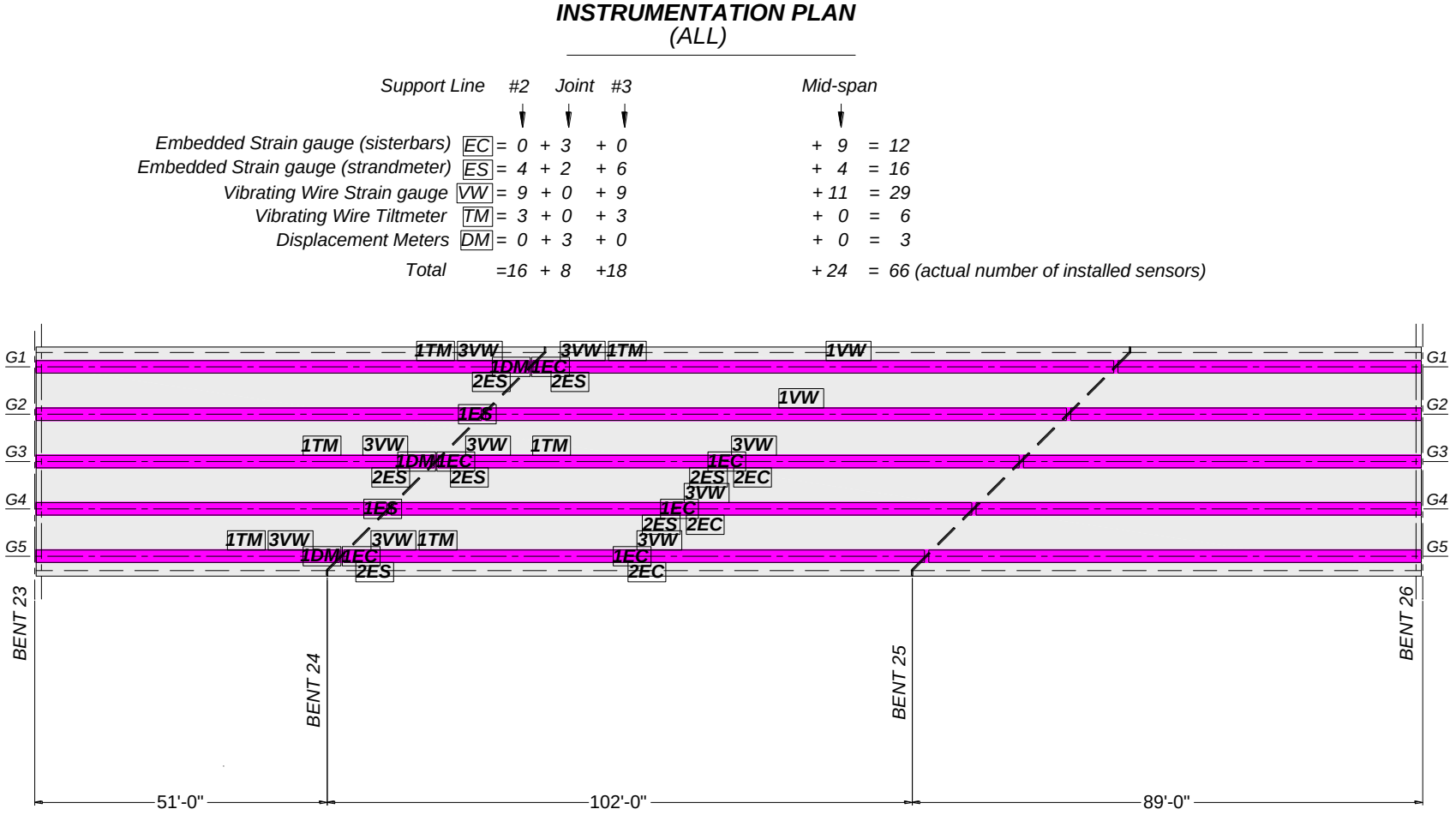

Figure 9
Instrumentation Plan for structural health monitoring of positive moment continuity detail in Bridge #2

Figure 10 shows the schematics of the sensor locations at the monitored sections. The embedded strandmeters (ES) were installed on hairpin bars or deck reinforcement at the girder ends and on prestressing strands at midspan. Sisterbars (EC) were placed next to reinforcing bars in the deck or prestressing strands in the girders. Surface-mounted sensors were installed using mechanical anchors to the girder's surface. Three vibrating wire gages (VW) were installed at each monitored location. At the support, both sides of the continuity diaphragm were instrumented to study its ability to transfer forces from girders in one span to girders in the adjacent span. Tiltmeters (TM) were also installed at both sides of the continuity diaphragm to provide additional information about the level of continuity that the adopted detail is able to provide. Finally, a gap meter (DM) was installed to measure the relative movement between the bottom of girder ends. A pictorial documentation of the installed sensors and more details about them (serial numbers, and multiplexer [MUX] channel connectivity) can be found in Appendix A.

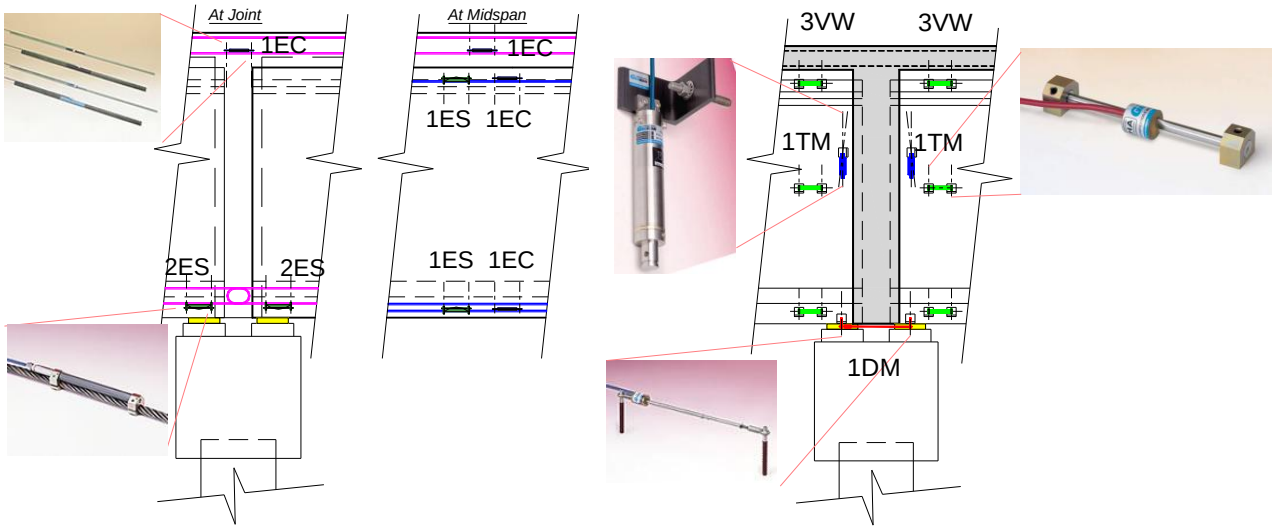

(a) Embedded sensors **(b) Surface-mounted sensors**

Figure 10
Sectional locations of embedded and surface-mounted sensors in Bridge #2

All the sensors were grouped into six multiplexers, which were then connected to a Campbell Scientific datalogger. The datalogger is powered by one DC battery, which is recharged by a solar panel. The datalogger is equipped with a cellular modem that allows remote access to the data through an internet (IP – Internet Protocol) connection as can be seen in Figure 11. Two monitoring setups were used for the project. The first temporary setup covered the period while the girders were curing in the casting yard. Out of the 22 installed embedded sensors, only 18 were connected to the monitoring system because some of the girders were stored far away from the datalogger, which rendered extending their wiring virtually

impossible. It should be noted that the final number of embedded sensors including those in the deck was 28. The casting yard setup lasted for 32 days until the girders had to be transported to the bridge site. The second monitoring setup was the permenant one, which came into service on January 9, 2009.

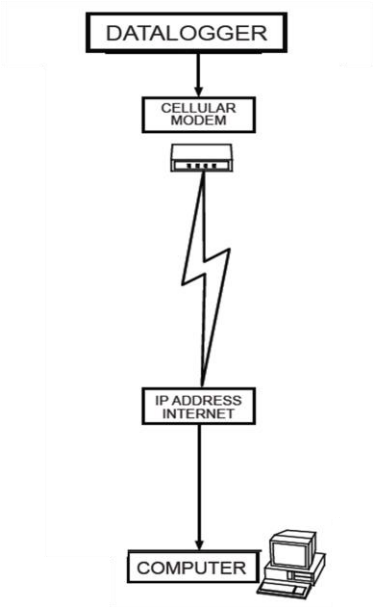

Figure 11
Communication between the datalogger (station) and the server

Data Processing

Raw data obtained directly from the logger had to be first processed before it could be interpreted. The processing includes cleaning the record from any outliers, joining or disjoining records in case data channel was changed during the monitoring period, and temperature correction as specified by the sensor manufacturer. The following few sections briefly describe all three steps of data processing.

Removal of Outliers. As stated earlier, average hourly readings were recorded during the normal operation of the datalogger. If for any reason one of the 24 readings averaged within an hour was bad (e.g. due to a lightning hit or low voltage input), the recorded hourly average was affected and became an undesirable datapoint. The large size of data (69 sensors over 24 months) made the task of removing outliers manually a daunting task. Several data cleaning scripts were tested before the research team developed its own data cleaning routine that performs the task on a global scale first before scrutinizing a smaller user-specified window for any datapoints that fall out of a user-specified range of acceptable tolerance. Figure 12 shows plots of the raw and cleaned data records for sensor

#22. It should be noted that the erratic readings during the period between 11/2009 and 03/2010 were due to inadequate power supply from the solar panel, which affected three sensors and was remedied in March 2010. In all cases, outlier datapoints were replaced with a Not-A-Number (`NaN`) record.

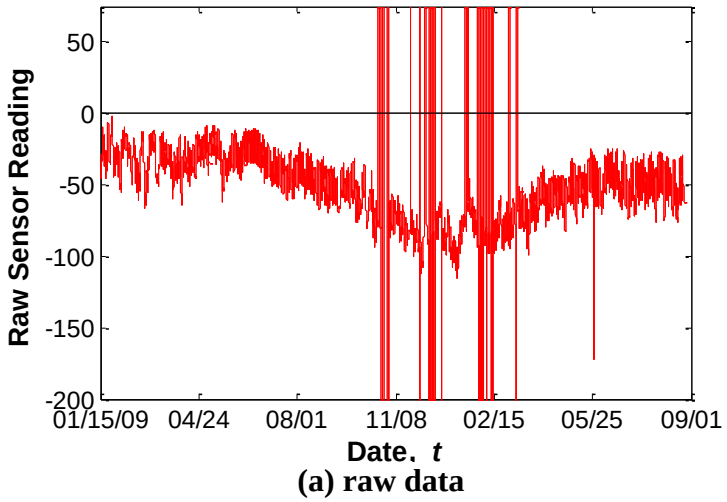

(a) raw data

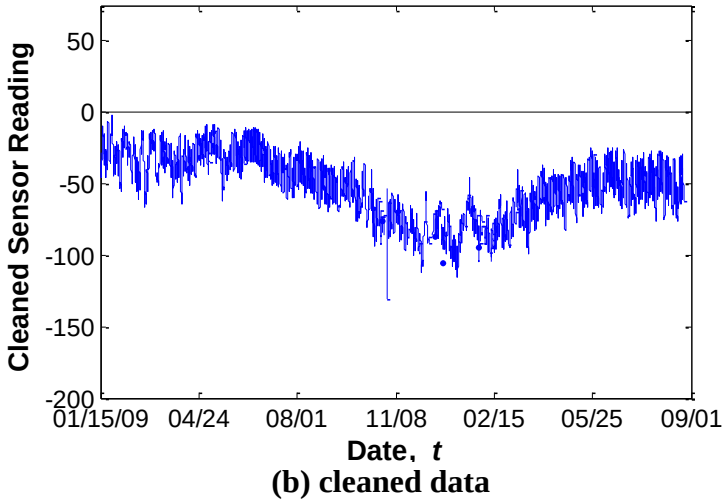

(b) cleaned data

Figure 12
Removal of outliers from raw data
(Sensor #22 – VW on G1 [bottom] at Bent 24 in Span 23)

Temperature Correction. The manufacturer of the vibrating wire gages used in this study recommends correcting the recorded raw data to account for temperature variations that affect the length of the vibrating wire inside the gages, and hence, affecting its readings. Temperature corrections were applied to all the sensors used in this study except for tiltmeters, for which temperature correction is not highly recommended. Figure 13 shows a plot of raw and temperature corrected data for a sisterbar and a strandmeter at the same

location (bottom of Girder 3 in the middle of Span 24). It can be seen in Figure 13(a) that the recorded raw data are quite different. This is mainly due to the different characteristics of both sensors such as different gage lengths. Figure 13(b) shows that once the temperature correction is applied, the trend and range of variations from both sensors match very well. The shift between the reading may be due to the condition at the initial stages when the girder concrete was poured. If another datum is chosen, the shift between the relative strain recorded by both sensor types would drop substantially.

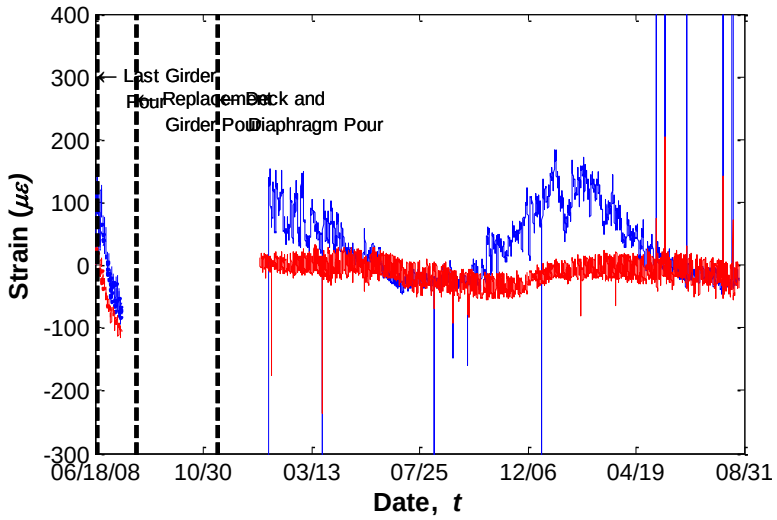

(a) raw data

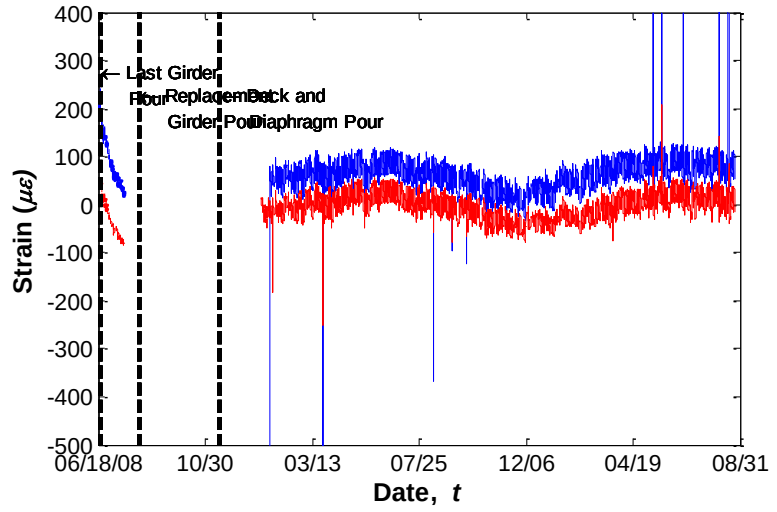

(b) temperature corrected data

Figure 13
Temperature correction
Sensors #88(ES) and #92(EC) in G3 (bottom) at Midspan 24

Joining Data Records. During the fine tuning process of the system, two of the sensors were found to be malfunctioning. Both sensors were tiltmeters. In the trouble shooting phase, the malfunctioning tiltmeters were moved to different logger channels before ultimately replacing them. The records from different sensors at the same location had to be joined from different channels in the system after adjusting the relative readings at the begining of each phase to the relative reading at the end of each phase. Figure 14 shows readings from tiltmeters on Girder G1 at both ends of the continuity diaphragm. It can be seen that one of the records reflects the expected trend due to seasonal temperature variations while the other one (on Span 24) was almost constant until it was replaced with a malfunctioning tiltmeter (period between June 2009 and October 2009).

Finally, when the sensor was replaced on October 7, 2009, a similar trend can be seen on both sides of the continuity diaphragm.

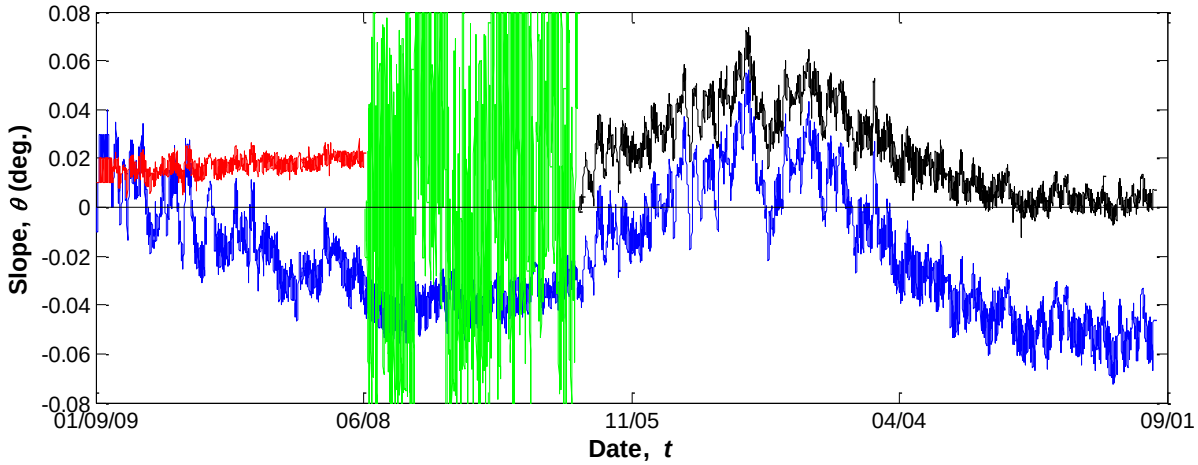

Figure 14
Joined data record for TM at G1 in Spans 23 and 24

Continuity Assessment

The level of continuity achieved by this detail was investigated using the acquired monitoring data. The sensors installed on both sides of the continuity diaphragm were used for that purpose. Readings from similar sensors (e.g., tiltmeters of both sides or strandmeters on hairpin bars on both sides) were compared. Theoretically, such readings should be equal to unity if full continuity is achieved. However, differences between the readings are always observed. The ratio between the readings from Span 23, R_{23} , and Span 24, R_{24} , was determined, and an overall index for the continuity was assessed based on the RMS (root mean square) of all ratios calculated during the entire project period.

Analytical Model

In this section, the analysis model used in conducting the parametric study is described. It is based on the RESTRAINT program that was developed as part of NCHRP Project 12-53 (Report 519) [*1*]. Because of the limitations that this program has, the research team modified it to expand its capabilities such that it could analyze a bridge with the configuration of Bridge #2. Furthermore, RESTRAINT was used to conduct parametric studies from which recommendations for the age of continuity were established.

RESTRAINT Program (NCHRP Report 519)

As mentioned earlier in the Introduction, Miller et al. developed an analytical model for the calculation of the restraining moment, M_r [*1*]. This spreadsheet analytical model was later used to conduct parametric studies on a continuous system with different moment connections. The model is based on BRIDGERM, which was developed as part of NCHRP Project 12-29 (Report 519) and was named RESTRAINT [*21*]. The program was initially developed to model a two-span continuous structure where the analysis is conducted on lines of girders and not the entire bridge. The model assumes that girders are supported at both ends. RESTRAINT uses a flexibility-based analysis where the structure is discretized into several elements to predict the time-dependent response of precast/prestressed concrete girders made continuous [*34*]. RESTRAINT accounts for the creep and shrinkage effects, prestress losses, age at loading, and construction sequence. Creep due to prestressing forces cause positive restraint moments in continuous bridges as a result of the upward camber movement. Conversely, creep due to superimposed dead loads (after the introduction of continuity) cause negative restraint moments. Shrinkage of the concrete deck due to loss of moisture also causes a downward deflection and, therefore, causes negative restraint moments. The program uses creep and shrinkage strains based on the relationships given in the ACI-209 report. The program also accounts for a loss of prestressing force using the method given in the Precast Concrete Institute (PCI) handbook. Within each span, shrinkage of the deck and girder is assumed to be uniform, while creep caused by dead load plus prestressing force is assumed to be parabolic. The program allows different casting dates for the diaphragm, i.e., introduction of continuity and deck pouring. Since the diaphragm is not prestressed, the creep due to prestressing is taken as zero. Furthermore, the differential shrinkage between the slab and diaphragm is assumed to be zero since they are usually cast together.

Limitations of RESTRAINT

RESTRAINT is capable of analyzing multispan bridges to estimate the restraint moment caused by the major factors that affect the behavior of continuous bridges, namely creep,

shrinkage, age on continuity, and prestress losses. However, the program has limitations to its range of applicability, which are summarized in the following:

- Span lengths have to be symmetric along the center of the bridge. In other words, if a three-span bridge is to be analyzed, the first and third spans have to be equal. This limitation rendered the program unusable for the analysis of Bridge #2, except for the Girder G3 line where the span lengths are symmetric. This limitation severely reduces the number of bridges within RESTRAINT's capabilities as many bridge span lengths are controlled by site conditions and cannot be freely configured to be symmetric.
- RESTRAINT does not provide an option to enter specific properties for the continuity diaphragm, since it is assumed that only one support exists at each bent. The research team was interested in studying the effect of changing the diaphragm stiffness to simulate the development of cracks in the diaphragm and its effect on the response of the bridge.
- Only typical AASHTO type girders (I through VI) could be analyzed using RESTRAINT. If the dimensions of the girders in a specific project or the strand layout do not conform to the standard AASHTO configurations, RESTRAINT cannot be used for the analysis. Furthermore, the strand layout is used for all spans regardless of the span length.

Modified Program mRESTRAINT

Because of the limitations listed in the previous section, the research team developed a modified version of the program mRESTRAINT. The modified program addresses all the aforementioned limitations and is part of the deliverables of this project. Appendix B presents a summary of the introduced modifications. It should be noted that mRESTRAINT range of analysis has been extended for girder ages up to 20,000 days (about 55 years).

The major challenge in modifying the program was introducing the unsymmetric configurations. Symmetry simplifies the analysis considerably, which is suitable for a spreadsheet application. Because of the complexity of moment calculations for unsymmetric general configurations, the introduced modifications were programmed in Visual Basic for Applications (VBA) within the spreadsheet. VBA is used in the original RESTRAINT for the graphical user interface (GUI). In mRESTRAINT, additional VBA code was added to calculate the restraint moment as a replacement to the spreadsheet calculations that limit its applicability. mRESTRAINT is an open source program and the additional code can be viewed from within Microsoft Excel.

Parametric Study

A parametric study was conducted to analyze different bridge configurations for the purpose of estimating the restraint moment, M_r. The results from the study were used to understand how each of the investigated parameters affected the development of the restraint moment. Based on these results, it was possible to establish minimum girder age so that a certain performance criterion (acceptable level of restraining moment, $M_{r,a}$) can be met.

In choosing the parameters to be included in the investigation, information published in the literature was used. The identified parameters were: (1) girder age at the time of introducing continuity and (2) stiffness of continuity diaphragm. In addition to these two parameters, the bridge configuration was also covered by studying cases with (3) different number of spans and (4) different span length ratios. Although `mRESTRAINT` is capable of analyzing bridges with up to five spans, only two-span and three-span bridges were covered. The justification behind limiting the number of spans to three is that the effect of additional spans becomes negligible on the continuity detail in question. The diaphragm stiffness, which is represented by its moment of inertia, I_d, is varied over a wide range. An uncracked diaphragm would have I_d equal to the gross moment of inertia, I_g, of the girder's cross sectional dimensions. If the diaphragm is completely damaged, I_d would be taken equal to zero. NCHRP Project 12-53 (Report 519) recommends that the age of continuity be taken equal to 90 days. Therefore, the range of this parameter was varied around that value. Table 4 lists the range of parameters covered in this study. A total of 120 cases were considered. They are designated with names that reflect the parameters for each case. For example, 2S-0.75R-0.5D-180C denotes that the number of spans (S) in the bridge is two with their span lengths ratio (R) of 0.75:1, ratio of diaphragm stiffness (D) equal to 0.5, i.e., $I_d = 0.5\ I_g$, and the corresponding age of continuity (C) is 180 days. Figure 15 shows a sample plot for the results from one set of analysis in which the effect of age on continuity is clear. As the age of girder at the time of introducing continuity increases, the restraint moment decreases. If the continuity is introduced after 180 days, no positive restraint moment is to be expected and the continuity diaphragm will be subjected to a negative restraint moment.

Table 4
Range of investigated parameters

Parameter		Investigated Values				
Number of Spans		2	3	—	—	—
Span Length Ratio	2 Spans	1 : 1	0.75 : 1	0.50 : 1	—	—
	3 Spans	1 : 1 : 1	1 : 1.5 : 1	1 : 2 : 1	—	—
Diaphragm Stiffness I_d		I_g	0.50 I_g	0.25 I_g	0.125 I_g	0.05 I_g
Age of Continuity (days)		28	60	90	180	—

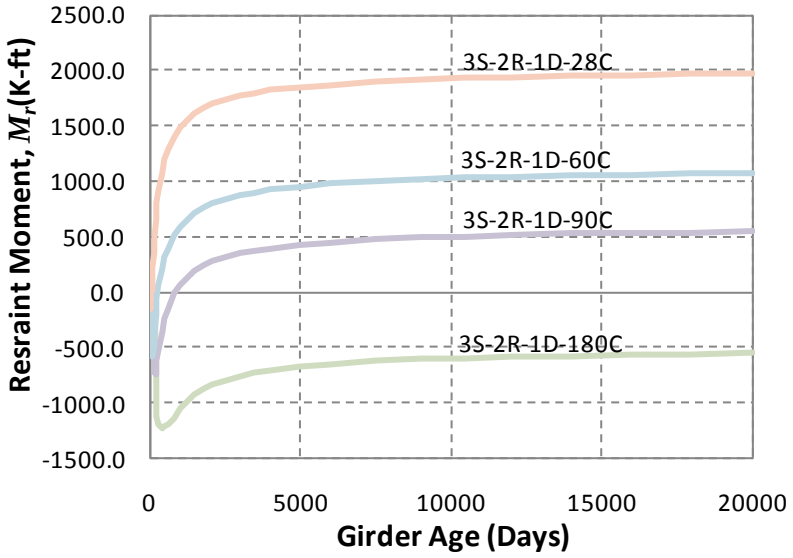

Figure 15
One set of results showing the effect of age of continuity on M_r

Methodology for Establishing Age of Continuity

The results from the parametric study were used to better understand the required girder age at which continuity can be introduced such that a prespecified restraint moment value is not to be exceeded. To limit cracking in the continuity diaphragm or girder ends due to positive restraint moments, acceptable restraining moment, $M_{r,a}$, levels were considered. In addition to the maximum design moment value recommended in NCHRP Report 519 $M_r = 1.2\ M_{cr}$, lower values were considered [*1*]. These are 50 percent, 25 percent, 10 percent, 5 percent and 0 percent of the cracking moment, M_{cr}. The acceptable $M_{r,a}$ values considered in this study were determined for the two elements susceptible to cracking at the joint, i.e., girder ends and diaphragm. The cracking moment for the diaphragm was calculated using the diaphragm's material properties and the following formula:

$$M_{cr} = \frac{f_r . I_g}{y_t} \quad (1)$$

where,

f_r = modulus of rupture for the diaphragm's concrete,
I_g = moment of inertia of the girder,
y_t = distance from neutral axis to the top of the girder,
P_e = prestressing force,
A_g = area of the girder, and
e = eccentricity.

Considering the cracking of girder ends, another value for the cracking moment was also considered based on the material properties of the prestressed girders. This value was used to determine appropriate continuity age that would not cause the girder ends to crack. Cracking at ends of prestressed girders is a serious issue especially if it takes place in the bottom flange. It could lead to a loss of anchoring the prestressing strands, which may adversely affect shear capacity at this critical location. Because of the existence of prestressing forces in the girder, the following formula was used:

$$M_{cr} = \left[\left(\frac{f_r . I_g}{y_t}\right) + \left(\frac{P_e . I_g}{A_g . y_t}\right) + P_e . e\right] \quad (2)$$

where,

P_e = prestressing force,
A_g = area of the girder, and
e = eccentricity.

In determining M_{cr} for prestressed girders, the effective prestress value is calculated at a transfer length of 4 in. from the girder end, which corresponds to the face of the diaphragm assuming that the girders are embedded 4 in. into the diaphragm as is the case for Bridge #2. The rate of prestress transfer is assumed to be linear for each case as shown in Figure 16 [*35*].

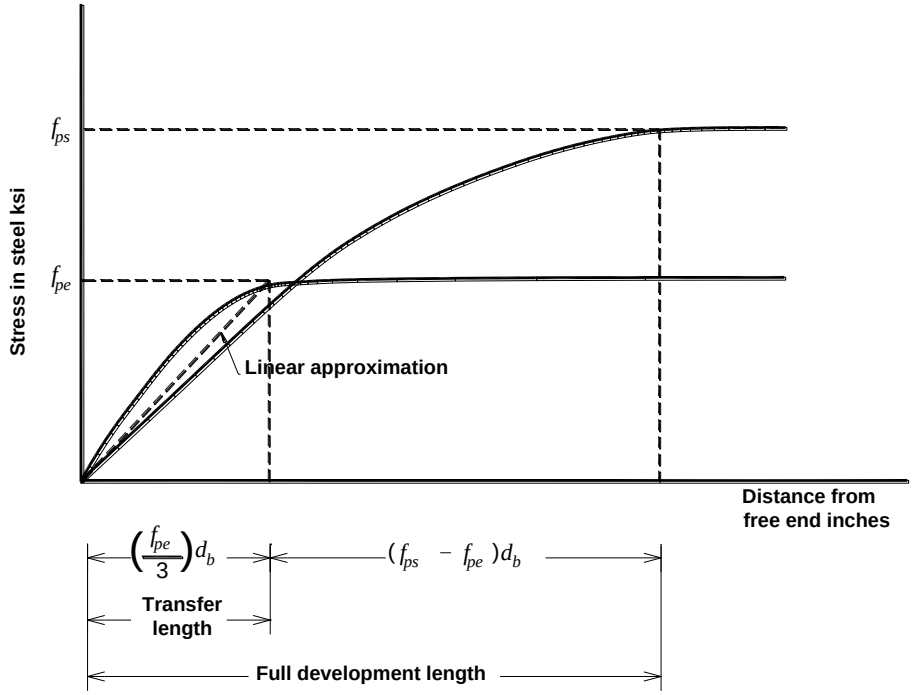

Figure 16
Transfer length model used in estimating M_{cr} at girder ends [*35*]

The transfer length (l_t) of the girder is calculated using the following equation:

$$l_t = \left(\frac{f_{pe}}{3}\right) d_b \tag{3}$$

where,
d_b = diameter of prestress strand, and
f_{pe} = effective prestress.

Once the cracking moment is determined, the preset acceptable positive restraint moment, $M_{r,a}$, is used to determined the age at which this moment level intercepts with a curve that represents the results for the same case with different continuity ages. This approach is illustrated in Figure 17. In the figure, three curves for the 2S-1R-1D, 2S-0.75R-1D, and 2S-0.5R-1D cases are plotted. These curves are obtained by connecting the points representing the restraint moment value and corresponding age continuity from the parametric study. Four points corresponding to results from 28, 56, 90, and 180 days are used to construct each curve. For an assumed $M_{r,a}$ value (horizontal dashed line), the horizontal line intercepts the three curves at approximately 48, 57, and 75 days (marked with a star on the *x*-axis). This approach is repeated for all analyzed cases. The results are then studied to evaluate the 90-day recommendation in NCHRP Report 322. More details about the approach and the results can be found elsewhere [*36*].

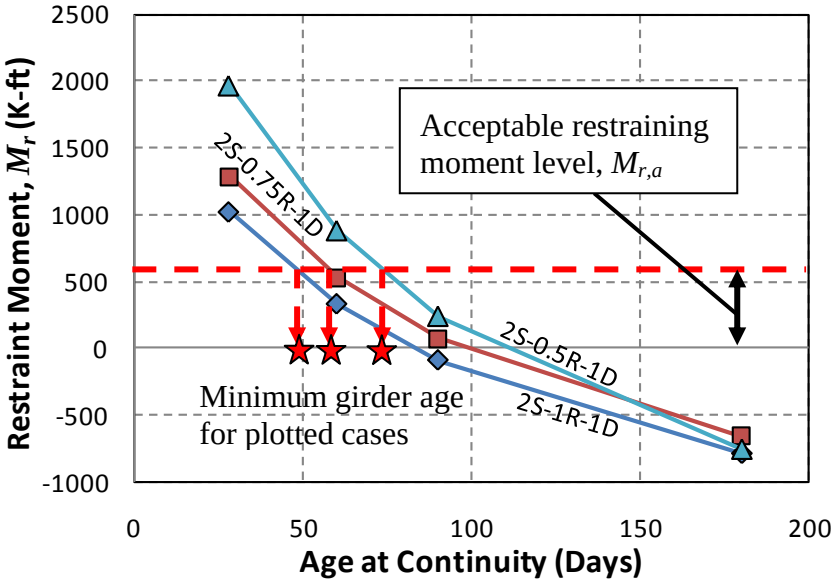

Figure 17
Determining girder age that achieves prespecified M_r criteria

Finite Element Models

Finite element analysis software ANSYS was used to model and analyze the behavior of Bridge #2 [*37*]. This section briefly describes the models that were used in the analysis. Material parameters used for different elements are also discussed here. The modeling of the material properties and boundary conditions are also described here. Details of the element types used in the analyses can be found in Appendix F.

Three models were built for this study. The first model is a global bridge model in which all three spans and five girders are modeled. This model is used for analyzing the global behavior of the bridge. The second model is the single girder model where all three spans are modeled, however, only one of the girders is analyzed. This model allows for more details in the analysis (e.g., sequence of construction) and is used to study the transfer of forces between girders in adjacent spans. A third more detailed model is the joint model. This very fine model focuses on one joint that allows the use of a finer mesh. It is used to study the stress distribution on a smaller scale than the previous models. All three models are described next.

Single-line Girder Model

The meshing of the girders in the cross-sectional view can be seen in Figure 18. The girder is modeled in such a way that the prestressing strands and the hairpin bar coincides with the boundary of the concrete element. A perfect bond assumption is implied since both concrete and reinforcement (strand and bar) elements share the same node. The location of the

prestressing strands and the hairpin bars is shown in Figure 18(b). Figure 19 shows a single-girder line model for Girder G3 where the middle span length is 102 ft. and the exterior spans are 70 ft. long. It can be seen that at the girder ends, a finer meshing is adopted to enhance the quality of the results where they are needed.

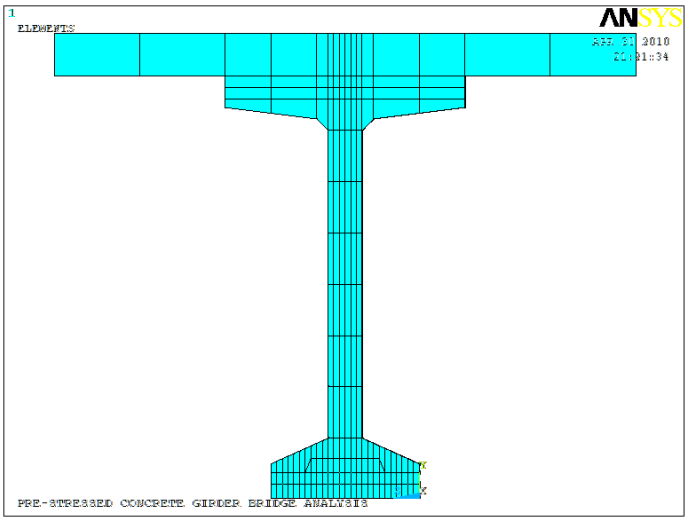

(a) Whole section

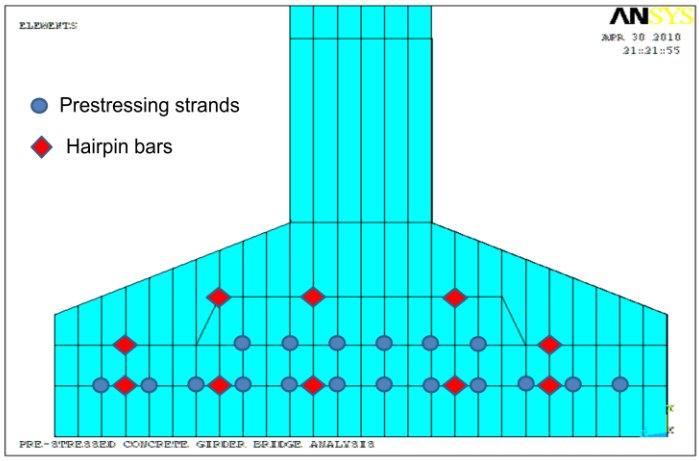

(b) Bottom flange showing reinforcement

Figure 18
Meshing of cross section

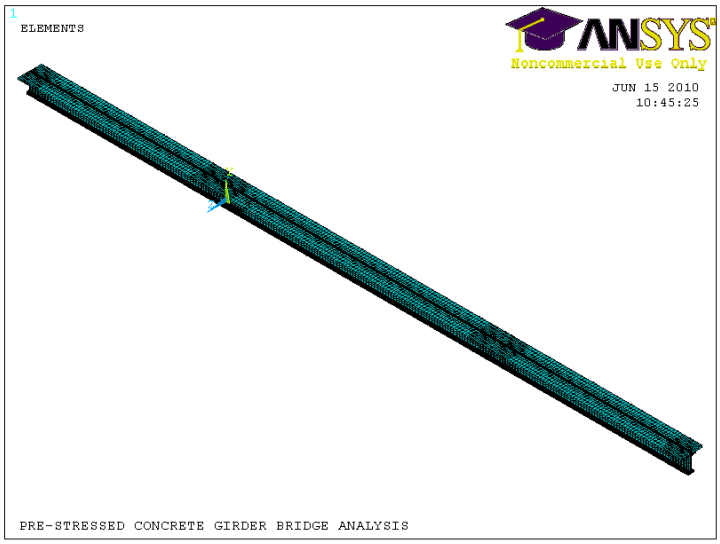

Figure 19
Centerline model for Girder G3

Material Properties. The bridge model is intended for elastic analysis. For this linear elastic material, properties are used here both for the concrete and for steel. The concrete strength for the bridge is different for different components. The strength of the concrete for the girder is not the same as for the deck and diaphragm. The input parameters for the concrete were the 28^{th} day's compressive strength, modulus of elasticity, the Poisson ratio, and the density of the concrete. The coefficient for thermal expansion of concrete is also used as an input parameter. However, the thermal conductivity and the specific heat of concrete are also used as an input parameter for thermal physics environment. Material properties for the prestressing steel and the hairpin bars were the elastic modulus and the Poisson ratio. Prestress is applied as an initial strain in the real constant parameter. Coefficient of thermal expansion is also used as an input parameter for temperature loading. For the thermal physics environment, the thermal conductivity and the specific heat are used as input parameters for the steel.

Boundary Conditions. After modeling the bridge, proper boundary conditions are applied to obtain the desired responses. The ends of the girder rest directly over the bent with or without the bearing pads. Thus a vertical reaction component develops there. Again to make the girder end continuous, diaphragms are poured in between the girder ends. In the model, the girder end nodes are constrained in the *y*-direction, preventing its movement in the vertical direction. However, to make the structure stable, a single node at the end of one girder is pinned, i.e., both the longitudinal and the transverse direction movement were restrained.

Two different physics environments were used in the analysis, namely the thermal and structural environments. The full-scale bridge was modeled before applying the thermal load on it. In this step, the temperature is applied at the node in different location following the AASHTO thermal gradient. Depending on the material properties and thermal conductivity, the thermal problem solved nodal temperatures for each element are ready for subsequent analyses. The solution is then stored in a result file, which is later called in for subsequent use in other loading steps.

In the structural physics environment, the loading is applied in such a way that it represents the actual construction sequence of the bridge. The same full scale bridge model is used for loading in these steps. In the first loading step, the prestressing effect and the self weight of the girder are considered, while ignoring the self weight of the deck, haunch, and diaphragm are not considered. In actual practice, for unshored construction, the erected girders act as a support for the deck and haunch concrete to be cast. Thus the weight of the wet concrete is taken entirely by the girder as if additional dead load is applied onto the girder. To capture this phenomenon, equal amount of loading is applied onto the girder in the following steps. After the deck concrete sets, it then acts as a composite bridge. Thus any additional loading is resisted by the composite action of the bridge. Therefore, in the next loading steps, the deck, haunch, and the diaphragm elements are activated with the material having negligible density, so that no other additional dead load is applied in the subsequent loading steps. Any superimposed dead load that is applied after the deck concrete hardens acts on the composite bridge. Thus, in the next loading steps, the additional superimposed dead load is applied over the deck in the fully activated composite bridge model. Thermal analysis steps are then applied on the whole bridge model followed by any live loading that may be present on the bridge.

Global Bridge Model

This model is a full representation of the entire bridge. It is basically a five, single-line girder model attached to each other. Each girder line has different span lengths, thus allowing for proper representation of the skew. The same element types used in the single-line girder model are also used in the global model. Figure 20 shows the finite element mesh of the global bridge model. The construction sequence was not accounted for in analyses conducted using this model. This simplification does not affect the quality of the results obtained using the global model since it was mainly used to study the effects of superimposed loads (e.g., live load cases). As such the stress buildup prior to the application of the superimposed loads was not of interest in these analyses.

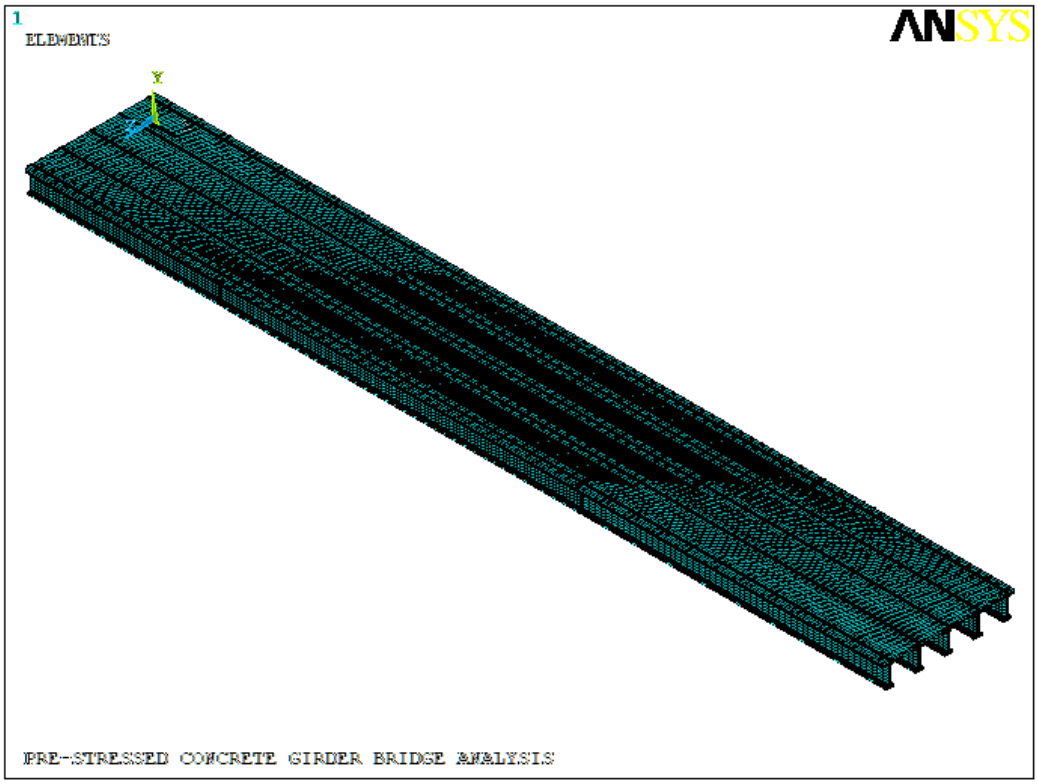

Figure 20
Global model for Bridge #2

Joint Model

To better understand the actual response of the hairpin bar under different types of loading without the need for unreasonable computing resources, a segment of the girder ends including the diaphragm is modeled separately. The segment of the girder at each end is taken equal to the height of the section from the bottom of the girder to top of the deck. The actual construction sequence leads to the development of a cold joint at the interface between the girder ends and diaphragm. Therefore a close contact exists at the interface, and an element CONTA178 models this contact having two nodes at the same location, one on each side, i.e., girder element and diaphragm element. The CONTA178 element joins these two nodes. This requires creating and meshing separate volumes that can be later moved adjacent to each other as can be seen in Figure 21.

The girder ends are supported on bearing pads that also modeled using SOLID45 elements. The transverse diaphragm is extended on both sides up to a distance of center to center of the girder spacing. The boundary condition for the transverse diaphragm is applied in such a way that the diaphragm is restrained in the *z* (transverse) direction, while being free to move in the *x* (longitudinal) and *y* (vertical) directions. The hairpin bar is modeled in such a way that

the hairpin bar from opposite girders are embedded in the diaphragm in a staggered configuration. The prestressing transfer length is introduced into the model by changing the initial prestressing strain linearly, starting at the girder ends, following the assumption made earlier [equation (3)].

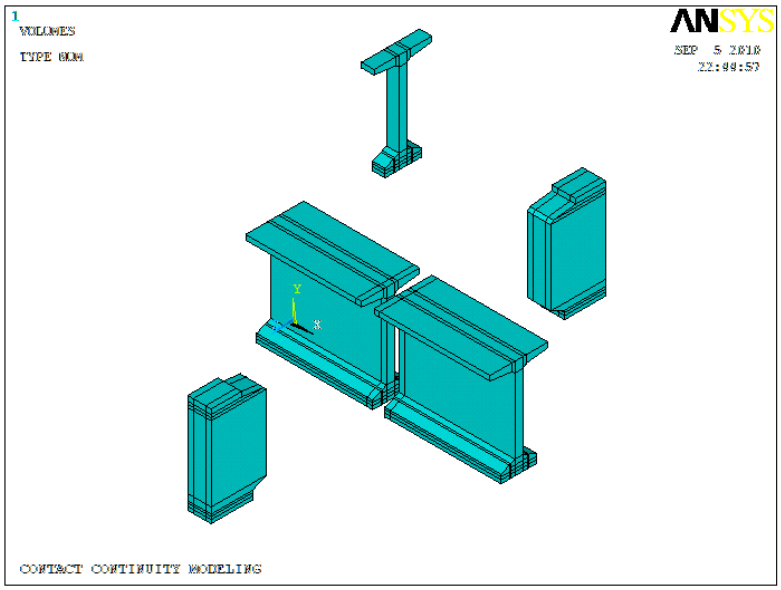

(a) solid volumes before meshing

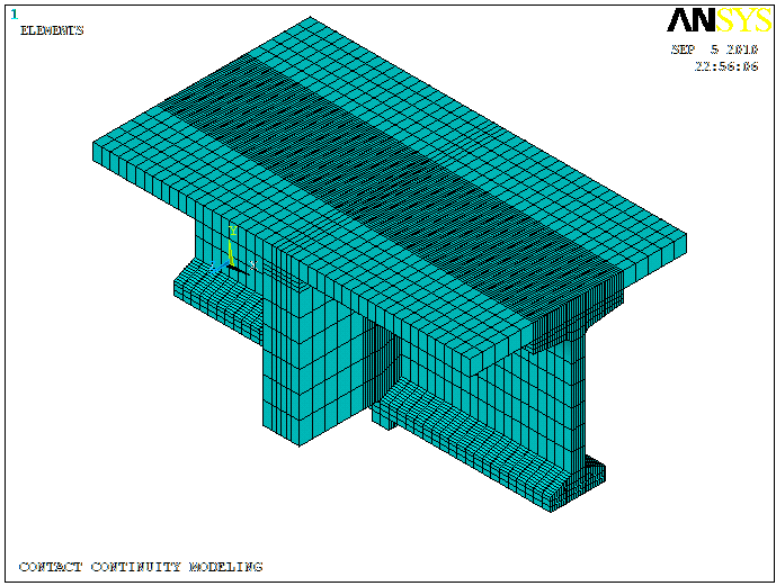

(b) finite element mesh

Figure 21
Creation of detailed joint model

Live Load Test

The research team conducted a live load test on the monitoring segment to assess the details' performance under truck loads. Both static and dynamic tests were carried out. Since the installed monitoring system is designed to capture long-term performance, it is not suitable for capturing fast changing readings due to moving loads. Therefore, additional sensors were installed for that purpose. The live load tests took place on August 19, 2010, after installing the additional sensors on August 18, 2010.

In this section, the live load setup is described and details about the additional sensors are provided.

Truck Description

Two trucks were acquired for the load test from the DOTD maintenance office in New Roads, LA. Both trucks were dump trucks and were loaded before the tests. The GVW for the first truck (Truck #1) was measured to be 57.0 kips and the second truck (Truck #2) was slightly lighter at 54.1 kips. Detailed axle dimensions and weights were also measured and can be found in Appendix D. The trucks were used in tandem for all the static cases, while only one truck was used at a time for the dynamic load test. It should be noted that the total weight of both trucks is substantially lower the design load according to AASHTO-LRFD for the bridge configuration on hand [*38*]. Nevertheless, the combined weight was considered suitable for achieving the goals of this task.

Static Load Tests

The first set of tests was static in nature. Both trucks were used in tandem in a prespecified loading position that would generate maximum effects intended for the study. A loading plan was submitted to the Project Review Committee (PRC) for approval prior to conducting the tests. The approved plan entailed nine loading positions. The first six loading positions targeted the generation of maximum positive moments at midspans of the tested segment, hence the *P*-designation for these cases. Another three loading positions were chosen for the purpose of generating the maximum negative moments at the monitored continuity diaphragm, hence the *N*-designation for these cases. These positions were determined using FE analyses using a sweeping technique of truck loads until the position that would generate the maximum targeted behavior was identified. Based on these FE analyses, the distance from a fixed reference was identified and used in the marking process. Table 5 lists a summary of the static live load test positions, the spans on which the trucks were loaded, and the targeted behavior. Despite the fact that the monitored bridge carries traffic in both directions, trucks were positioned as shown in Figure 22 for all considered cases. This minor

variance from real life traffic is not significant since the important factor is the center of gravity of the applied load.

The approved live load test plan was then executed by first marking the bridge deck with the truck locations as can be seen in Figure 23 for three of the tested positions (P1, P4, and N2). The marked location indicated the position of the center of the rear axle for a two-axle assumed truck. As mentioned earlier, the rate of data recording was 24 readings per hour, which were then averaged and stored for retrieval. This rate translated into one reading every 2.5 minutes. To ensure that more than one data point was collected for each static load position, the trucks were asked to stay at each position for a period equal to or longer than 11 minutes. During this period, at least three and probably four readings were recorded for each loading case. In between loading positions (P1 and P2, P3 and P4, P6 and N1, N1 and N2, and N2 and N3), the trucks were driven on the tested bridge segment to help determine a reference datum for the recorded readings. Figure 24 shows the actual trucks in two of the static loading positions, namely P1 and N1.

The research team recorded the time at the beginning and at the end of each loading case from the logger's clock. These times are essential for associating the recorded data with the proper loading case.

Table 5
Description of static live load positions

Position	Loaded Span(s)	Targeted Action	Effect on Continuity Detail
P1	23	Positive moment at midspan – G3-G5	Closing – One side
P2	24	Positive moment at midspan – G3-G5	Closing – One side
P3	25	Positive moment at midspan – G3-G5	Open – One side
P4	23	Positive moment at midspan – G1-G3	Closing – One side
P5	24	Positive moment at midspan – G1-G3	Closing – One side
P6	25	Positive moment at midspan – G1-G3	Open – One side
N1	23 & 24	Negative moment at Bent 24 – G3-G5	Closing – Both side
N2	23 & 24	Negative moment at Bent 24 – G2-G4	Closing – Both side
N3	23 & 24	Negative moment at Bent 24 – G1-G3	Closing – Both side

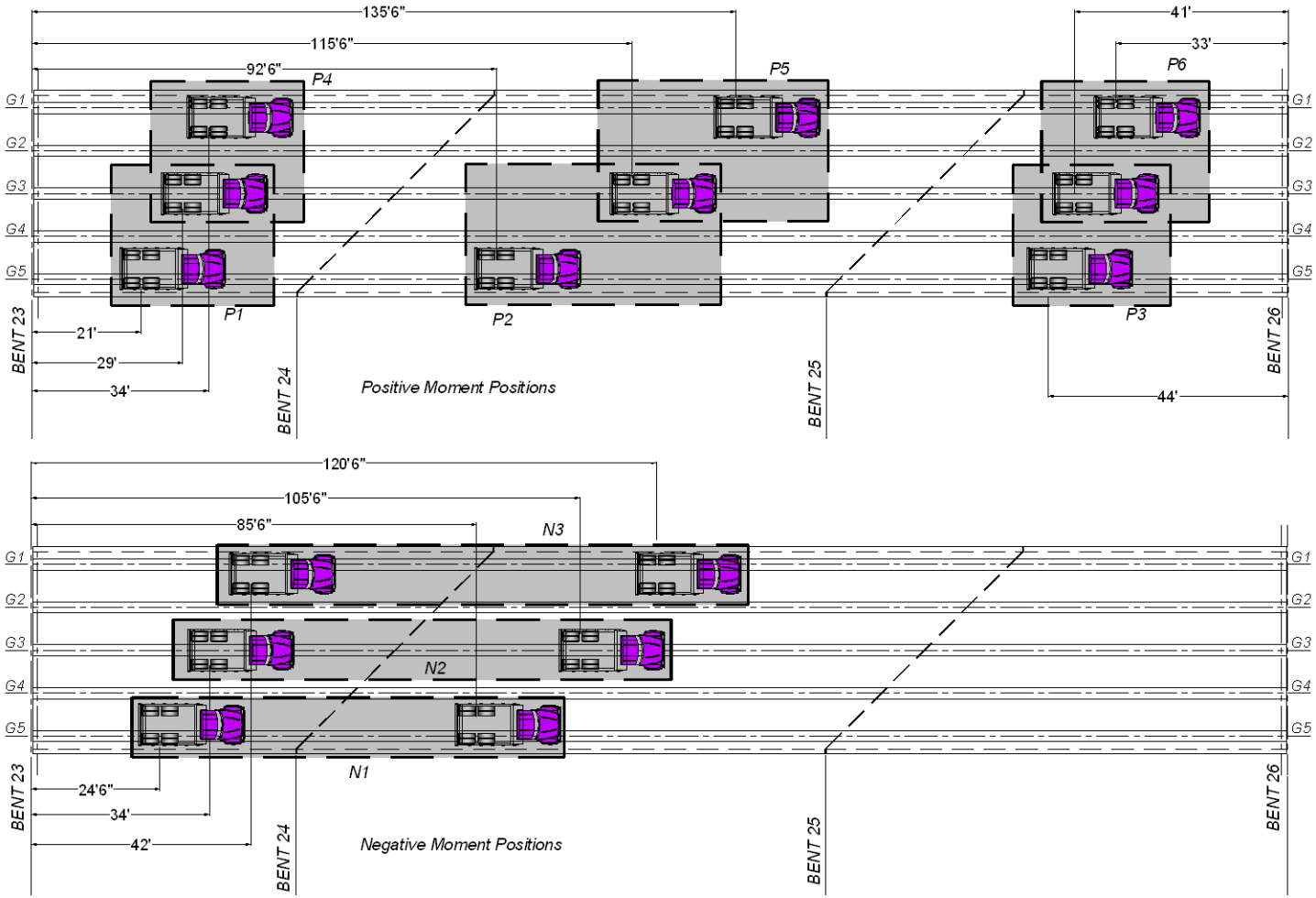

Figure 22
Load test truck positions (distance with reference to middle of rear drive axle – see Figure 132)

Figure 23
Marking the bridge deck at truck positions for static live load test

(a) Position P1

(b) Position N1

Figure 24
Actual Trucks #1 and #2 in position for two of the nine static load positions

Additional Sensors for Dynamic Tests

Before conducting the live load test, 10 additional surface mounted sensors were installed on two separate lines across the bridge. The first five sensors were installed on the bottom flange of the prestressed girders at the middle of Span 24. The other sensors were installed at the continuity diaphragm at Bent 24. The installed sensors utilized a technology different than the vibrating wire technology employed in the main monitoring system. These analog sensors can acquire data at a much faster rate, which renders them more suitable for dynamic load testing.

In addition to the additional strain gages, an accelerometer was installed on the bottom flange of Girder G3 at the middle of Span 24.

Dynamic Load Tests

Dynamic loading tests were performed on three traffic lanes using both Truck #1 (heavier one) and Truck #2 (lighter one). Due to the limitation of site conditions, the truck speeds are low as described below. Since the bridge was not yet open to traffic, the actual traffic lanes were not striped at the time of conducting the load test. The lane definition and truck positions for this discussion are defined as:

- Path A (left lane): the left tire was about 6 ft. from the left curb.
- Path B (center lane): the truck was at the center of bridge.
- Path C (right lane): the right tire was about 6 ft. from the right curb.

Figure 25 shows the truck driven paths during the dynamic load tests. Three dynamic tests were conducted:

- Dynamic Test 1: Truck #2 (34 mph) followed by Truck #1 (30 mph) in Path B (center lane). The two trucks were not on bridge at the same time.
- Dynamic Test 2: Truck #2 (34 mph) followed by Truck #1 (31 mph) in Path A (left lane). The two trucks were not on bridge at the same time.
- Dynamic Test 3: Truck #2 (34 mph) followed by Truck #1 (34 mph) in Path C (right lane). The two trucks were not on bridge at the same time.

Before the dynamic test, three crawling tests corresponding to the dynamic test with a truck speed of about 3 mph were conducted. The truck positions were intended to be the same as dynamic tests. However, truck positions in the dynamic test were more difficult to control. In the crawling tests, Truck #1 was followed by Truck #2. The two trucks were not on bridge at the same time.

- Crawling Test 1: Truck #1 (3 mph) followed by Truck #2 (3 mph) in Path A. The two trucks were not on bridge at the same time.
- Crawling Test 2: Truck #1 (3 mph) followed by Truck #2 (3 mph) in Path B. The two trucks were not on bridge at the same time.
- Crawling Test 3: Truck #1 (3 mph) followed by Truck #2 (3 mph) in Path C. The two trucks were not on bridge at the same time.

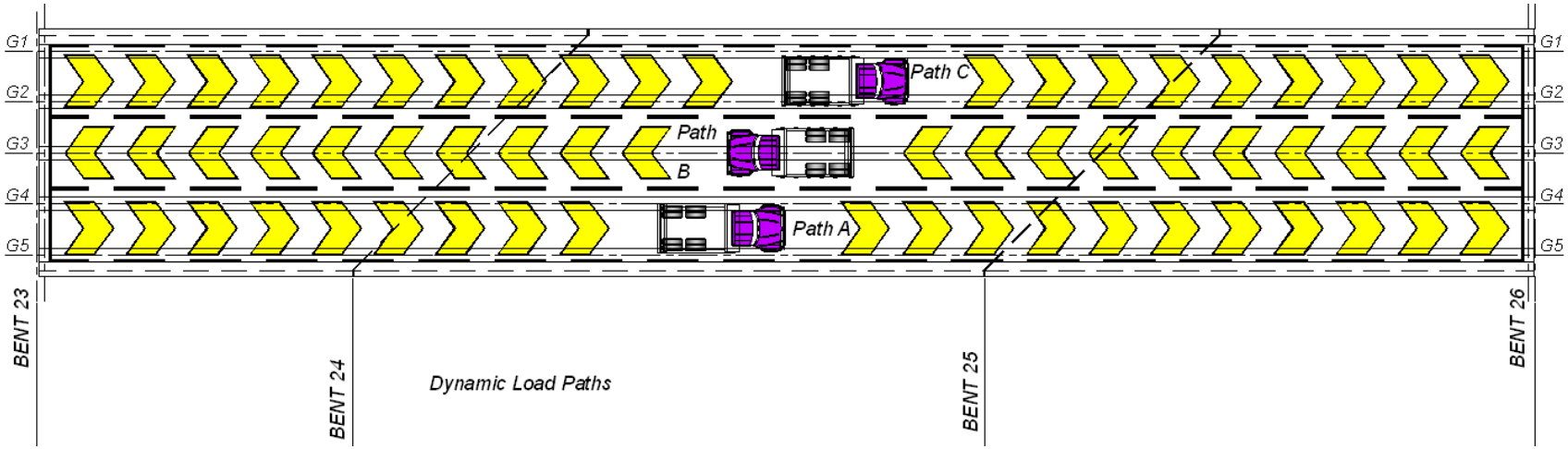

Figure 25
Truck paths for the dynamic load tests

Temperature Effect

During the course of the static load tests, which started at 9:00 a.m. and continued until about 2:30 p.m., the temperature at the bridge site rose about 10ºF. This rise in temperature affected both sensor readings and the structural response. While the first is correctable using the temperature correction formulas provided by the sensor manufacturer, the second is real and will have to be discounted from the recorded readings. More important is the temperature gradient whose effect on the continuity detail was more severe since it caused the bridge to camber up, hence applying an opening action on the joint. In comparison to temperature gradient effect, uniform temperature change applies uniform extension or contraction on the bridge girders and hence the joint. Figure 26 shows a plot of the temperature rise from five deck sensors and three bottom girder sensors. It should be noted that the five deck sensors were at a depth of about 6 in. from the deck surface. Temperatures above 110ºF were recorded manually by the research team on the deck surface during the course of the static load test.

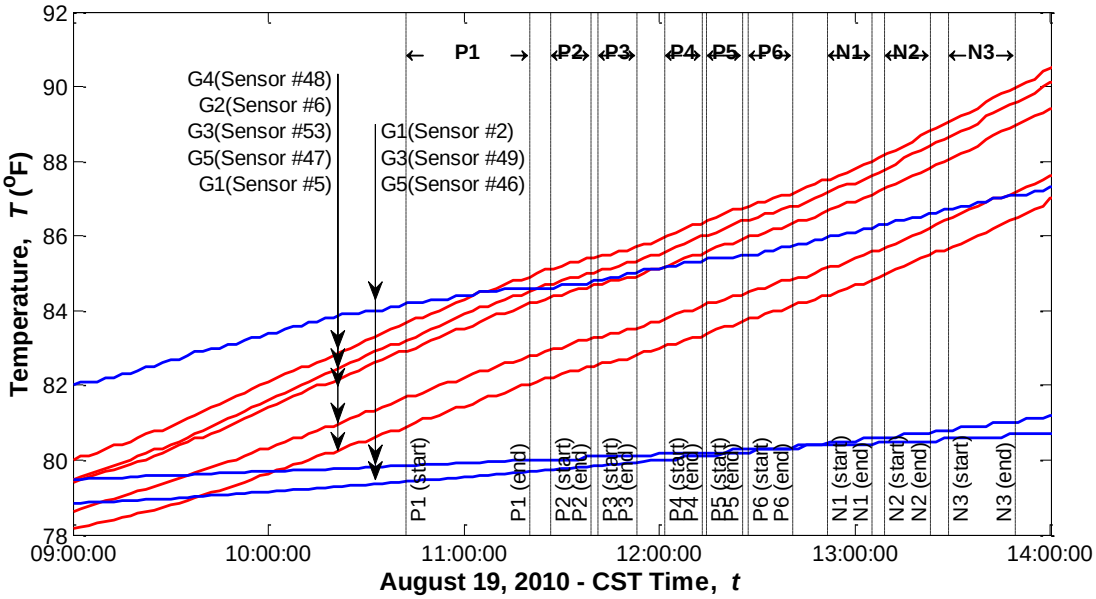

Figure 26
Temperature increase during the time of conducting static load tests

Because of the aforementioned temperature changes, sensor readings kept changing as a result of the thermal movements of the structure. Identifying the appropriate datum from which the effect of the static live load were to be measured was carefully studied. The identified datum was identified with the help of the six periods where the trucks were driven on the bridge. The following section shows a sample sensor reading for illustration purposes. Plots of all sensor readings during the static live load tests can be seen in Appendix E.

Sample Sensor Reading

All sensor readings were acquired at the highest rate allowed by the monitoring system for the static load cases (1 reading / sensor / 2.5 minutes). The first step in the data processing was to correct the readings for temperature effects with respect to the initial reading at the beginning of the test, which was taken at 9:00 a.m. on August 19, 2010. Once the data were corrected for the temperature effect, periods when no trucks were present on the bridge were identified. A fictitious line was drawn to connect the average readings during each one of the six "no load" periods to serve as the temperature adjusted datum.

Figure 27 shows a sample plot for one of the strandmeters installed on the hairpin bars in G3 of Span 23 (Sensor #50). Two plots are shown for the sensor strain readings. The first one (dashed line) is for the raw readings before temperature corrections, while the second plot, which is marked by squares, represents the temperature corrected readings as per the manufacturer's recommendations.

The first observation from this figure was that the strain rose about 400 $\mu\varepsilon$ by the end of the static load test (2:00 p.m.) relative to the starting time (9:00 a.m.) not considering the truck effects. This leads to an apparent erroneous increase in strains for all loading cases regardless of whether they cause positive or negative moments at the location of the sensor. After identifying the no-load periods on the chart, an adjusted datum can be constructed as shown in the figure. As can be seen, this temperature-adjusted datum intersects with the sensor readings more than once. The difference between the temperature-adjusted datum and the temperature-corrected sensor readings is the relative sensor reading. It is clear that some load cases cause positive strains (opening action), while the majority cause negative strains (closing action). In the figure, the relative sensor reading during the P2 load case is clearly identified. The result is a negative strain of about -47.7 $\mu\varepsilon$. A positive strain of about +18 $\mu\varepsilon$ can be identified for the P3 load case. It should be noted that P2 causes a negative moment at this sensor location, while P3 causes a positive moment at the sensor location.

The approach described in this section was used to interpret the live load static test readings for all sensors. The results are plotted in Appendix E.

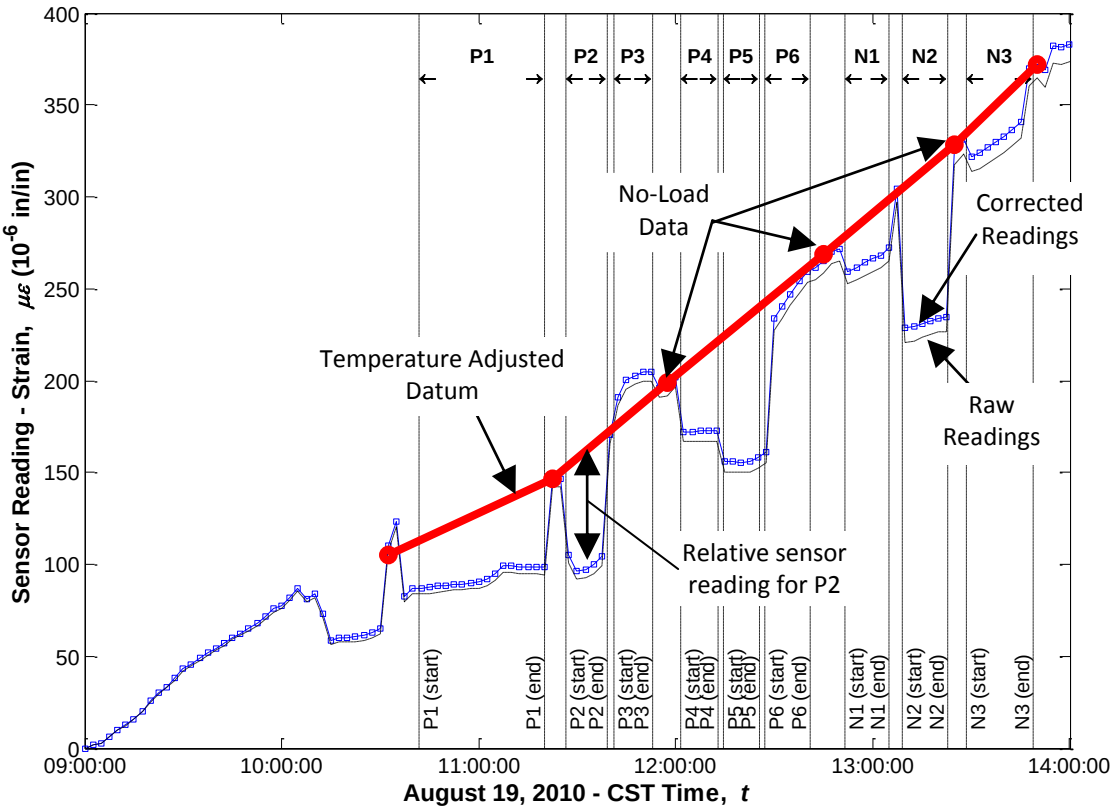

Figure 27
Sample sensor reading during static live load testing (Sensor #50 – G3, Span 23, hairpin bar)

DISCUSSION OF RESULTS

In this section, the results from all approaches described in the Methodology section are presented. An enormous amount of results has been obtained over the period of the project. In this section, the key results that are pertinent to the objective of the project will be presented.

Structural Health Monitoring Data

Temperature Data

Each of the installed sensors (embedded and surface-mounted) records two readings. The first is the response reading for that sensor type (e.g., strain for sisterbars) and the second is the temperature at the location of the sensor. As such, plots of the temperature at the monitored locations is possible over the entire length of the monitoring period including the curing period at the casting yard for some of the girders. In many monitored sections, there are several sensors across the height of the girder. This means that data temperature gradients can also be plotted. This section presents the results for the three sections in Girders G3, G4, and G5 at midspan.

Figure 28 shows the temperatures at midspan sections of G3, G4, and G5 in Span 24 at three locations, namely deck, top girder flange, and bottom girder flange. It can be seen that the seasonal changes cause a huge temperature fluctuations from a minimum of about 20ºF to 115ºF. The highest temperatures are always recorded in the deck because of the direct exposure to sunlight. Sunlight exposure also causes larger daily variations in the deck than the other sensors as evident by comparing the range of daily amplitude from deck and girder flanges. The only exception to this general statement is the bottom flange sensor in Girder G5. Daily variations at that location are higher than those at the other bottom flanges. This phenomenon puzzled the research team until it was noticed that G5 gets exposed to sunlight since it is an exterior girder. This observation will help explain many of the different observations associated with Girder G5. It should also be noted that while on site, the research team checked the on the shaded parts of the deck surface and compared to the sunlit parts of the deck surface using a laser gun device. The difference in temperature between these two locations on the deck surface was about 10-15ºF. Therefore, the bridge railing next to Girder G5 casts its shade on the top of the girder while the bottom flange is heated by direct exposure to sunlight.

These temperatures are also used to plot a representative temperature gradient by subtracting the bottom flange temperature readings from the deck temperature readings. The temperature gradient plot in Figure 30 is for G3. It shows that the difference in temperature between the

deck sensor and the bottom flange is as high as +16ºF and as low as a –7ºF. It should be noted that the deck sensor is installed on the bottom layer of deck reinforcement, which means that the deck surface temperature is even hotter. This means that the actual temperature gradient can easily exceed 20ºF. Such a high temperature gradient can cause the structure to undergo substantial deformations, especially if it is a large structure such as a bridge.

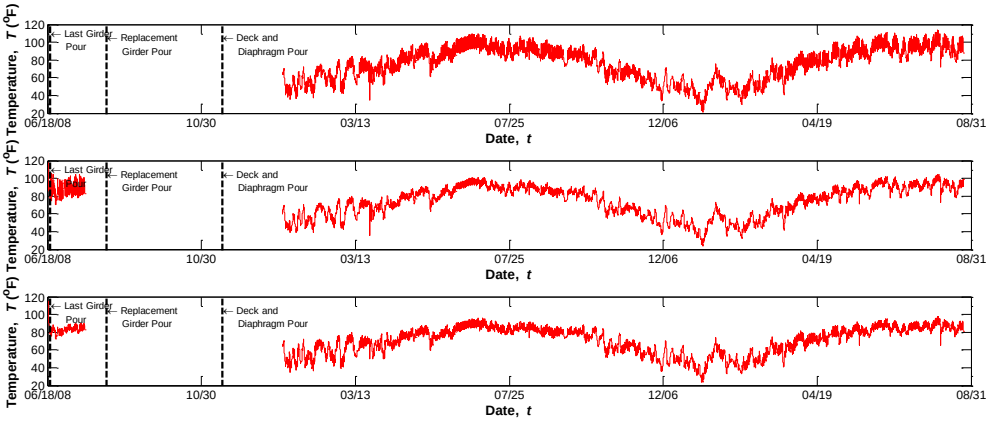

(a) Girder G3

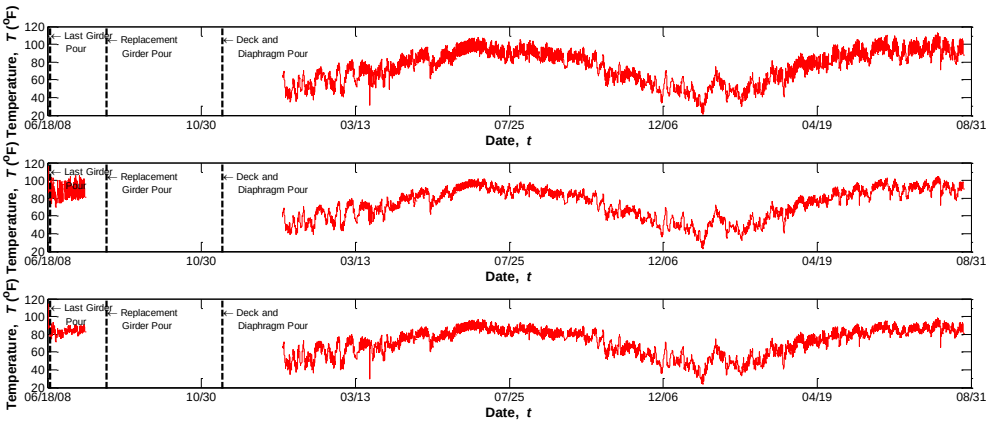

(b) Girder G4

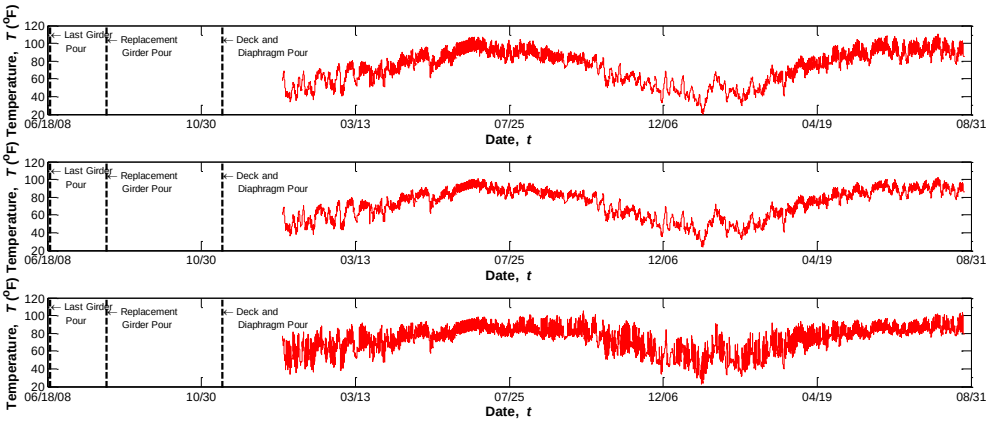

(c) Girder G5

Figure 28
Temperature readings in deck, top, and bottom girder flanges (Span 24)

Figure 29
Sunlight hitting the bottom flange of G5 while the top flange is shaded by the overhang

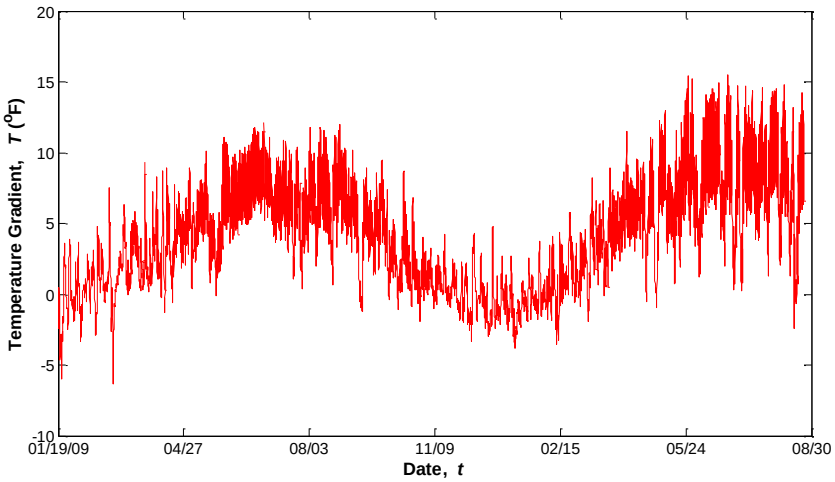

Figure 30
Temperature gradient (Girder G3 in the middle of Span 24)

Strains in Hairpin Bars

Strains from the hairpin bars are presented in this section for all three monitored joints connecting Span 23 and Span 24 at Girders G1, G3, and G5. No strandmeters were installed on the hairpin bars in Girder G5 in Span 23 as mentioned earlier. At each monitored location, two strandmeters were installed. The average of both readings is used as a representation of the condition in the hairpin reinforcement. Figure 31 shows two plots for a monitored joint. The top and bottom plot for each girder represent the strain in the hairpin bars installed on the Span 23 side and the on the Span 24 side, respectively. As can be seen from the plots, the recorded strains from Girders G1 and G5 are similar in behavior. The daily range of

fluctuations is about 100 microstrains (με). This can be added to a seasonal change (difference between low temperature in winter and low temperature in summer) in strains of another 100 με. The behavior of Girder G3 is completely different. Seasonal changes of about 200 με can be seen between the low temperatures 12/06/2009 and 08/31/2010. Furthermore, the daily fluctuations are substantially higher for this girder as they are in the range of about 500 με. This behavior was intriguing to the research team. After checking that the data processing is not the cause of the large difference between the strains in this girder and the other two, a visual inspection was conducted, which revealed that a crack developed in the bottom flange of Girder G3 – Span 24 at the interface with the continuity diaphragm. Figure 32 shows the crack when it was marked on May 5, 2009. The crack width was about 0.013 in. and barely visible because of its location. Subsequent inspection on October 22, 2010, revealed that the crack has extended across the entire bottom flange and that its width has also increased (over 0.02 in.). No cracks were found in the bottom flange of G3 on the other side (Span 23). However, the high strains indicate that the girder may be cracked in the embedded portion inside the diaphragm. A similar inspection of Girders G1 and G5 did not reveal cracks in the bottom flanges of these girders.

The strains at the girder's bottom flanges were also investigated to understand the dissipation of these high strains in the hairpin bars 18 in. away from the continuity diaphragm's face, which is where the vibrating wire gages were installed (top, middle, and bottom). Figure 33 shows the strain records from the surface mounted gages on the bottom flanges on Girders G1, G3, and G5 on both sides of the continuity diaphragm, i.e., Span 23 and Span 24. It can be seen that the daily strain changes are about 30-40 με for all locations except for Girder G3 (both sides) and Girder G1 (Span 24) where the daily strain changes are about 70-80 με. By comparison with the readings from the strandmeters on the hairpin bars, the changes are much less in all cases. The drop in daily strain changes at the surface-mounted VW gages can be attributed to the fact the tensile force in the hairpin bars has been distributed into a larger area of the girder 18 in. from the diaphragm face. At girder ends, the hairpin bars are the sole resistance of tensile forces. Because Girder G3 is cracked at the face of the diaphragm, the tensile force is still mainly resisted by the hairpin bars. However, because no further cracks took place in the girder beyond the observed crack inward, the tensile force is effectively distributed into the girder. The high strain changes from the surface-mounted VW gage on Girder G1 (Span 24) is also higher than G5 and G1 (Span 23), which may indicate that a crack has taken place at this location. Visual inspection has not revealed any cracks at this location.

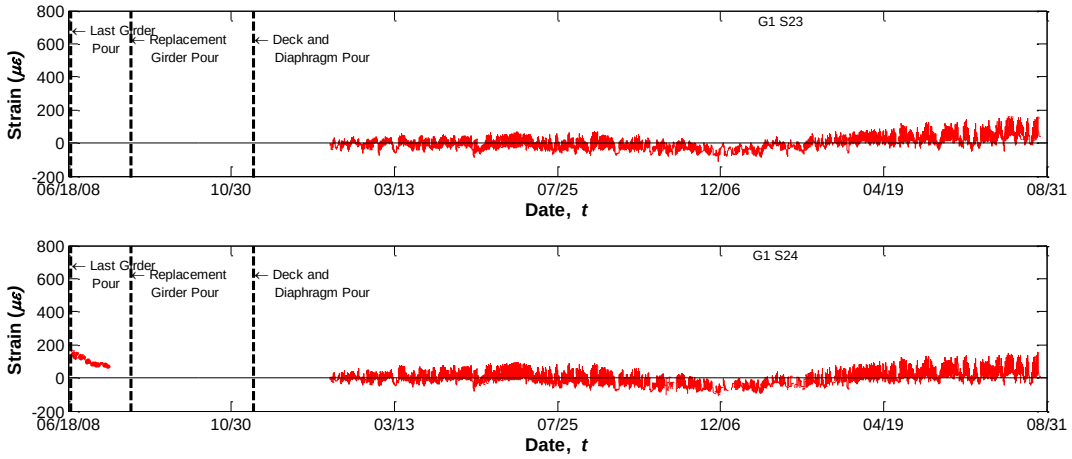

(a) Girder G1

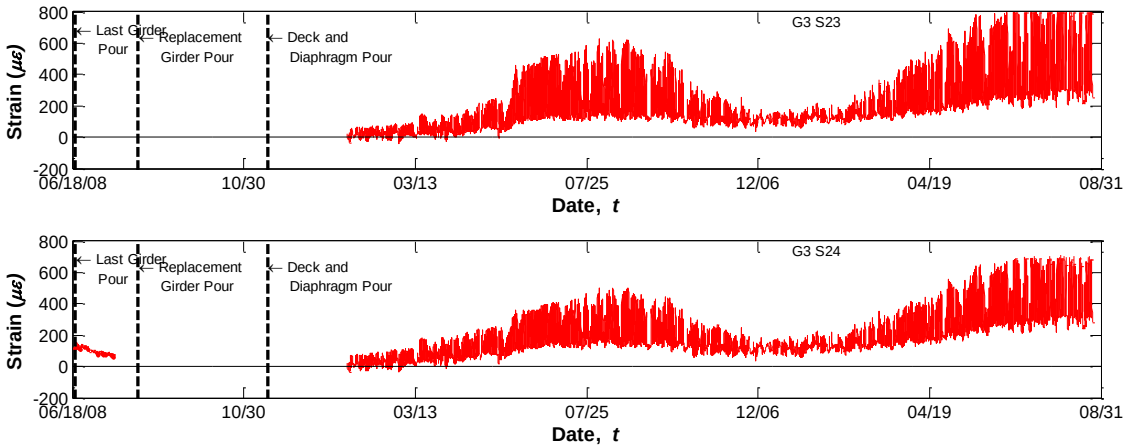

(b) Girder G3

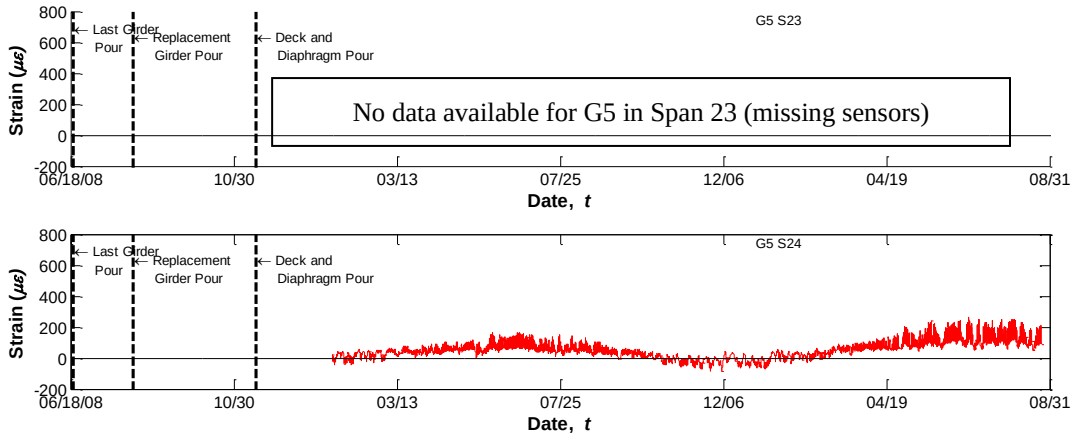

(c) Girder G5

Figure 31
Strains in hairpin bars at both sides of continuity diaphragm

(a) May 5, 2009 (at Bent 24)

(b) October 22, 2010 (at Bent 24)

(c) November 5, 2010 (at Bent 25)

Figure 32
Observed crack at bottom flange of Girder G3 – Span 24

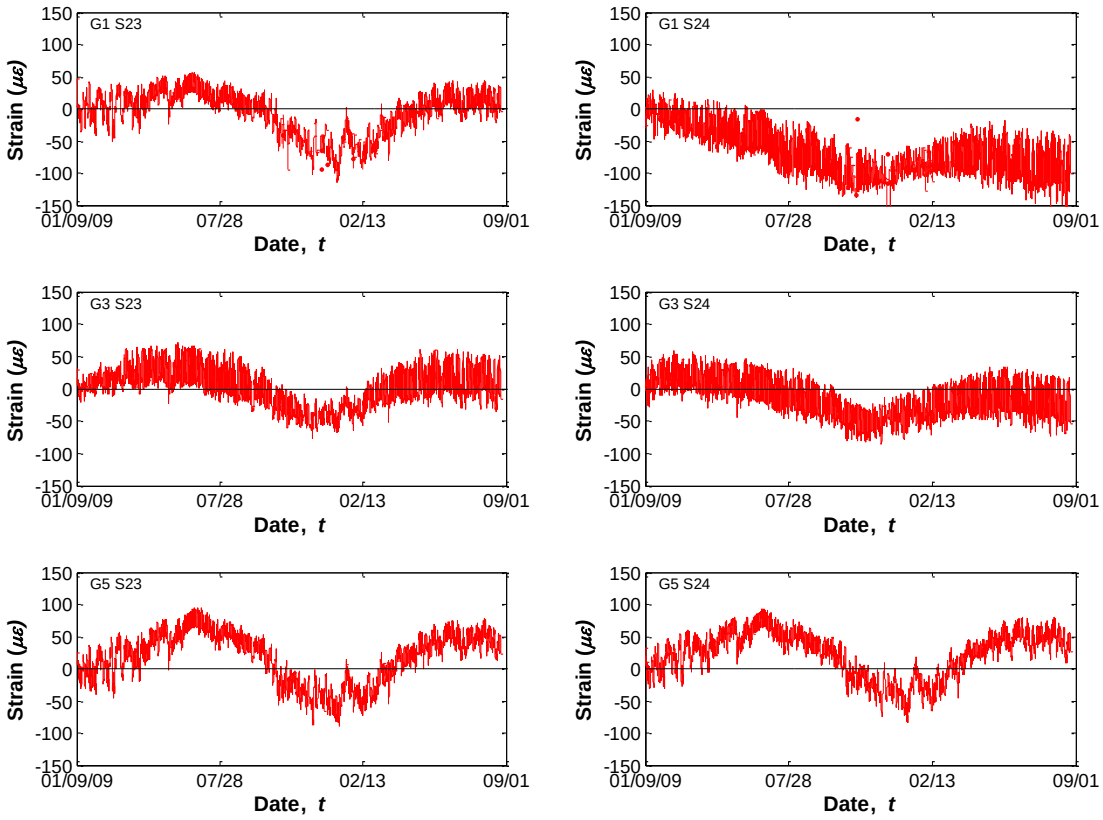

Figure 33
Surface-mounted VW strains at bottom flanges on both sides of continuity diaphragm (Girders G1, G3, and G5)

Relative Movement between Bottom Flanges in Adjacent Spans

The relative movement between the bottom flanges at the ends of the adjacent girders on both sides of the continuity diaphragm was investigated using the gapmeters (DM) installed at Girders G1, G3, and G5. Any displacement captured by the gapmeters would indicate the relative movement between the bottom flanges of the girders. Positive displacements mean that the distance between the bottom flanges have increased, i.e., the girders are applying tension on the diaphragm, and vice versa. Figure 34 shows a plot of the temperature corrected readings from all three gapmeters, which were installed on Girders G1, G3, and G5 across the continuity diaphragm at Bent 24. It can be seen from the figure that Girders G1 and G5 experienced far less seasonal and daily changes than Girder 3. This observation confirms the earlier discussions of the hairpin and vibrating wire strain readings presented in light of the existence of the crack in Girder G3 (Span 24). Quantitatively, the gage lengths for these extended DM gages were 46.0in., 43.0in., and 45.5in. for Girders G1, G3, and G5, respectively. This means that if a joint was cast monolithic with the girders, the resulting daily strain changes would have been equal to about 0.0150/46=326 $\mu\varepsilon$, 0.0325/43=756$\mu\varepsilon$,

and 0.0175/45.5=385$\mu\varepsilon$ for Girders G1, G3, and G5, respectively. Of course, the cold joint between the precast girders and the cast-in-place diaphragm allows some movement, and the hairpin bars are not as efficient as if the positive moment reinforcement were coupled between both girders. Cracking in the diaphragm and/or the girders within the gage length also increases the displacement. Therefore, the strain readings recorded by the strandmeters on the hairpin bars and the surface-mounted VW gages are expected to be lower than this apparent strain from the gapmeters. It should also be noted that the daily changes are less in the cold months (December, January, and February) than in the summer. This is due to the smaller temperature gradients during cold months (see Figure 30), which in turn reduces girder rotations at the joint.

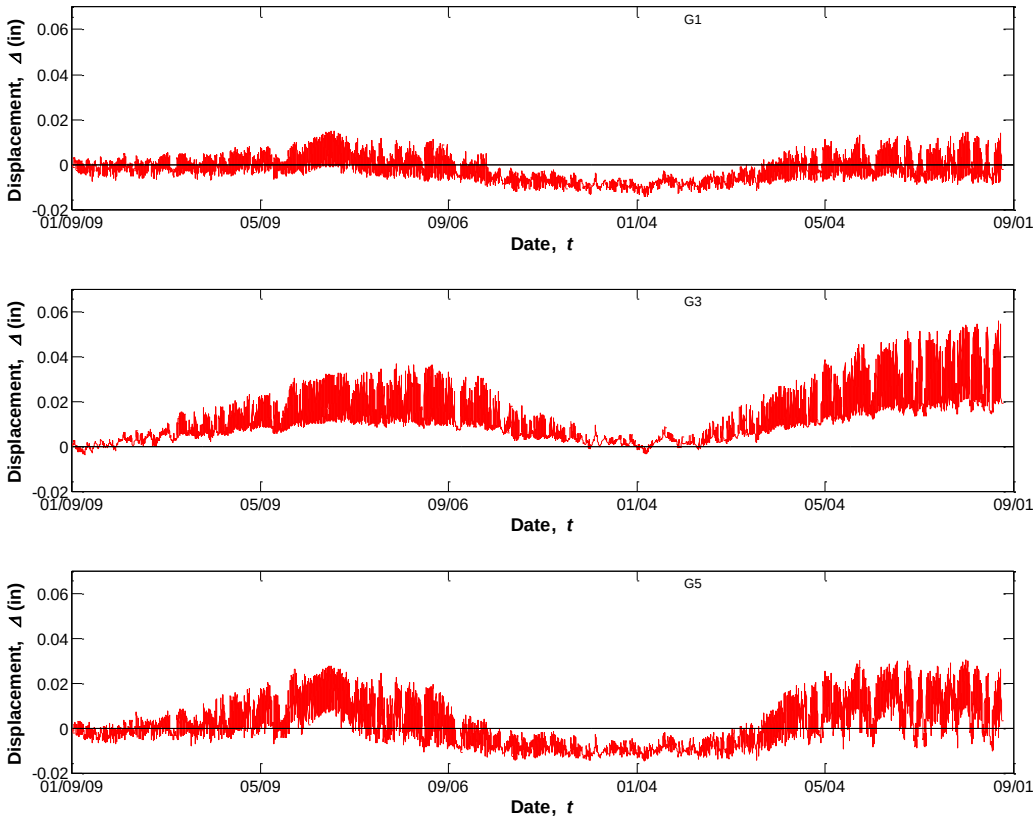

Figure 34
Gapmeter displacements for Girders G1, G3, and G5

Differential Shrinkage between Deck and Girder Concrete

Of the several factors that cause long-term deformations in precast PSC slab-on-girder bridges, differential shrinkage between the cast-in-place deck and the precast girder is of interest. The ages of the girders at the time of introducing continuity are summarized in Table 6.

Table 6
Technical specifications of employed sensors

Girder	Girder Pour Date	Diaphragm Pour Date	Age at Continuity (days)
G3	6/18/2008	11/18/2008	153
G4	6/18/2008		153
G5*	8/9/2008		101

* Replacement girder

It can be seen that all girders exceed the 90-day girder age recommendation from NCHRP Report 519 [*1*]. It can also be seen that the G5 replacement girder was younger than the other girders in the monitored segment by 52 days. Figure 35 shows plots from the sisterbars in the deck and top flanges at Girders G3, G4, and G5 locations. It can be seen that the deck strains are almost identical (decreased about 75$\mu\varepsilon$ over the monitoring period) for all three girders since they all share the same reference point, i.e., time load was applied or deck shrinkage ensued. The girder top flange strains decreased about 100$\mu\varepsilon$ for Girders G3 and G4 during the same period. A lesser amount of about 50 $\mu\varepsilon$ was recorded for Girder G5. It should be noted that the shown strains are summative, i.e., they include the effect of deck shrinkage, and creep due to prestressing forces, and creep due to dead load effects and temperature changes. The latter are seasonal or daily events and can be easily seen in the plots. Therefore the discussed strains are the average strains to eliminate any daily temperature change effects. Isolating the differential shrinkage strains from the creep induced strains is not possible without making analytical assumptions. As such, it can be said that the combined effect of creep and shrinkage together is presented in the shown plots. Girder G5, which was 101 days old at the time the continuity diaphragm was poured, would then have more upward (camber) movement due to prestressing creep than the other girders (G3 and G4). Therefore, the difference between the deck strain and the girder's top flange strains were different. The plotted strain records showed that the difference between the deck and top flange strains ($\varepsilon_{deck} - \varepsilon_{girder}$) was about -25 $\mu\varepsilon$ for Girders G3 and G4 and +25 $\mu\varepsilon$ for Girder G5. While these differential strains may be considered minor, their trends confirm that girders' ages are a major factor in the performance of the continuity detail. It should be noted that the period between pouring the deck and continuity diaphragm (11/8/2008) and the date when the monitoring system was installed at the bridge site (1/9/2009) is 52 days when much of the initial deck shrinkage takes place. Unfortunately, no data is available from this period.

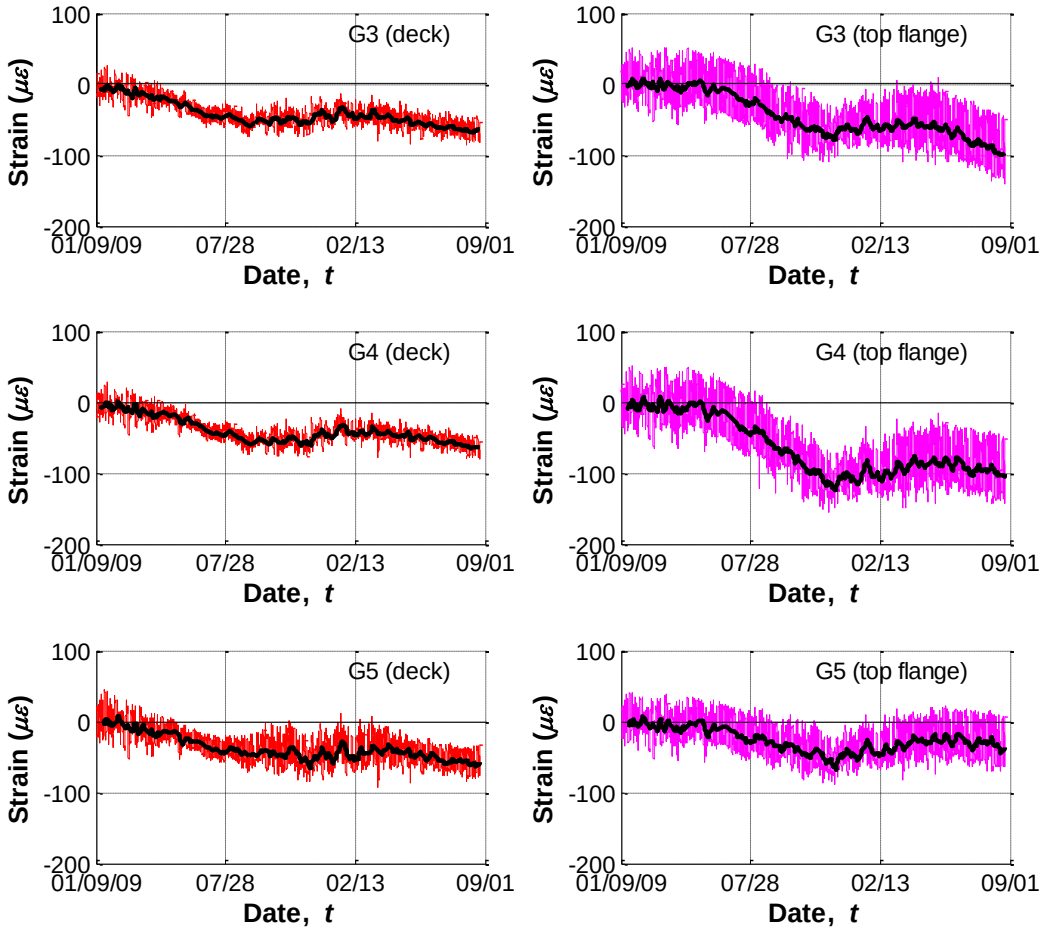

Figure 35
Strain records in deck and top flange at Girder G3, G4, and G5 locations

Rotation of Girder Ends in Adjacent Spans

Figure 36 shows plots of the recorded rotations from the tiltmeters installed on the webs at girder ends on both sides of the monitored continuity diaphragm (Bent 24). As mentioned earlier, erroneous readings from the titlmeters on Girders G1 and G5 led to changing two of them in June 2009 and October 2009. The tiltmeters installed on Girder G3 did not exhibit any such problems and were left untouched since their installation in January 2009. That is why their records cover the entire period since the monitoring system was installed and until the time of preparing this report as can be seen in Figure 36. Conversely, the rotation records for Girders G1 and G5 were truncated and zeroed at the time they were last adjusted.

It can be seen from the plots that rotations on both sides of the continuity diaphragm follow the same trend. This means that the girders are rotating in the same direction, which indicates that the continuity diaphragm is doing its job of providing continuity between the girders. Had there been an expansion joint between these girders, the camber of the girders (due to

creep or temperature gradient) would cause opposite signs of girder end rotation as can be seen in Figure 37. In the case of an expansion joint, the rotation angles θ_r and θ_l is of opposite signs. This can also happen if a continuity diaphragm connects both girder ends; however, there is also the possibility that one girder's movement overcomes the other resulting in similar rotation signs on both sides of the diaphragm. The records of girder end rotations show both cases for the continuity diaphragm detail. Most of the time, however, the sign for rotation angles θ_r and θ_l is similar.

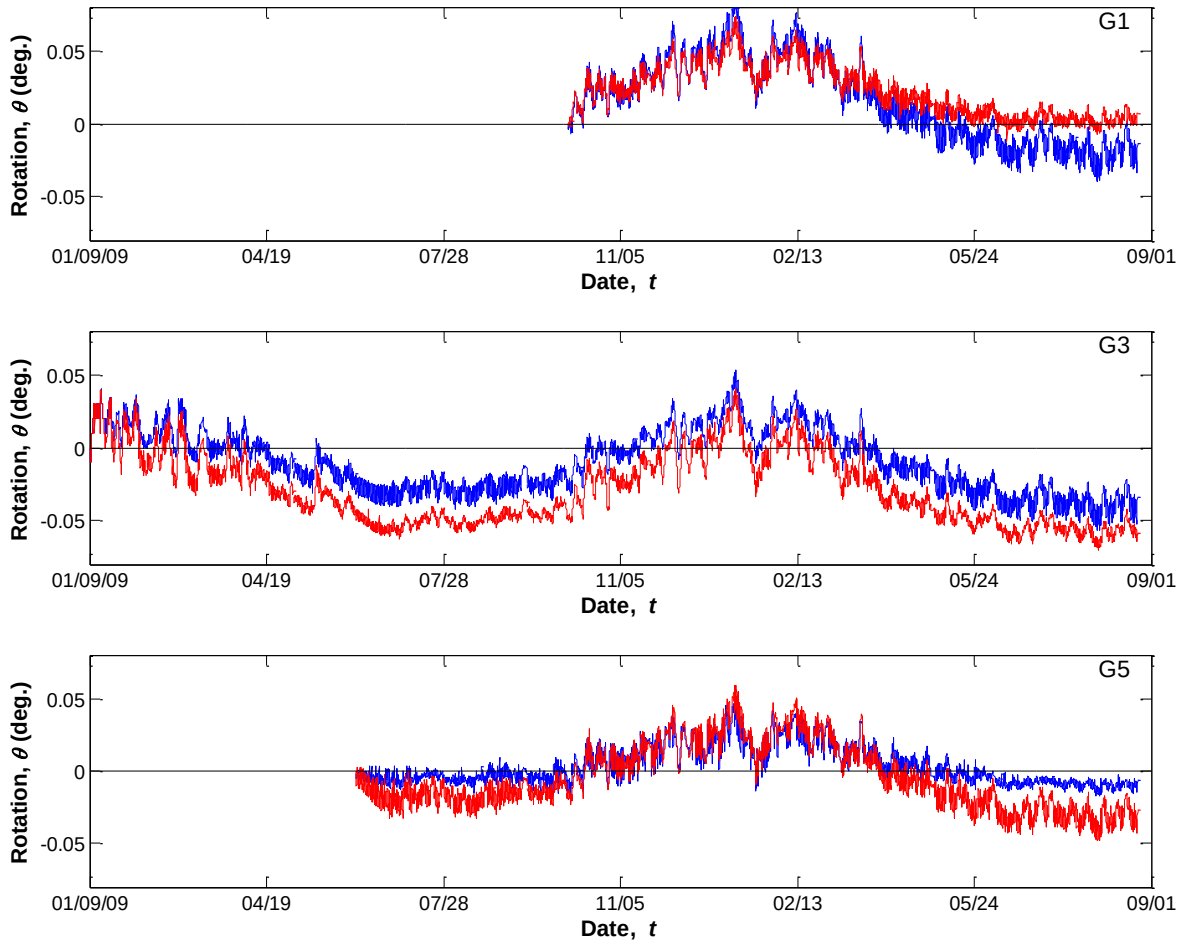

Figure 36
Rotation of girder ends (G1, G3, and G5)

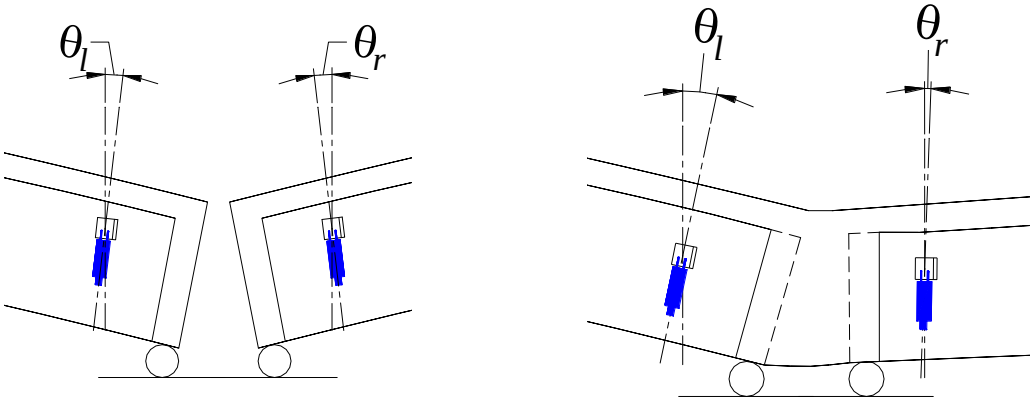

(a) no continuity diaphragm **(a) with continuity diaphragm**

Figure 37
Schematic of girder end rotations

Creep of Girders During Curing Period

This section presents the strain records for three of the monitored girders while in the casting yard. The three girders are the longest span girder (G3, G4, and G5). It should be noted that the presented results for Girder G5 are from the original girder that was rejected by the contractor. The results from this girder are still valid for the curing period. Three curves are shown for each girder representing the strain in the bottom flange at the girder ends, and at the top and bottom flanges at the midspan. Since Girder G4 was not one of the monitored girders at the continuity detail, only two curves are plotted.

The trends for all three girders are almost identical. The strains dropped at the midspan, where the full prestressing effect acted on the section, more than they did at the girder end, where little prestressing effect acted at a few inches from the girder end. At the midspan, strains in the top flanges decreased at a lesser rate than the bottom flange. The top flanges' daily strain fluctuations were also larger than the other two locations, i.e., bottom flange. This is expected since the wide top flange of the bulb-T girders were exposed to direct sunlight, while the bottom flanges were always in the shade (see Figure 53). The strain records presented in the figures during the curing period showed that the strain was still dropping until the datalogger was disconnected in preparation for the girder transportation. This confirms that the girders will continue to creep after being transported to the bridge site.

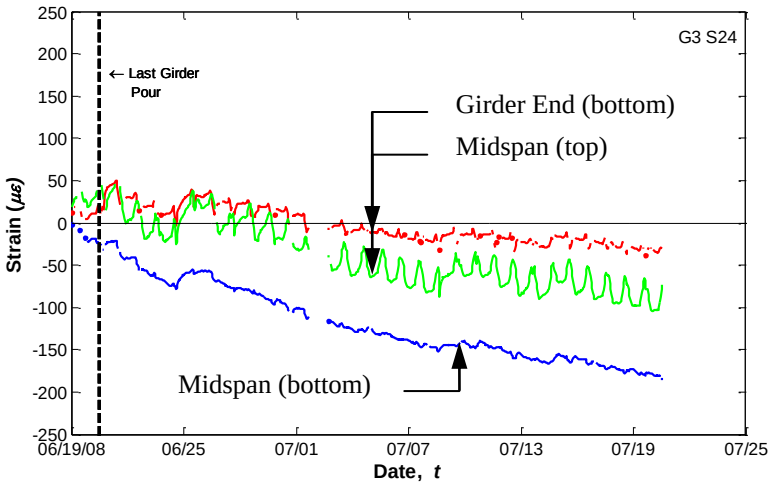

(a) Girder G3

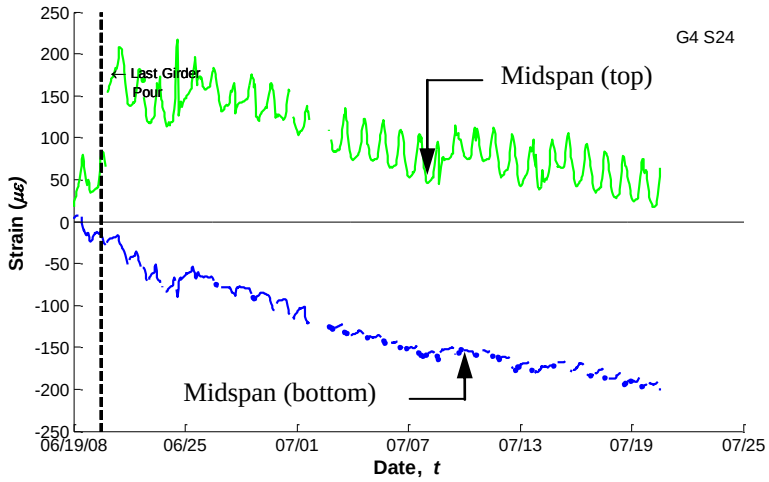

(b) Girder G4

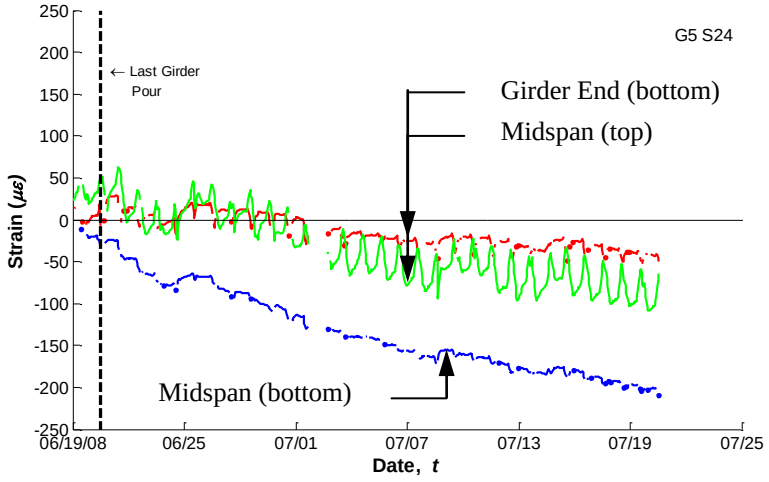

(c) Girder G5 (rejected girder readings)

Figure 38
Early strains in Span 24 Girders G3, G4, and G5 while curing in casting yard

Deck Cracking

The research team visited the bridge site numerous times during the period of the project. During each visit, a visual inspection of the deck surface cracking was conducted. Hairline cracks were observed as early as May 2009 (5.5 months after establishing continuity). The cracks were very limited in width (0.001 in.) and location. They mainly ran across the deck at an angle equal to the skew angle of the bents, i.e., over the continuity diaphragm. Cracking is typical in bridge decks, especially continuous ones. Nevertheless, the likelihood of having deck cracking over continuity supports is reduced if the detail relieves the movement of the girders (such as the case of continuous decks with no continuity diaphragms), which reduces the continuity moment between spans. Figure 39 shows two of the observed cracks in the deck of the monitored segment. In Figure 39(a), which depicts the deck in the middle of the roadway, the crack is at an angle with the deck grooving. Figure 39(b) shows the crack over the support in the overhang part of the deck, i.e., outside the exterior girders. Since the continuity diaphragm is not extended outside the exterior girder, the deck crack in the overhang region is free from the diaphragm's influence and, therefore, propagates along the shortest distance to the edge of the deck. This explains the crack orientation in Figure 39(b), which is parallel to the deck grooving.

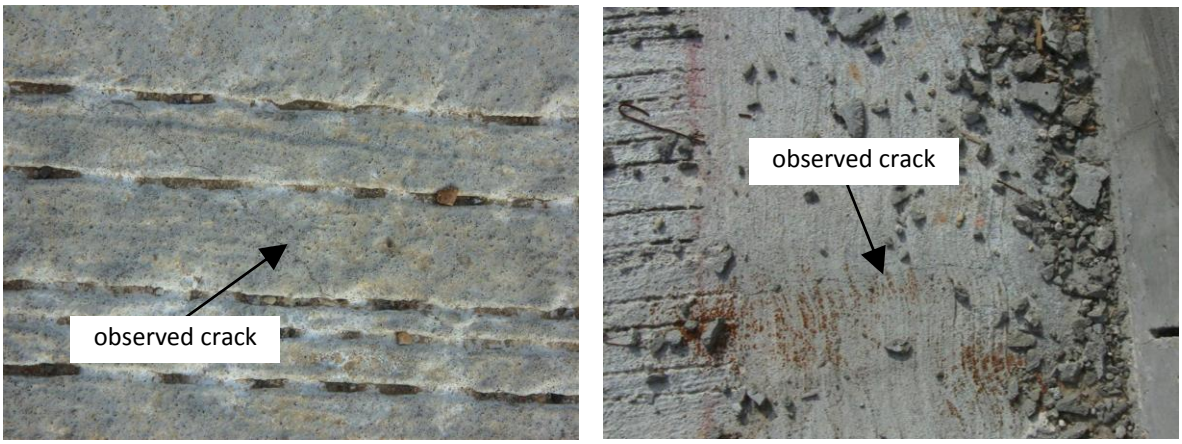

(a) in the middle of deck (skewed) **(b) in overhang (perpendicular)**

Figure 39
Observed deck cracks over continuity detail

Continuity Assessment

The ratio between strain readings obtained from strandmeters on hairpin bars located on both sides of the continuity diaphragm are plotted in Figure 40 versus the recorded temperature. It should be noted that these plots are based on a minimum threshold for strain readings to eliminate erroneous values that result from the division by small numbers. The RMS values

calculated for the two plots shown in Figure 40 were found to be 64 percent for Girder G1 and 89 percent for Girder G3. These results indicate that the new diaphragm detail introduces continuity between adjacent girders albeit at a lesser level than full continuity, i.e., RMS = 1.0.

After further assessment of the continuity level using tiltmeter readings, curvature assessment from multiple sensors along the girder height is needed. Additionally, the change in continuity level over time may also reveal valuable information about the long-term performance of the new continuity detail.

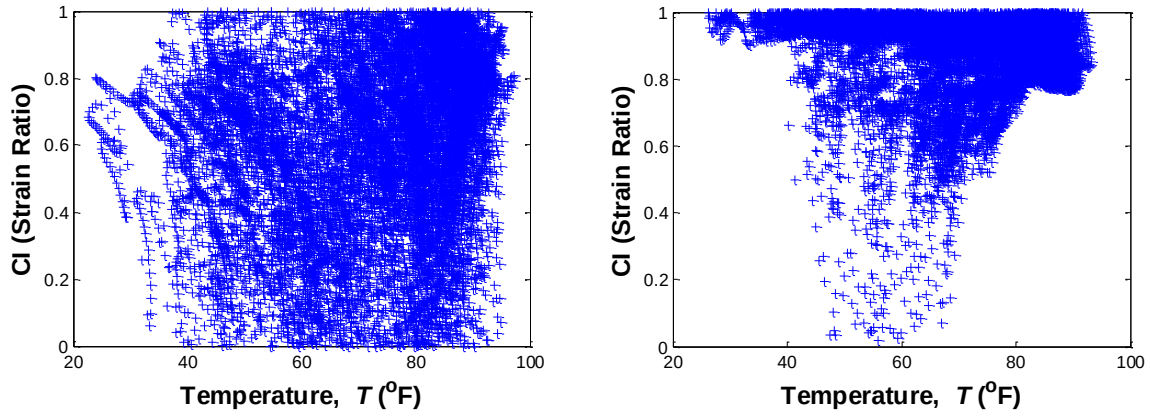

(a) Girder G1 **(b) Girder G3**

Figure 40
Ratio between hairpin strains

Results from Parametric Study using mRESTRAINT

The results from all the cases analyzed using mRESTRAINT are given in Appendix G. The trend of all plots are identical to that reported in NCHRP Report 519 [*1*]. The restraint moment starts as a negative moment on the continuity diaphragm. This is mainly caused by the deck shrinkage. As the girder creep keeps increasing the restraint moment trend starts reversing direction. Girder creep causes a positive restraint moment. If the effect of the girder creep is higher than the other negative-moment causing effects, the connection will eventually be subjected to a positive moment. By using the procedure described in the section titled "Methodology for Establishing Age of Continuity," minimum girder age at continuity that achieves prespecified acceptable restraint moment levels, $M_{r,a}$, were determined. Table 7 through Table 10 list the results from this study. It can be seen that the recommended 90-day age of continuity meets the demands for some of the cases presented in the tables. However, girder ages exceeding this limit were also obtained for many cases. This shows that one continuity age requirement may not be adequate for all bridge configurations. Furthermore, these dates were determined using the creep and shrinkage models in the original RESTRAINT program. In other words, it does not account for thermal variations, especially temperature gradients. From the observations of the research team, thermal effects are probably the most important factor in developing the restraint moment. The girder ages presented in Table 7 through Table 10 would probably be lower if the thermal effects were considered.

Another observation from the results in Table 7 through Table 10 is that three-span bridge configurations seem to require longer girder age than two-span configurations for the same criterion. This may be attributed to the fact that middle spans in three-span configurations are stiffer than exterior spans, thus causing a higher restraint moment. Configurations with spans are only restrained on one side and hence are less stiff than the middle span of a three-span bridge configuration of similar specification.

Table 7
Minimum girder age at continuity (in days) that meets acceptable restraint moment levels, $M_{r,a}$, (7500 days – diaphragm cracking moment)

Case	$M_{r,a}$				
	0.0 M_{cr}	**0.05 M_{cr}**	**0.10 M_{cr}**	**0.25 M_{cr}**	**0.50 M_{cr}**
2S-1R-1D	81	80	79	77	72
2S-0.75R-1D	94	93	91	88	84
2S-0.5R-1D	106	104	102	97	89
2S-1R-0.5D	81	80	79	77	72
2S-0.75R-0.5D	95	93	92	88	84
2S-0.5R-0.5D	107	105	103	97	89
2S-1R-0.25D	81	80	79	76	71
2S-0.75R-0.25D	95	94	92	88	84
2S-0.5R-0.25D	109	107	105	98	89
2S-1R-0.125D	81	80	79	75	70
2S-0.75R-0.125D	97	95	93	89	83
2S-0.5R-0.125D	113	111	108	100	88
2S-1R-0.05D	81	80	78	73	66
2S-0.75R-0.05D	101	99	96	89	81
2S-0.5R-0.05D	126	122	117	105	87
Average (2 spans)	**97**	**95**	**93**	**88**	**81**
3S-1R-1D	101	98	96	89	81
3S-1.5R-1D	102	100	98	91	82
3S-2R-1D	129	126	123	116	102
3S-1R-0.5D	101	98	96	89	81
3S-1.5R-0.5D	102	100	98	91	82
3S-2R-0.5D	130	127	124	116	102
3S-1R-0.25D	101	98	95	88	80
3S-1.5R-0.25D	103	101	98	91	81
3S-2R-0.25D	131	128	125	116	101
3S-1R-0.125D	101	98	95	87	77
3S-1.5R-0.125D	104	101	99	90	80
3S-2R-0.125D	134	131	127	117	100
3S-1R-0.05D	100	96	92	84	70
3S-1.5R-0.05D	109	105	101	89	74
3S-2R-0.05D	144	139	134	119	94
Average (3 spans)	**113**	**110**	**107**	**98**	**86**
Average (all)	**105**	**102**	**100**	**93**	**83**

Table 8
Minimum girder age at continuity (in days) that meets acceptable restraint moment levels, $M_{r,a}$, (20000 days – diaphragm cracking moment)

Case	$M_{r,a}$				
	0.0 M_{cr}	**0.05 M_{cr}**	**0.10 M_{cr}**	**0.25 M_{cr}**	**0.50 M_{cr}**
2S-1R-1D	83	83	82	79	75
2S-0.75R-1D	99	97	96	92	87
2S-0.5R-1D	111	109	107	102	92
2S-1R-0.5D	83	83	82	79	74
2S-0.75R-0.5D	99	98	96	92	87
2S-0.5R-0.5D	112	110	108	102	93
2S-1R-0.25D	83	82	81	79	74
2S-0.75R-0.25D	100	99	97	92	86
2S-0.5R-0.25D	115	112	110	104	93
2S-1R-0.125D	83	82	81	78	72
2S-0.75R-0.125D	102	100	98	92	86
2S-0.5R-0.125D	119	116	114	106	93
2S-1R-0.05D	83	82	80	76	68
2S-0.75R-0.05D	106	104	101	92	84
2S-0.5R-0.05D	132	128	123	111	90
Average (2 spans)	**101**	**99**	**97**	**92**	**84**
3S-1R-1D	107	104	102	95	85
3S-1.5R-1D	106	104	102	96	86
3S-2R-1D	135	132	129	121	108
3S-1R-0.5D	107	104	102	94	85
3S-1.5R-0.5D	107	105	102	96	86
3S-2R-0.5D	136	133	130	122	108
3S-1R-0.25D	107	104	101	93	84
3S-1.5R-0.25D	108	105	103	96	85
3S-2R-0.25D	137	134	131	122	107
3S-1R-0.125D	107	104	101	92	81
3S-1.5R-0.125D	109	106	104	95	84
3S-2R-0.125D	141	137	134	123	106
3S-1R-0.05D	106	102	98	88	74
3S-1.5R-0.05D	114	110	106	94	78
3S-2R-0.05D	151	146	141	126	101
Average (3 spans)	**118**	**115**	**112**	**104**	**91**
Average (all)	**110**	**107**	**105**	**98**	**87**

Table 9
Minimum girder age at continuity (in days) that meets acceptable restraint moment levels, $M_{r,a}$, (7500 days – PSC girder cracking moment)

Case	$M_{r,a}$				
	0.0 M_{cr}	**0.05 M_{cr}**	**0.10 M_{cr}**	**0.25 M_{cr}**	**0.50 M_{cr}**
2S-1R-1D	81	79	78	72	64
2S-0.75R-1D	94	91	89	84	76
2S-0.5R-1D	106	102	99	89	80
2S-1R-0.5D	81	79	77	72	63
2S-0.75R-0.5D	95	91	89	84	75
2S-0.5R-0.5D	107	103	100	89	79
2S-1R-0.25D	81	79	77	71	62
2S-0.75R-0.25D	95	92	89	84	74
2S-0.5R-0.25D	109	105	101	89	78
2S-1R-0.125D	81	79	77	70	59
2S-0.75R-0.125D	97	93	89	83	72
2S-0.5R-0.125D	113	108	103	89	76
2S-1R-0.05D	81	78	75	66	54
2S-0.75R-0.05D	101	96	90	81	65
2S-0.5R-0.05D	126	118	110	88	68
Average (2 spans)	**97**	**93**	**90**	**81**	**70**
3S-1R-1D	101	96	91	82	66
3S-1.5R-1D	102	98	94	84	69
3S-2R-1D	129	123	118	102	79
3S-1R-0.5D	101	96	91	81	65
3S-1.5R-0.5D	102	98	94	84	68
3S-2R-0.5D	130	124	118	102	78
3S-1R-0.25D	101	95	90	80	63
3S-1.5R-0.25D	103	99	94	83	66
3S-2R-0.25D	131	125	119	100	76
3S-1R-0.125D	101	95	89	78	59
3S-1.5R-0.125D	104	99	94	82	62
3S-2R-0.125D	134	127	120	99	73
3S-1R-0.05D	100	93	87	71	52
3S-1.5R-0.05D	109	102	95	77	54
3S-2R-0.05D	144	134	124	93	59
Average (3 spans)	**113**	**107**	**101**	**86**	**66**
Average (all)	**105**	**100**	**95**	**84**	**68**

Table 10
Minimum girder age at continuity (in days) that meets acceptable restraint moment levels, $M_{r,a}$, (20000 days – PSC girder cracking moment)

Case	$M_{r,a}$				
	0.0 M_{cr}	**0.05 M_{cr}**	**0.10 M_{cr}**	**0.25 M_{cr}**	**0.50 M_{cr}**
2S-1R-1D	83	82	80	75	66
2S-0.75R-1D	99	96	93	87	78
2S-0.5R-1D	111	108	104	93	83
2S-1R-0.5D	83	82	80	75	66
2S-0.75R-0.5D	99	96	93	86	78
2S-0.5R-0.5D	112	109	105	94	82
2S-1R-0.25D	83	81	80	74	64
2S-0.75R-0.25D	100	97	93	86	77
2S-0.5R-0.25D	115	110	106	94	81
2S-1R-0.125D	83	81	79	72	61
2S-0.75R-0.125D	102	98	94	86	75
2S-0.5R-0.125D	119	114	109	94	79
2S-1R-0.05D	83	80	77	68	55
2S-0.75R-0.05D	106	101	95	83	68
2S-0.5R-0.05D	132	124	116	92	71
Average (2 spans)	**101**	**97**	**94**	**84**	**72**
3S-1R-1D	107	102	97	86	70
3S-1.5R-1D	106	103	99	88	72
3S-2R-1D	135	129	124	108	83
3S-1R-0.5D	107	102	97	85	69
3S-1.5R-0.5D	107	103	99	87	71
3S-2R-0.5D	136	130	124	107	83
3S-1R-0.25D	107	102	96	84	67
3S-1.5R-0.25D	108	103	99	87	70
3S-2R-0.25D	137	131	125	106	80
3S-1R-0.125D	107	101	95	82	63
3S-1.5R-0.125D	109	104	99	85	66
3S-2R-0.125D	141	133	126	105	77
3S-1R-0.05D	106	98	91	75	54
3S-1.5R-0.05D	114	107	100	81	56
3S-2R-0.05D	151	140	130	100	63
Average (3 spans)	**118**	**113**	**107**	**91**	**70**
Average (all)	**110**	**105**	**100**	**87**	**71**

Results from Live Load Test

The sensor readings from the live load test are plotted in Appendix E. The sensor readings for each individual loading position were extracted using the approach described in the "Sample Sensor Reading" section (see Figure 27). As can be expected, not all sensors were highly strained by all loading positions because of their location with respect to the position of the trucks. Therefore, a minimum threshold strain was set to discard readings that were too small to be considered reliable. The results were compared to analytical results from the Global FE model. Figure 41 shows a plot of the vertical displacement contours for the P5 load case. P5 is a case that causes positive moments in Span 24 (middle span). The two trucks were positioned over Girder G1, G2, and G3. As a result, downward deformations at this location could be seen in Figure 41. At the same time, upward movement of girders in adjacent spans (23 and 25) took place.

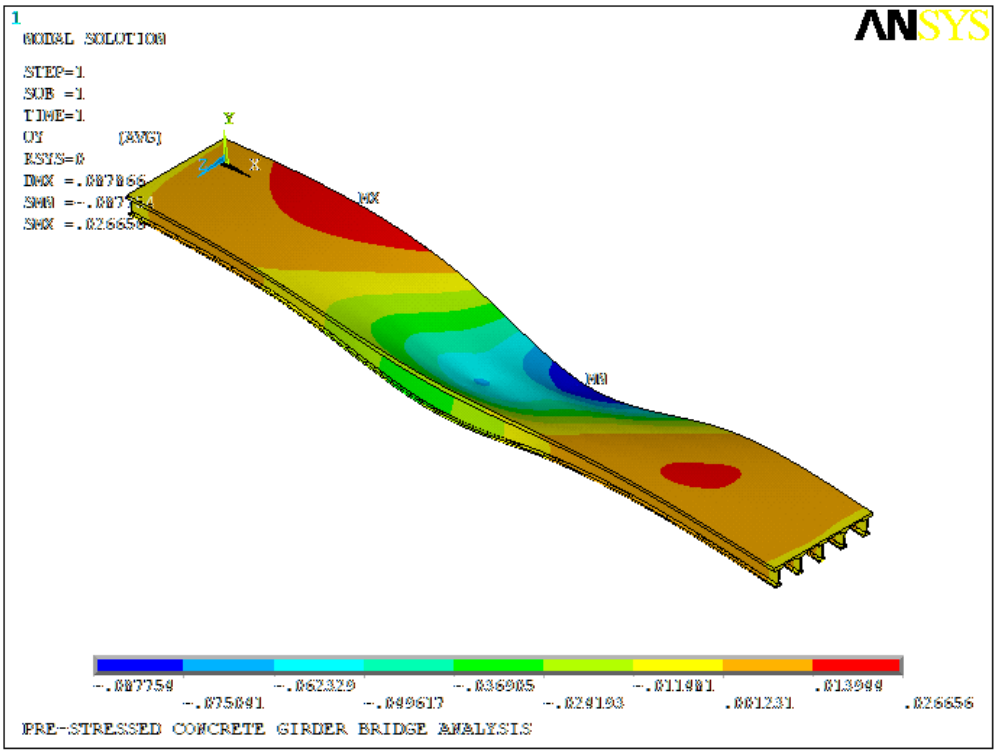

Figure 41
Contours of vertical displacement (Case P5)

One interesting observation was that the hairpin strain records confirmed that forces were transferred from Span 25 (loaded span) to Span 23 (monitored span) for load positions P3 and P6. These two cases caused positive moments on the monitored continuity detail. Figure 42 shows the magnitude of the strains, which are larger for Girder G3 than G1. A similar observation was related to the recorded negative strains for load positions P2 and P5. Both

were load cases that target positive moment in the middle of Span 24. Therefore, trucks were positioned over Span 24. The trucks would, however, apply negative moments on the continuity diaphragm if it performed as intended. In both load positions (P2 and P5), the hairpin bars experienced negative strains that were, as expected, higher than the positive strains discussed earlier. Like the P3 and P6 load cases, the sensors were in one span and the loads acted on another for these two cases. Hence, the ability of the new detail to transfer forces between spans was confirmed. It should be noted that results from Girders G1 and G3 were only presented since Girder G5 was not instrumented on the hairpin bars in Span 23 and, therefore, a plot was not provided.

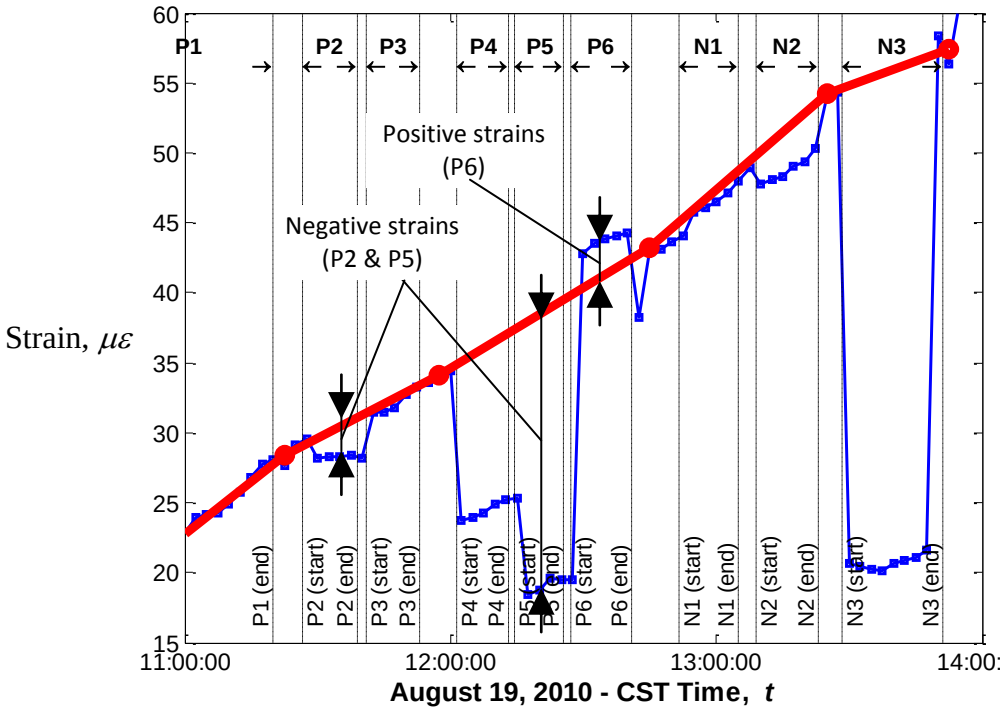

Girder G1 – Span 23 –Sensor #3

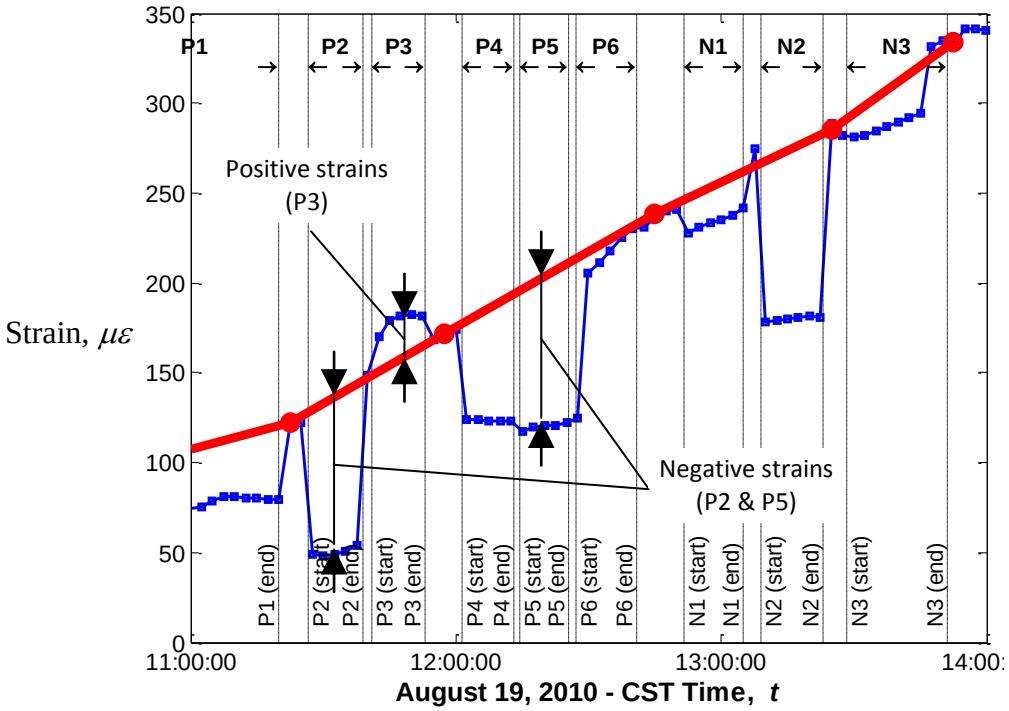

Girder G3 – Span 23 –Sensor #51

Figure 42
Strains in hairpin bars showing positive values for faraway load cases

Feedback from Contractors

During the installation process, discussions with the precaster and the contractor's site engineers about the continuity detail ensued. The precaster's point of view can be summarized in the following points:

- Hairpin bars require special end of girder forms, which can be made of multiple wooden or steel pieces. Extra attention is required to prevent leaking between the pieces. Wooden forms are not reusable as they are specific for each design and therefore many of them will have to be manufactured for any given project. Steel forms are costlier and if not many girders are cast with the same detail, it adds to the cost.
- The labor involved in adding hairpin bars is minimal. A maximum estimate to insert the bars and tie them is 30 minutes per girder.

As expected, the precaster would rather not have to install hairpin bars because of the additional effort, albeit minimal. The casting yard engineer indicated that inserting hairpin bars is not any worse than dealing with skews. They would do it if they have to, but would rather not.

Stronger comments about the detail came from the contractor. The project engineer for Bridge #2 indicated the following:

- Hairpin bars add difficulties to the girder installation process. First, particular attention needs to be paid to the alignment of the bars in the girder, so there isn't a conflict in the field with the dowels or adjacent girder loops. Also, threading the diaphragm steel through these loops is difficult, as this is done after the girders are erected, which makes the workspace congested.
- The additional cost for this type of continuity diaphragm is approximately 15-20 percent more than conventional diaphragms, due mainly to the extra time it takes to construct them.
- The contractor would rather build conventional DOTD diaphragms than the NCHRP Report 519 positive moment continuity detail.

CONCLUSIONS

Summary

A detailed study on the performance of the NCHRP Report 519 continuity detail has been conducted [*1*]. The study involved the installation of a structural health monitoring system on a newly constructed bridge from the John James Audubon Project. Bridge #2 was chosen for the study because it is skewed and uses Bulb-T (BT-72) girders. The 96-channel monitoring system included embedded and surface-mounted sensors that measure strains, rotations, and gap openings. Data from almost a 24-month period has been collected including some data from the period when the girders were curing in the casting yard. The data was processed and analyzed to better understand the performance of the new detail.

Analytical models were also developed to study the restraint moment acting on this type of detail. First, the program that resulted from the NCHRP Report 519 study is modified to expand its applicability to bridges like the monitored bridge segment, i.e., unsymmetric span lengths and different girder configurations. The modified program (`mRESTRAINT`) was used to conduct a parametric study to determine minimum girder age requirements that meet prespecified design criteria. Three finite element models were also developed to study the global behavior as well and the local stress distribution in bridges employing the new detail.

Finally, a live load test was conducted on the monitored bridge segment. Static and dynamic load tests were carried out. The results from the live load tests were analyzed to study the performance of the new detail under live loads.

Conclusions

The conclusions from this study can be summarized in the following:

1. Positive moments develop in bridges employing the new continuity detail. They are caused by long-term effects such as girder creep and thermal variations.

2. The continuity detail has the ability to transfer forces from one girder end to the adjacent girder end across the continuity diaphragm.

3. Positive restraint moment can cause cracking in the diaphragm and/or girder ends. Both types of cracking affect the performance of the diaphragm and hence the bridge. More importantly, girder cracking may have adverse effects on the durability and on the shear capacity of the girders. Therefore, special care should be given to the level of positive restraint moment during design.

4. Seasonal and daily temperature variations can cause large restraint moments in the bridge, especially temperature gradients. The level of restraint moment due to the combined seasonal and daily temperature is probably the most important factor in the design of this detail, since the designer has no influence on the temperatures at the bridge site. The other positive-moment causing factor, i.e., girder creep caused by prestressing forces, can be greatly reduced by not introducing continuity until a large portion of the creep takes place prior to pouring the diaphragm.

5. It appears based on the parametric study that the girder age at which continuity can be introduced to achieve acceptable positive moment levels varies based on bridge configuration. Therefore, the recommended 90-day age from NCHRP Report 519 will need to be evaluated for each design project using the modified `RESTRIANT` program (`mRESTRAINT`) after superimposing the positive moments caused by thermal gradients.

6. The live load test revealed that the continuity detail transferred negative and positive moments across the diaphragm. The strains from the live load test were much lower compared to other long-term effects. Even if the actual design load were to be applied (approximately twice the test live load), the strains would still be small. Therefore, the live load case should be considered in the design; however, it is not the most demanding action on the detail.

7. The construction cost of the detail is not substantial for the precaster although they would rather build girders without the detail. The contractor's critique of the new detail was stronger than the precaster's. The contractor is of the opinion that the continuity diaphragm, especially for skewed bridge configurations, is cumbersome and adds to the construction time. Simpler details would expedite the construction of slab-on-girder bridges.

8. The monitored segment was skewed. Skewed configurations cause additional straining actions that do not develop in non-skew bridge configurations. Therefore, the skew effect may have exacerbated the straining actions on the continuity detail. However, this hypothesis will need to be explored further through analytical or field investigations before it is confirmed.

RECOMMENDATIONS

The research team recommends that the employment of this new detail be allowed only after a thorough investigation of its benefits, both structurally and economically, on a per project basis. When employed, the design should account for factors affecting the development of the positive moment acting on the continuity detail including creep due to prestressing forces, differential shrinkage, and seasonal as well as daily thermal variations. Special consideration shall be given to the effects of temperature gradient in the design of this detail.

Simpler details expedite the construction of this type of bridge needed to be one of the studied alternatives for new projects. *Partial Integration* is one such detail that eliminates the expansion joint without developing large continuity moment over the supports. This can be achieved by pouring continuous decks over simply supported girders.

The modified `RESTRAINT` program (`mRESTRAINT`) does not consider temperature gradient effects, which is one of the most important causes of positive restraint moment. It is therefore recommended that thermal effects be studied using other structural analysis tools. Future modifications of `mRESTRAINT` to include the effect of thermal gradients are possible and recommended to keep the design of the new detail in one tool.

The John James Audubon Project involves many bridges that employ the new detail. This is an excellent long-term test bed for the performance of the new detail. It is recommended that visual inspections of the hundreds of constructed joints, similar to the one investigated in this report, be conducted. This opportunity can provide invaluable long-term performance information.

ACRONYMS, ABBREVIATIONS, AND SYMBOLS

AASHTO	The American Association of State Highway and Transportation Officials
A_g	Area of girder
A_c	Gross area of concrete
A_{tr}	Concrete deck slab area with transformed reinforcement area
A_s	Area of steel
C	Calibration factor for the sensor
CIP	Cast-in-place
CTL	Concrete Technologies Laboratory
D	Ratio of diaphragm stiffness
Dr_L, Dr_M, Dr_H	Relative densities corresponding to low, medium and high compressibility conditions.
d_b	Diameter of prestress strand
DOT	Department of Transportation
DOTD	Department of Transportation and Development
E	Modulus of elasticity
EC	Sisterbar
$E_{c\ deck}$	Modulus of elasticity of deck concrete
E_{qt}	Equation of time
ES	Strandmeter
e	Eccentricity
f_1	Natural frequency of the datum
f_2	Natural frequency of the measured readings
f_r	Modulus of rupture
f_{pe}	Effective prestress
f_{psi}	Stress in the strand at the service limit state
f_{pul}	Stress in the strand at the strength limit state
GVW	Gross Vehicle Weight
GUI	Graphical User Interface
g	Acceleration due to gravity
ID	Intermediate Diaphragm
I_{dia}	Diaphragm Moment of Inertia
I_g	Girder Moment of Inertia
I_0	Extraterrestrial solar radiation
k	Gauge constant

L_i	Span length for Span *i*
LRFD	Load and Resistance Factor Design
LSD	Limit State Design
LTRC	Louisiana transportation research center
l_t	Transfer length
l_{dsh}	Total length of extended strand
MUX	Multiplexer
M_{cr}	Cracking moment
M_r	Restraint Moment
$M_{r,a}$	Allowable Restraint Moment
n	Modular ratio
NaN	Not a number
NCHRP	National Cooperative Highway Research Program
NOOA	National Oceanic and Atmospheric Administration
PCA	Portland Cement Association
PCBT	Precast concrete bulb tee girders
PCI	Prestressed Concrete Institute
PSC	prestressed concrete
PRC	Project Review Committee
P_e	Effective prestressing force
ppm	Parts per million
PVC	Poly vinyl chloride
R	Ratio of span lengths
RMS	Root Mean Square
R_0	Initial sensor reading in digit
R_1	Current sensor reading in digit
SHM	Structural Health Monitoring
T_0	Initial temperature
T_1	Current temperature
T_{solar}	Solar time
TM	Tiltmeter
VBA	Visual Basic
VDOT	Virginia Department of Transportation
VW	Vibrating wire strain gauge
w	Hour angle
x_i	Monitored data
$\overline{x}$	Mean

y_t	Distance from neutral axis to the top of girder
$\mu\varepsilon$	Microstrain
ε_{sh}	Unrestrained shrinkage strain
σ	Standard deviation
ρ	Density
θ	Slope

REFERENCES

1. Miller, R. A.; Castrodale, R.; Mirmiran, A.; and Hastak, M. "Connection of Simple-Span Precast Concrete Girders for Continuity." NCHRP Report 519, Transportation Research Board, Washington, D.C., 2004.
2. Okeil, A. M.; and El-Safty, A. K. "Partial Continuity in Bridge Girders With Jointless Decks," *Practice Periodical on Structural Design and Construction*, ASCE, Vol. 10, No. 4, 2005, pp. 229-238.
3. Loveall, C. L. "Jointless Bridge Decks," *Civil Engineering*, ASCE, Vol. 55, No. 11, 1985, pp. 64-67.
4. Wasserman, E. P. "Jointless Bridge Decks," *AISC Engineering Journal*, AISC, Vol. 24, No. 3, 1987, pp. 93-100.
5. Russell, H. G.; and Gerken, L. J. "Jointless Bridges – the Knowns and the Unknowns," *Concrete International*, ACI, Vol. 16, No. 4, 1994, pp. 44-48.
6. Burke, M. P., Jr. "Integral Bridges: Attributes and Limitations," ACI National Concrete Engineering Conference, Chicago, IL, 1992.
7. Burke, M. P., Jr. "Semi Integral Bridges: Movements and Forces," *Transportation Research Record*, National Research Council, Vol. 1460, 1994, pp. 1-7.
8. Burke, M. P., Jr. "Reducing Bridge Damage Caused By Pavement Forces," *Concrete International*, ACI, Vol. 26, No. 2, 2004, pp. 83-89.
9. Alampalli, S.; and Yannotti, A. P. "In-Service Performance of Integral Bridges and Jointless Decks," *Transportation Research Record*, National Research Council, Vol. 1624, 1998, pp. 1-7.
10. Thippeswamy, H. K.; GangaRao, H. V. S.; and Franco, J. M. "Performance Evaluation of Jointless Bridges," *Journal of Bridge Engineering*, ASCE, Vol. 7, No. 5, 2002, pp. 276-289.
11. Demartini, C. J.; and Haywood, R. J. "Repair of the Southern Approach to the Story Bridge by Elimination of the Contraction Joints," Autostrads Conference, Brisbane, Australia, 1991, pp. 357-370.
12. Pierce, P. "Jointless Redecking," *Civil Engineering*, ASCE, Vol. 61, No. 9, 1991, pp. 60-64.
13. Caner, A.; and Zia, P. "Behavior and Design of Link Slabs for Jointless Bridge Decks," *PCI Journal*, PCI, Vol. 43, No. 3, 1998, pp. 68-80.
14. Caner, A.; Dogan, E.; and Zia, P. "Seismic Performance of Multisimple-Span Bridges Retrofitted With Link Slabs," *Journal of Bridge Engineering*, ASCE, Vol. 7, No. 2, 2002, pp. 85-93.
15. Wing, K. M.; and Kowalsky, M. J. "Behavior, Analysis, and Design of an Instrumented Link Slab Bridge," *Journal of Bridge Engineering*, ASCE, Vol. 10, No. 3, 2005, pp. 331-344.
16. Siros, K. A.; and Spyrakos, C. C. "Creep Analysis of Hybrid Integral Bridges," *Transportation Research Record*, National Research Council, Vol. 1476, 1995, pp. 147-154.

17. Gastal, F.; and Zia, P. "Analysis of Bridge Beams With Jointless Decks," IABSE Symposium, Lisbon, Portugal, 1989, pp. 555-560.
18. Richardson, D. R. "Simplified Design Procedures for the Removal of Expansion Joints from Bridges Using Partial Debonded Continuous Decks." M.Sc., North Carolina State University, 1989.
19. Thippeswamy, H. K.; and GangaRao, H. V. S. "Analysis of In-Service Jointless Bridges," *Transportation Research Record*, National Research Council, Vol. 1476, 1995, pp. 162-170.
20. Zia, P.; Caner, A.; and El-Safty, A. "Jointless Bridge Decks." Research Report No. FHWA/NC/95-006, Center for Transportation Engineering Studies, 1995.
21. Oesterle, R. G.; Glikin, J. D.; and Larson, S. C. "Design of Precast Prestressed Bridge Girders Made Continuous." NCHRP Report No. 322, Transportation Research Board, Washington, D.C., 1989.
22. Newhouse, C. D. "Design and Behavior of Precast, Prestressed Girders Made Continuous – An Analytical and Experimental Study." Ph.D. Dissertation, Department of Civil and Environmental Engineering, Virginial Polytechnic Institute and State University, 2005.
23. Saber, A.; Toups, J.; Guice, L.; and Tayebi, A. "Continuity Diaphragm for Skewed Continuous Span Precast Prestressed Concrete Girder Bridges." 383, Louisiana Transportation Research Center, Baton Rouge, LA, 2004.
24. Saber, A. "Field Verification for the Effectiveness of Continuity Diaphragms for Skewed Continuous P/C P/S Concrete Girder Bridges." 440, Louisiana Transportation Research Center, Baton Rouge, LA, 2009.
25. Cai, S. C. S.; and Avent, R. R. "Assessing the Needs for Intermediate Diaphragms in Prestressed Concrete Bridges." 420, Louisiana Transportation Research Center, Baton Rouge, LA, 2008.
26. Mattock, A. H. "Precast-Prestressed Concrete Bridges, 5. Creep and Shrinkage Studies," *Journal of the PCA Research and Development Laboratories*, Vol. 3, No. 2, 1961, pp. 32-66.
27. Freyermuth, C. L. "Design of Continuous Highway Bridges With Precast, Prestressed Concrete Girders," *Journal of the Prestressed Concrete Institute*, Vol. 14, No. 2, 1969, pp. 14-39.
28. Peterman, R. J.; and Ramirez, J. A. "Restraint Moments in Bridges With Full-Span Prestressed Concrete Form Panels," *PCI Journal*, Precast/Prestressed Concrete Institute, Vol. 43, No. 1, 1998, pp. 54-73.
29. McDonagh, M. D.; and Hinkley, K. B. "Resolving Restraint Moments: Designing for Continuity in Precast Prestressed Concrete Girder Bridges," *PCI Journal*, Precast/Prestressed Concrete Institute, Vol. 48, No. 4, 2003, pp. 104-119.
30. ASTM Standard C 39. "Standard Test Method for Compressive Strength of Cylindrical Concrete Specimens," ASTM International, West Conshohocken, PA, 2005.
31. ASTM Standard C 469 . "Standard Test Method for Static Modulus of Elasticity and Poisson's Ratio of Concrete in Compression," ASTM International, West Conshohocken, PA, 2002.

32. ASTM Standard C 78. “Standard Test Method for Flexural Strength of Concrete (Using Simple Beam With Third-Point Loading),” ASTM International, West Conshohocken, PA, 2002.
33. ASTM Standard C 496. “Standard Test Method for Splitting Tensile Strength of Cylindrical Concrete Specimens,” ASTM International, West Conshohocken, PA, 2004.
34. Mirmiran, A.; Kulkarni, S.; Castrodale, R.; Miller, R.; and Hastak, M. “Nonlinear Continuity Analysis of Precast, Prestressed Concrete Girders With Cast-in-Place Decks and Diaphragms,” *PCI Journal*, Precast/Prestressed Concrete Institute, Vol. 46, No. 5, 2001, pp. 60-80.
35. Nilson, A. H. Design of Prestressed Concrete., 1987.
36. Chebole, V. “Continuity Moment Assessment in Prestressed Concrete Bridge Girders.” M.S. Thesis, Louisiana State University, Baton Rouge, Louisiana, USA, 2010.
37. ANSYS. “Theory Reference,” ANSYS, Inc., Canonsburg, PA, 2008.
38. AASHTO. LRFD Bridge Design Specifications. American Association of State Highway and Transportation Officials, Washington, D.C., 2008.

APPENDIX A

Picture Documentation and more Details of Installed Sensors

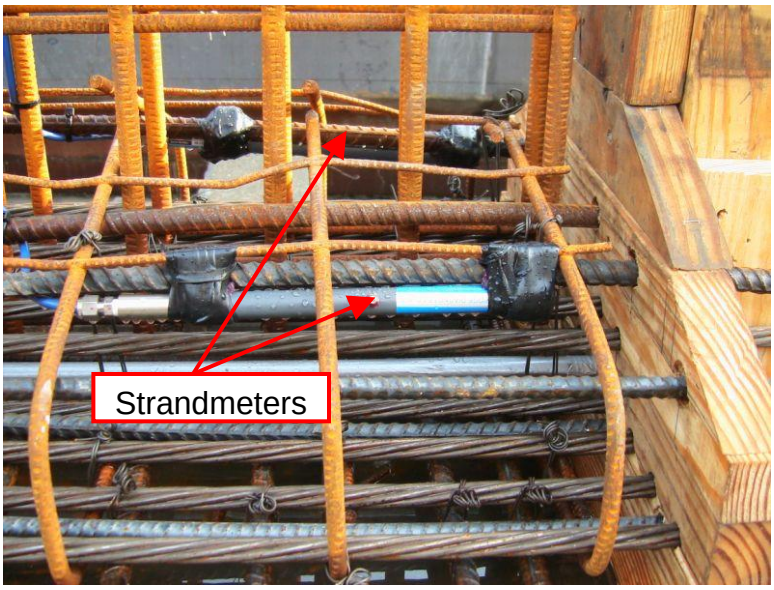

Figure 43
Strandmeters installed on hairpin bars at girder ends

Figure 44
Sisterbar installed next to a prestressing strand at midspan

Figure 45
Strandmeters installed on reinforcing bars in deck over continuity diaphragm

Figure 46
Sisterbars installed next to reinforcing bars in deck over continuity diaphragm

Figure 47
Surface-mounted sensors (vibrating wire gages and tiltmeters) at girder ends

Figure 48
Gap meter installed on brackets connected to girder ends at continuity diaphragm

Figure 49
Protection of wiring for embedded sensors prior to concrete casting

Figure 50
Surge protectors installed on one of every two embedded sensors at the same location

Figure 51
Solar panel powering the monitoring system

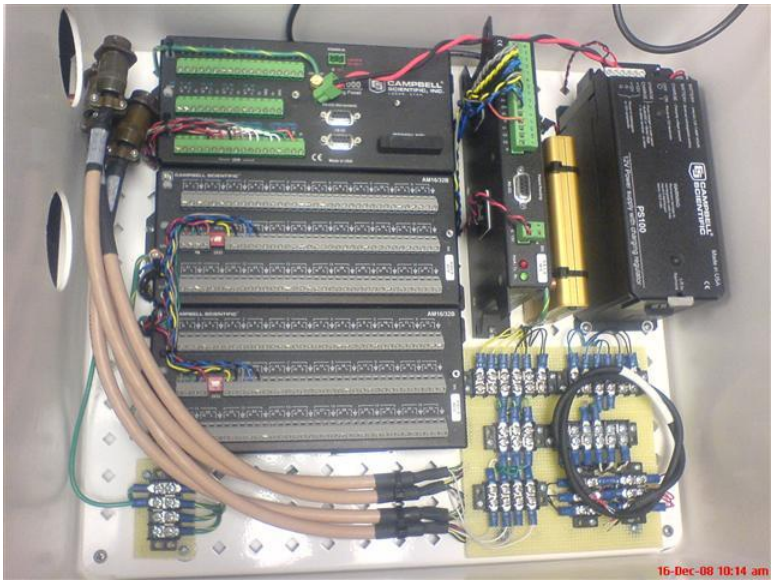

Figure 52
Campbell Scientific datalogger

Figure 53
Datalogger location while monitoring of curing girders in casting yard

Figure 54
Datalogger location in the complete system at bridge site (Bent 24)

Figure 55
Curing of bridge deck

Table 11
Installed sensor details

MUX 1					
Logger Ch.	Mux Chan	SN	Type	Cal	Location
1	1	7885	ES	3.07	G1 Span 24 (Support - Bottom)
2	2	7886	ES	3.06625	G1 Span 24 (Support - Bottom)
3	3	10244	ES	3.04125	G1 Span 23 (Support - Bottom)
4	4	10245	ES	3.04375	G1 Span 23 (Support - Bottom)
5	5	22073	EC	0.347	G1 Span 24 (Support - Top)
6	6	20554	ES	3.07	G2 Span 24 (Support - Top)
7	7	15373	TM	0.002488	G1 Main Span 24 (+ Towards Mid Span)
8	8	15963	TM	0.002452	G1 Main Span 23 (+ Towards Mid Span)
9	9	21547	DM2	0.0004124	G1 Connection
10 through 16	10 - 16	-	-	-	

MUX 2					
Logger Ch.	Mux Chan	SN	Type	Cal	Location
17	1	-	VW	0.96	G1 Span 24 (Support -Top)
18	2	-	VW	0.96	G1 Span 24 (Support - Middle)
19	3	-	VW	0.96	G1 Span 24 (Support - Bottom)
20	4	-	VW	0.96	G1 Span 23 (Support -Top)
21	5	-	VW	0.96	G1 Span 23 (Support -Middle)
22	6	-	VW	0.96	G1 Span 23 (Support -Bottom)
23 through 32	7 - 16	-	-	-	-

MUX 3					
Logger Ch.	Mux Chan	SN	Type	Cal	Location
33	1	-	VW	0.96	G5 Span 24 (Support -Top)
34	2	-	VW	0.96	G5 Span 24 (Support - Middle)
35	3	-	VW	0.96	G5 Span 24 (Support - Bottom)
36	4	-	VW	0.96	G5 Span 23 (Support - Top)
37	5	-	VW	0.96	G5 Span 23 (Support - Middle)
38	6	-	VW	0.96	G5 Span 23 (Support - Bottom)
39	7	-	VW	0.96	G3 Span 24 (Support - Top)
40	8	-	VW	0.96	G3 Span 24 (Support - Middle)
41	9	-	VW	0.96	G3 Span 24 (Support - Bottom)
42	10	-	VW	0.96	G3 Span 23 (Support - Top)
43	11	-	VW	0.96	G3 Span 23 (Support - Middle)
44	12	-	VW	0.96	G3 Span 23 (Support - Bottom)
45	13	10240	ES	3.0525	G5 Span 24 (Support - Bottom)
46	14	10241	ES	3.05	G5 Span 24 (Support - Bottom)
47	15	10432	EC	0.346	G5 Span 24 (Support - Top)
48	16	20552	ES	3.06375	G4 Span 24 (Support - Top)

Table 11 (continued)
Installed sensor details

MUX 4					
Logger Ch.	Mux Chan	SN	Type	Cal	Location
49	1	7882	ES	3.06625	G3 Span 24 (Support - Bottom)
50	2	10242	ES	3.045	G3 Span 23 (Support - Bottom)
51	3	10243	ES	3.05	G3 Span 23 (Support - Bottom)
52	4	10252	ES	3.05	G3 Span 24 (Support - Bottom)
53	5	22072	EC	0.355	G3 Span 24 (Support - Top)
54	6	15966	TM	0.002518	G5 Main Span 24 (+ Towards Bent 24)
55	7	15964	TM	0.002468	G3 Main Span 24 (+ Towards Main Span)
56	8	15965	TM	0.002449	G3 Main Span 23 (+ Towards Mid Span)
57	9	15967	TM	0.002465	G5 Main Span 23 (+ Towards Mid Span)
58	10	21549	DM2	0.0004115	G3 Connection
59	11	21548	DM2	0.0004107	G5 Connection
60 through 64	12 - 16	-	-	-	-

MUX 5					
Logger Ch.	Mux Chan	SN	Type	Cal	Location
65	1	-	VW	0.96	G5 Span 24 (Midspan - Top)
66	2	-	VW	0.96	G5 Span 24 (Midspan - Middle)
67	3	-	VW	0.96	G5 Span 24 (Midspan - Bottom)
68	4	10430	EC	0.345	G5 Span 24 (Midspan - Top)
69	5	10431	EC	0.343	G5 Span 24 (Midspan- Bottom)
70	6	10435	EC	0.354	G5 Span 24 (Midspan - Deck)
71	7	-	VW	0.96	G2 Span 24 (Midspan - Bottom)
72	8	-	VW	0.96	G1 Span 24 (Midspan - Bottom)
73 through 80	9 - 16	-	-	-	-

MUX 6					
Logger Ch.	Mux Chan	SN	Type	Cal	Location
81	1	-	VW	0.96	G3 Span 24 (Midspan -Top)
82	2	-	VW	0.96	G3 Span 24 (Midspan - Middle)
83	3	-	VW	0.96	G3 Span 24 (Midspan - Bottom)
84	4	-	VW	0.96	G4 Span 24 (Midspan -Top)
85	5	-	VW	0.96	G4 Span 24 (Midspan -Middle)
86	6	-	VW	0.96	G4 Span 24 (Midspan -Bottom)
87	7	7883	ES	3.0475	G3 Span 24 (Midspan -Top)
88	8	7884	ES	3.075	G3 Span 24 (Midspan -Bottom)
89	9	10250	ES	3.05625	G4 Span 24 (Midspan - Bottom)
90	10	10251	ES	3.02625	G4 Span 24 (Midspan - Top)
91	11	10426	EC	0.343	G4 Span 24 (Midspan - Top)
92	12	10427	EC	0.351	G4 Span 24 (Midspan - Bottom)
93	13	10428	EC	0.349	G3 Span 24 (Midspan -Top)
94	14	10429	EC	0.351	G3 Span 24 (Midspan -Bottom)
95	15	10433	EC	0.351	G3 Span 24 (Midspan - Deck)
96	16	10434	EC	0.344	G4 Span 24 (Midspan - Deck)

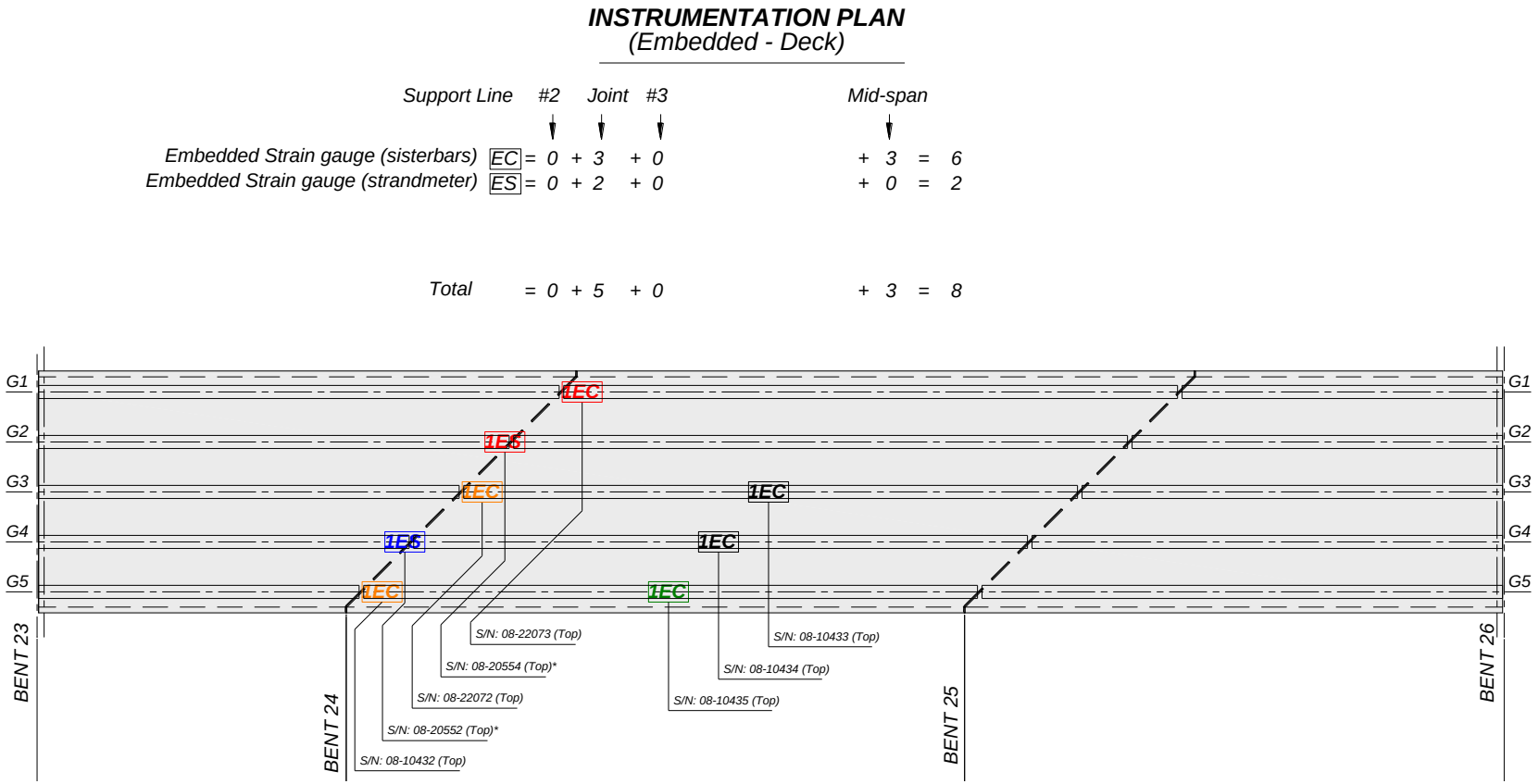

Figure 56
Distribution of embedded sensors in deck

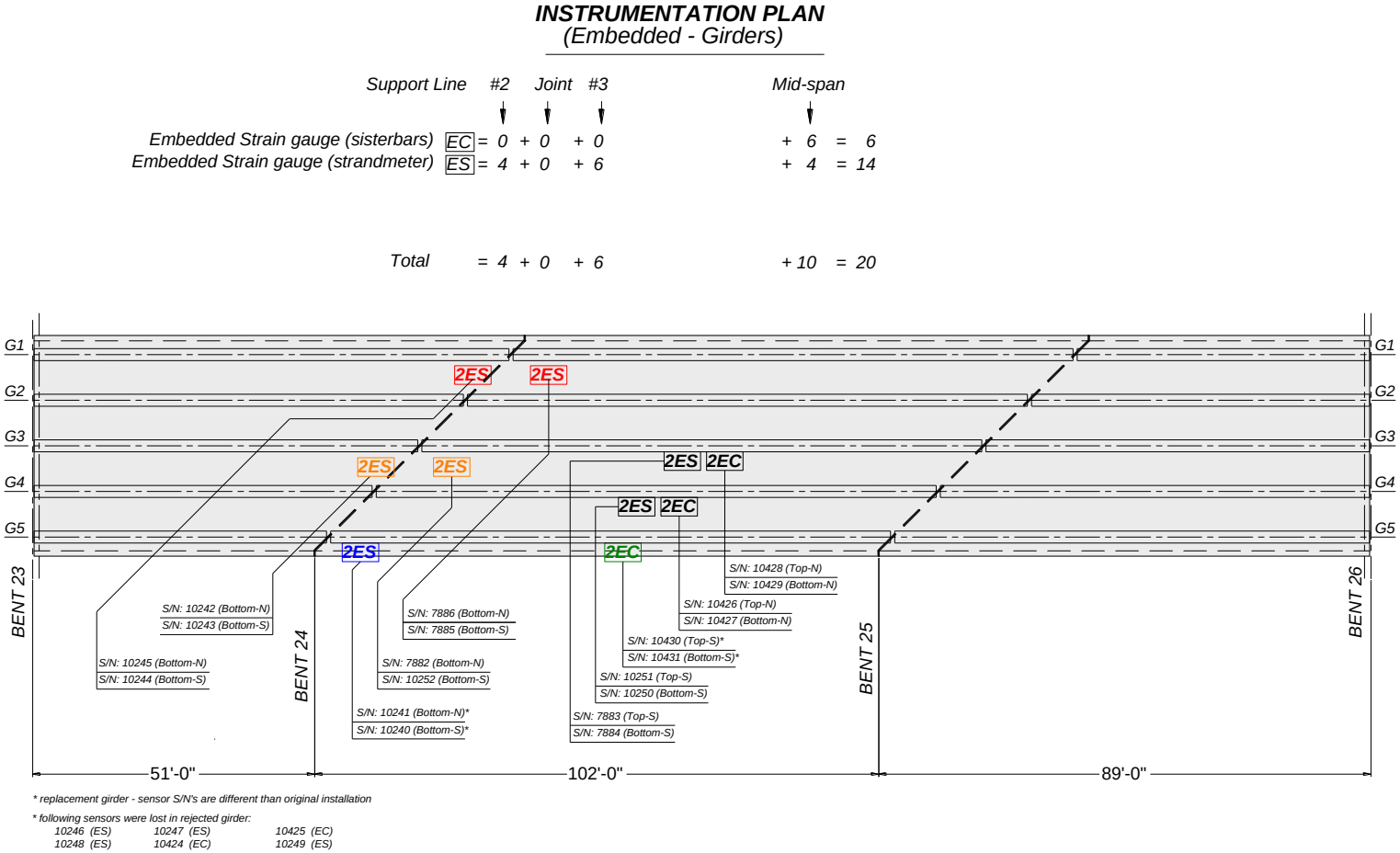

Figure 57
Distribution of embedded sensors in girders

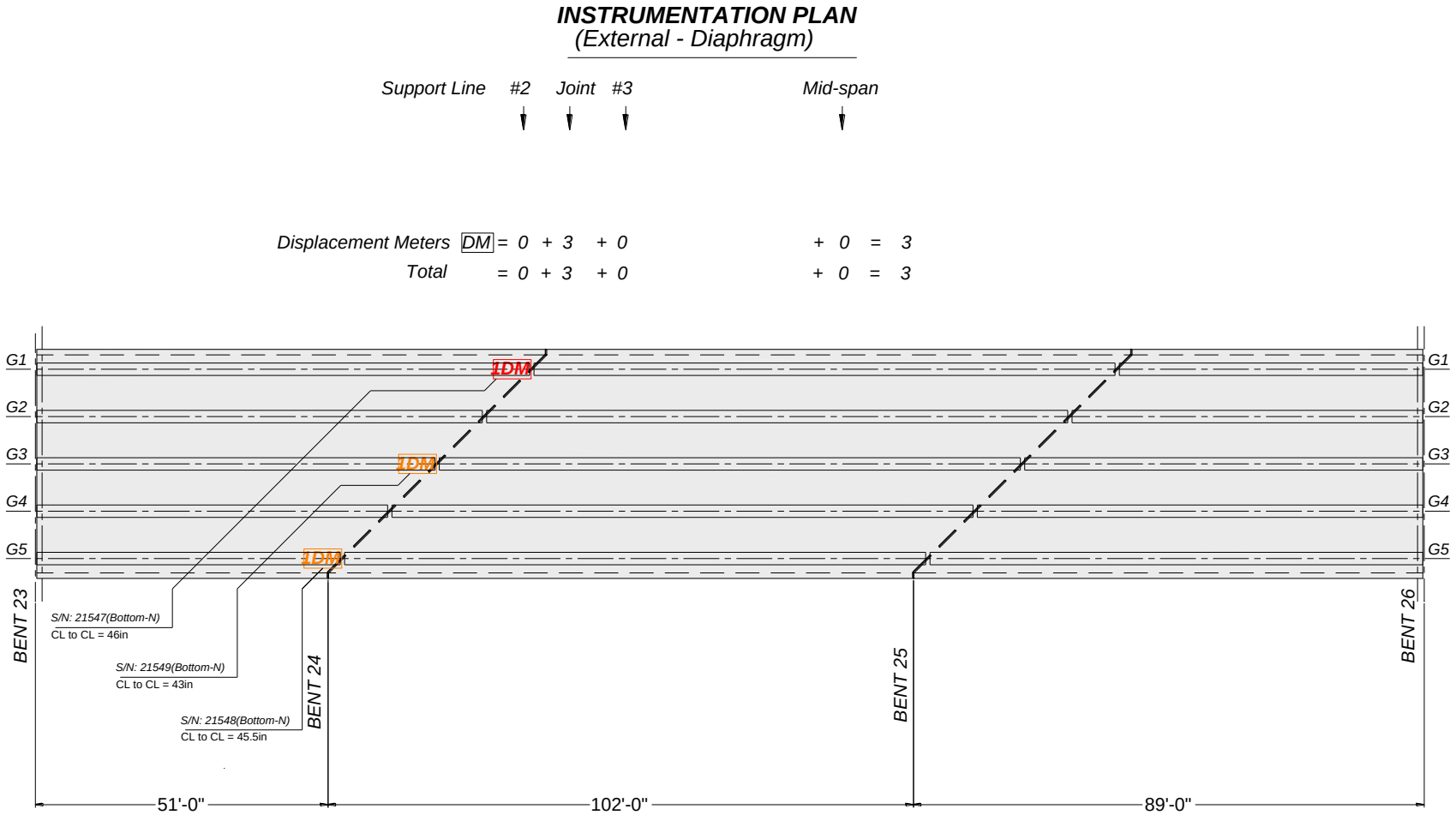

Figure 58
Distribution of gap meters

INSTRUMENTATION PLAN
(External - Girders)

	Support Line	#2	Joint	#3	Mid-span	
Vibrating Wire Strain gauge	VW	= 9	+ 0	+ 9	+ 11	= 29
Vibrating Wire Tiltmeter	TM	= 3	+ 0	+ 3	+ 0	= 6
Total		= 12	+ 0	+12	+ 11	= 35

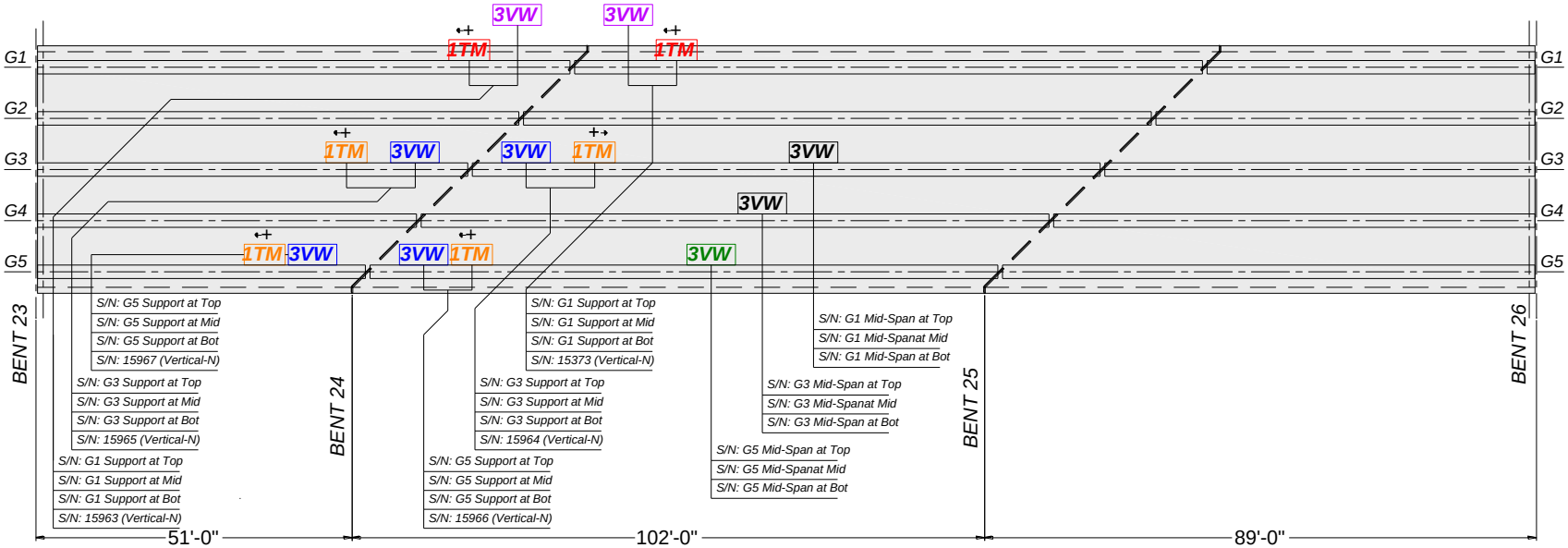

Figure 59
Distribution of surface mounted sensors

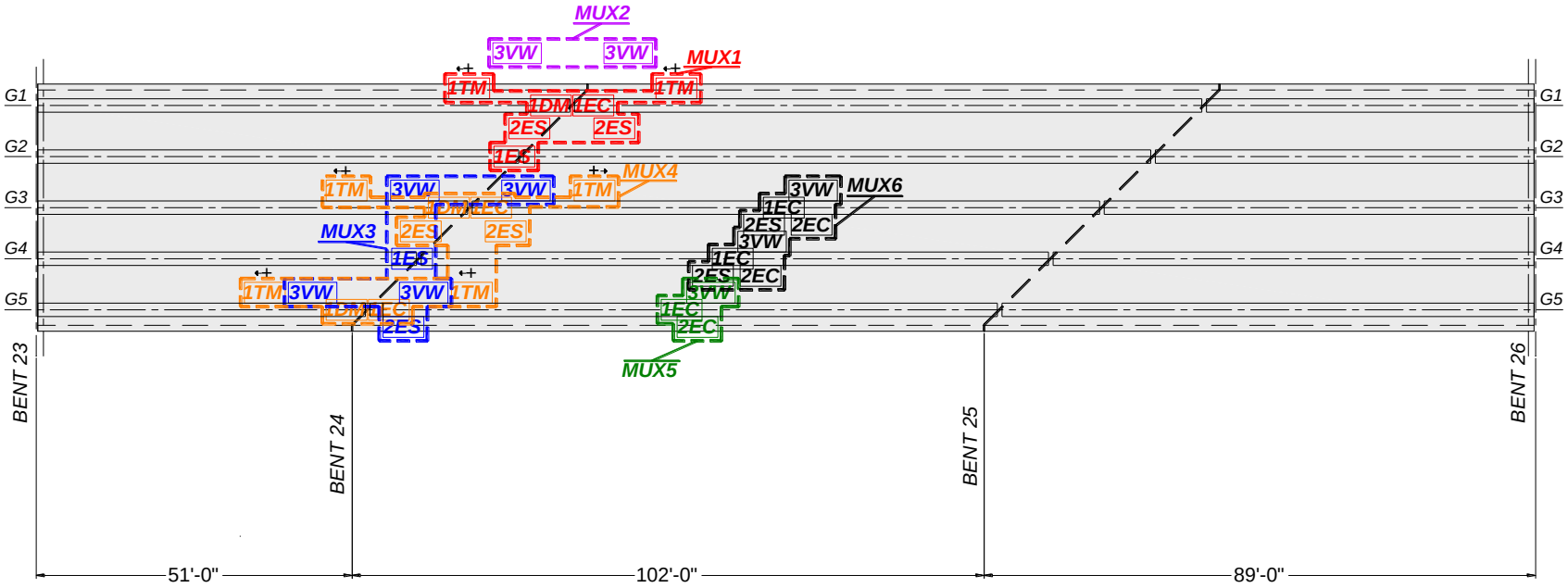

Figure 60
Distribution of sensors on system multiplexers (MUX1 through MUX6)

APPENDIX B

Major Modifications to RESTRAINT Program

This appendix presents the major modifications by the research team of the RESTRAINT program. Screen captures of the input forms (windows) of the original, and the modified, RESTRAINT are presented.

N/A

Original RESTRAINT

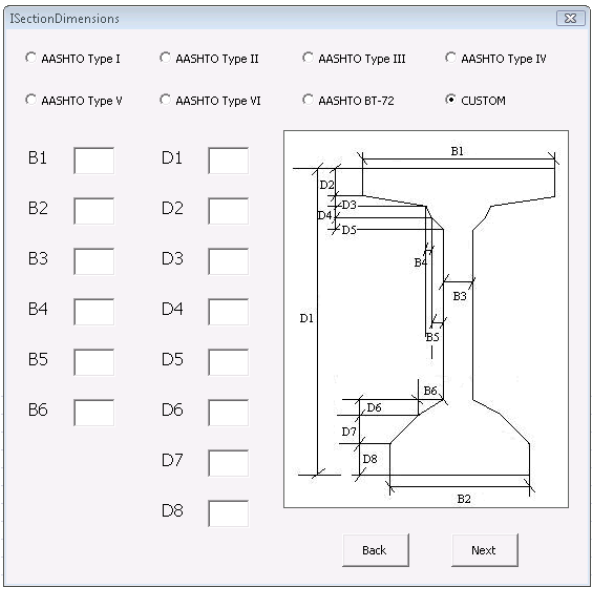

Modified mRESTRAINT

Figure 61
Introducing custom cross-sectional dimensions of I-girders

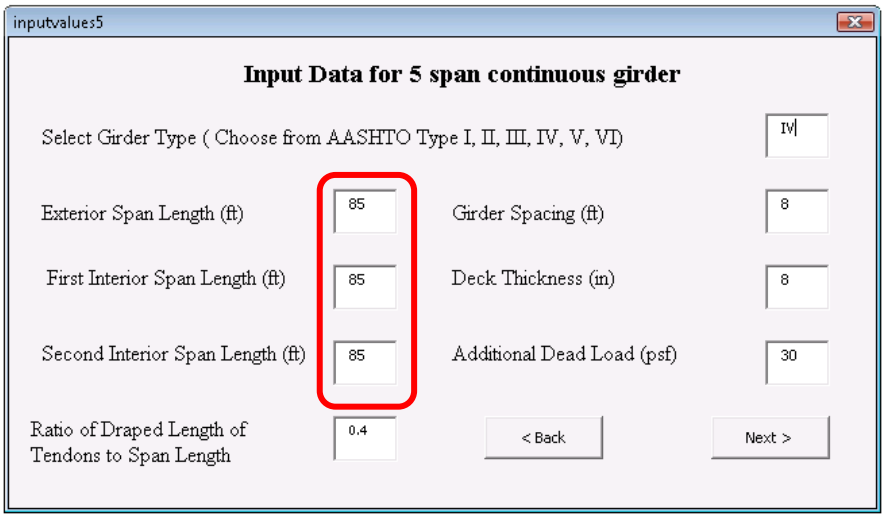

Original `RESTRAINT`

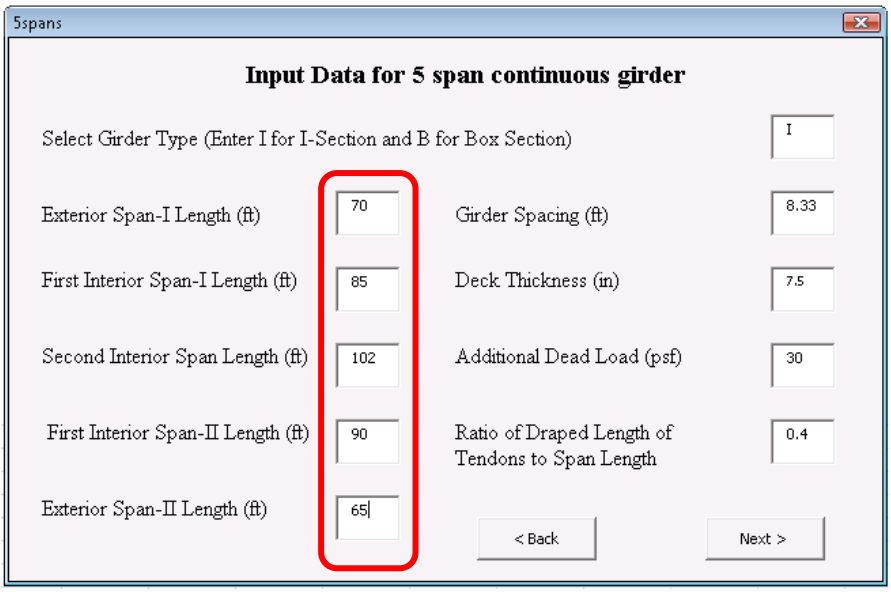

Modified `mRESTRAINT`

Figure 62
Allowing unsymmetric span lengths for bridges with more than two spans

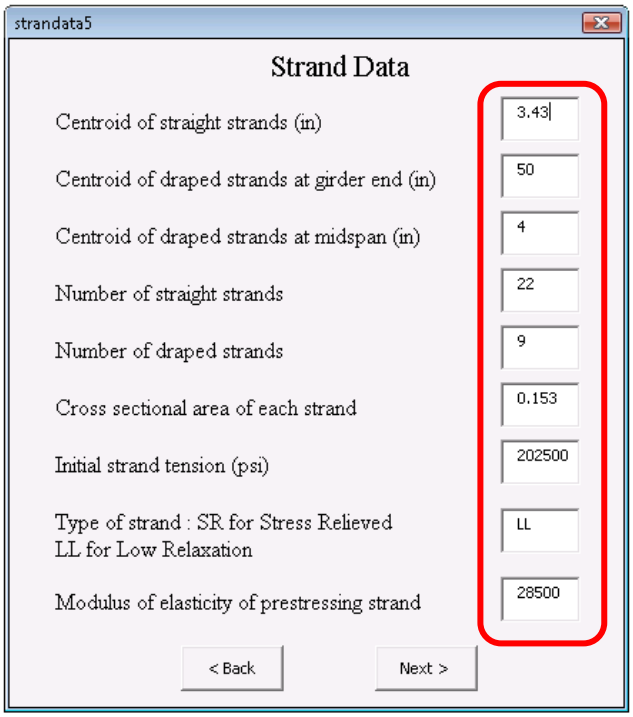

Original `RESTRAINT`

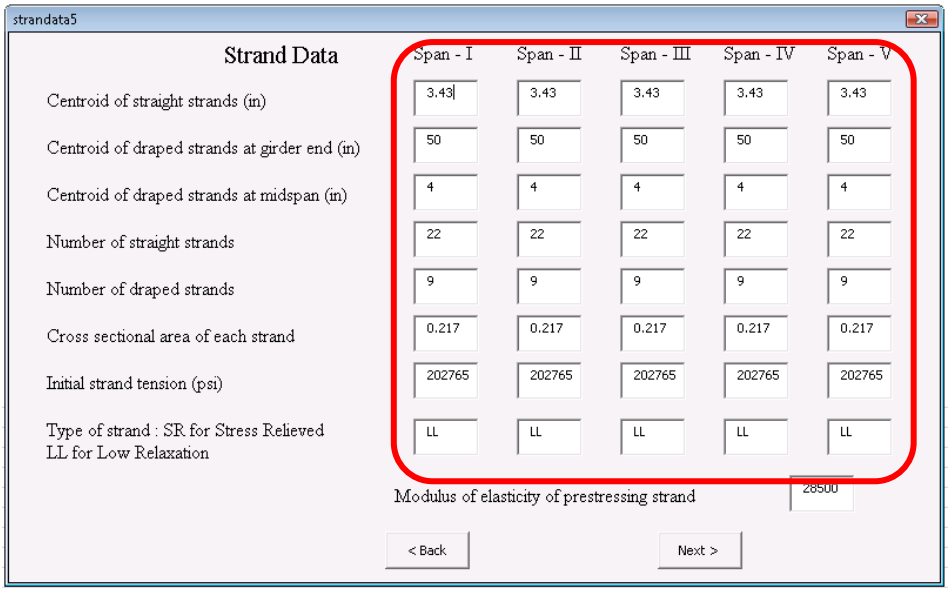

Modified `mRESTRAINT`

Figure 63
Introducing different strand configurations for each span length

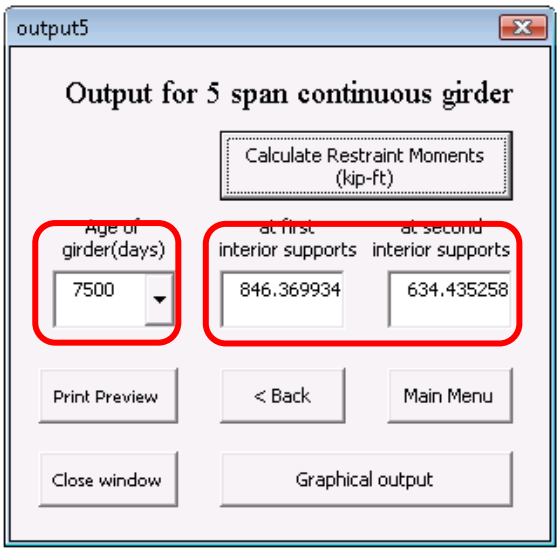

Original `RESTRAINT`

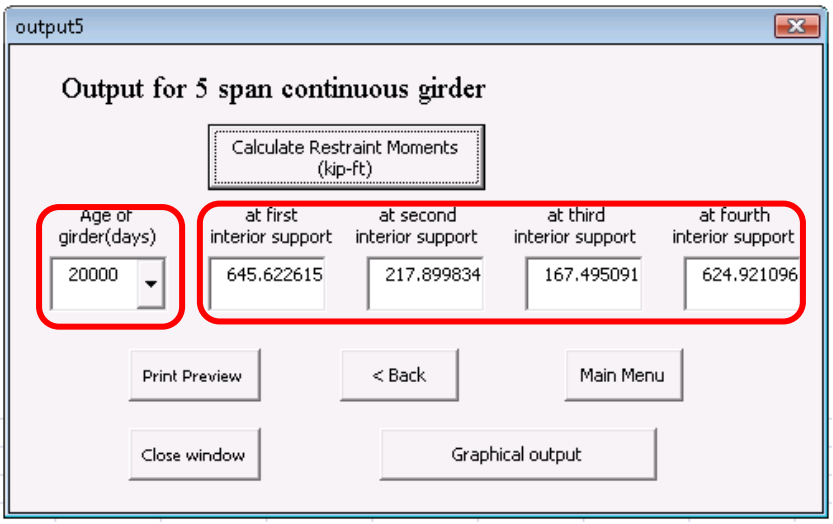

Modified `mRESTRAINT`

Figure 64
Resulting output for a five span bridge which also shows the age extension to 20000 days

APPENDIX C

Recorded Readings from all Sensors

The following plots are a documentation of all sensor readings obtained during the monitoring period of the project June 18, 2008, through December 10, 2010 for 18 embedded sensors that were connected to the casting yard logger and later to the current system datalogger. The plots for the remaining sensors cover the period from January 9, 2009, through December 10, 2010.

Note: Three plots are provided for each sensor. The first is the temperature reading obtained from the vibrating wire gage readings. The second and third are plots of the relative uncorrected and relative temperature corrected sensor readings (e.g., strain, gap, slope).

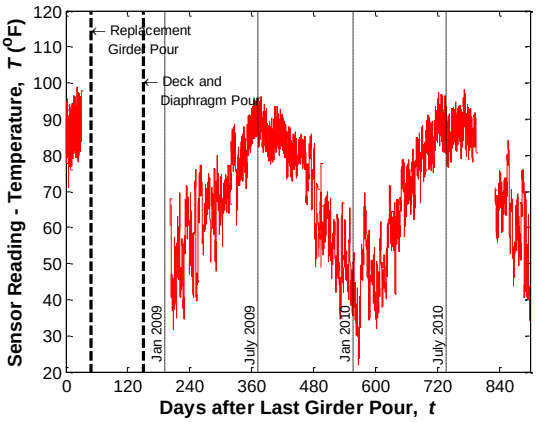

a) Temperature reading of the sensor

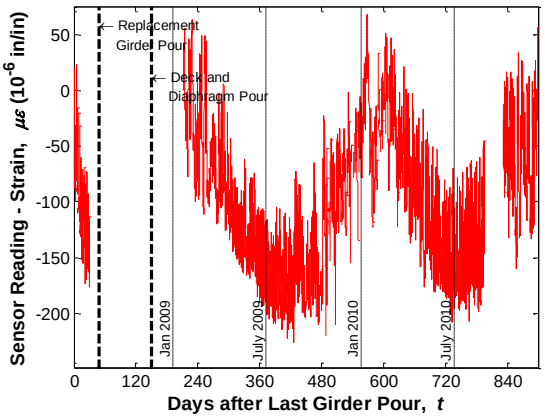

b) Sensor reading without temperature correction

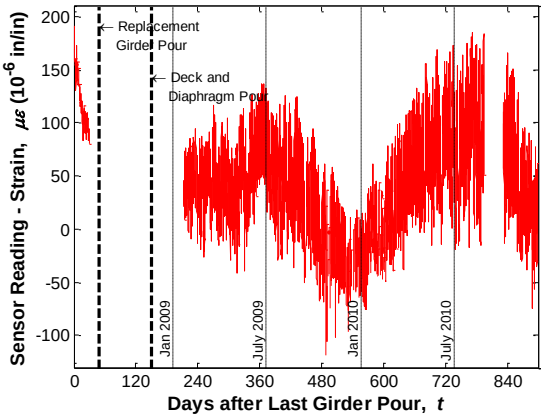

c) Sensor reading after temperature correction

Figure 65
Sensor No. 1, Location G1S24, Support Bottom (ES)

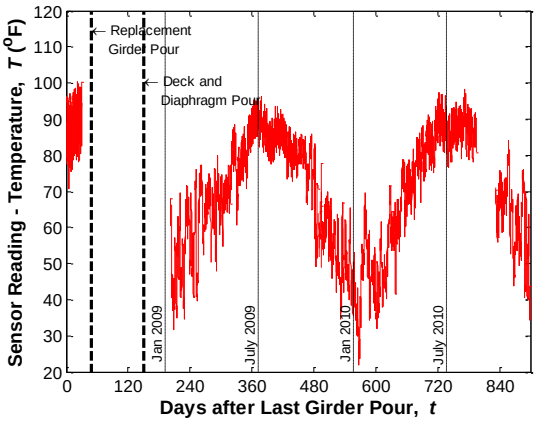

a) Temperature reading of the sensor

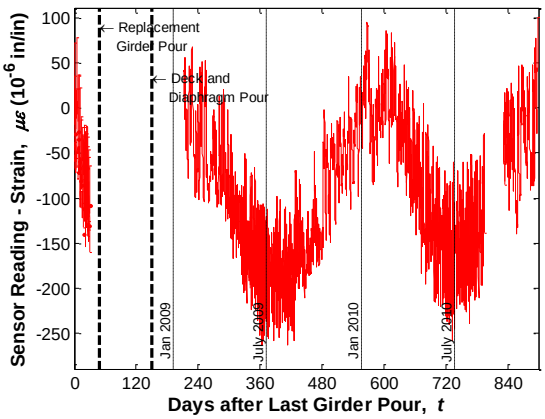

b) Sensor reading without temperature correction

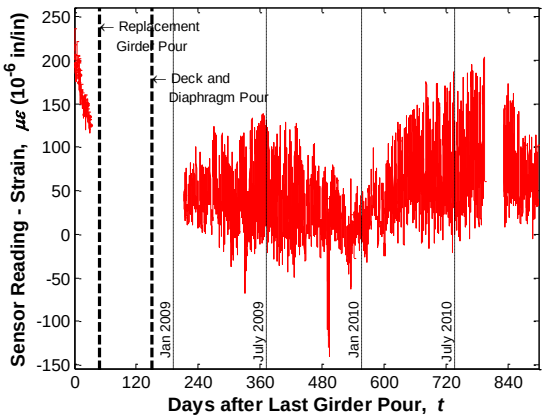

c) Sensor reading after temperature correction

Figure 66
Sensor No. 2, Location G1S24, Support Bottom (ES)

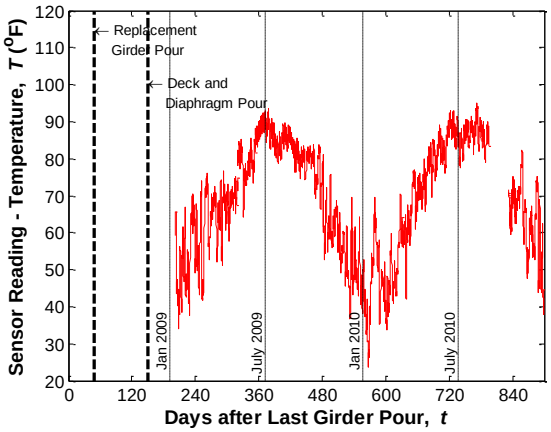

a) Temperature reading of the sensor

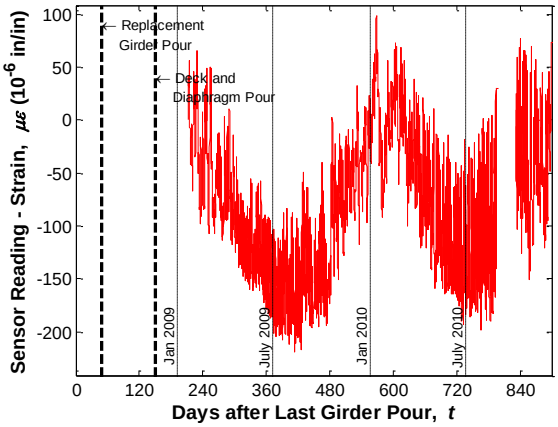

b) Sensor reading without temperature correction

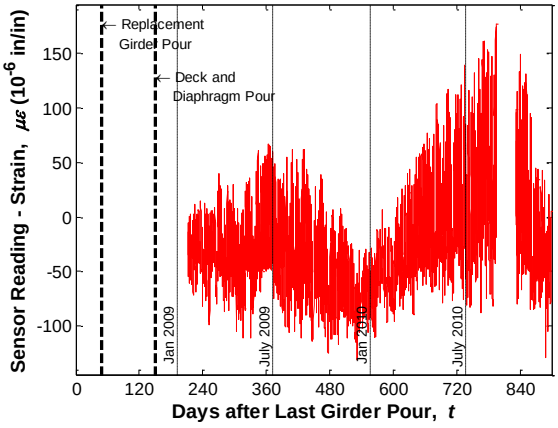

c) Sensor reading after temperature correction

Figure 67
Sensor No. 3, Location G1S23, Support Bottom (ES)

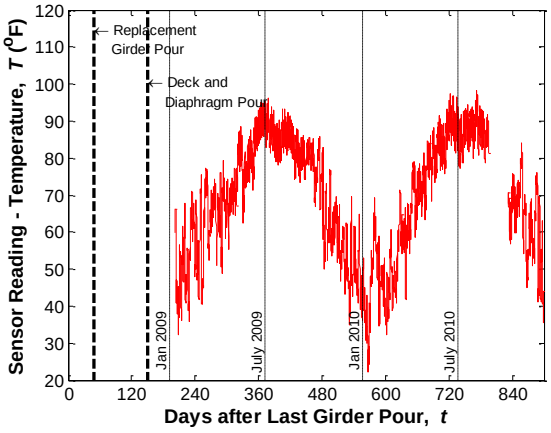

a) Temperature reading of the sensor

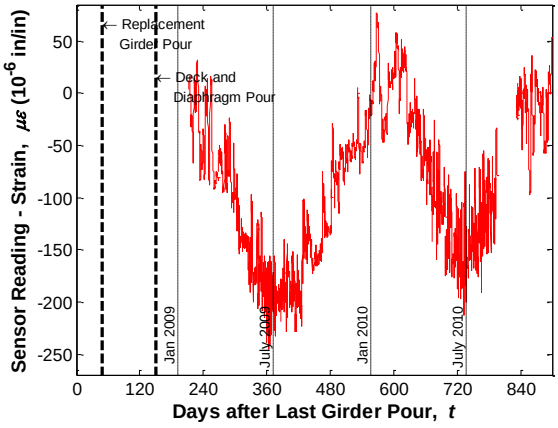

b) Sensor reading without temperature correction

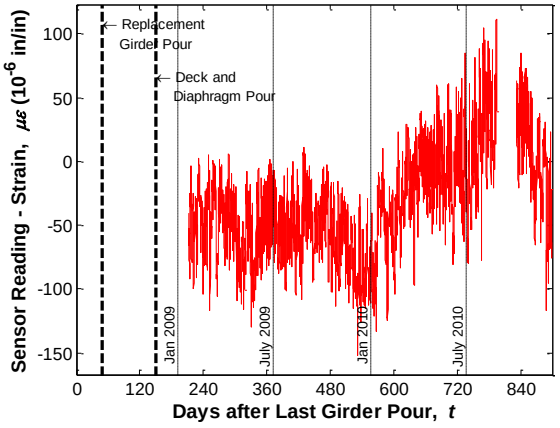

c) Sensor reading after temperature correction

Figure 68
Sensor No. 4, Location G1S23, Support Bottom (ES)

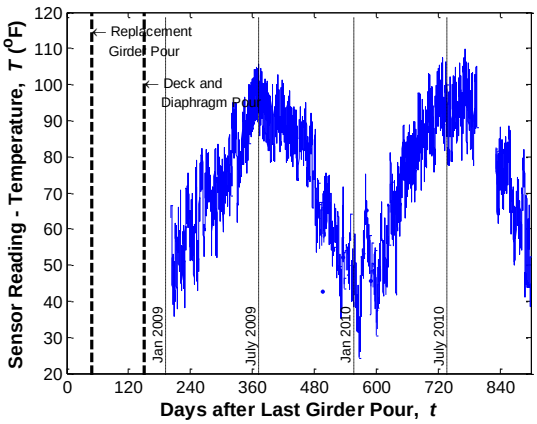

a) Temperature reading of the sensor

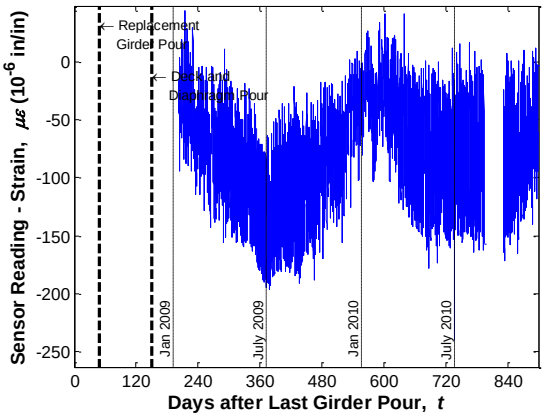

b) Sensor reading without temperature correction

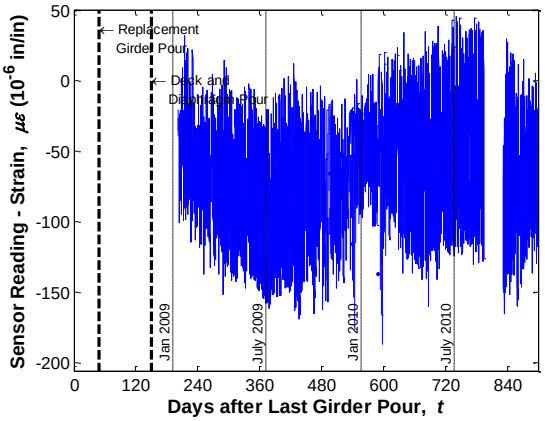

c) Sensor reading after temperature correction

Figure 69
Sensor No. 5, Location G1S24, Support Top (EC)

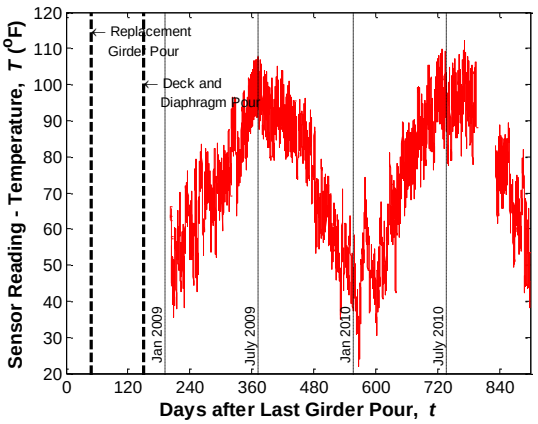

a) Temperature reading of the sensor

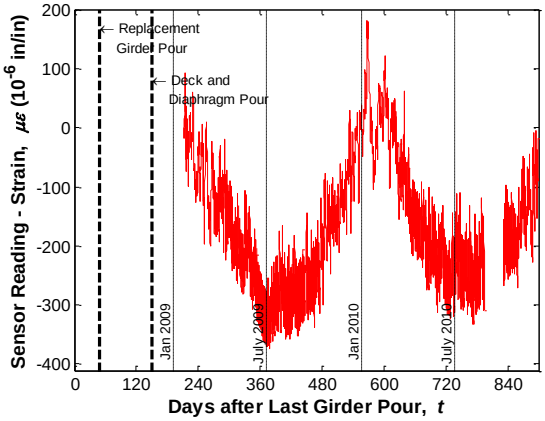

b) Sensor reading without temperature correction

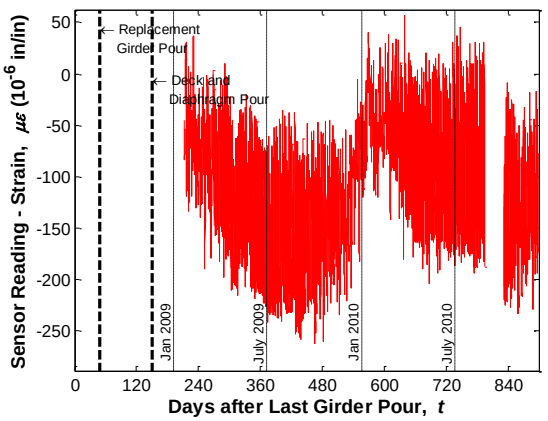

c) Sensor reading after temperature correction

Figure 70
Sensor No. 6, Location G2S24, Support Top (ES)

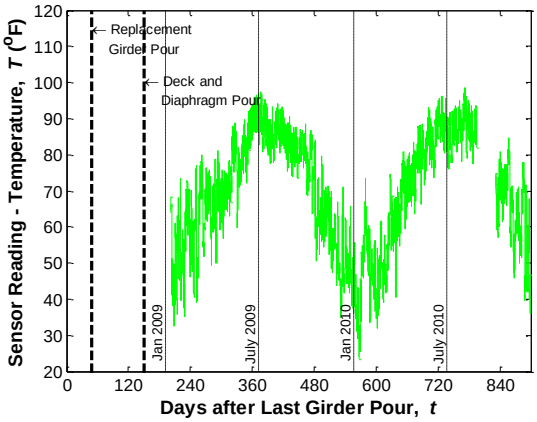

a) Temperature reading of the sensor

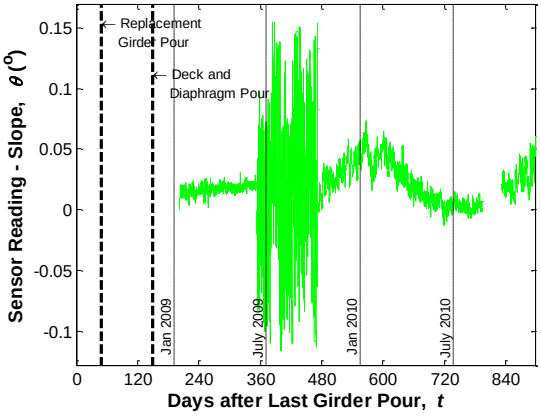

b) Sensor reading without temperature correction

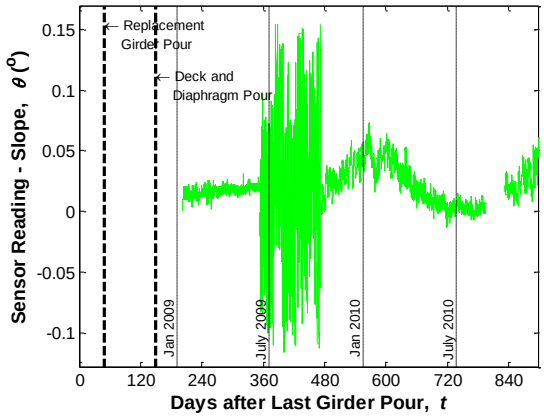

c) Sensor reading after temperature correction

Figure 71
Sensor No. 7, Location G1S24, Support (TM)

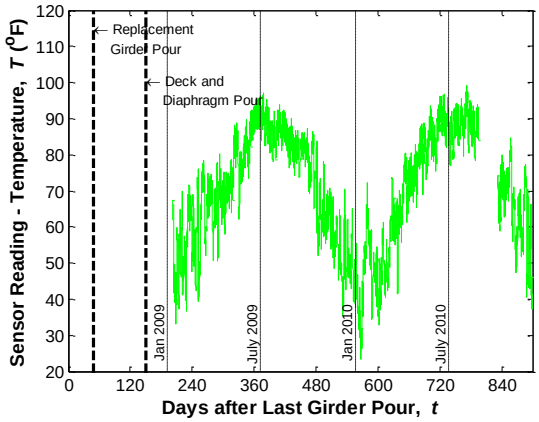

a) Temperature reading of the sensor

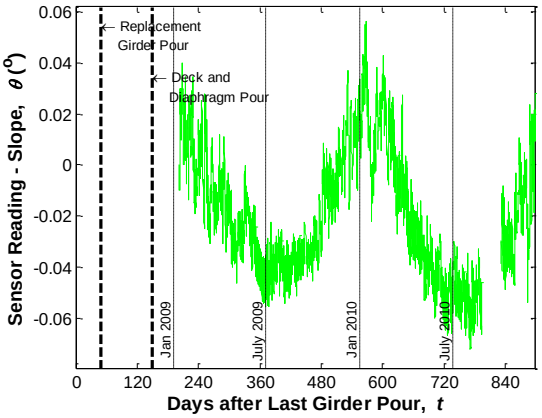

b) Sensor reading without temperature correction

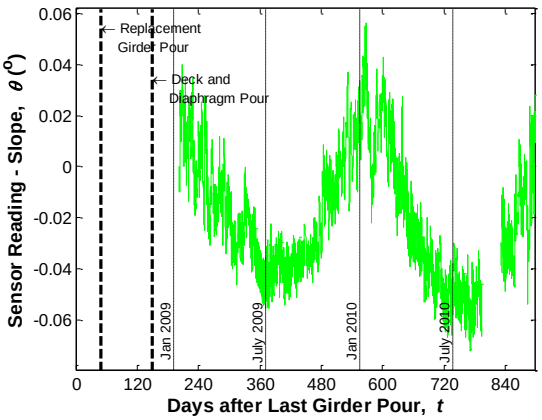

c) Sensor reading after temperature correction

Figure 72
Sensor No. 8, Location G1S23, Support (TM)

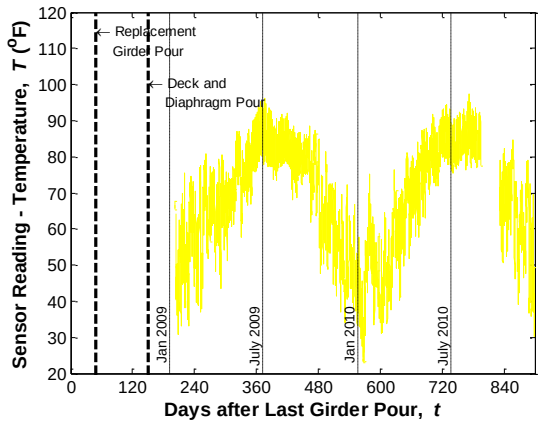

a) Temperature reading of the sensor

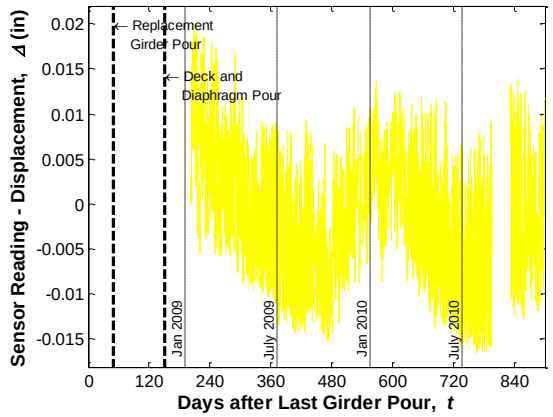

b) Sensor reading without temperature correction

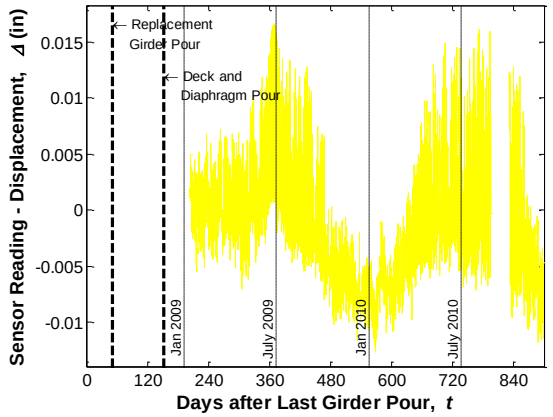

c) Sensor reading after temperature correction

Figure 73
Sensor No. 9, Location G1, End Connection (DM)

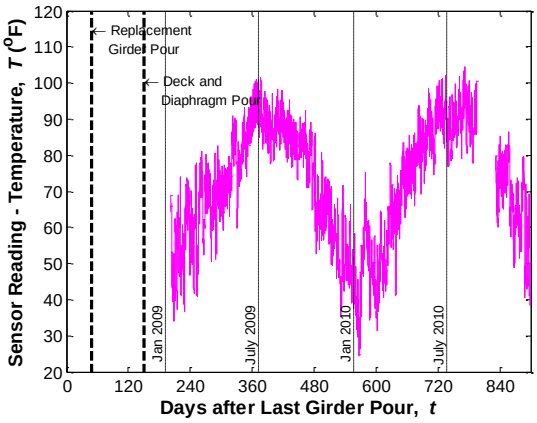

a) Temperature reading of the sensor

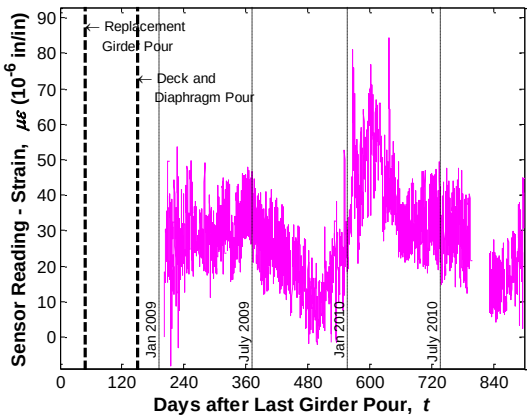

b) Sensor reading without temperature correction

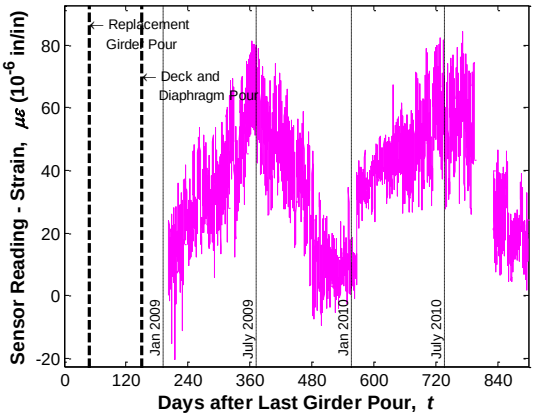

c) Sensor reading after temperature correction

Figure 74
Sensor No. 17, Location G1S24, Support Top (VW)

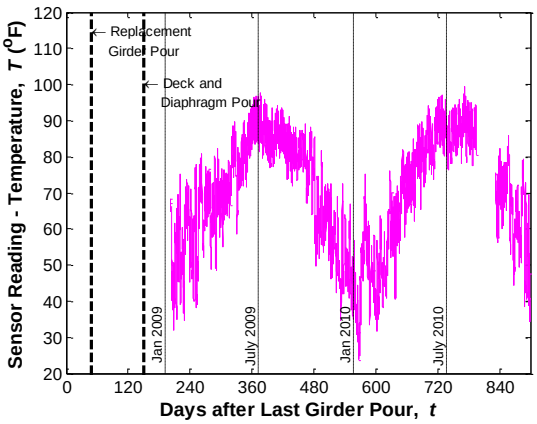

a) Temperature reading of the sensor

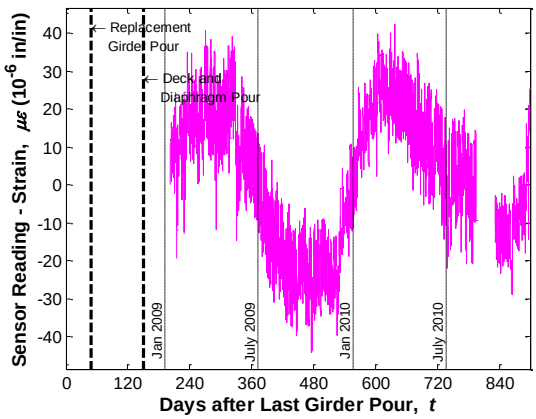

b) Sensor reading without temperature correction

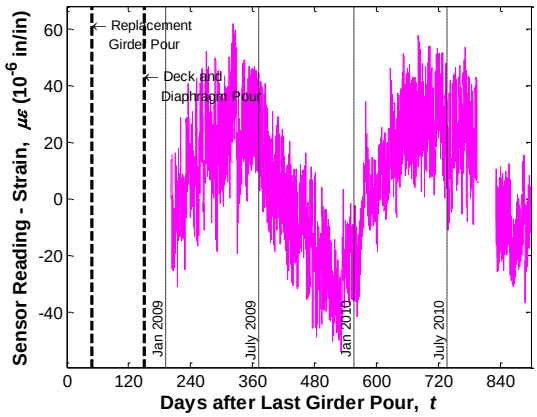

c) Sensor reading after temperature correction

Figure 75
Sensor No. 18, Location G1S24, Support Middle (Vibrating wire gauge)

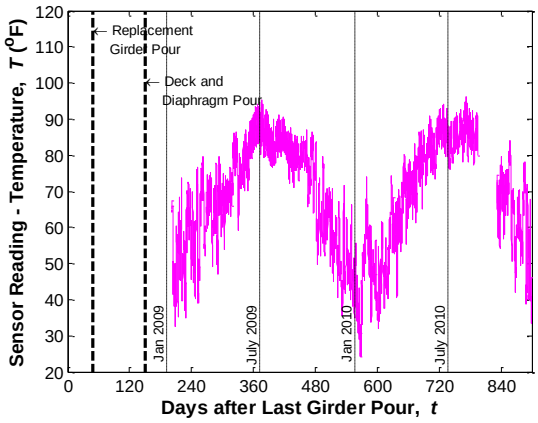

a) Temperature reading of the sensor

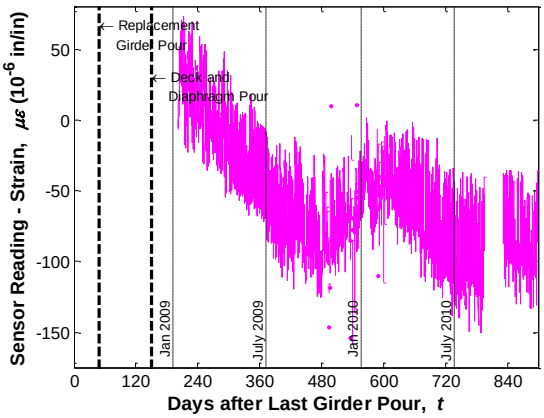

b) Sensor reading without temperature correction

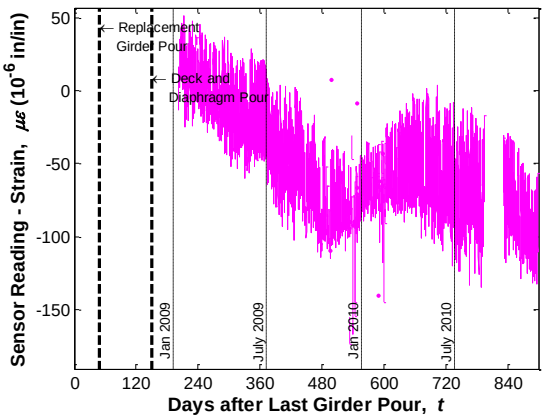

c) Sensor reading after temperature correction

Figure 76
Sensor No. 19, Location G1S24, Support Bottom (Vibrating wire gauge)

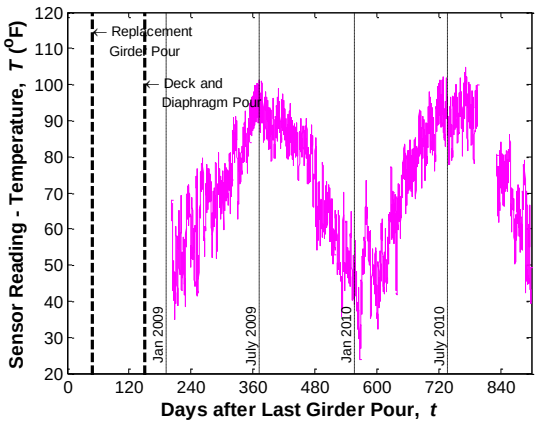

a) Temperature reading of the sensor

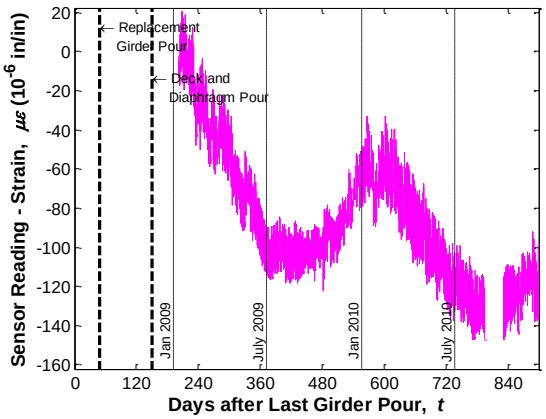

b) Sensor reading without temperature correction

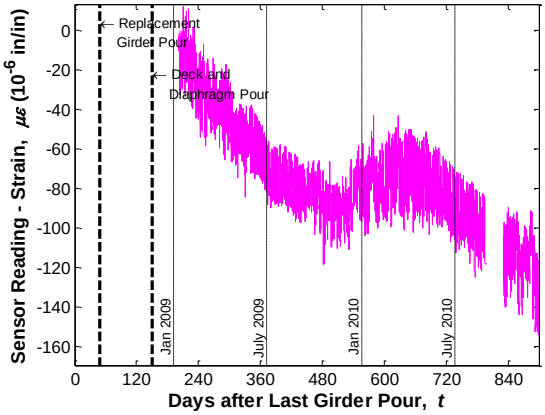

c) Sensor reading after temperature correction

Figure 77
Sensor No. 20, Location G1S23, Support Top (VW)

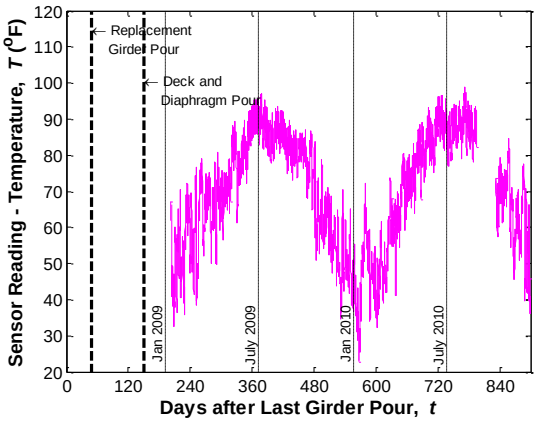

a) Temperature reading of the sensor

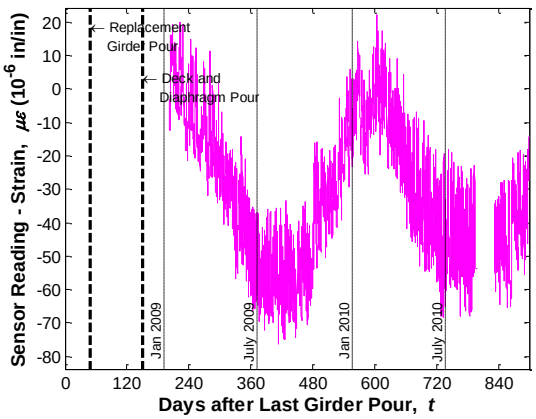

b) Sensor reading without temperature correction

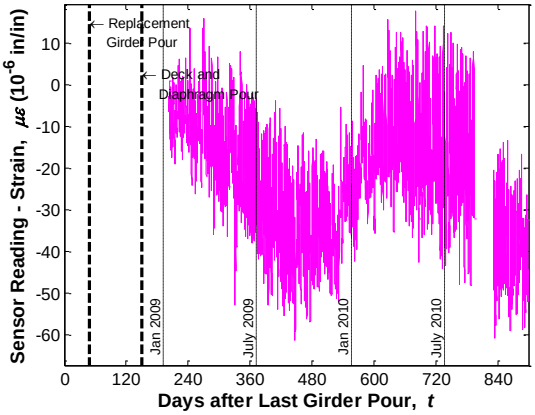

c) Sensor reading after temperature correction

Figure 78
Sensor No. 21, Location G1S23, Support Middle (VW)

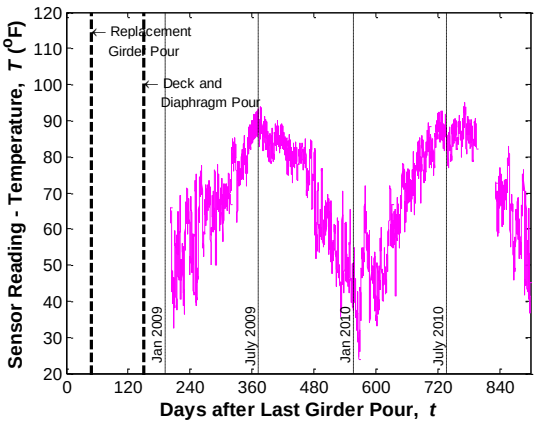

a) Temperature reading of the sensor

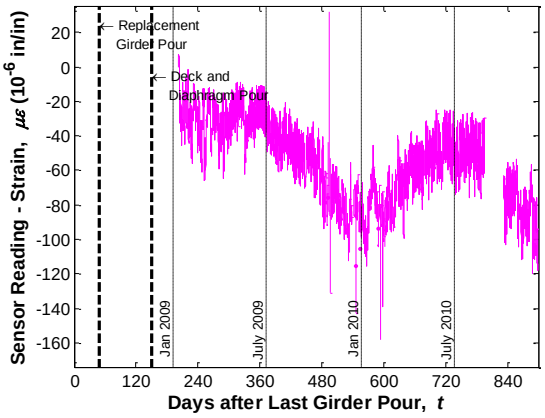

b) Sensor reading without temperature correction

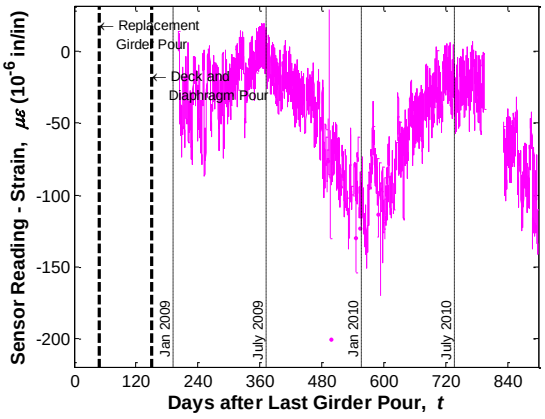

c) Sensor reading after temperature correction

Figure 79
Sensor No. 22, Location G1S23, Support Bottom (VW)

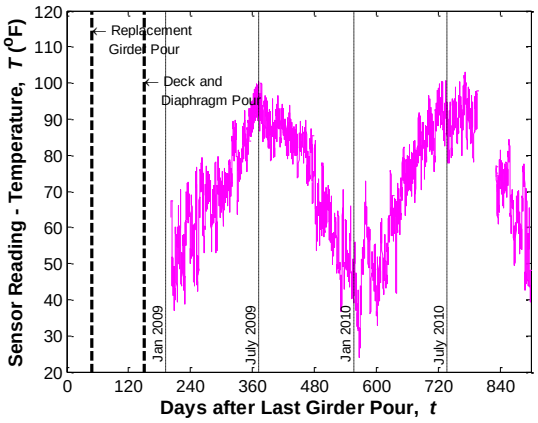

a) Temperature reading of the sensor

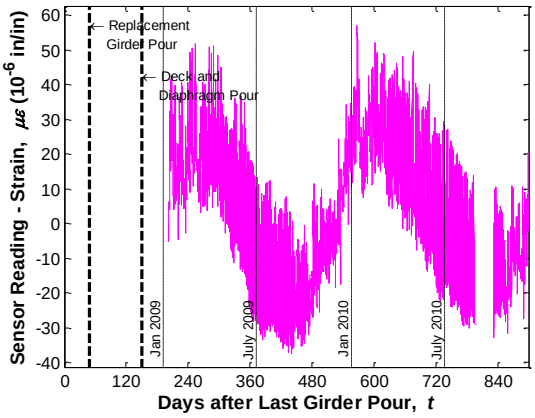

b) Sensor reading without temperature correction

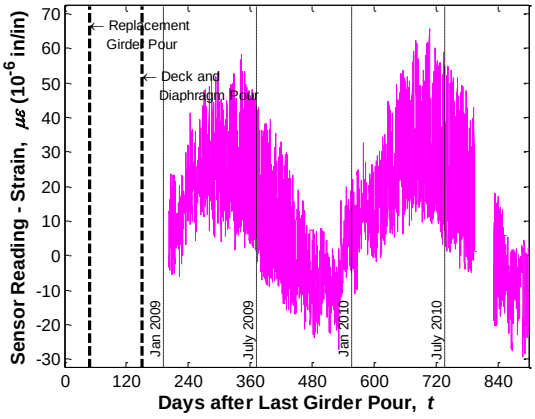

c) Sensor reading after temperature correction

Figure 80
Sensor No. 33, Location G5S24, Support Top

(VW)

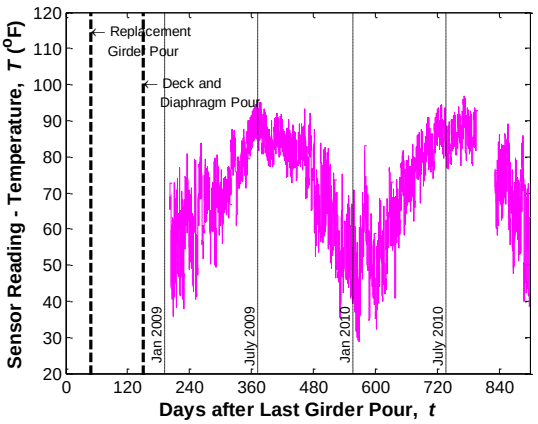

a) Temperature reading of the sensor

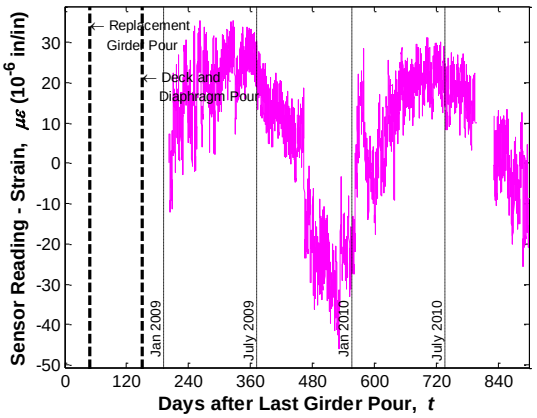

b) Sensor reading without temperature correction

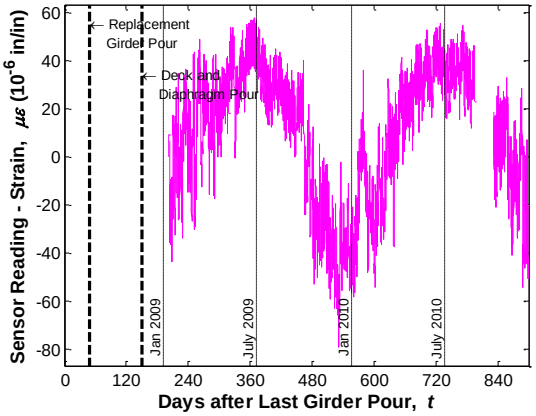

c) Sensor reading after temperature correction

Figure 81
Sensor No. 34, Location G5S24, Support Middle (VW)

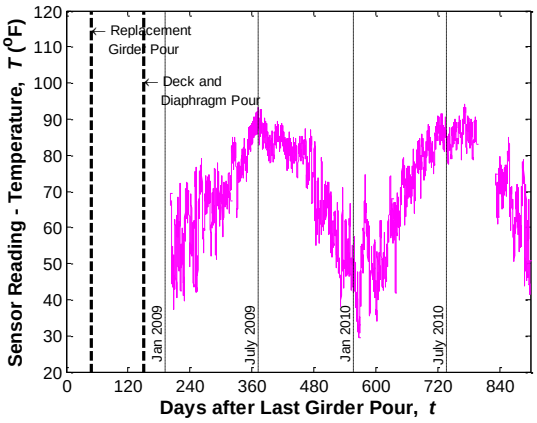

a) Temperature reading of the sensor

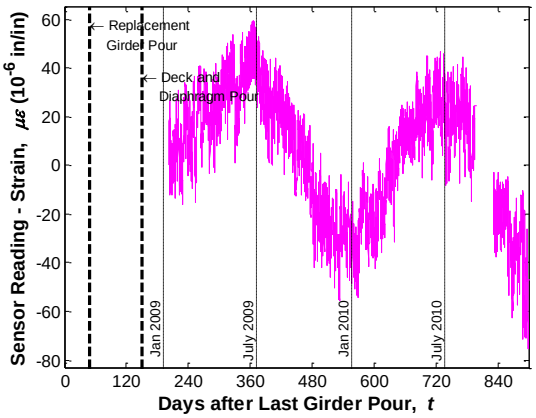

b) Sensor reading without temperature correction

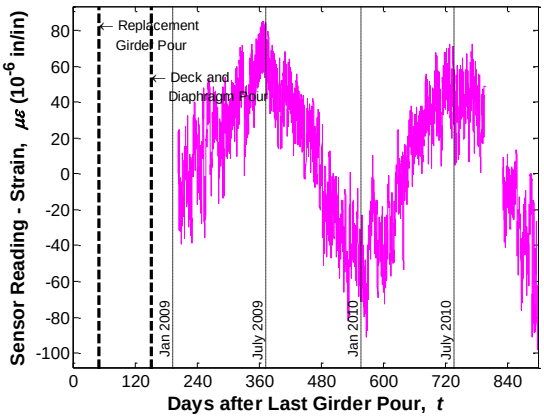

c) Sensor reading after temperature correction

Figure 82
Sensor No. 35, Location G5S24, Support Bottom (VW)

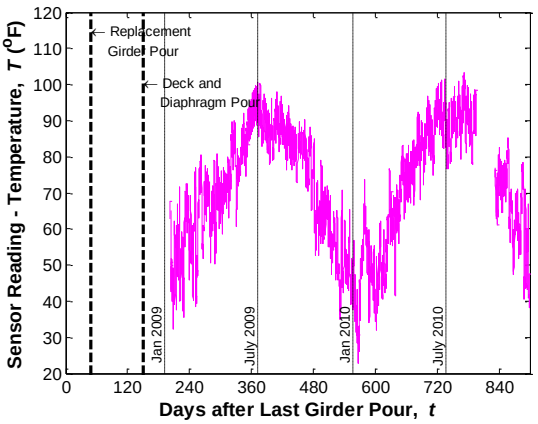

a) Temperature reading of the sensor

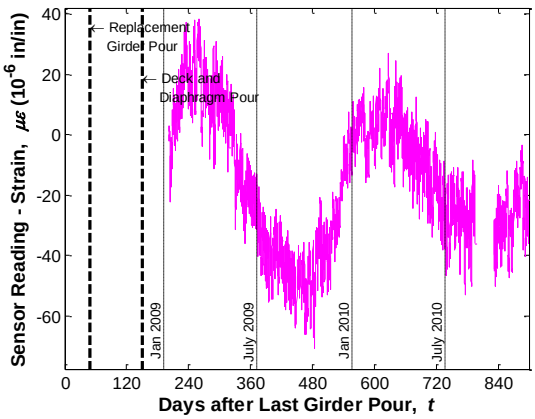

b) Sensor reading without temperature correction

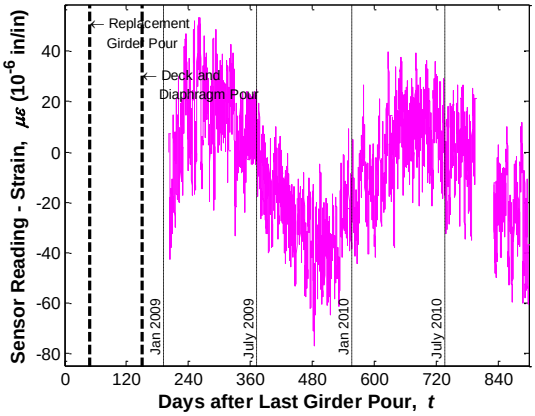

c) Sensor reading after temperature correction

Figure 83
Sensor No. 36, Location G5S23, Support Top (VW)

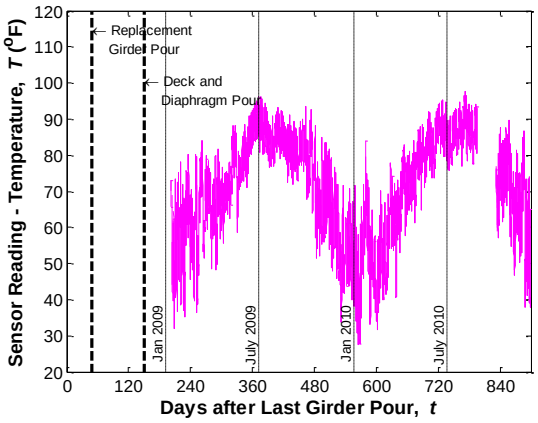

a) Temperature reading of the sensor

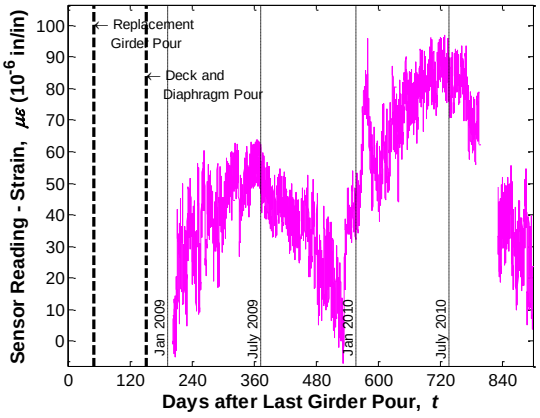

b) Sensor reading without temperature correction

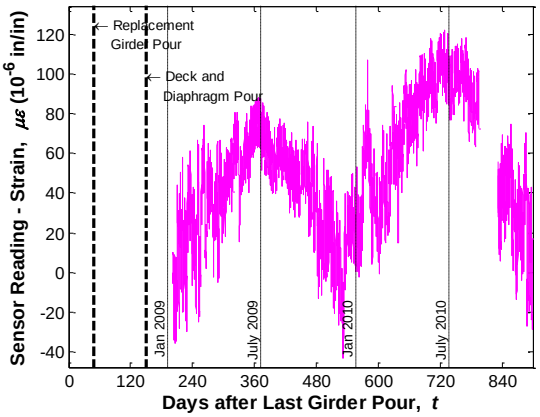

c) Sensor reading after temperature correction

Figure 84
Sensor No. 37, Location G5S23, Support Middle (VW)

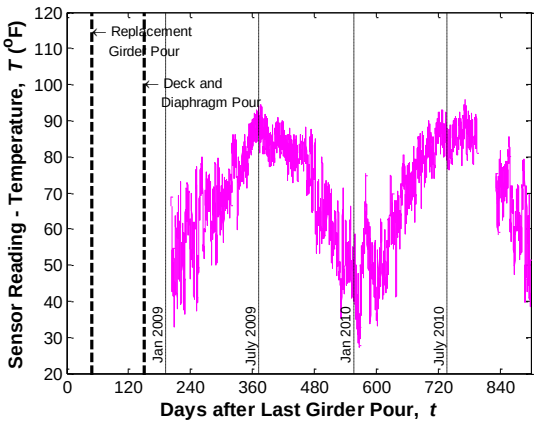

a) Temperature reading of the sensor

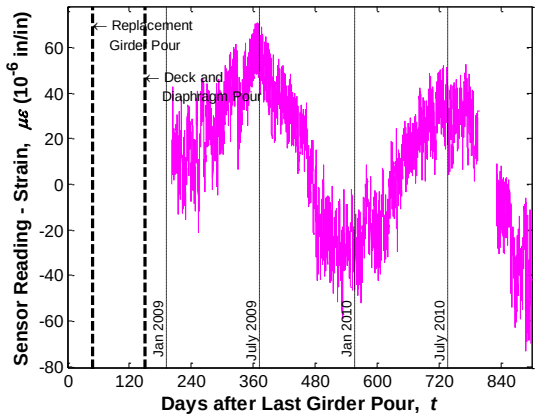

b) Sensor reading without temperature correction

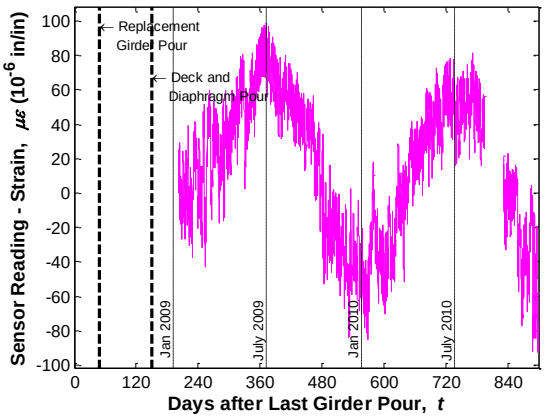

c) Sensor reading after temperature correction

Figure 85
Sensor No. 38, Location G5S23, Support Bottom (VW)

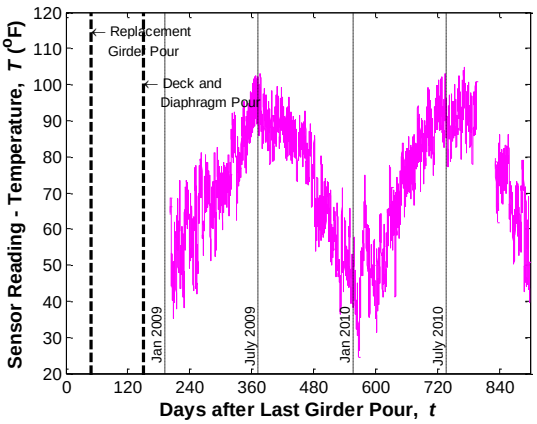

a) Temperature reading of the sensor

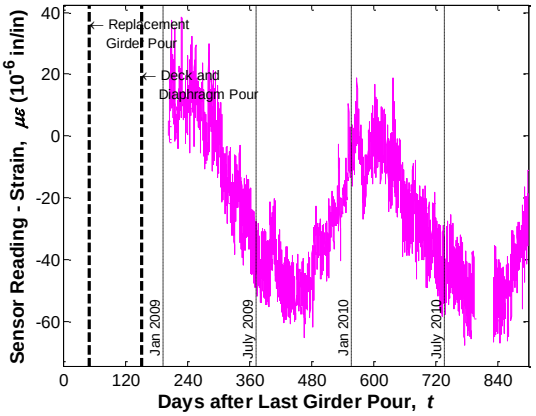

b) Sensor reading without temperature correction

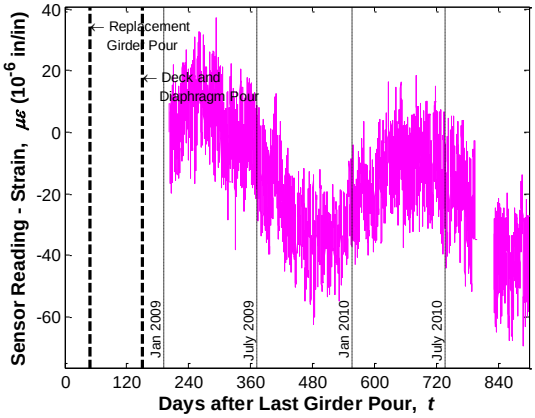

c) Sensor reading after temperature correction

Figure 86
Sensor No. 39, Location G3S24, Support Top (VW)

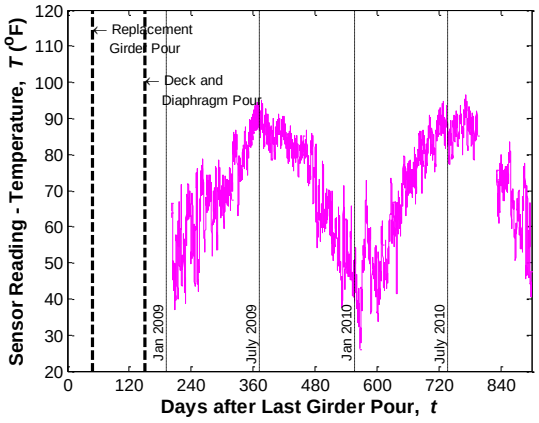

a) Temperature reading of the sensor

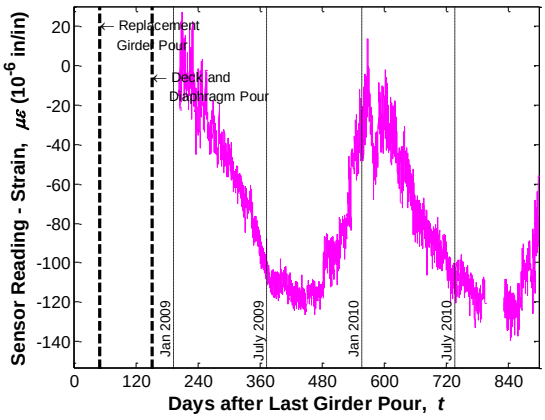

b) Sensor reading without temperature correction

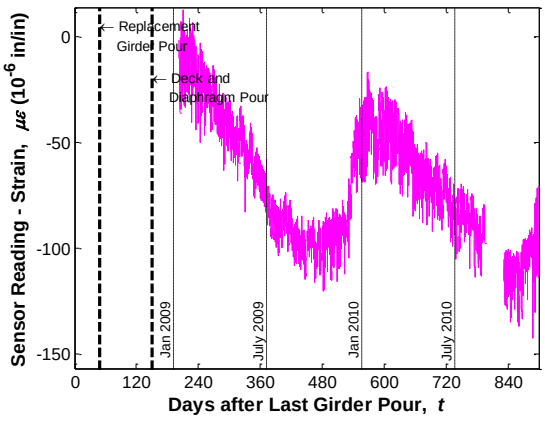

c) Sensor reading after temperature correction

Figure 87
Sensor No. 40, Location G3S24, Support Middle (VW)

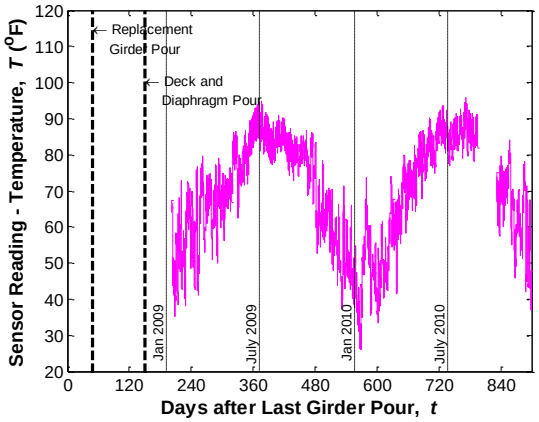

a) Temperature reading of the sensor

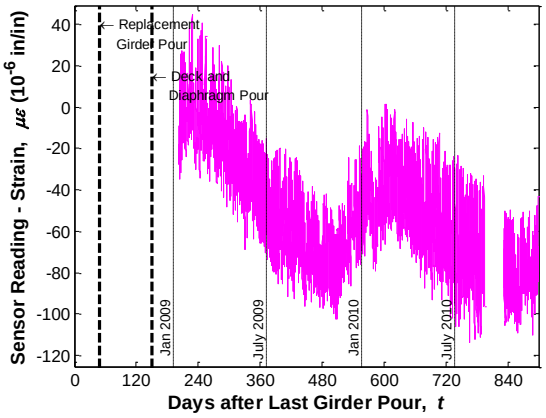

b) Sensor reading without temperature correction

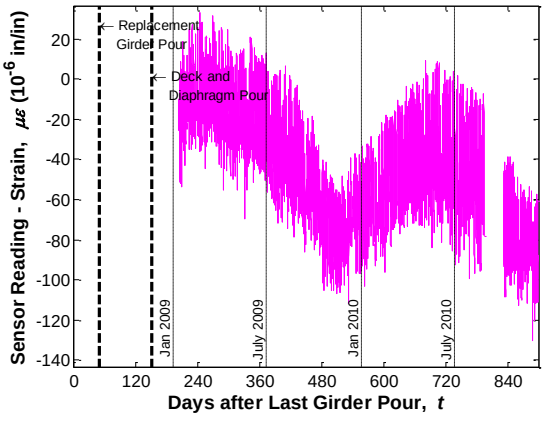

c) Sensor reading after temperature correction

Figure 88
Sensor No. 41, Location G3S24, Support Bottom (VW)

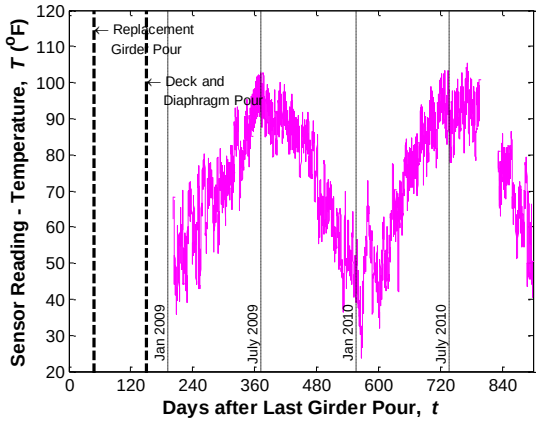

a) Temperature reading of the sensor

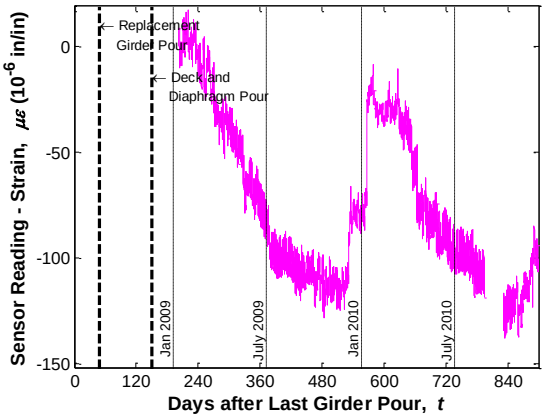

b) Sensor reading without temperature correction

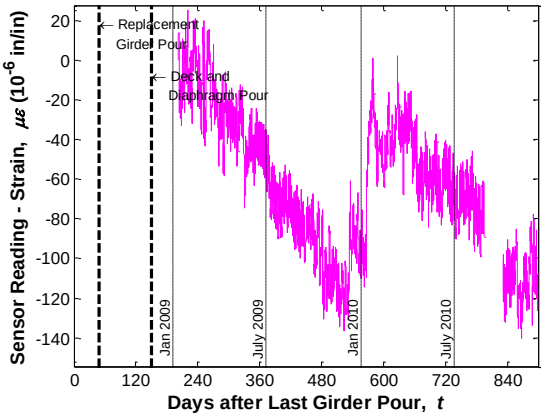

c) Sensor reading after temperature correction

Figure 89
Sensor No. 42, Location G3S23, Support Top (VW)

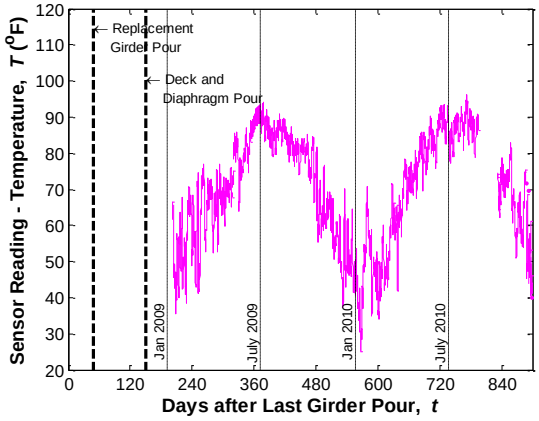

a) Temperature reading of the sensor

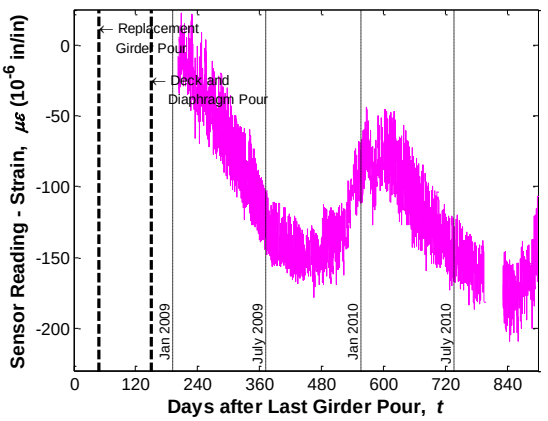

b) Sensor reading without temperature correction

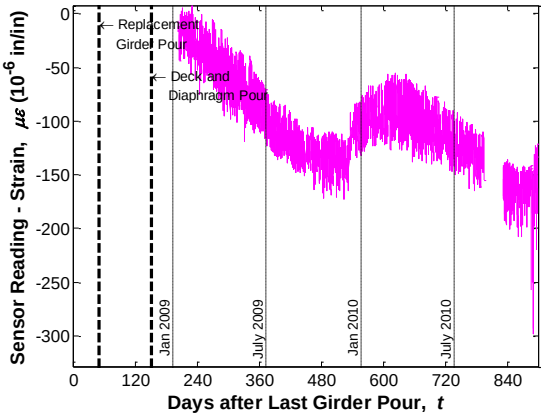

c) Sensor reading after temperature correction

Figure 90
Sensor No. 43, Location G3S23, Support Middle (VW)

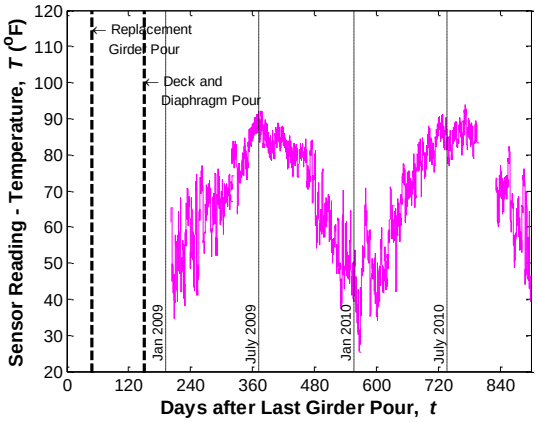

a) Temperature reading of the sensor

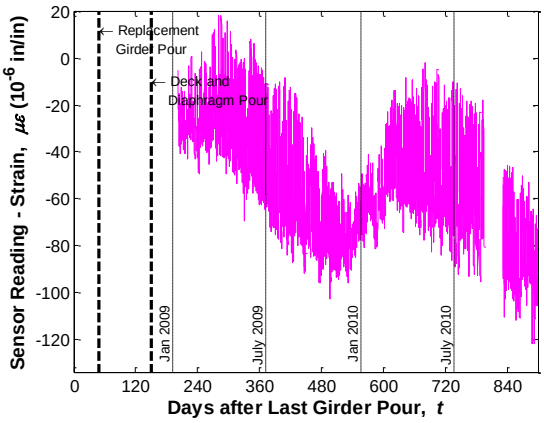

b) Sensor reading without temperature correction

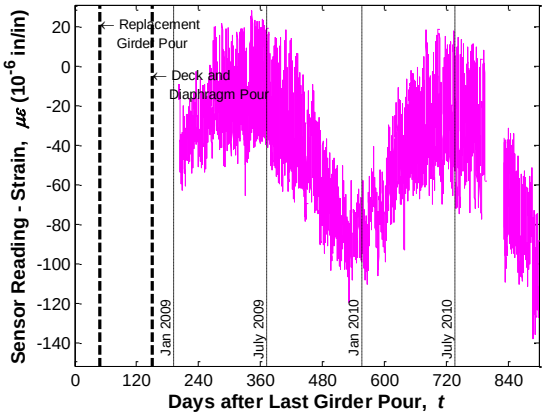

c) Sensor reading after temperature correction

Figure 91
Sensor No. 44, Location G3S23, Support Bottom (VW)

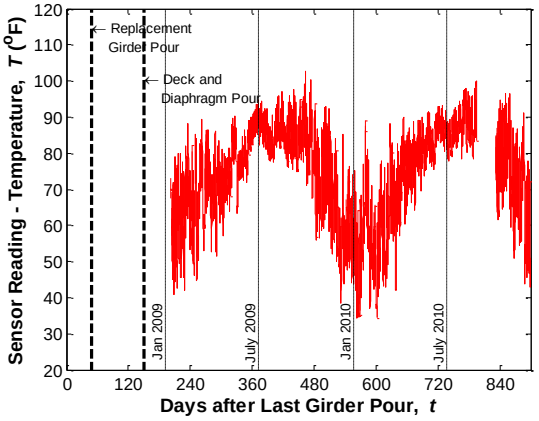

a) Temperature reading of the sensor

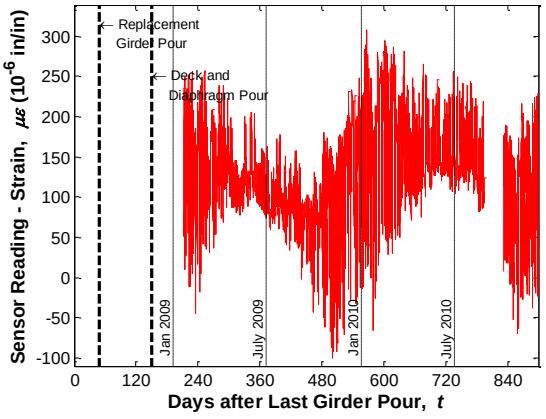

b) Sensor reading without temperature correction

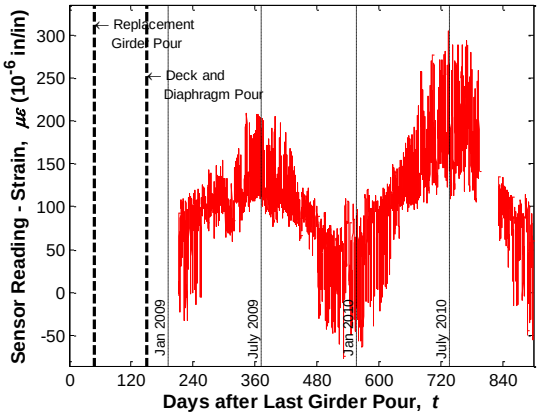

c) Sensor reading after temperature correction

Figure 92
Sensor No. 45, Location G5S23, Support Bottom (ES)

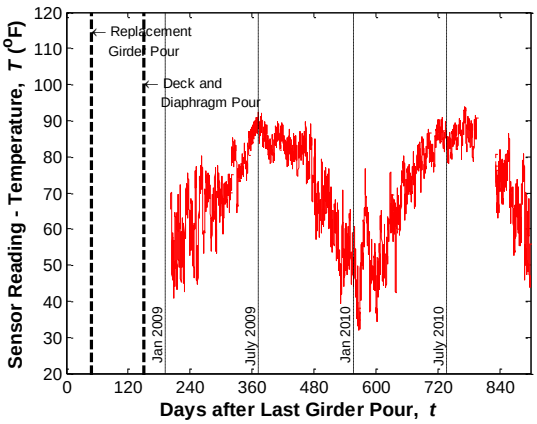

a) Temperature reading of the sensor

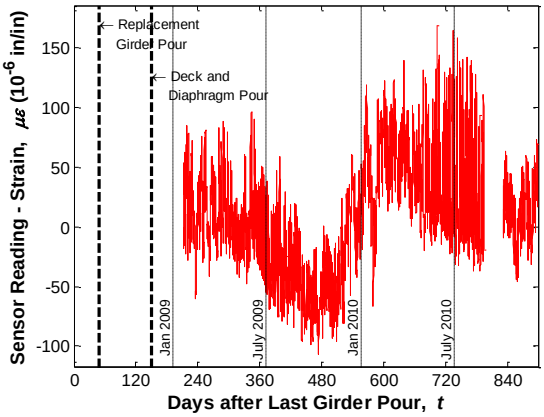

b) Sensor reading without temperature correction

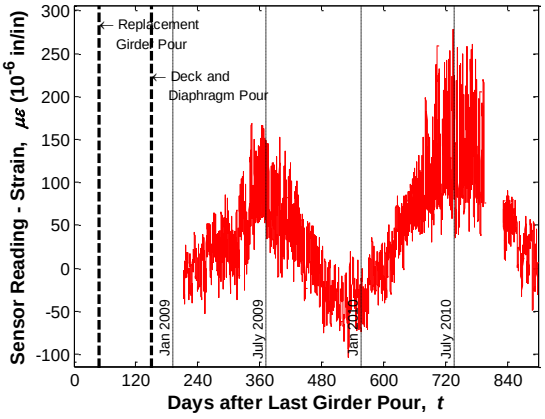

c) Sensor reading after temperature correction

Figure 93
Sensor No. 46, Location G5S23, Support Bottom (ES)

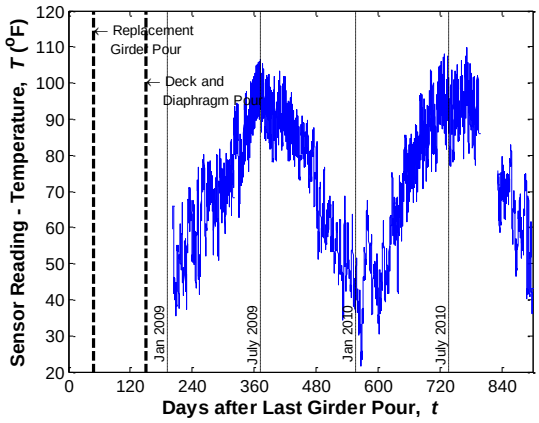

a) Temperature reading of the sensor

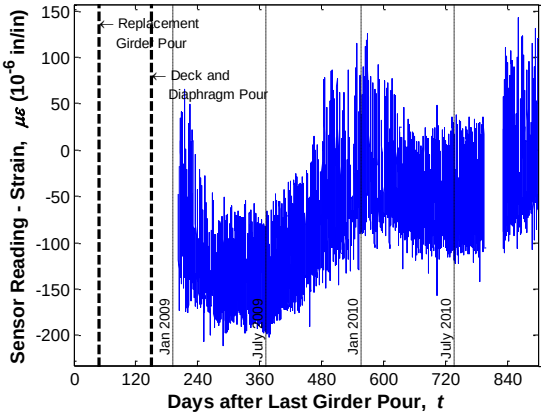

b) Sensor reading without temperature correction

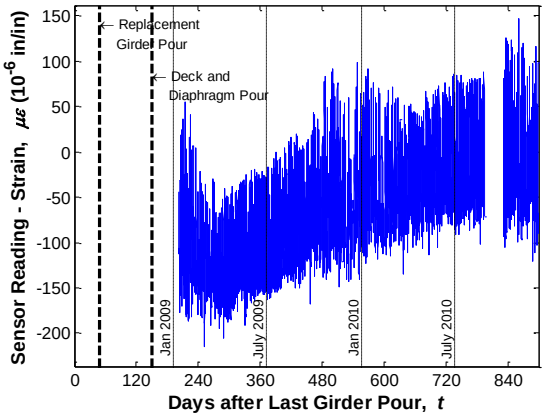

c) Sensor reading after temperature correction

Figure 94
Sensor No. 47, Location G5S24, Support Top (EC)

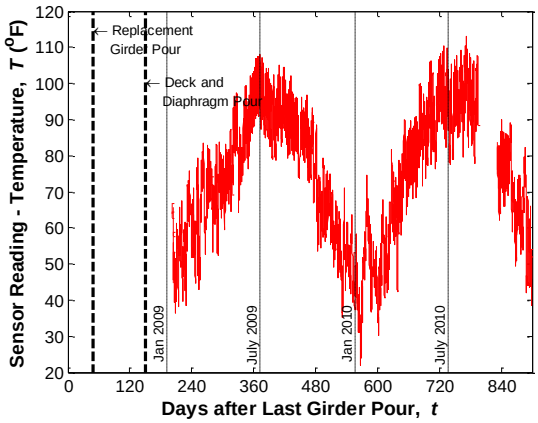

a) Temperature reading of the sensor

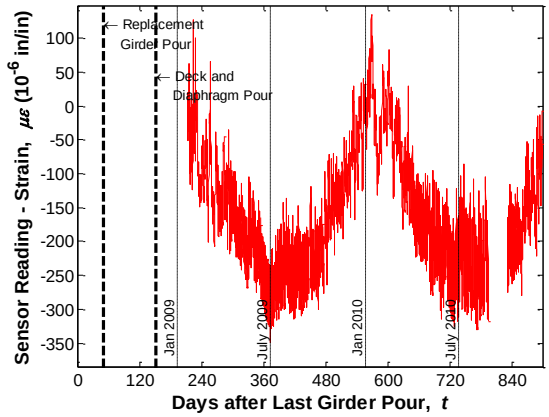

b) Sensor reading without temperature correction

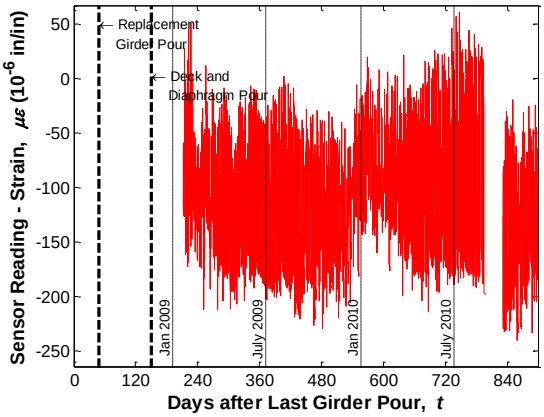

c) Sensor reading after temperature correction

Figure 95
Sensor No. 48, Location G4S24, Support Top (ES)

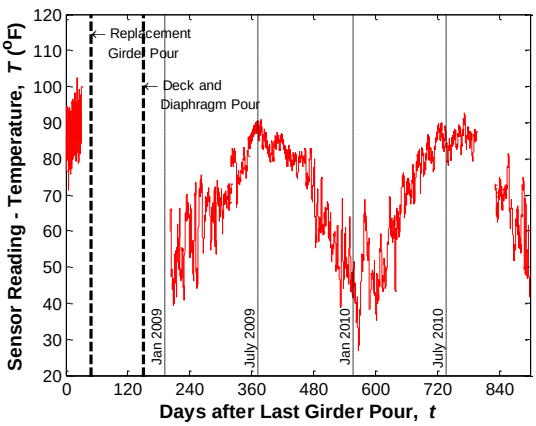

a) Temperature reading of the sensor

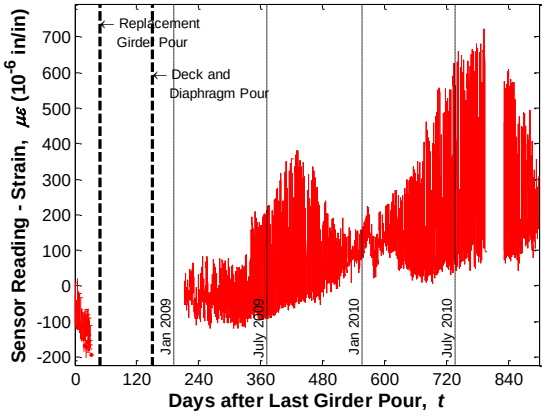

b) Sensor reading without temperature correction

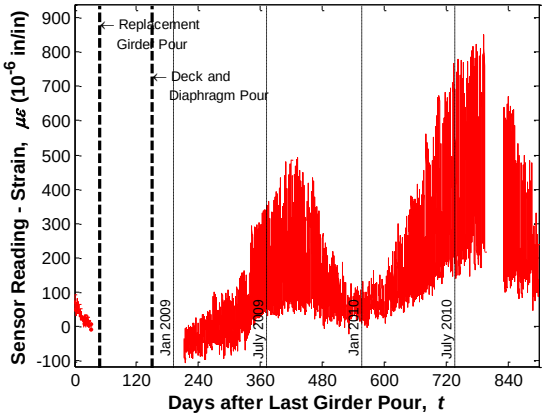

c) Sensor reading after temperature correction

Figure 96
Sensor No. 49, Location G3S24, Support Bottom (ES)

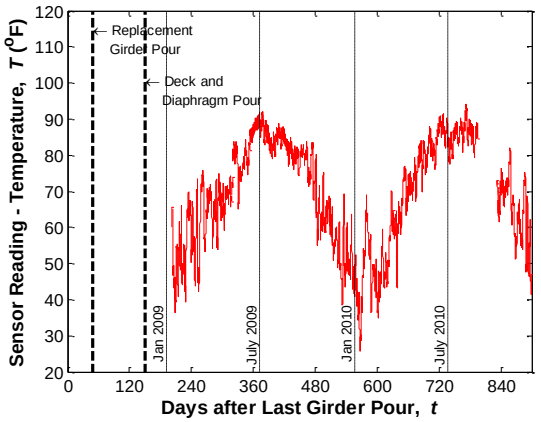

a) Temperature reading of the sensor

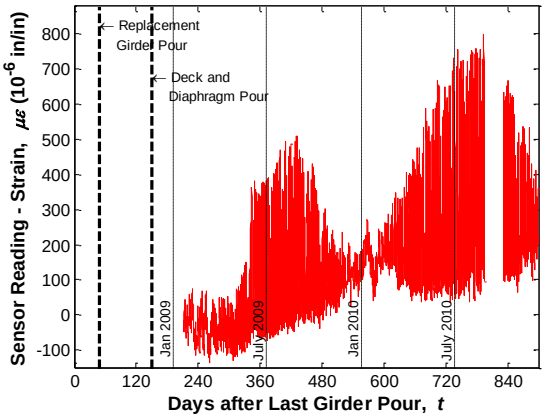

b) Sensor reading without temperature correction

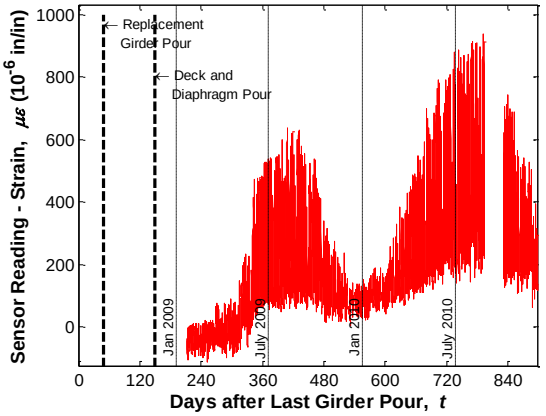

c) Sensor reading after temperature correction

Figure 97
Sensor No. 50, Location G3S23, Support Bottom (ES)

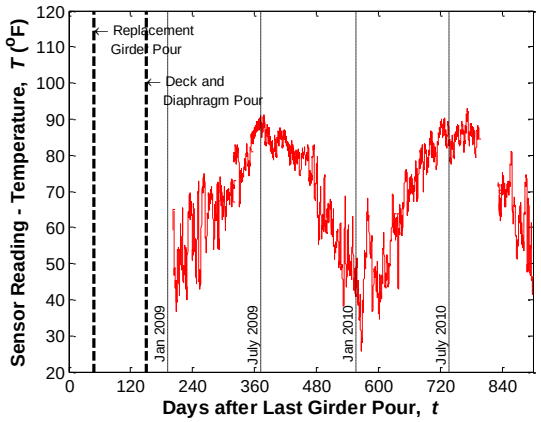

a) Temperature reading of the sensor

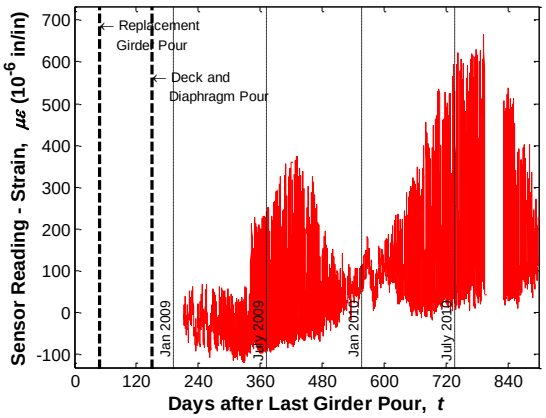

b) Sensor reading without temperature correction

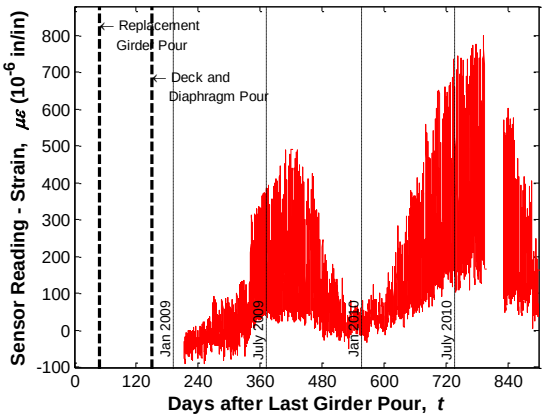

c) Sensor reading after temperature correction

Figure 98
Sensor No. 51, Location G3S23, Support Bottom (ES)

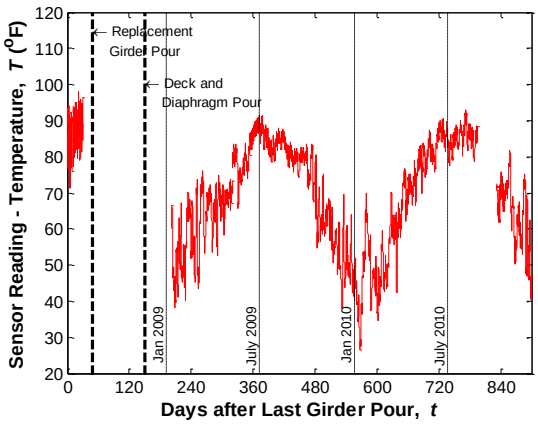

a) Temperature reading of the sensor

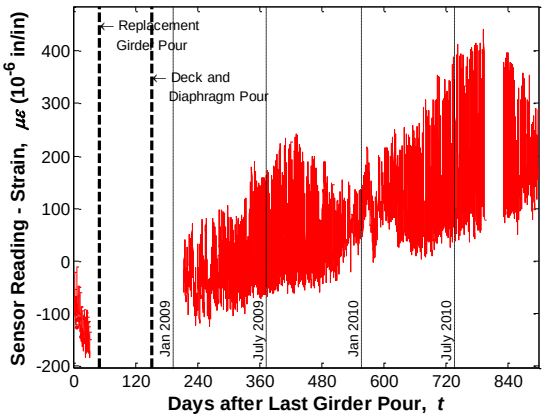

b) Sensor reading without temperature correction

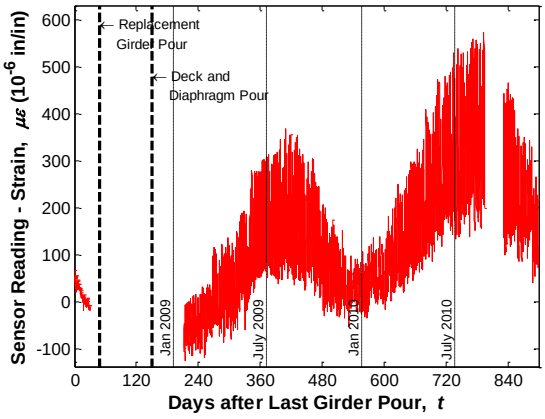

c) Sensor reading after temperature correction

Figure 99
Sensor No. 52, Location G3S24, Support Bottom (ES)

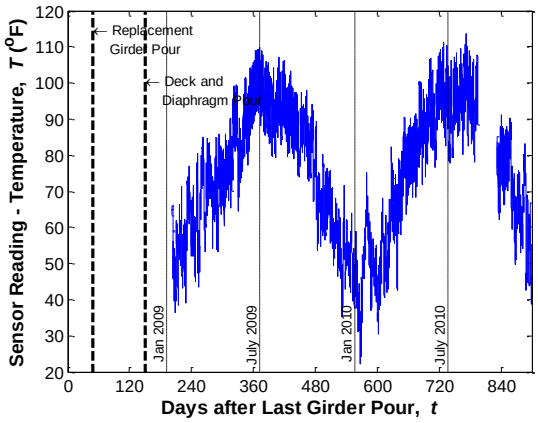

a) Temperature reading of the sensor

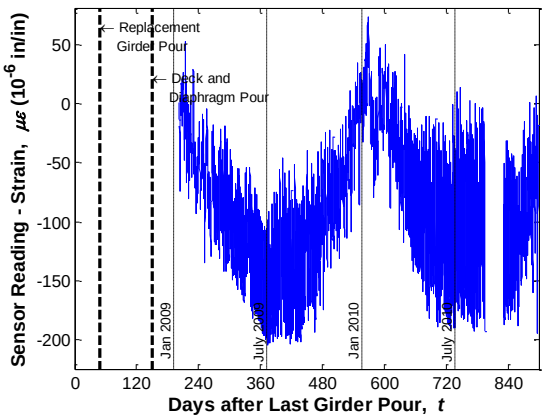

b) Sensor reading without temperature correction

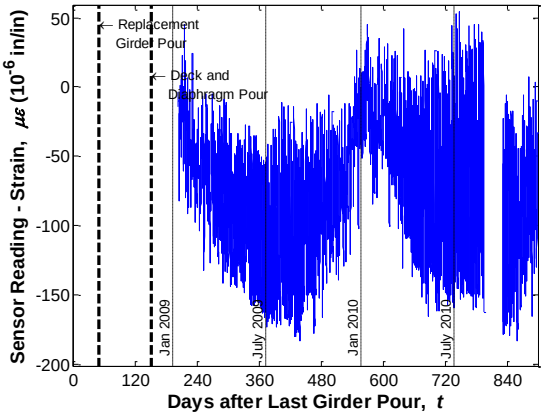

c) Sensor reading after temperature correction

Figure 100
Sensor No. 53, Location G3S24, Support Top (EC)

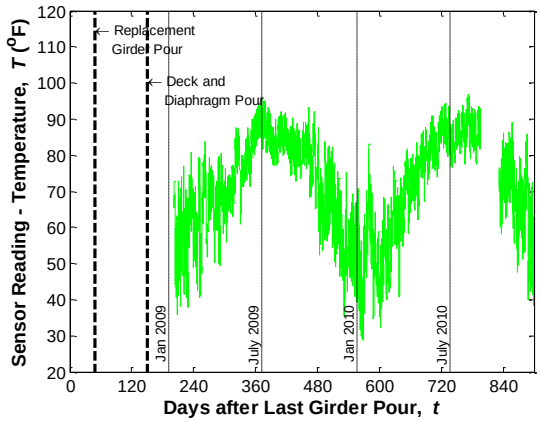

a) Temperature reading of the sensor

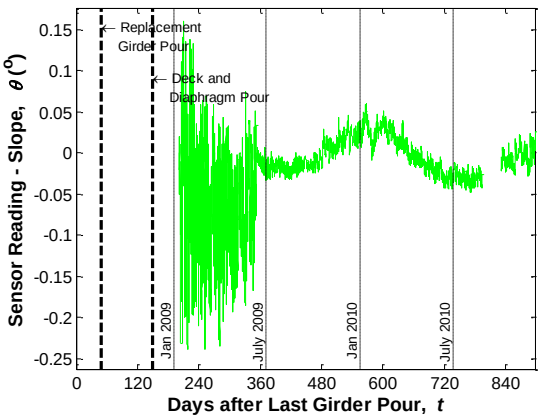

b) Sensor reading without temperature correction

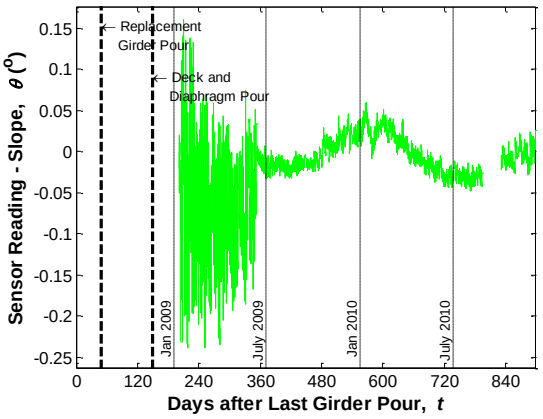

c) Sensor reading after temperature correction

Figure 101
Sensor No. 54, Location G5S24, Support (TM)

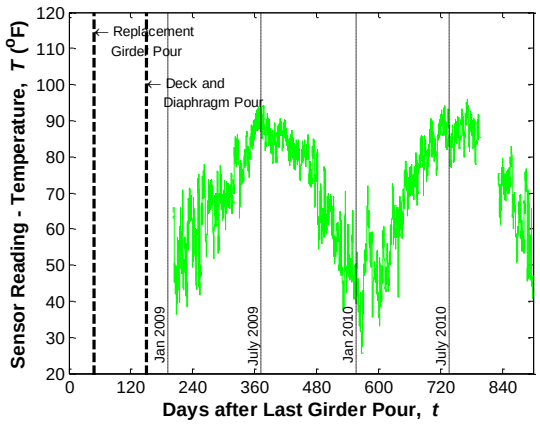

a) Temperature reading of the sensor

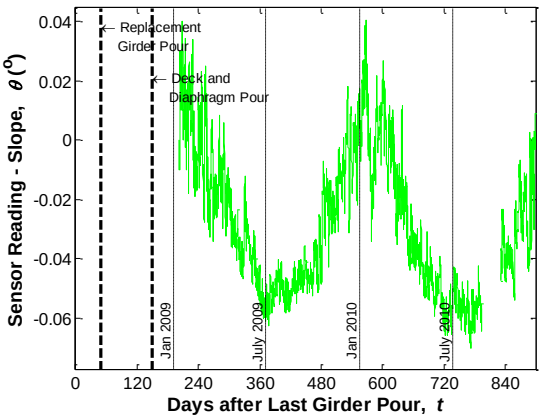

b) Sensor reading without temperature correction

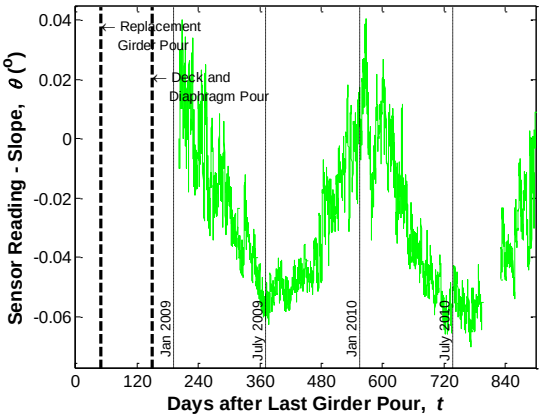

c) Sensor reading after temperature correction

Figure 102
Sensor No. 55, Location G3S24, Support (TM)

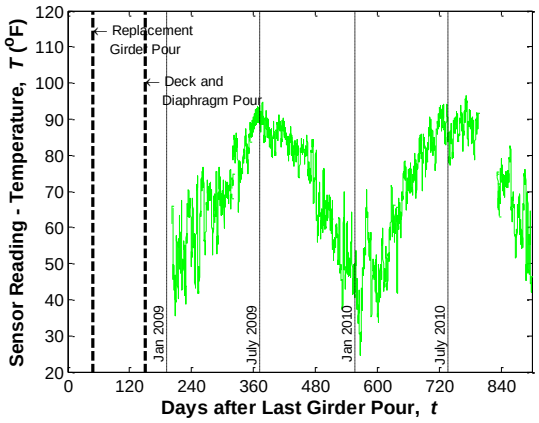

a) Temperature reading of the sensor

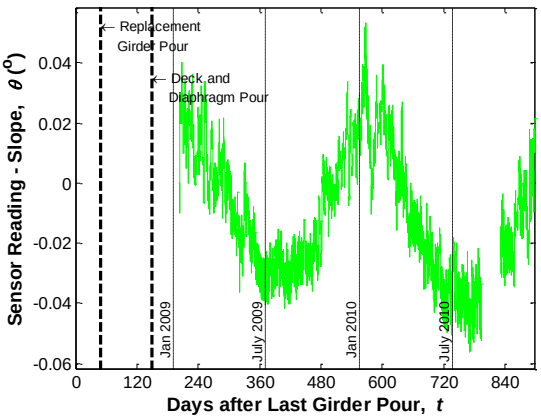

b) Sensor reading without temperature correction

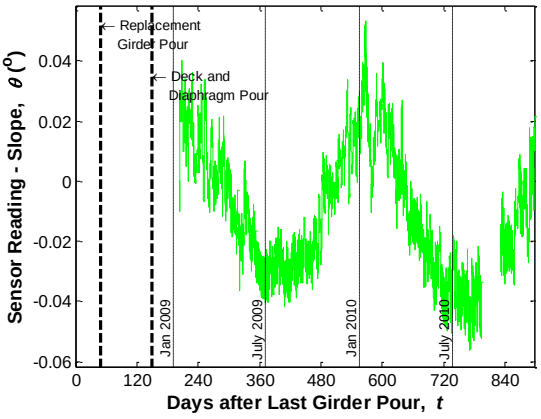

c) Sensor reading after temperature correction

Figure 103
Sensor No. 56, Location G3S23, Support (TM)

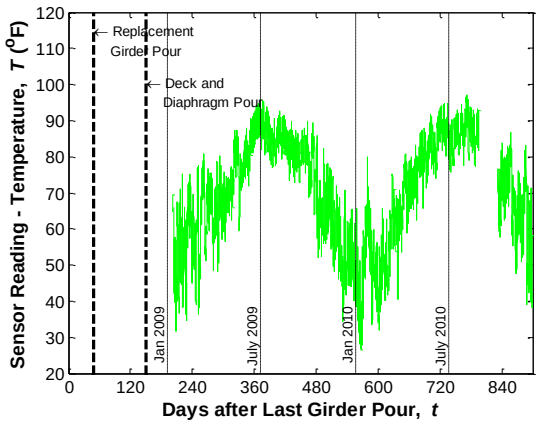

a) Temperature reading of the sensor

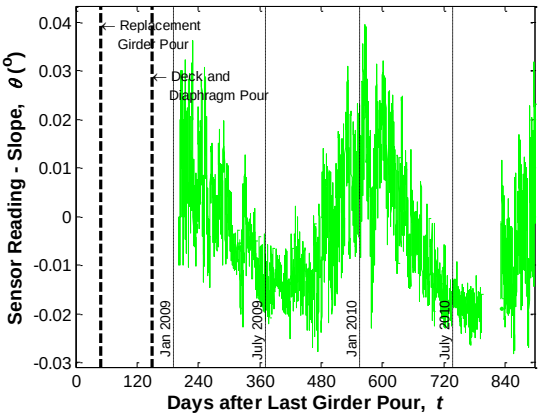

b) Sensor reading without temperature correction

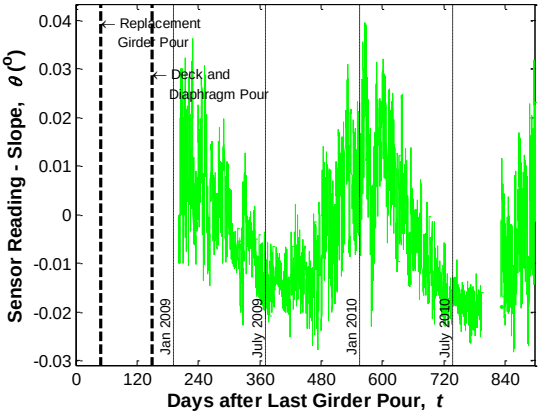

c) Sensor reading after temperature correction

Figure 104
Sensor No. 57, Location G5S23, Support (TM)

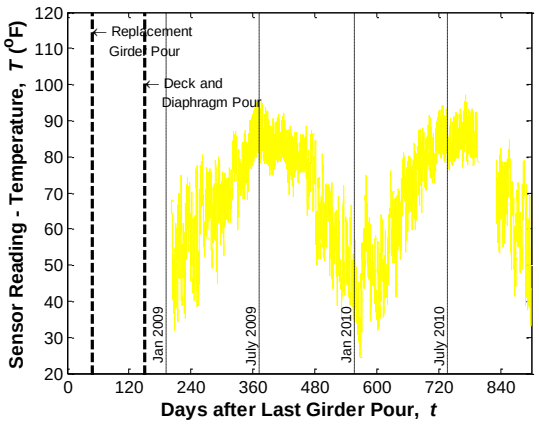

a) Temperature reading of the sensor

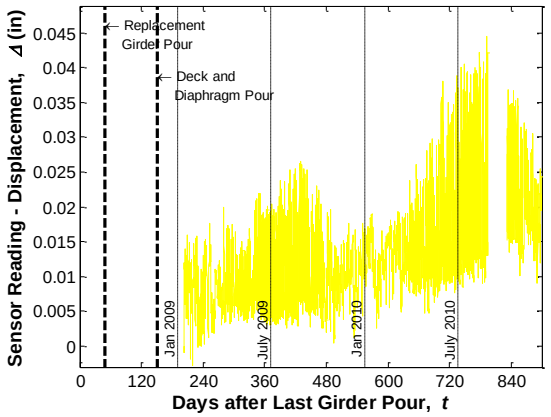

b) Sensor reading without temperature correction

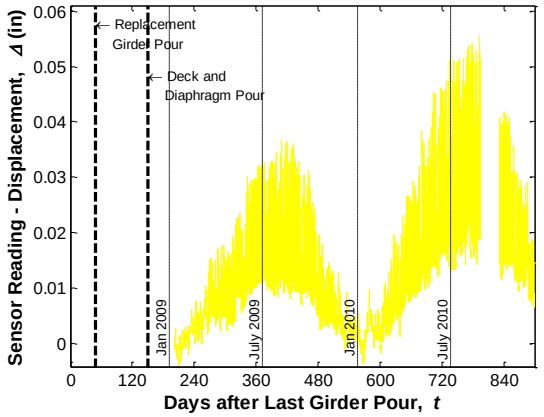

c) Sensor reading after temperature correction

Figure 105
Sensor No. 58, Location G3, End Connection (DM)

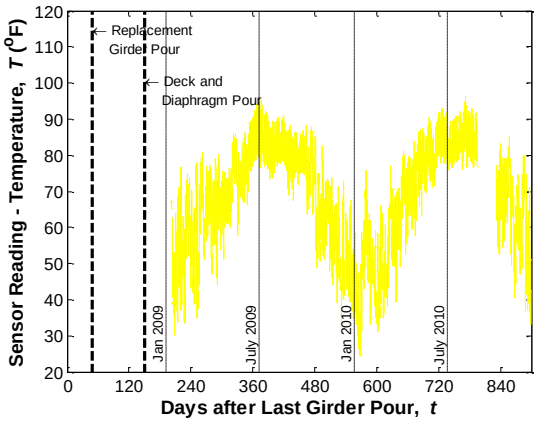

a) Temperature reading of the sensor

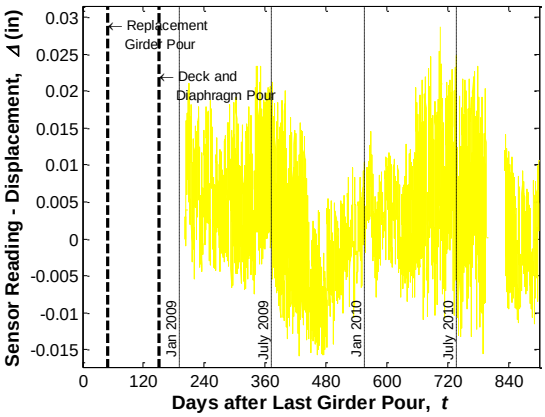

b) Sensor reading without temperature correction

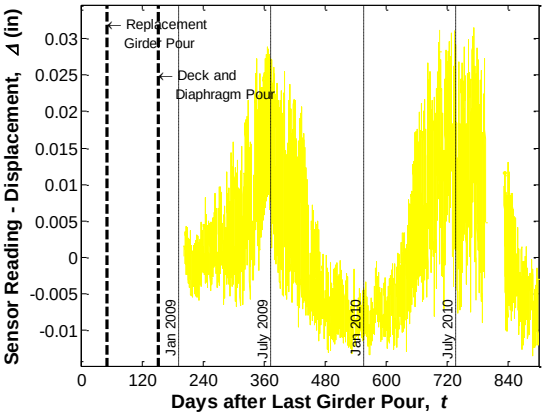

c) Sensor reading after temperature correction

Figure 106
Sensor No. 59, Location G5, End Connection (DM)

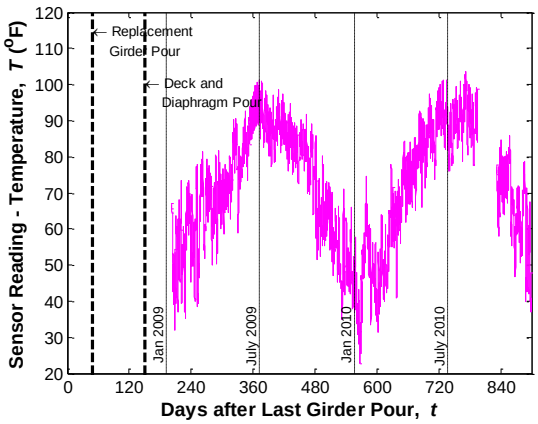

a) Temperature reading of the sensor

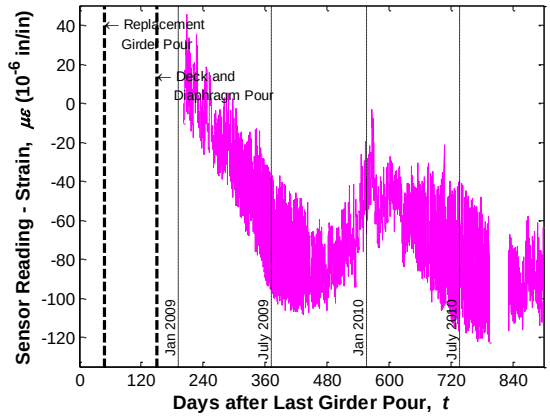

b) Sensor reading without temperature correction

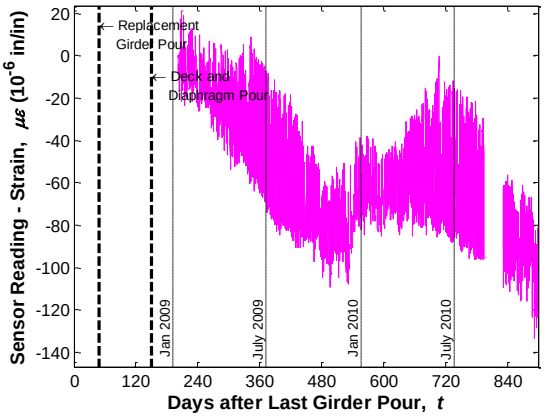

c) Sensor reading after temperature correction

Figure 107
Sensor No. 65, Location G5S24, Midspan Top (VW)

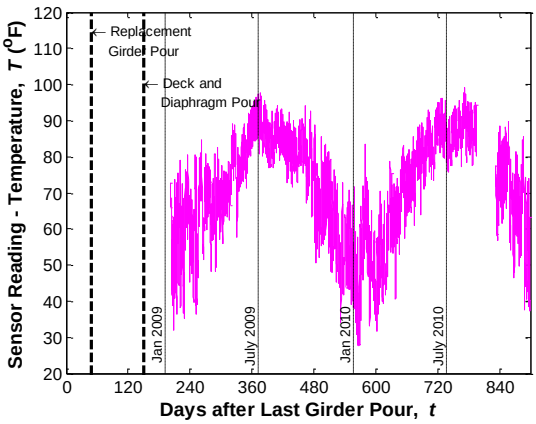

a) Temperature reading of the sensor

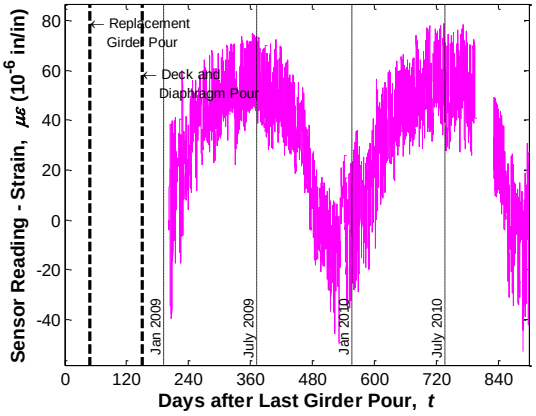

b) Sensor reading without temperature correction

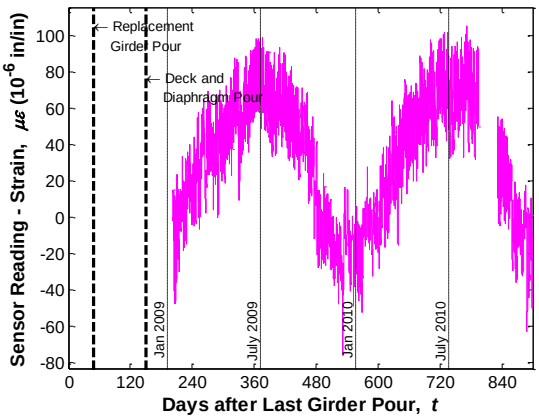

c) Sensor reading after temperature correction

Figure 108
Sensor No. 66, Location G5S24, Midspan Middle (VW)

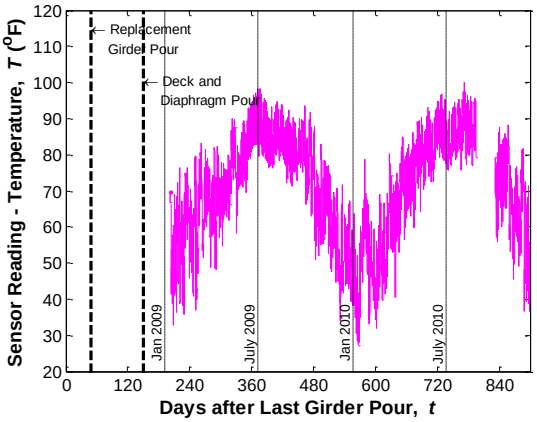

a) Temperature reading of the sensor

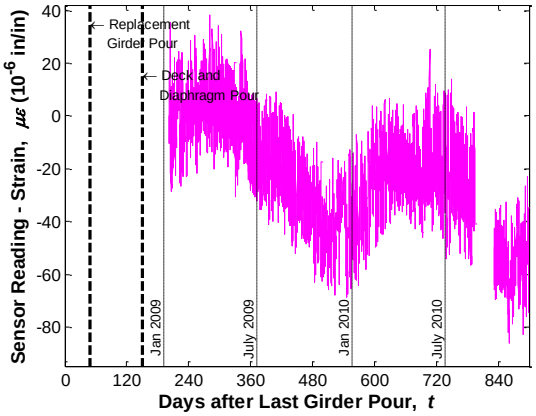

b) Sensor reading without temperature correction

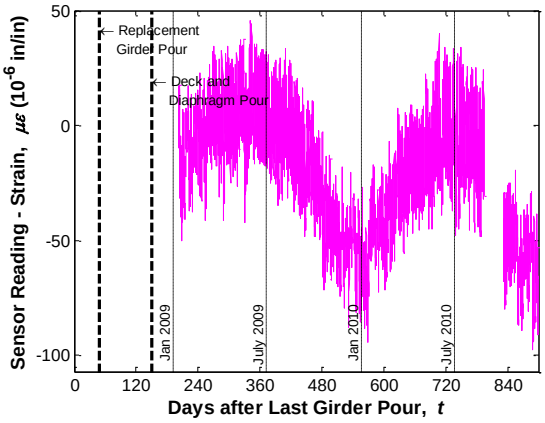

c) Sensor reading after temperature correction

Figure 109
Sensor No. 67, Location G5S24, Midspan Bottom (VW)

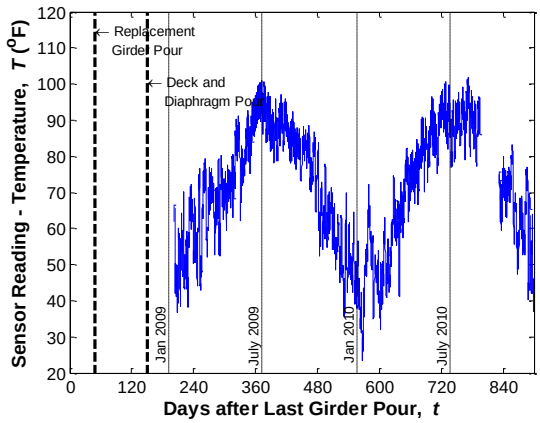

a) Temperature reading of the sensor

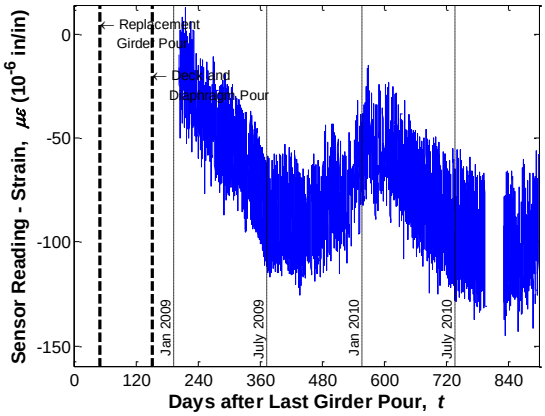

b) Sensor reading without temperature correction

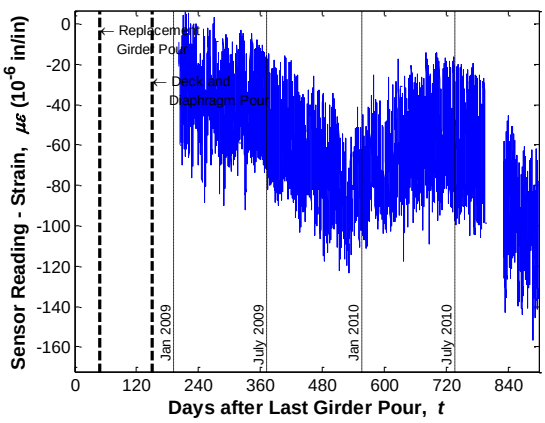

c) Sensor reading after temperature correction

Figure 110
Sensor No. 68, Location G5S24, Midspan Top (EC)

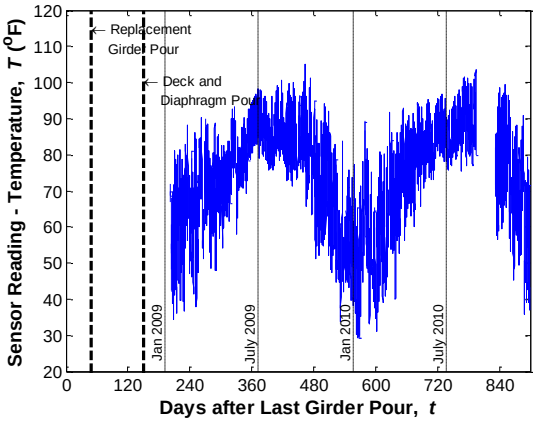

a) Temperature reading of the sensor

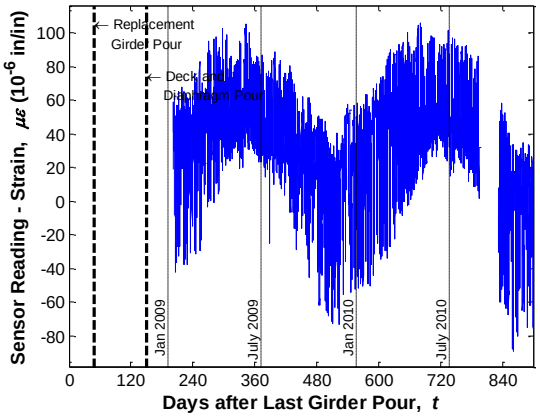

b) Sensor reading without temperature correction

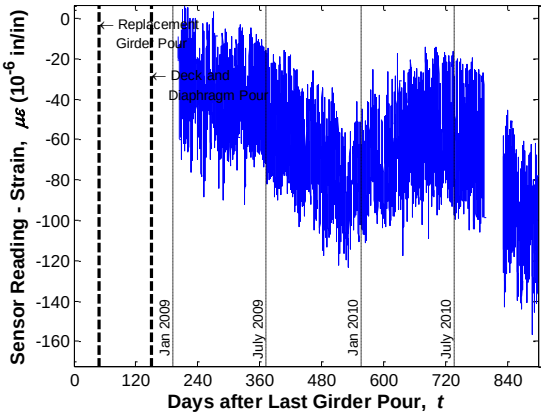

c) Sensor reading after temperature correction

Figure 111
Sensor No. 69, Location G5S24, Midspan Bottom (EC)

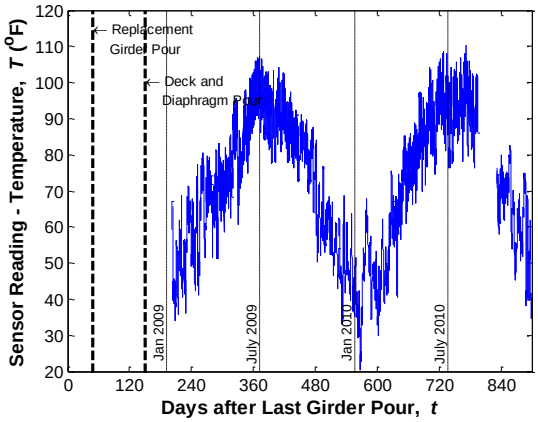

a) Temperature reading of the sensor

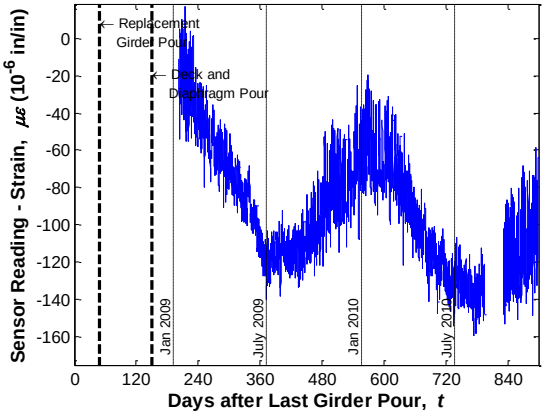

b) Sensor reading without temperature correction

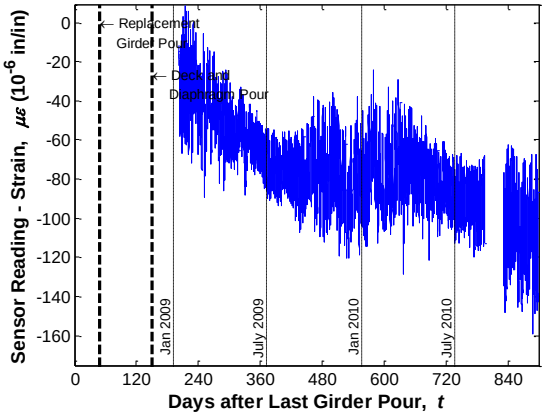

c) Sensor reading after temperature correction

Figure 112
Sensor No. 70, Location G5S24, Midspan Deck (EC)

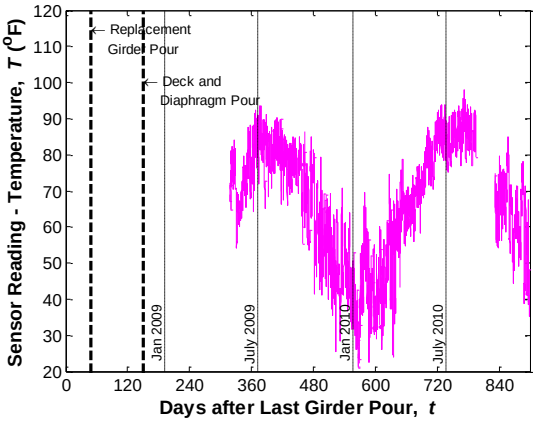

a) Temperature reading of the sensor

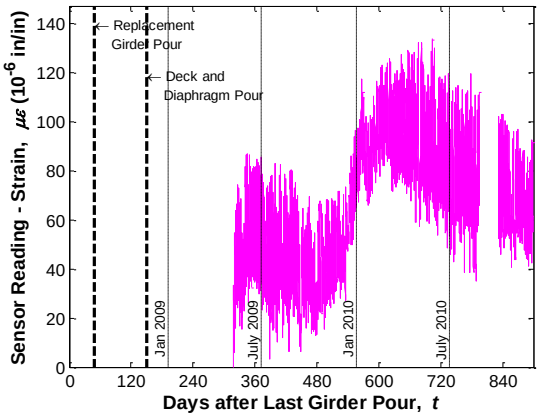

b) Sensor reading without temperature correction

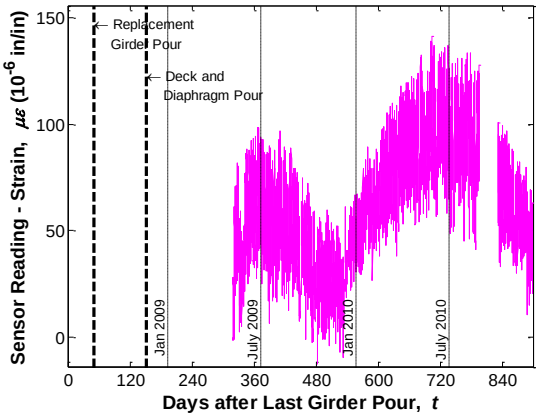

c) Sensor reading after temperature correction

Figure 113
Sensor No. 71, Location G1S24, Midspan Bottom (VW)

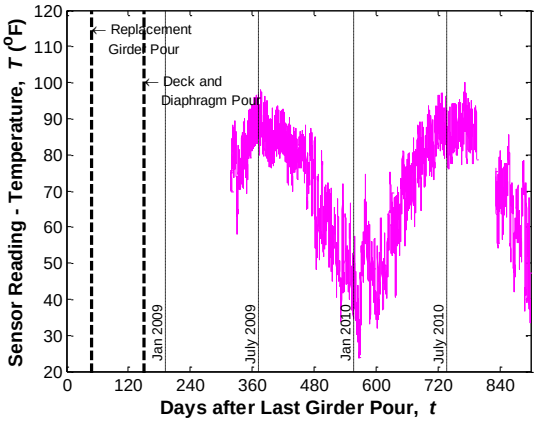

a) Temperature reading of the sensor

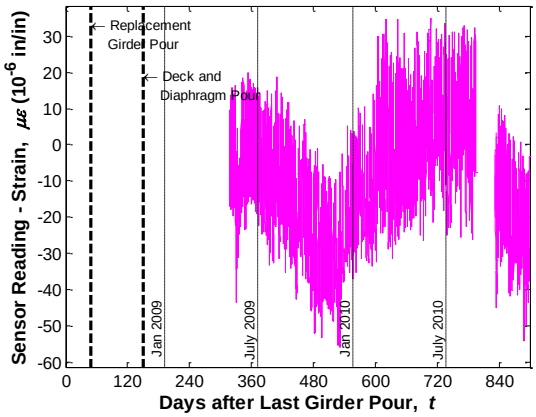

b) Sensor reading without temperature correction

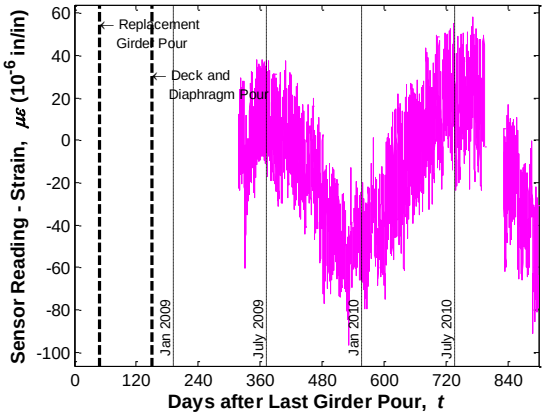

c) Sensor reading after temperature correction

Figure 114
Sensor No. 72, Location G2S24, Midspan Bottom (VW)

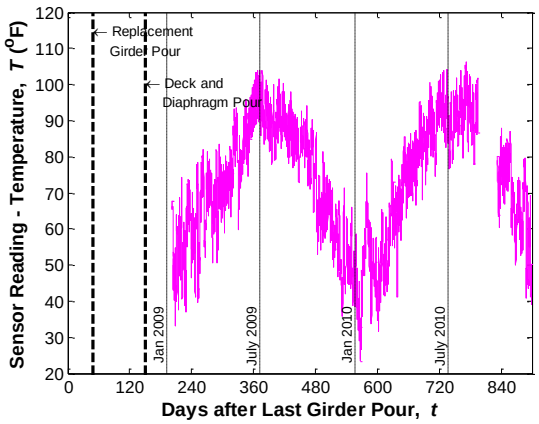

a) Temperature reading of the sensor

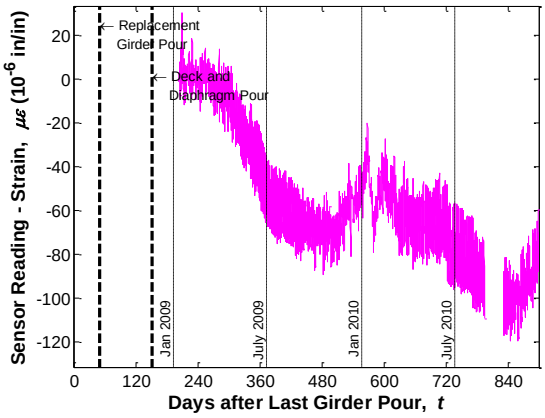

b) Sensor reading without temperature correction

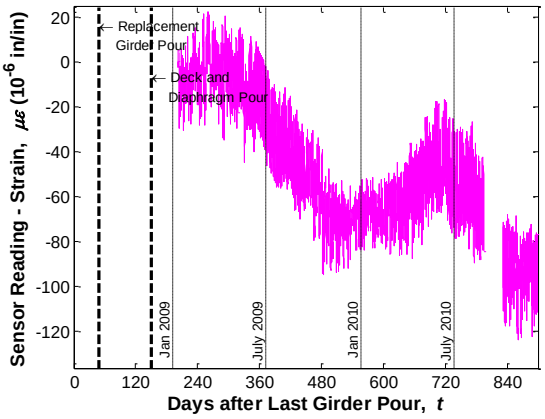

c) Sensor reading after temperature correction

Figure 115
Sensor No. 81, Location G3S24, Midspan Top (VW)

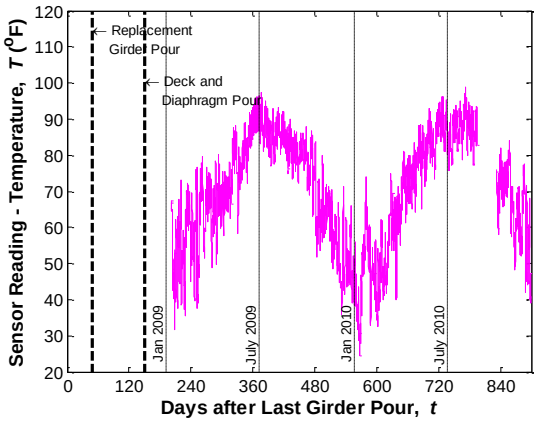

a) Temperature reading of the sensor

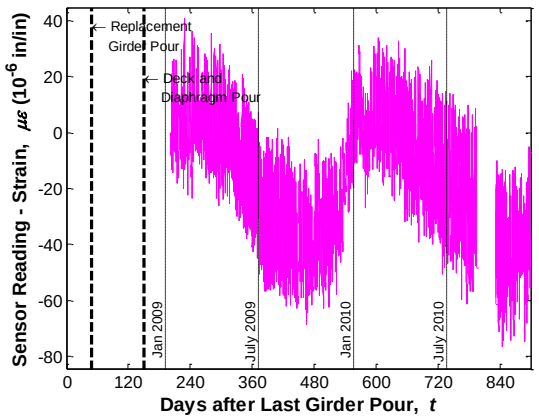

b) Sensor reading without temperature correction

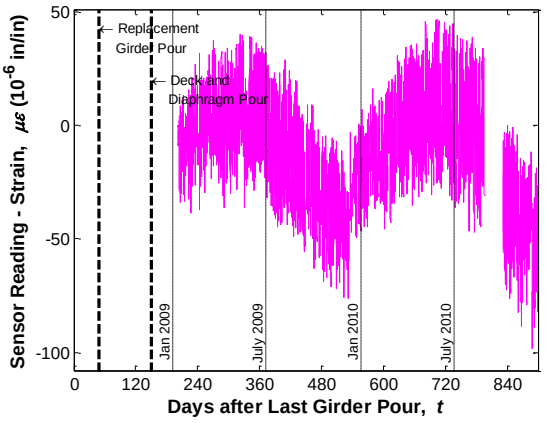

c) Sensor reading after temperature correction

Figure 116
Sensor No. 82, Location G3S24, Midspan Middle (VW)

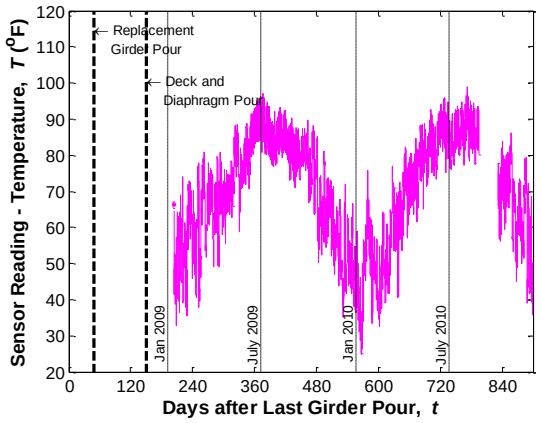

a) Temperature reading of the sensor

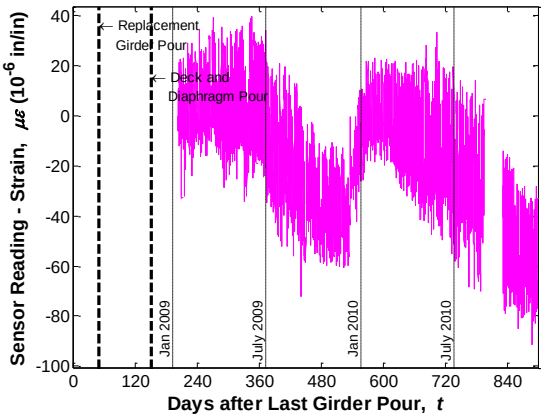

b) Sensor reading without temperature correction

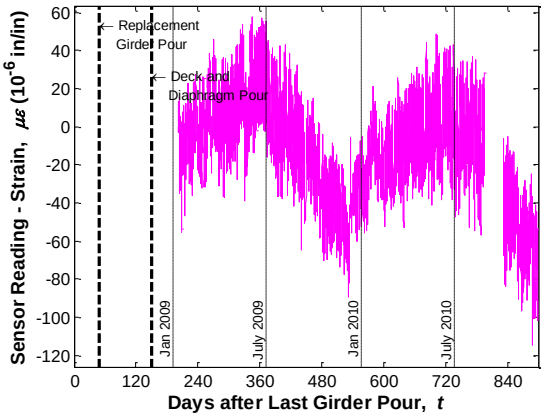

c) Sensor reading after temperature correction

Figure 117
Sensor No. 83, Location G3S24, Midspan Bottom (VW)

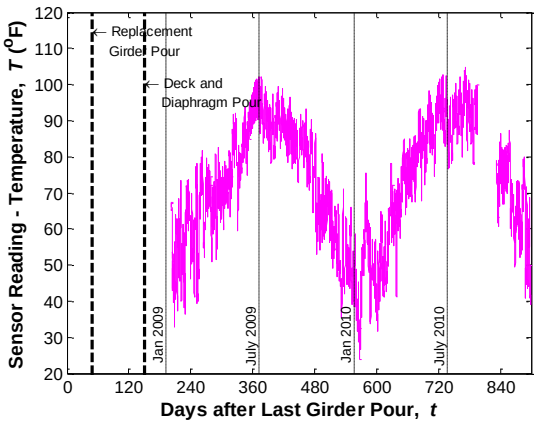

a) Temperature reading of the sensor

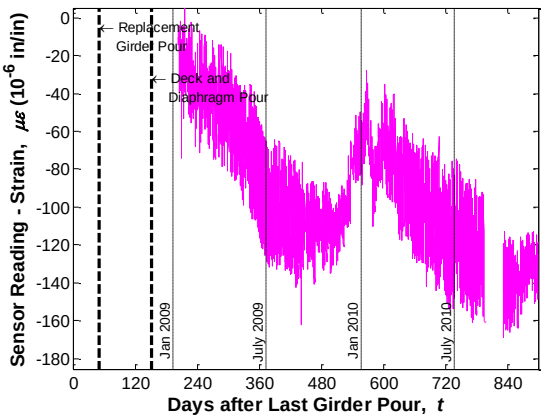

b) Sensor reading without temperature correction

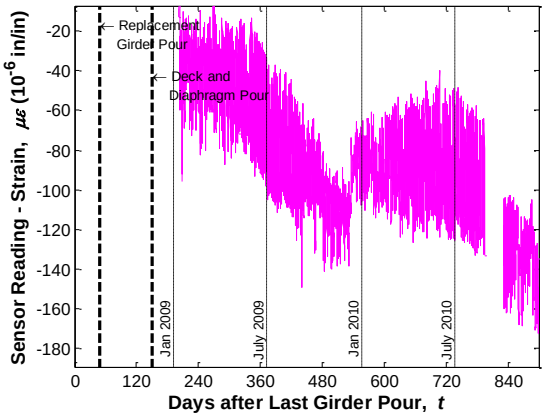

c) Sensor reading after temperature correction

Figure 118
Sensor No. 84, Location G4S24, Midspan Top (VW)

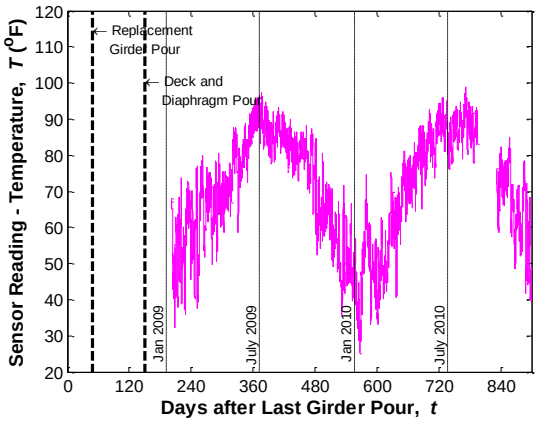

a) Temperature reading of the sensor

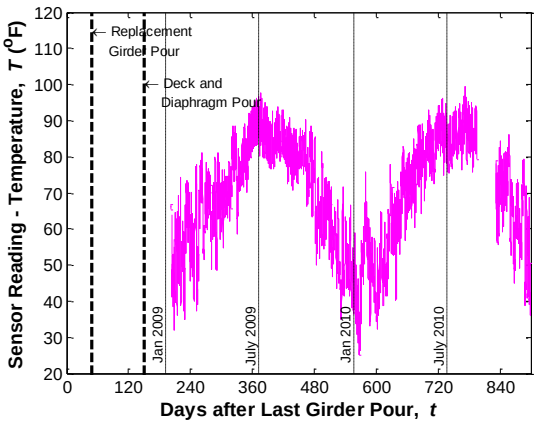

a) Temperature reading of the sensor

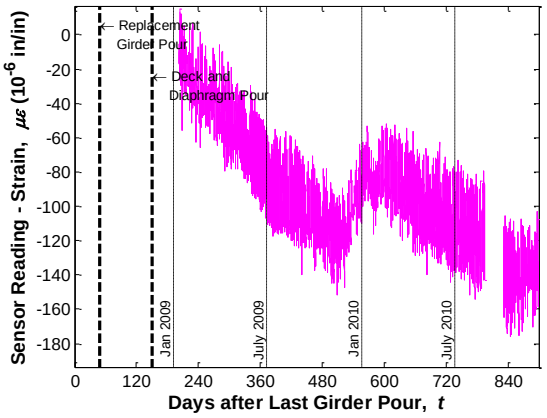

b) Sensor reading without temperature correction

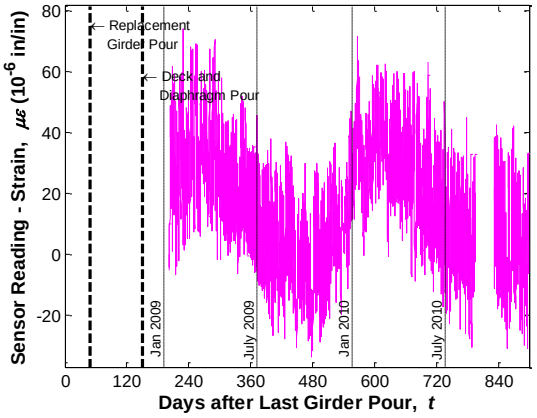

b) Sensor reading without temperature correction

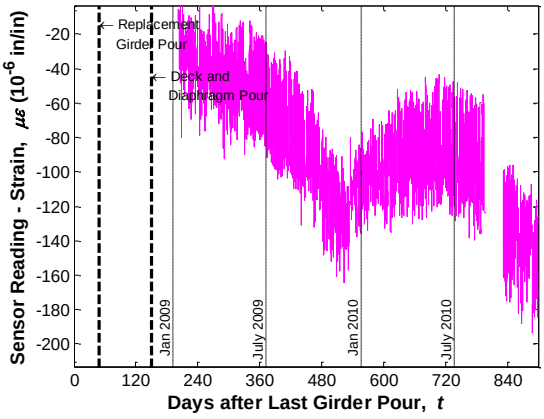

c) Sensor reading after temperature correction

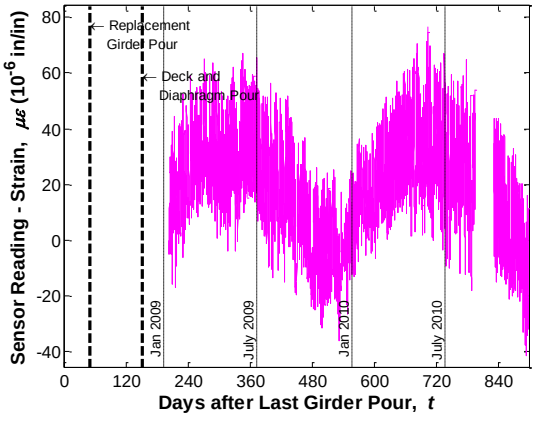

c) Sensor reading after temperature correction

Figure 119
Sensor No. 85, Location G4S24, Midspan Middle (VW)

Figure 120
Sensor No. 86, Location G4S24, Midspan Bottom (VW)

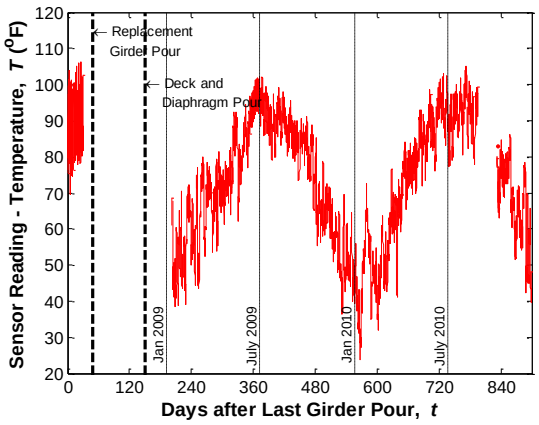

a) Temperature reading of the sensor

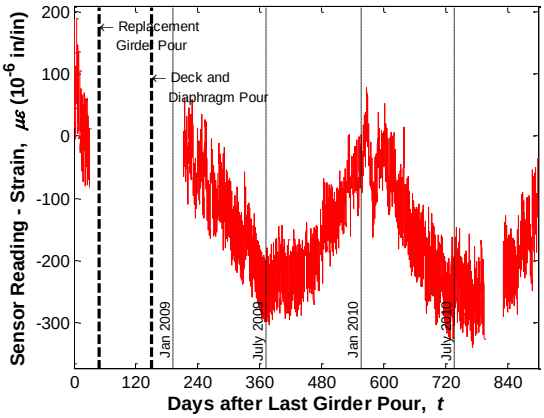

b) Sensor reading without temperature correction

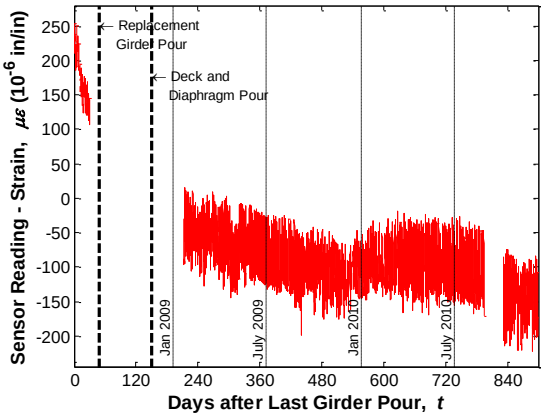

c) Sensor reading after temperature correction

Figure 121
Sensor No. 87, Location G3S24, Midspan Top (ES)

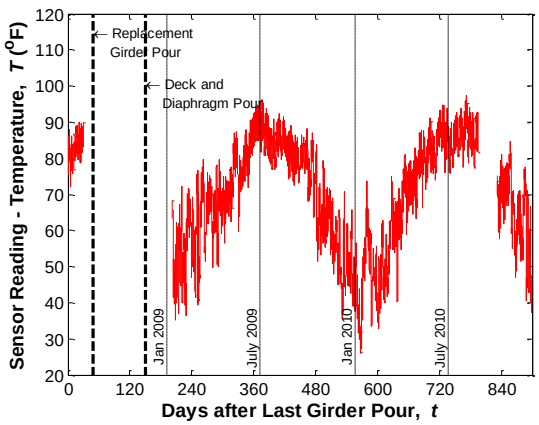

a) Temperature reading of the sensor

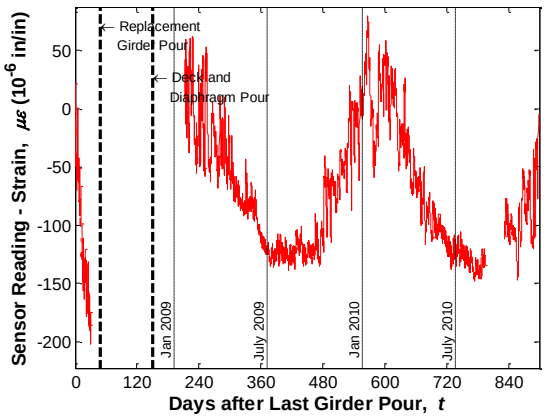

b) Sensor reading without temperature correction

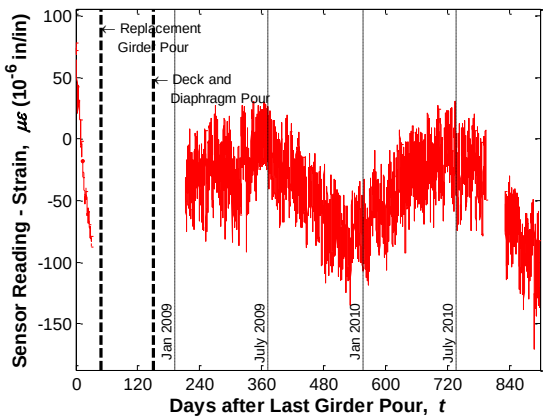

c) Sensor reading after temperature correction

Figure 122
Sensor No. 88, Location G3S24, Midspan Bottom (ES)

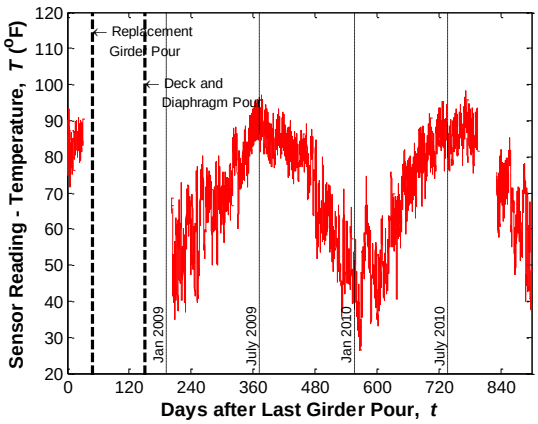

a) Temperature reading of the sensor

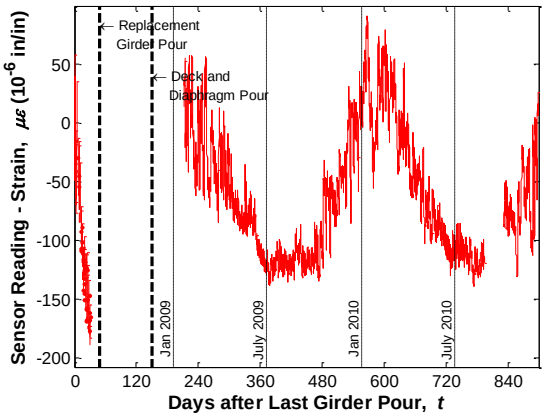

b) Sensor reading without temperature correction

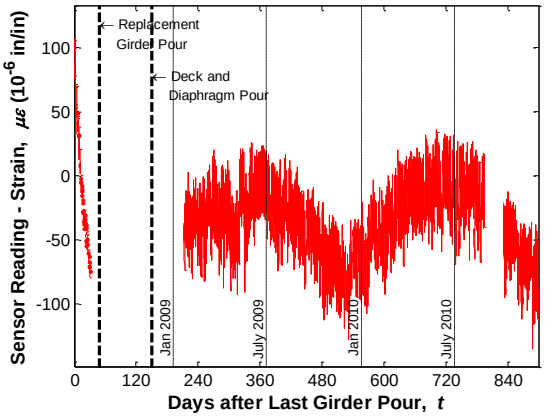

c) Sensor reading after temperature correction

Figure 123
Sensor No. 89, Location G4S24, Midspan Bottom (ES)

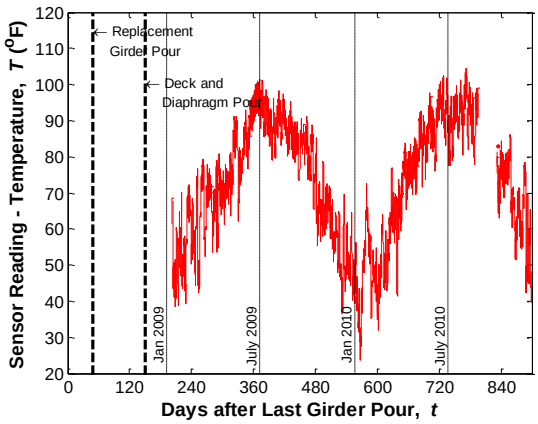

a) Temperature reading of the sensor

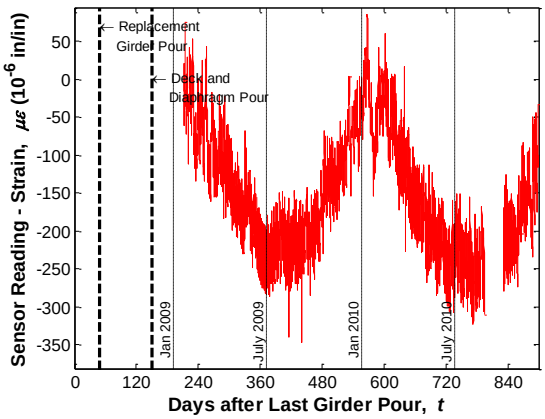

b) Sensor reading without temperature correction

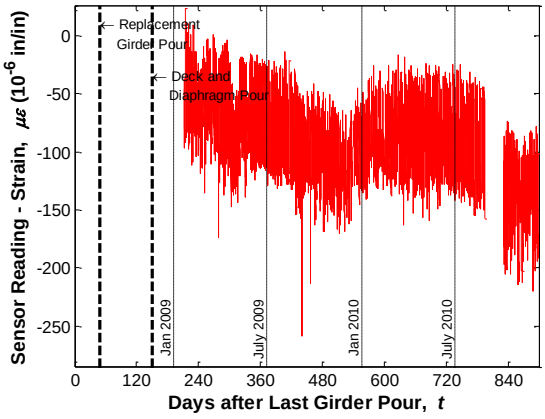

c) Sensor reading after temperature correction

Figure 124
Sensor No. 90, Location G4S24, Midspan Top (ES)

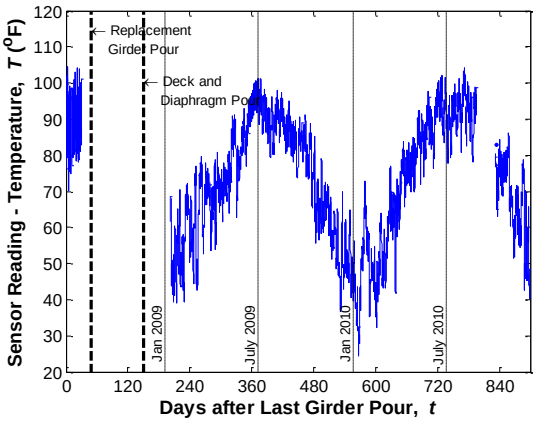

a) Temperature reading of the sensor

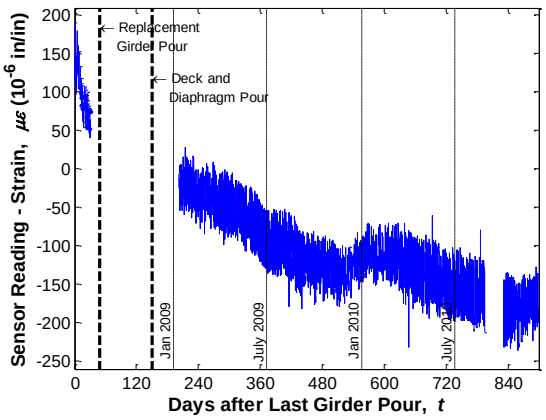

b) Sensor reading without temperature correction

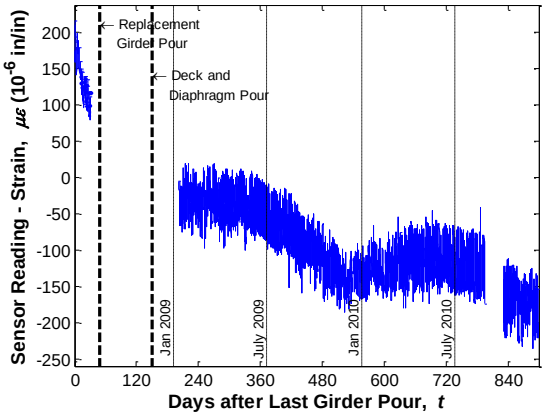

c) Sensor reading after temperature correction

Figure 125
Sensor No. 91, Location G4S24, Midspan Top (EC)

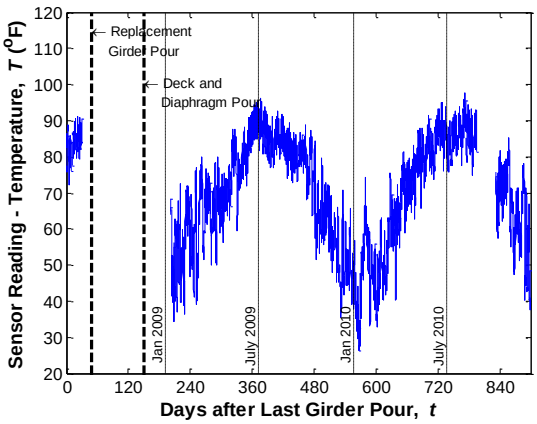

a) Temperature reading of the sensor

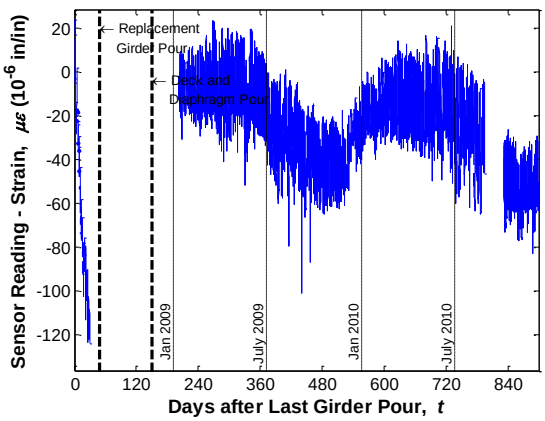

b) Sensor reading without temperature correction

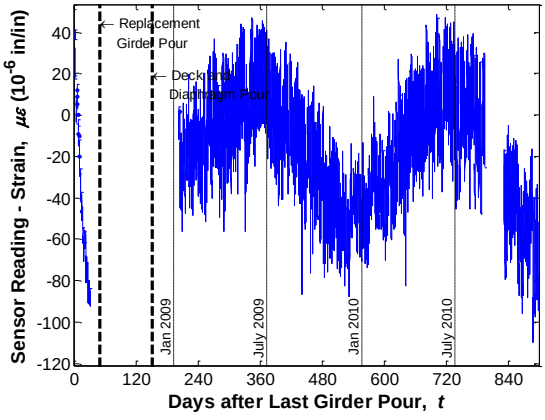

c) Sensor reading after temperature correction

Figure 126
Sensor No. 92, Location G4S24, Midspan Bottom (EC)

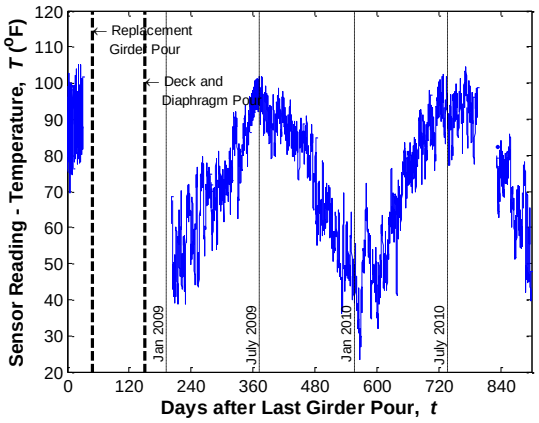

a) Temperature reading of the sensor

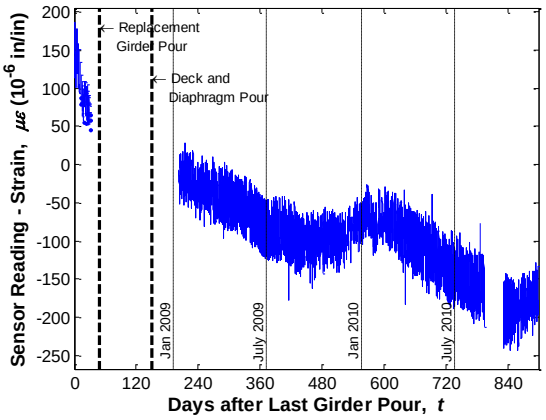

b) Sensor reading without temperature correction

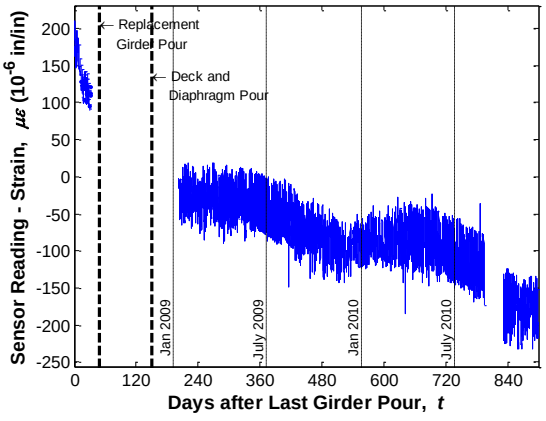

c) Sensor reading after temperature correction

Figure 127
Sensor No. 93, Location G3S24, Midspan Top (EC)

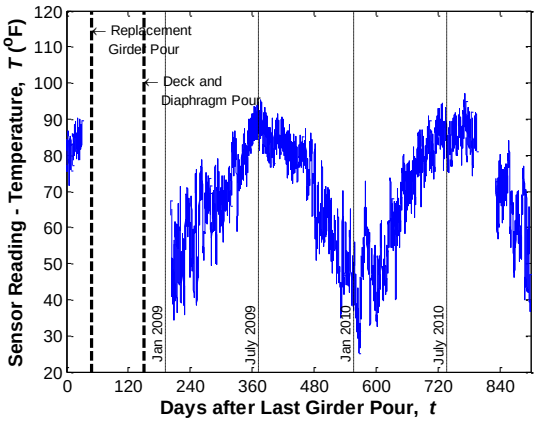

a) Temperature reading of the sensor

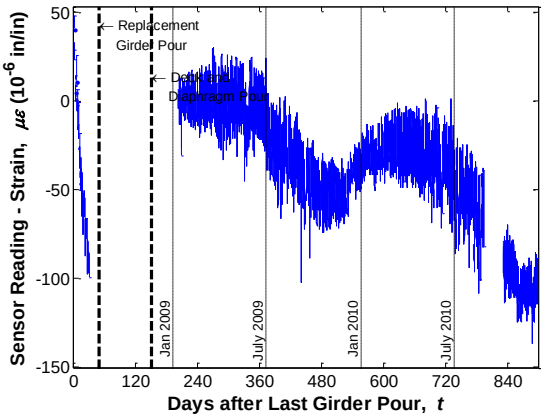

b) Sensor reading without temperature correction

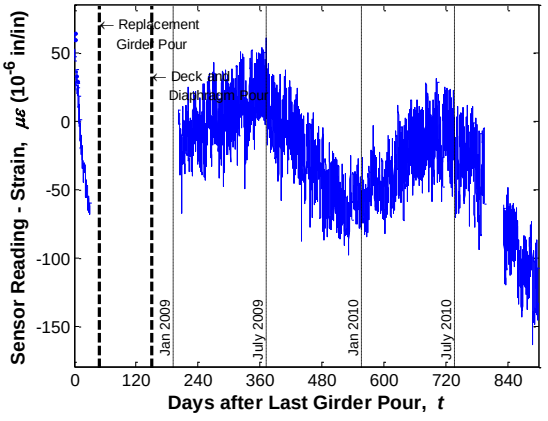

c) Sensor reading after temperature correction

Figure 128
Sensor No. 94, Location G3S24, Midspan Bottom (EC)

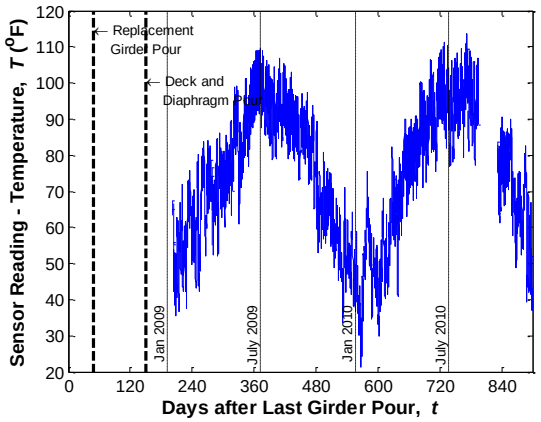

a) Temperature reading of the sensor

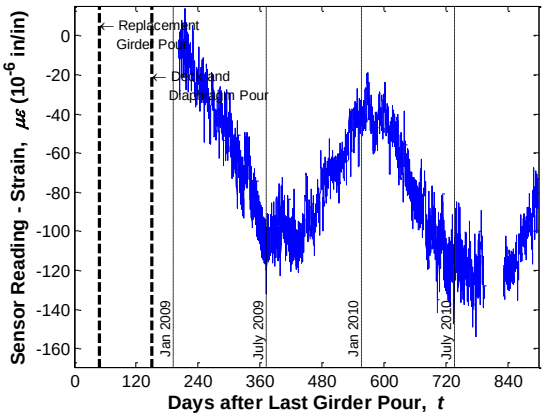

b) Sensor reading without temperature correction

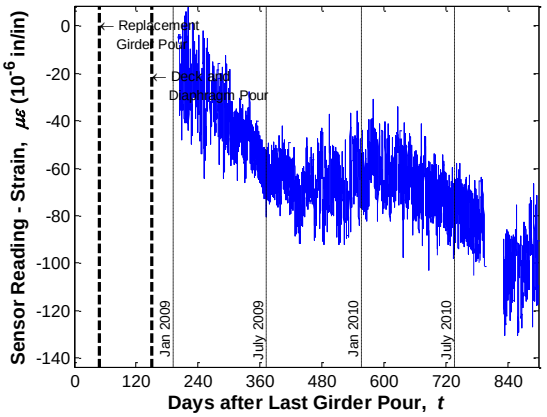

c) Sensor reading after temperature correction

Figure 129
Sensor No. 95, Location G3S24, Midspan Deck (EC)

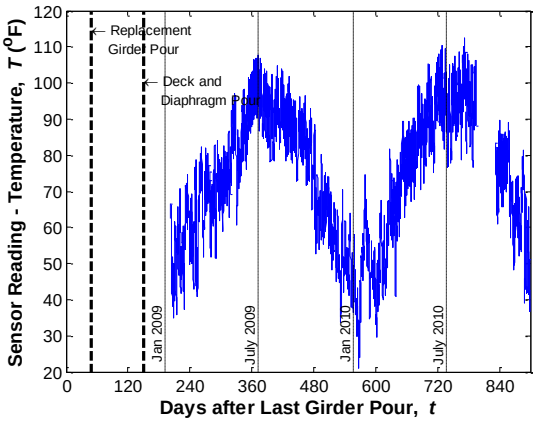

a) Temperature reading of the sensor

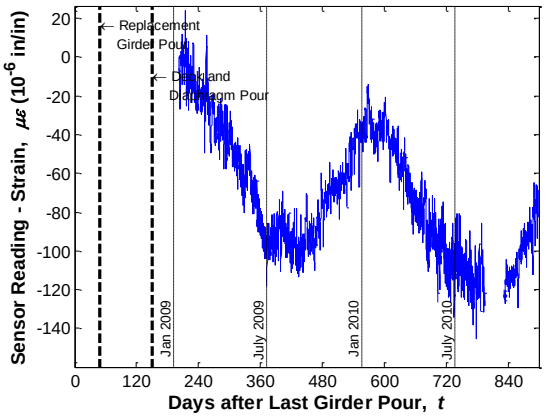

b) Sensor reading without temperature correction

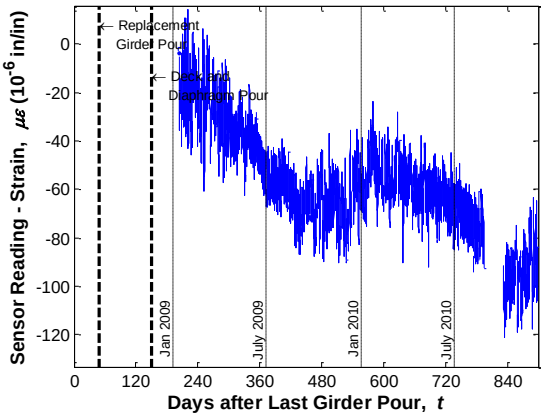

c) Sensor reading after temperature correction

Figure 130
Sensor No. 96, Location G4S24, Midspan Deck (EC)

APPENDIX D

Dimensions and Weights of Trucks Used in Live Load Tests

Two dump trucks from the DOTD maintenance office in New Roads, LA were used to load the monitored segment of Bridge #2 as described earlier. The trucks were loaded before the tests and measurements of axle dimensions and weights were recorded. The research team measured the dimensions, while the Weights and Standards Police used portable scales to weigh both trucks (see Figure 131). Figure 132 shows the recorded dimensions and axle weights for both trucks. The dimensions are almost identical for both trucks except for the fact that the distance between the front axle and rear axle group is longer for Truck #1 (156-227) by 3 in. than Truck #2 (156-091). The gross vehicle weights were recorded to be 57.0 kips and 54.1 kips for Truck #1 and Truck #2, respectively.

Figure 131
Portable scales used in weighing individual truck axles

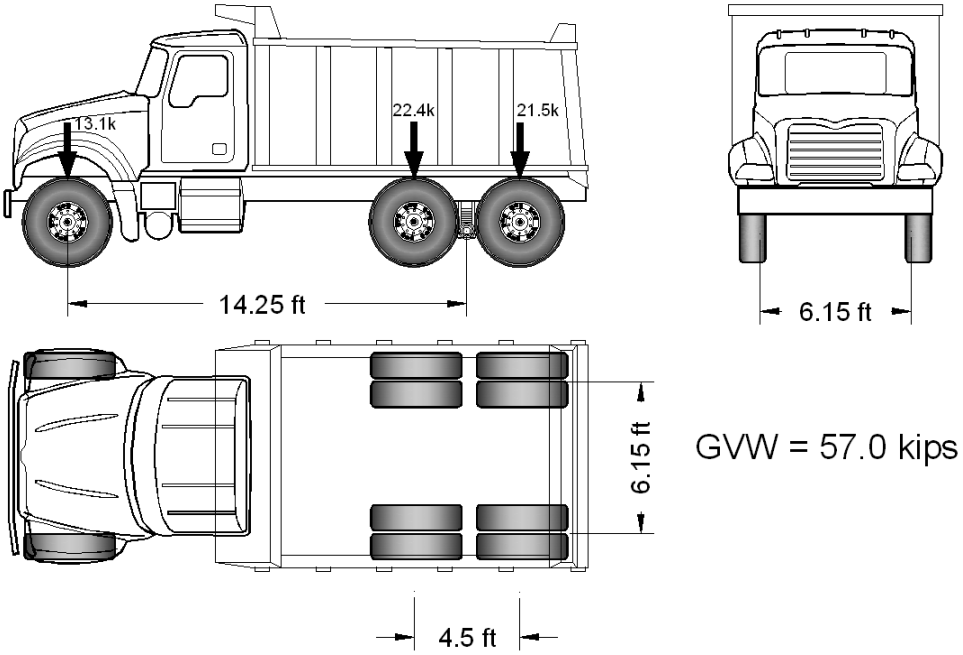

(a) Truck #1 (156-227)

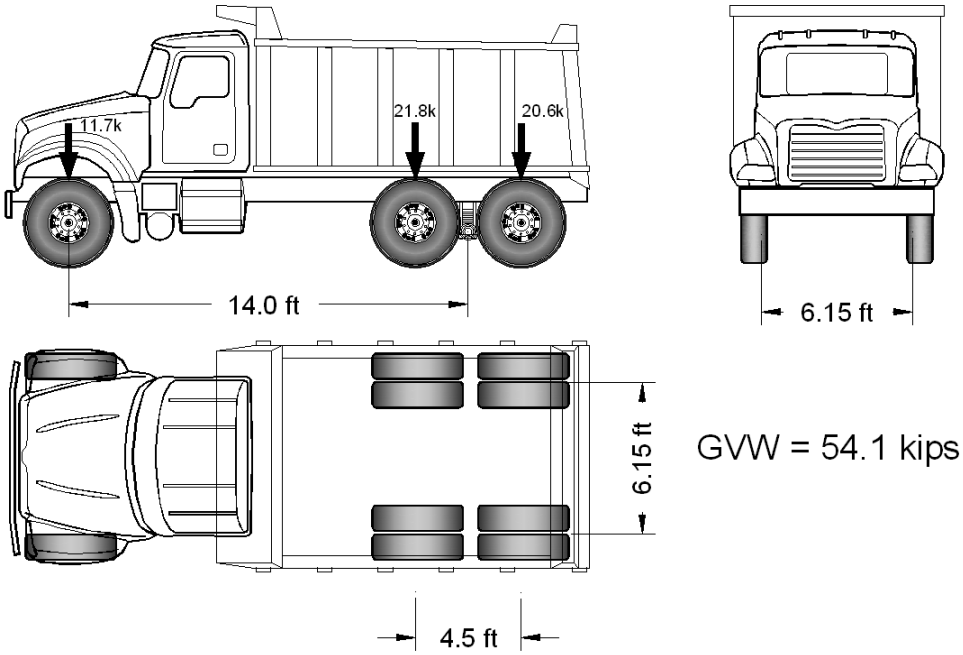

(a) Truck #2 (156-091)

Figure 132
Dimensions and weights of trucks used in live load tests

APPENDIX E

Plots of Sensor Readings During Static Live Load Tests

The following plots are a documentation of all sensor readings obtained during the static live load tests.

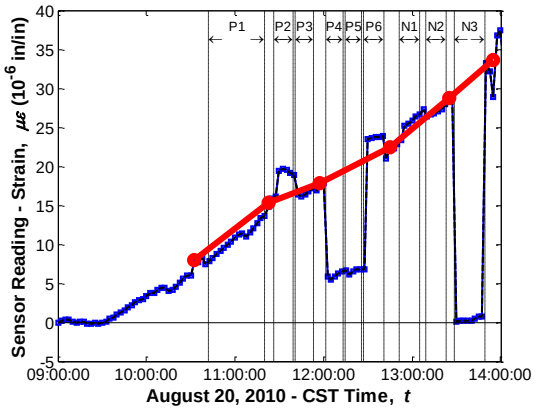

Figure 133
Sensor No. 1, Location G1S24, Support Bottom (Strandmeter)

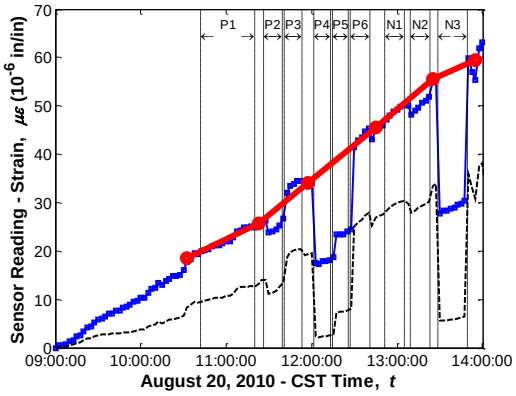

Figure 134
Sensor No. 2, Location G1S24, Support Bottom (Strandmeter)

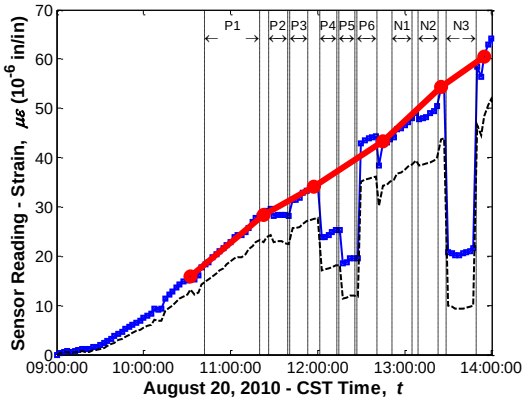

Figure 135
Sensor No. 3, Location G1S23, Support Bottom (Strandmeter)

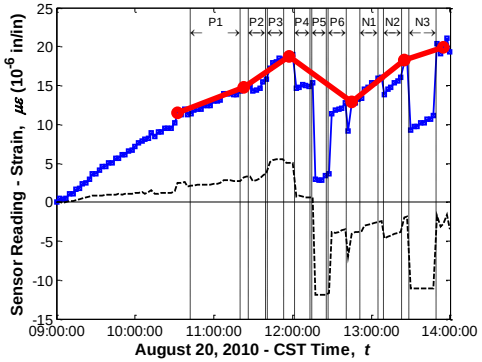

Figure 136
Sensor No. 4, Location G1S23, Support Bottom (Strandmeter)

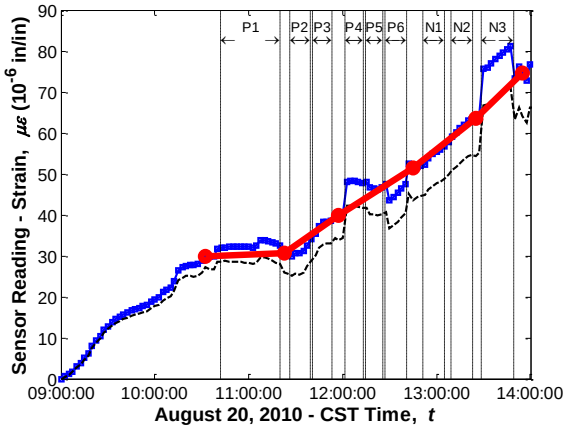

Figure 137
Sensor No. 5, Location G1S24, Support Top (Sisterbar)

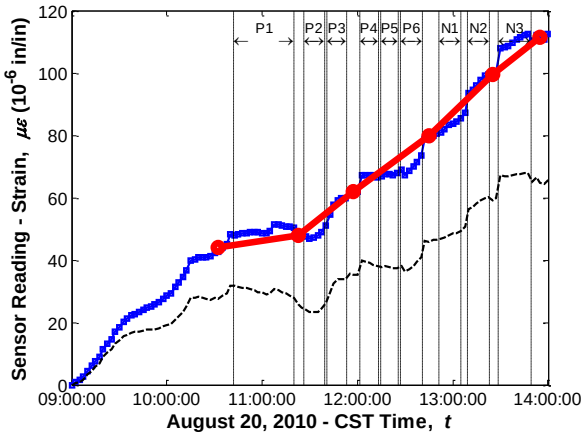

Figure 138
Sensor No. 6, Location G2S24, Support Top (Strandmeter)

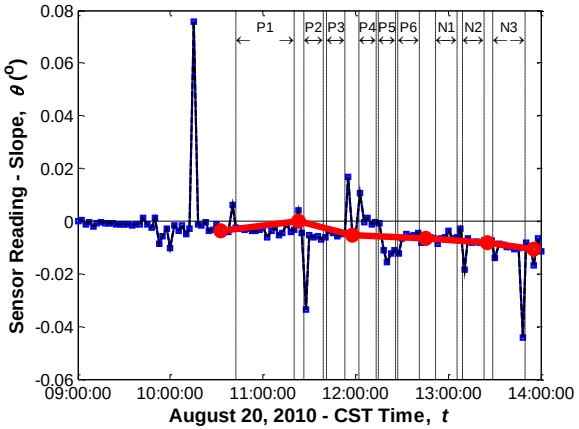

Figure 139
Sensor No. 7, Location G1S24, Support (Tiltmeter)

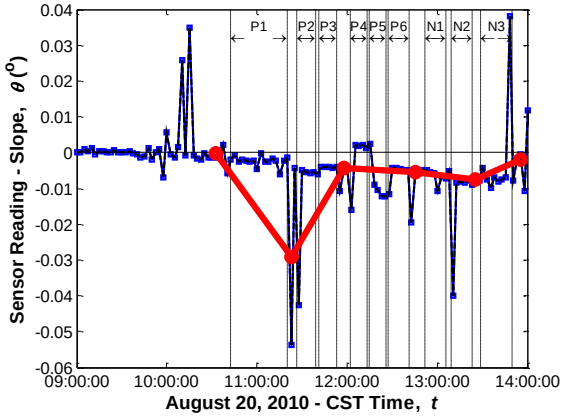

Figure 140
Sensor No. 8, Location G1S23, Support (Tiltmeter)

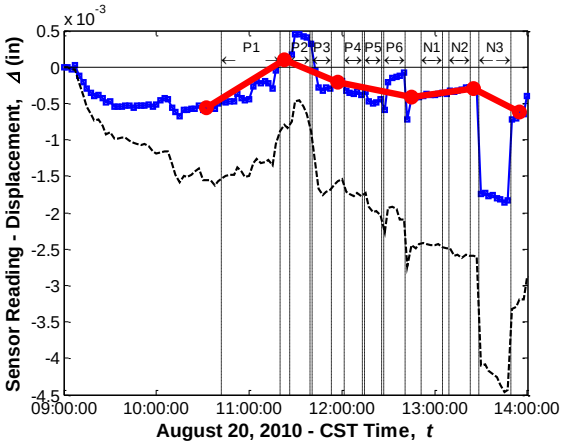

Figure 141
Sensor No. 9, Location G1, End Connection
(Displacement meter)

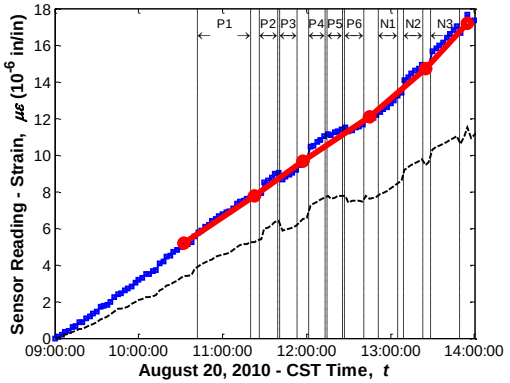

Figure 142
Sensor No. 17, Location G1S24, Support Top
(Vibrating wire gauge)

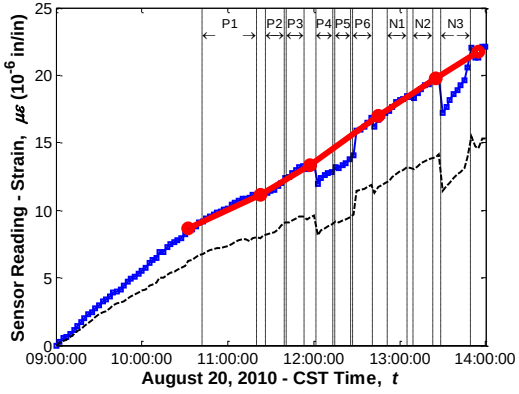

Figure 143
Sensor No. 18, Location G1S24, Support Middle
(Vibrating wire gauge)

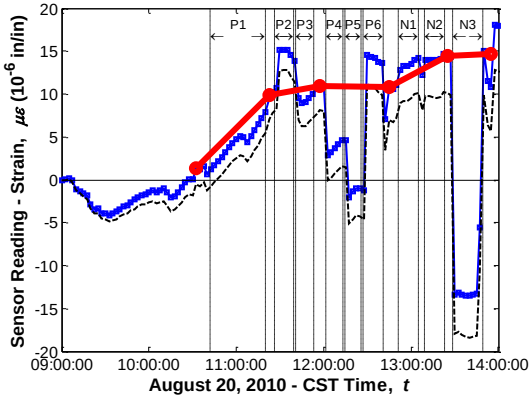

Figure 144
Sensor No. 19, Location G1S24, Support Bottom
(Vibrating wire gauge)

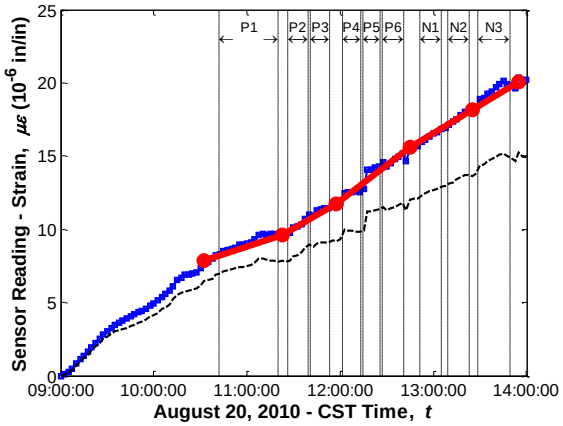

Figure 145
Sensor No. 20, Location G1S23, Support Top (Vibrating wire gauge)

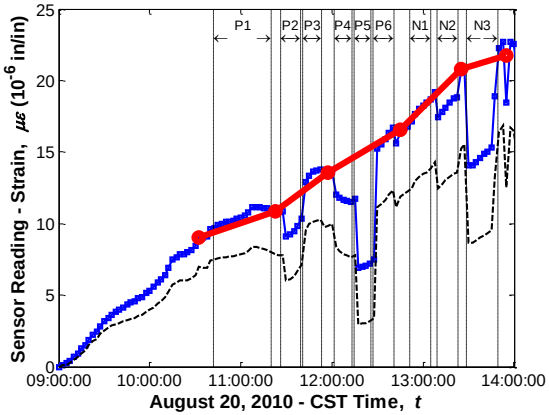

Figure 146
Sensor No. 21, Location G1S23, Support Middle (Vibrating wire gauge)

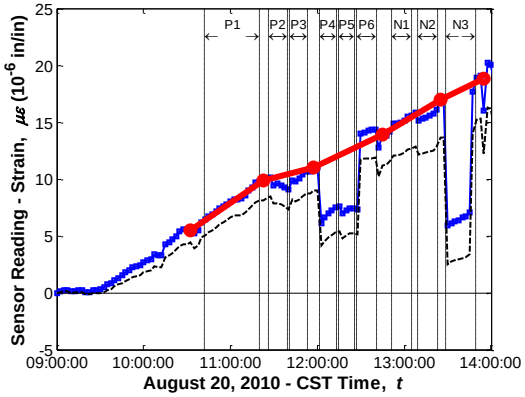

Figure 147
Sensor No. 22, Location G1S23, Support Bottom (Vibrating wire gauge)

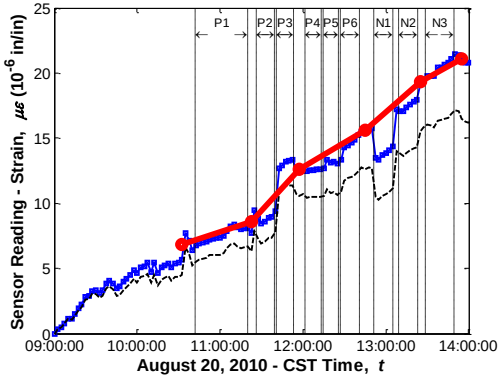

Figure 148
Sensor No. 33, Location G5S24, Support Top (Vibrating wire gauge)

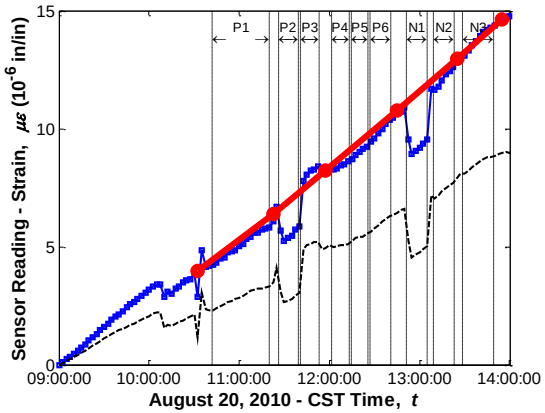

Figure 149
Sensor No. 34, Location G5S24, Support Middle (Vibrating wire gauge)

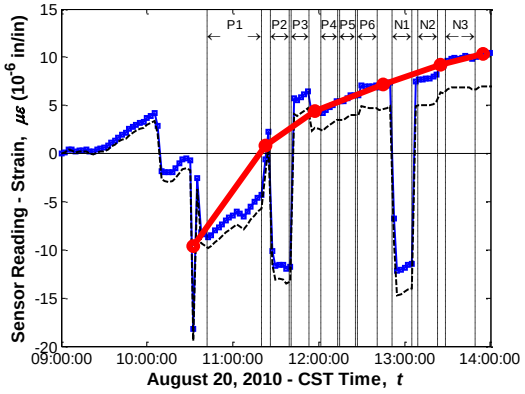

Figure 150
Sensor No. 35, Location G5S24, Support Bottom (Vibrating wire gauge)

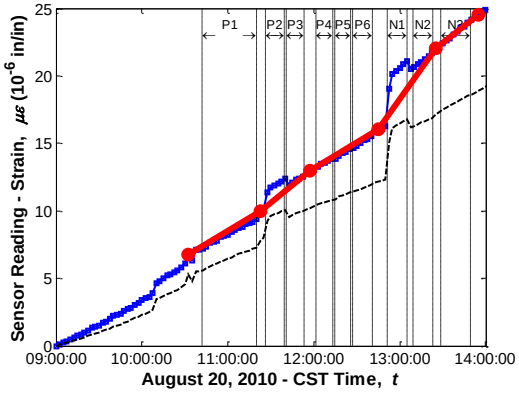

Figure 151
Sensor No. 36, Location G5S23, Support Top (Vibrating wire gauge)

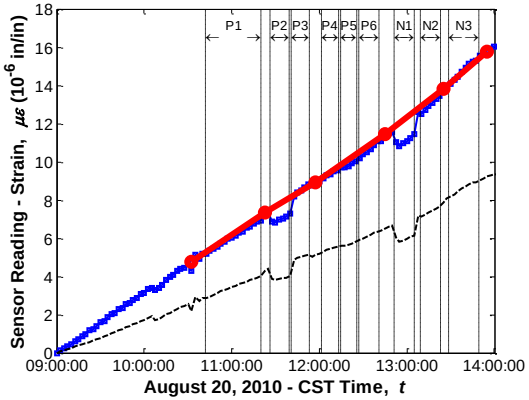

Figure 152
Sensor No. 37, Location G5S23, Support Middle (Vibrating wire gauge)

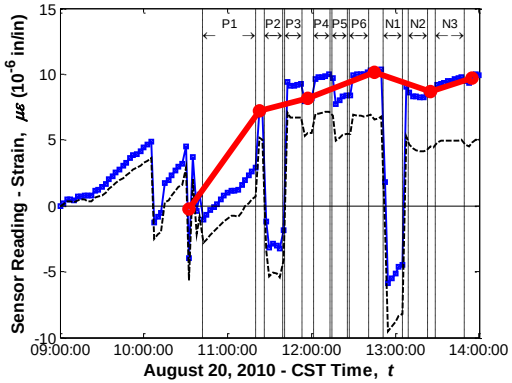

Figure 153
Sensor No. 38, Location G5S23, Support Bottom (Vibrating wire gauge)

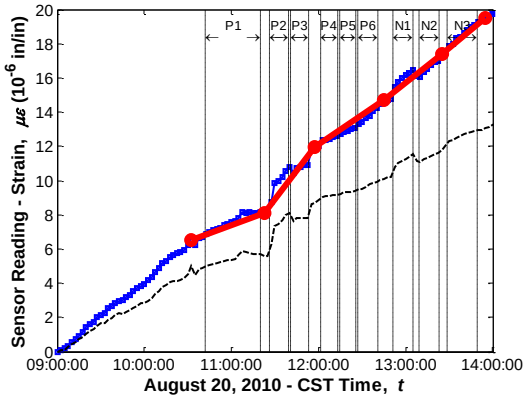

Figure 154
Sensor No. 39, Location G3S24, Support Top (Vibrating wire gauge)

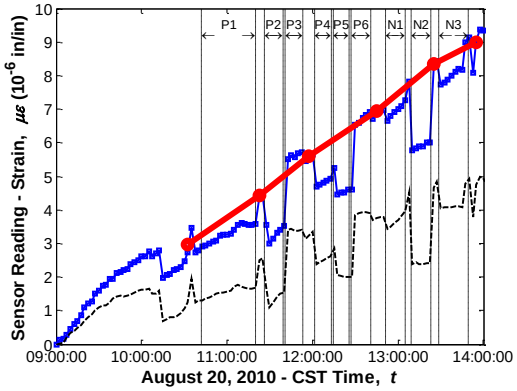

Figure 155
Sensor No. 40, Location G3S24, Support Middle (Vibrating wire gauge)

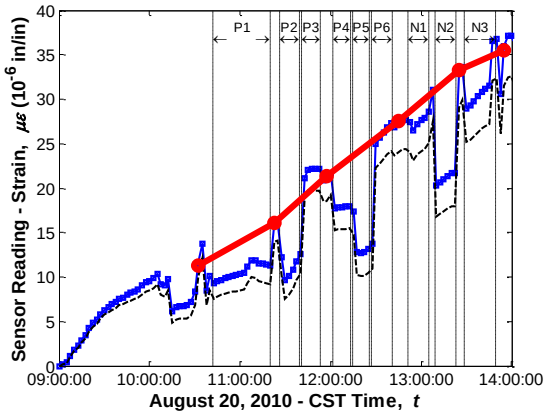

Figure 156
Sensor No. 41, Location G3S24, Support Bottom (Vibrating wire gauge)

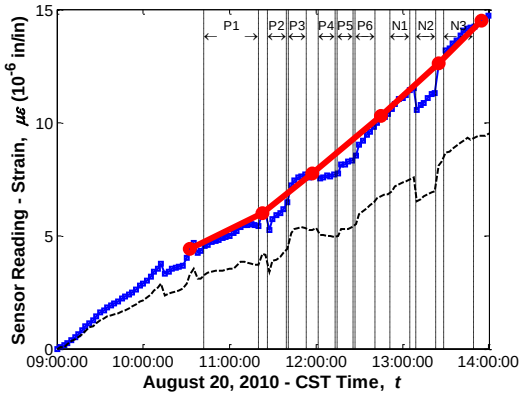

Figure 157
Sensor No. 42, Location G3S23, Support Top (Vibrating wire gauge)

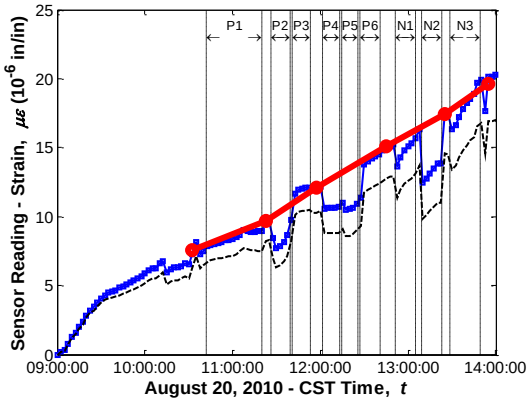

Figure 158
Sensor No. 43, Location G3S23, Support Middle (Vibrating wire gauge)

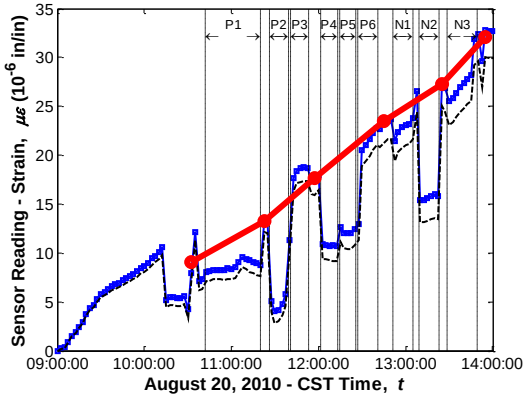

Figure 159
Sensor No. 44, Location G3S23, Support Bottom Vibrating wire gauge)

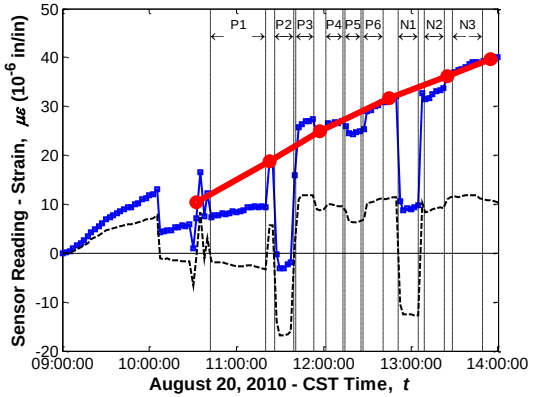

Figure 160
Sensor No. 45, Location G5S24, Support Bottom (Strandmeter)

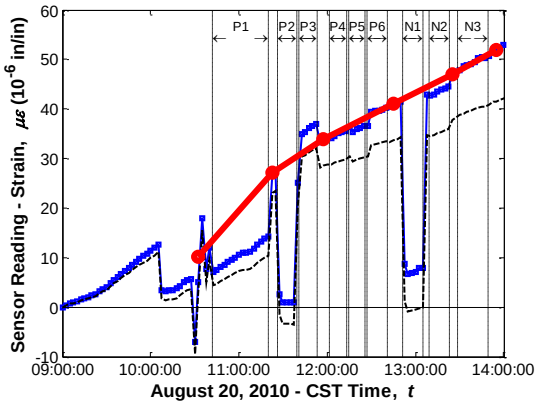

Figure 161
Sensor No. 46, Location G5S24, Support Bottom (Strandmeter)

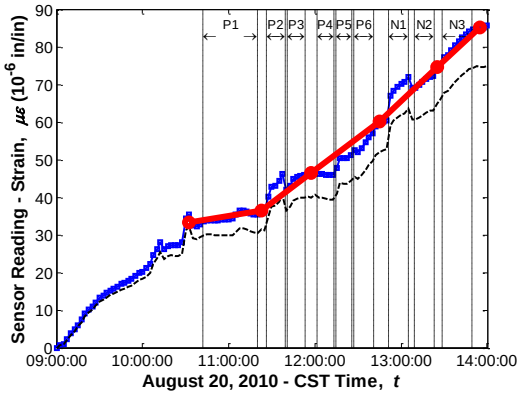

Figure 162
Sensor No. 47, Location G5S24, Support Top (Sisterbar)

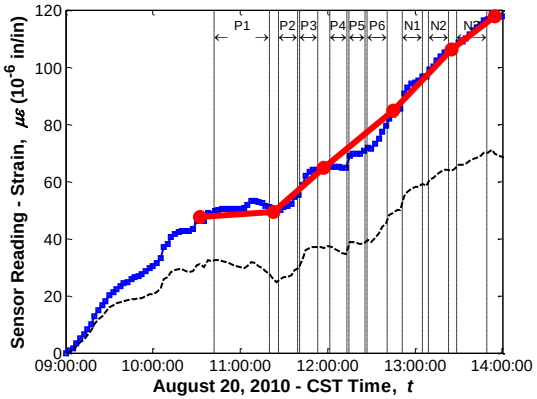

Figure 163
Sensor No. 48, Location G4S24, Support Top (Strandmeter)

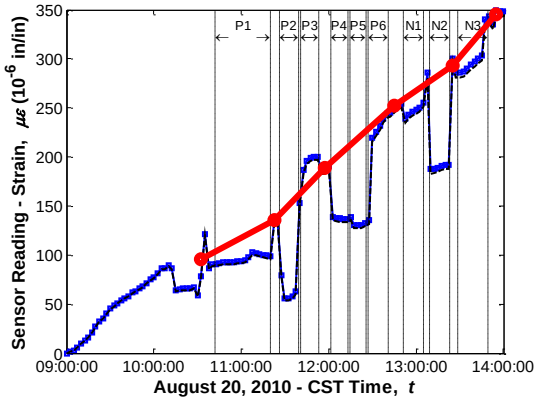

Figure 164
Sensor No. 49, Location G3S24, Support Bottom (Strandmeter)

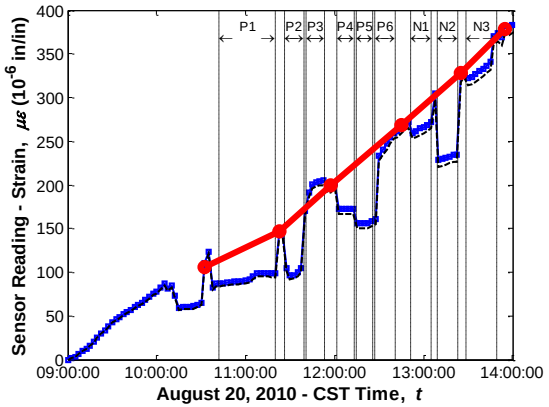

Figure 165
Sensor No. 50, Location G3S23, Support Bottom (Strandmeter)

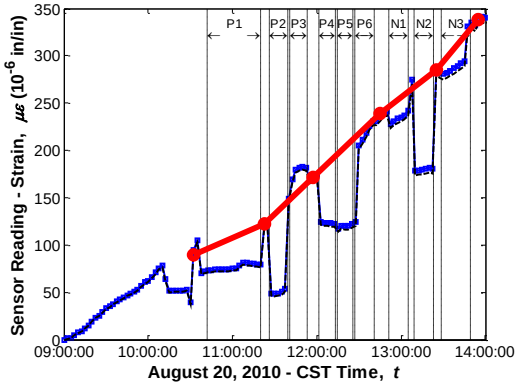

Figure 166
Sensor No. 51, Location G3S23, Support Bottom (Strandmeter)

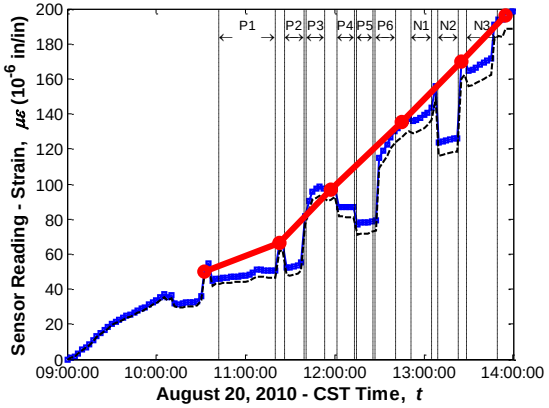

Figure 167
Sensor No. 52, Location G3S24, Support Bottom (Strandmeter)

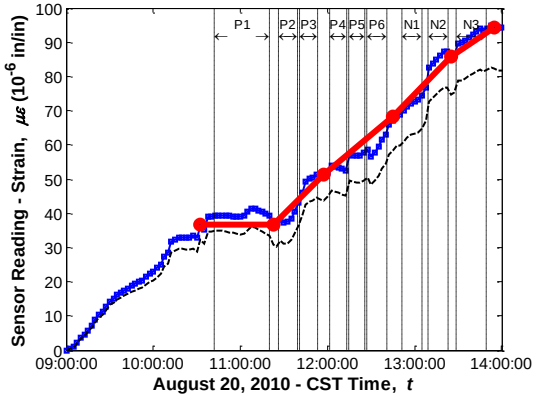

Figure 168
Sensor No. 53, Location G3S24, Support Top (Sisterbar)

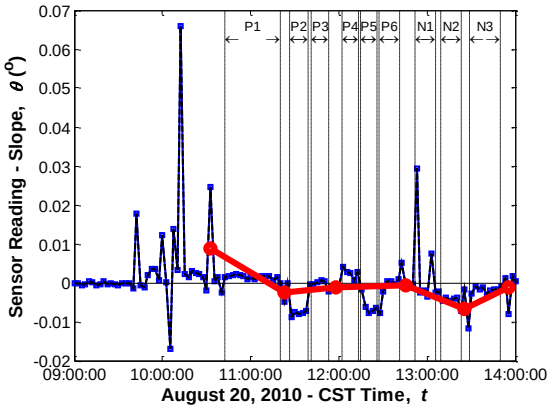

Figure 169
Sensor No. 55, Location G3S24, Support
(Tiltmeter)

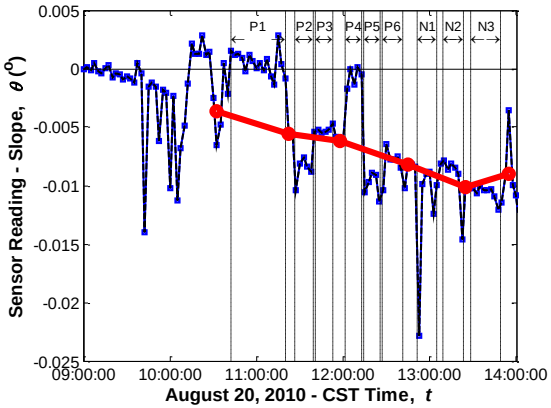

Figure 170
Sensor No. 56, Location G3S23, Support
(Tiltmeter)

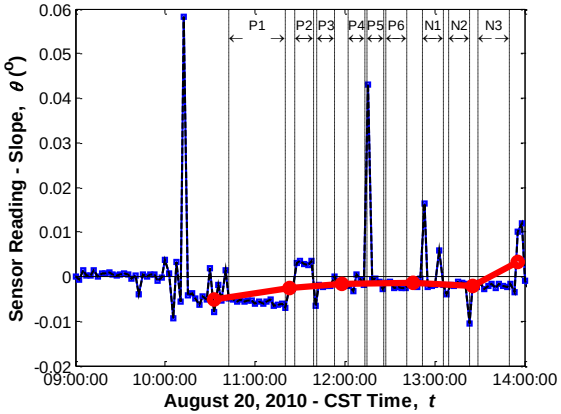

Figure 171
Sensor No. 57, Location G5S23, Support
(Tiltmeter)

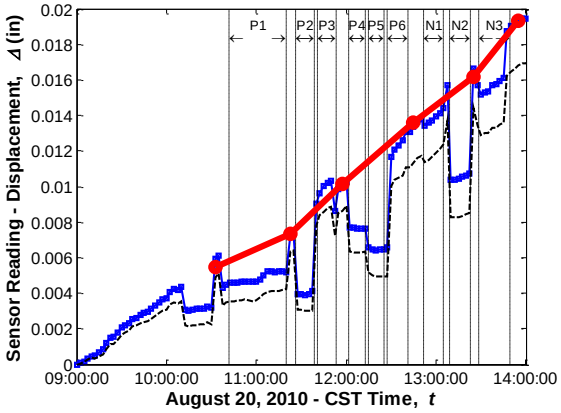

Figure 172
Sensor No. 58, Location G3, End Connection
(Displacement meter)

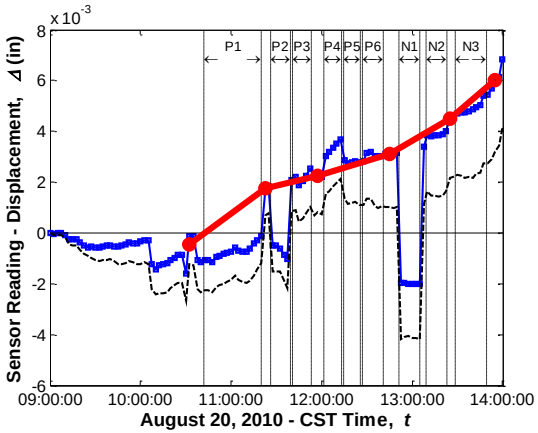

Figure 173
Sensor No. 59, Location G5, End Connection (Displacement meter)

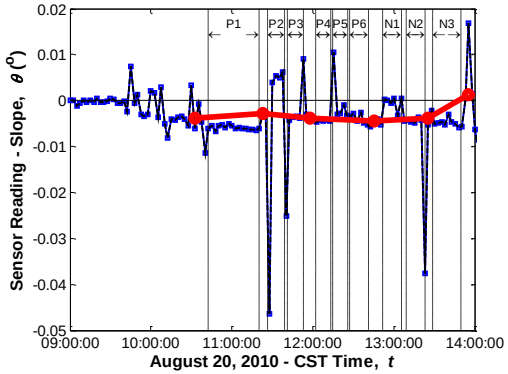

Figure 174
Sensor No. 60, Location G5S24, Support (Tiltmeter)

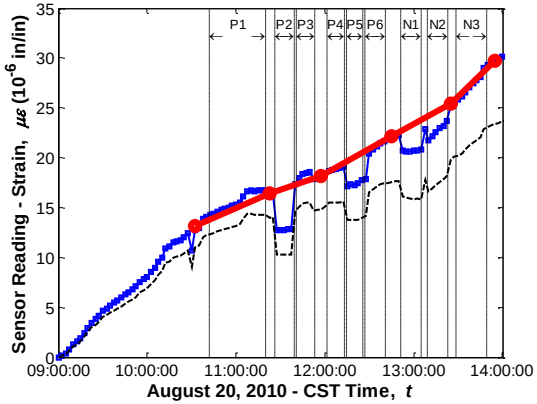

Figure 175
Sensor No. 65, Location G5S24, Midspan Top (Vibrating wire gauge)

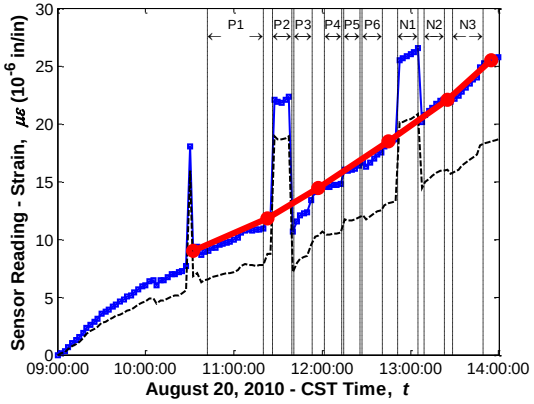

Figure 176
Sensor No. 66, Location G5S24, Midspan Middle (Vibrating wire gauge)

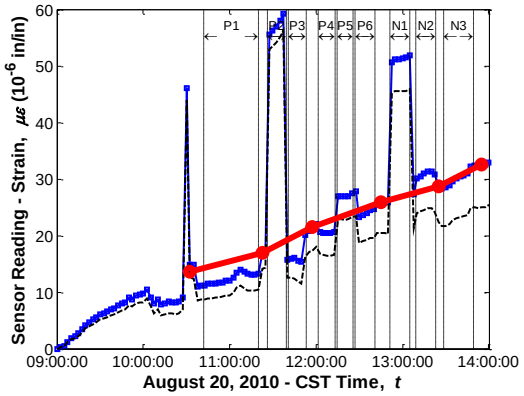

Figure 177
Sensor No. 67, Location G5S24, Midspan Bottom (Vibrating wire gauge)

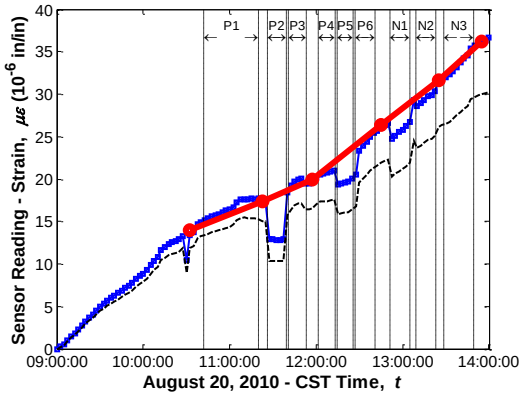

Figure 178
Sensor No. 68, Location G5S24, Midspan Top (Sisterbar)

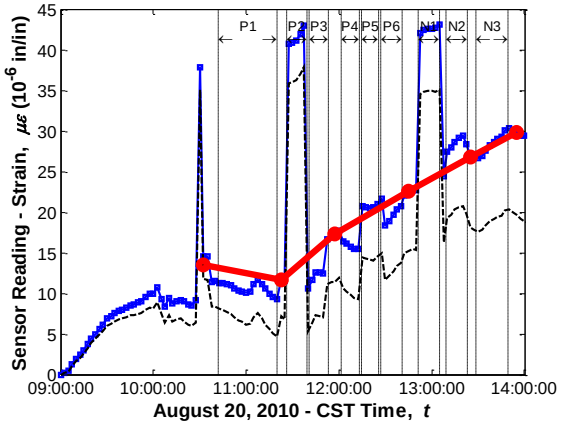

Figure 179
Sensor No. 69, Location G5S24, Midspan Bottom (Sisterbar)

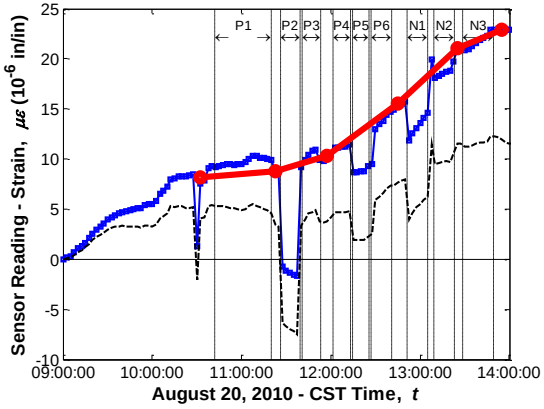

Figure 180
Sensor No. 70, Location G5S24, Midspan Deck (Sisterbar)

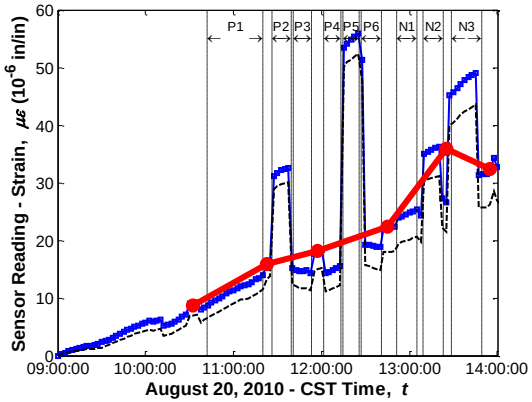

Figure 181
Sensor No. 71, Location G1S24 Midspan Bottom (Vibrating wire gauge)

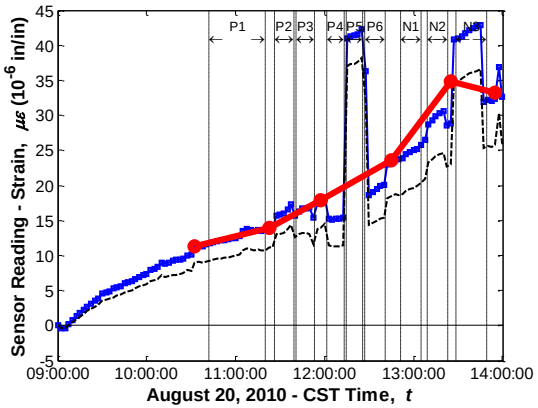

Figure 182
Sensor No. 72, Location G2S24 Midspan Bottom (Vibrating wire gauge)

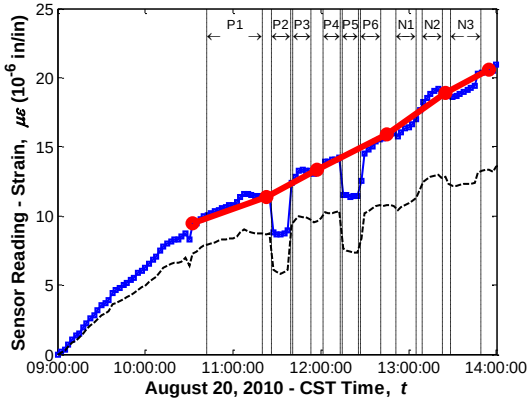

Figure 183
Sensor No. 81, Location G3S24, Midspan Top (Vibrating wire gauge)

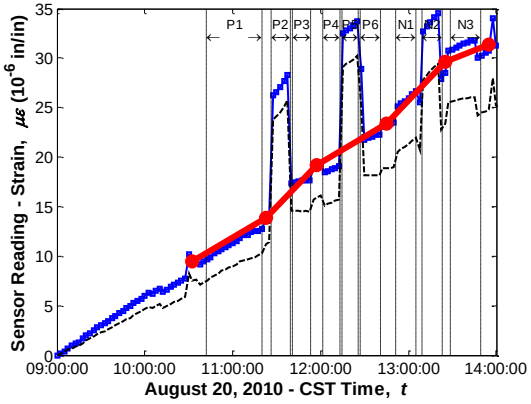

Figure 184
Sensor No. 82, Location G3S24, Midspan Middle (Vibrating wire gauge)

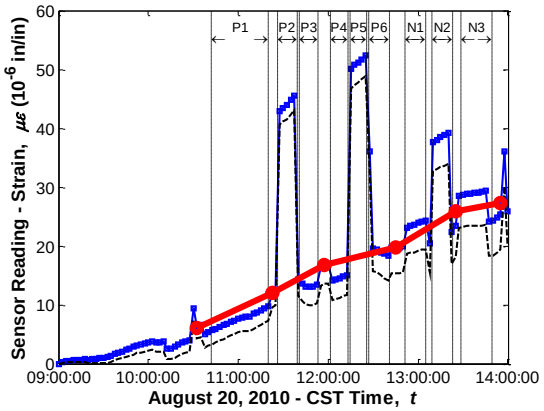

Figure 185
Sensor No. 83, Location G3S24, Midspan Bottom (Vibrating wire gauge)

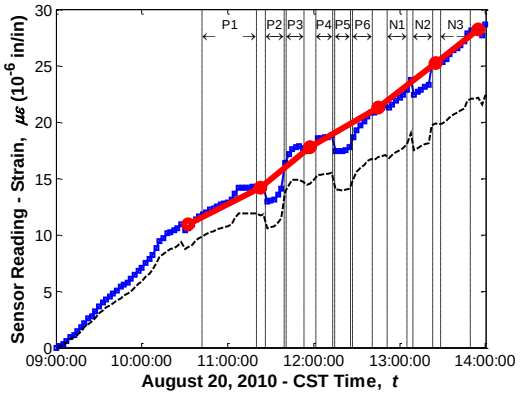

Figure 186
Sensor No. 84, Location G4S24, Midspan Top (Vibrating wire gauge)

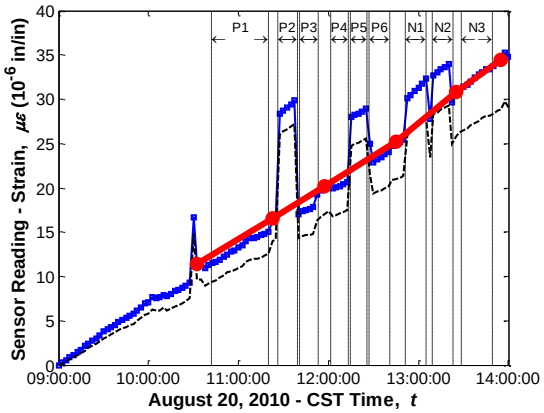

Figure 187
Sensor No. 85, Location G4S24, Midspan Middle (Vibrating wire gauge)

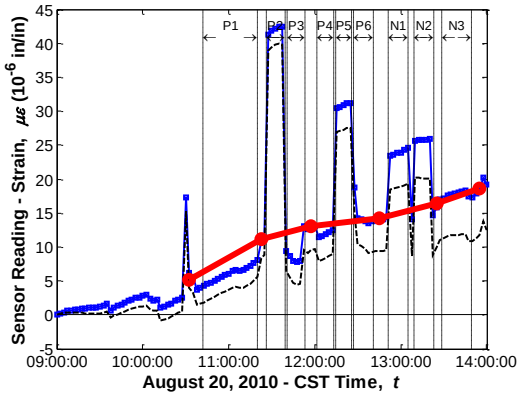

Figure 188
Sensor No. 86, Location G4S24, Midspan Bottom (Vibrating wire gauge)

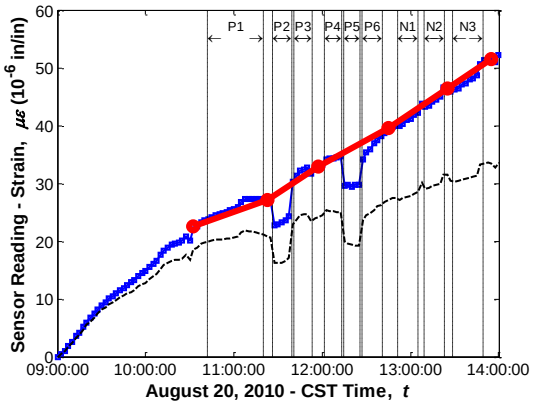

Figure 189
Sensor No. 87, Location G3S24, Midspan Top
(Strandmeter)

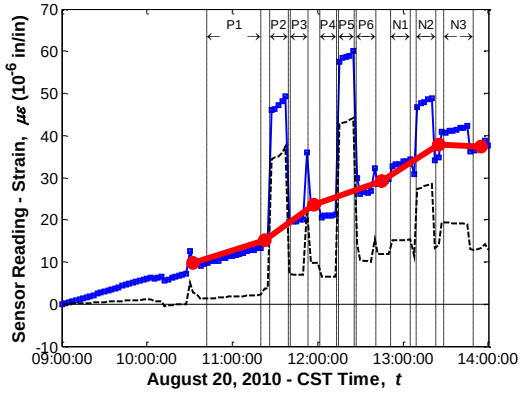

Figure 190
Sensor No. 88, Location G3S24, Midspan Bottom
(Strandmeter)

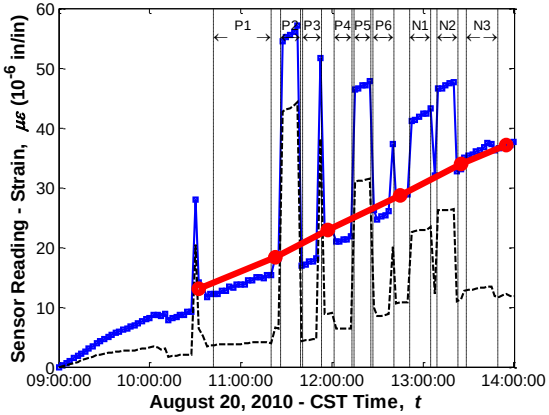

Figure 191
Sensor No. 89, Location G4S24, Midspan Bottom
(Strandmeter)

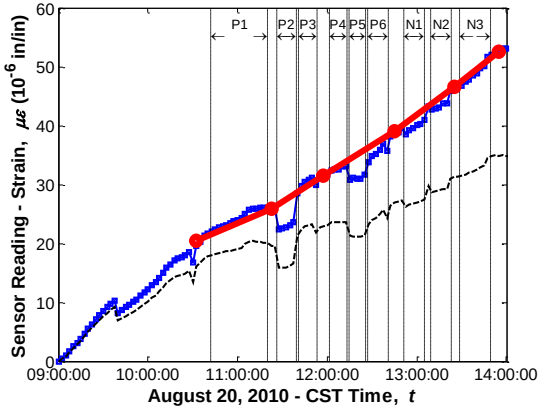

Figure 192
Sensor No. 90, Location G4S24, Midspan Top
(Strandmeter)

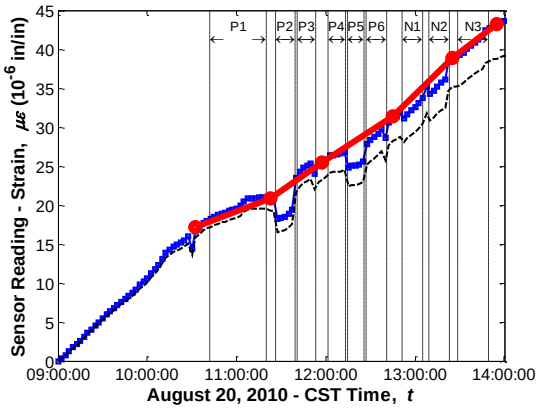

Figure 193
Sensor No. 91, Location G4S24, Midspan Top (Sisterbar)

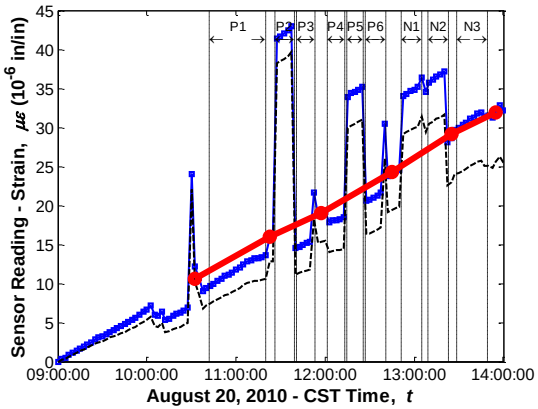

Figure 194
Sensor No. 92, Location G4S24, Midspan Bottom (Sisterbar)

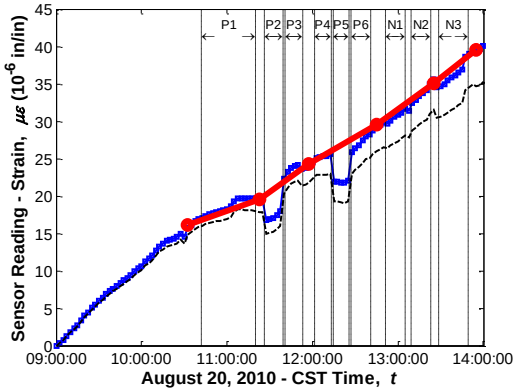

Figure 195
Sensor No. 93, Location G3S24, Midspan Top (Sisterbar)

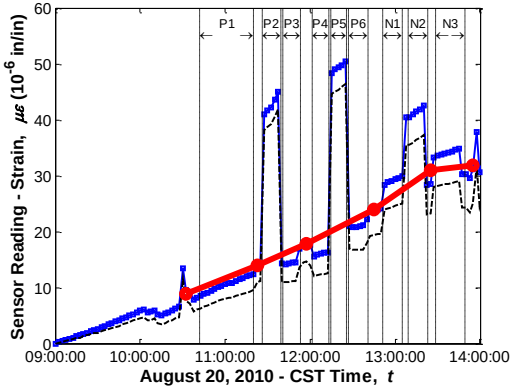

Figure 196
Sensor No. 94, Location G3S24, Midspan Bottom (Sisterbar)

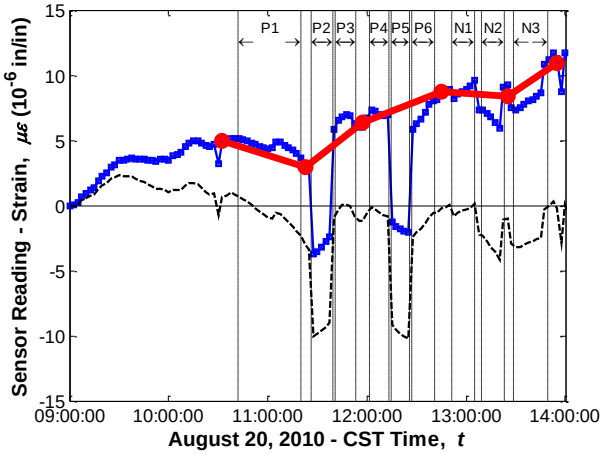

Figure 197
Sensor No. 95, Location G3S24, Midspan Deck (Sisterbar)

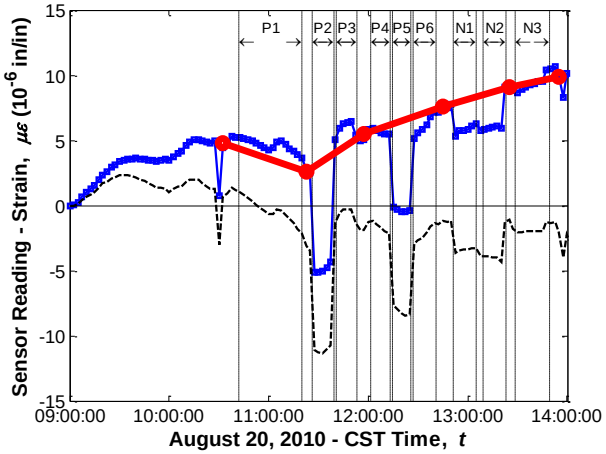

Figure 198
Sensor No. 96, Location G4S24, Midspan Deck (Sisterbar)

APPENDIX F

Element Types Used in Finite Element Analyses

This appendix describes the finite element types that were utilized in building the finite element models described in the "Finite Element Models" section of the report. Two categories of finite elements were used since ANSYS uses different elements for different physical environments. The first group of elements was used to perform thermal analyses, while the second group of elements was used to perform the stress analyses. A couple field analysis stores the results from the former (thermal analysis), which are then imposed of the model that performs the latter (stress analysis).

Elements used in Thermal Analyses

SOLID5. The SOLID5 is a 3D eight node element with up to six degrees of freedom in each node. The element has the thermal and structural field capability with limiting coupling. The geometry, node locations, and the co-ordinate system of this element are shown in Figure 199.

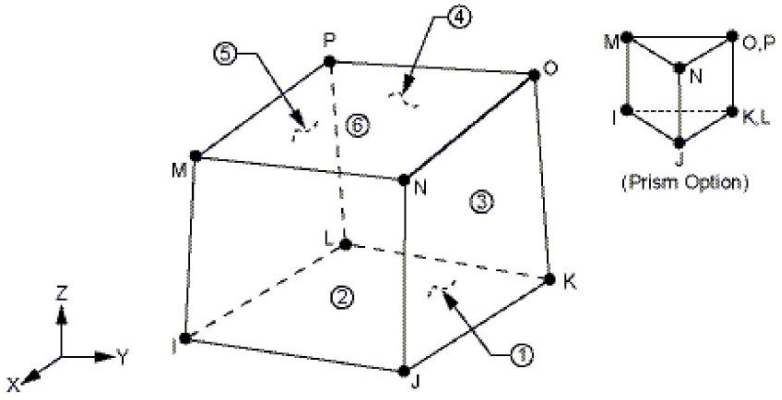

Figure 199
Geometry, node location, and coordinate for SOLID5 element

This element was used to model the concrete in the thermal physics analysis. Temperature was applied at the selected nodes as a body force. ANSYS solves for the temperature and provides the solution as temperature degrees of freedom at each node. This temperature was stored in the results file, which was then called at later stage to couple the analysis.

LINK68. The LINK68 is a 3-D uniaxial element with two degrees of freedom at each node. The element has capabilities to conduct heat and electrical current between its nodes.

The geometry, node locations, and coordinate systems for this element are shown in Figure 200.

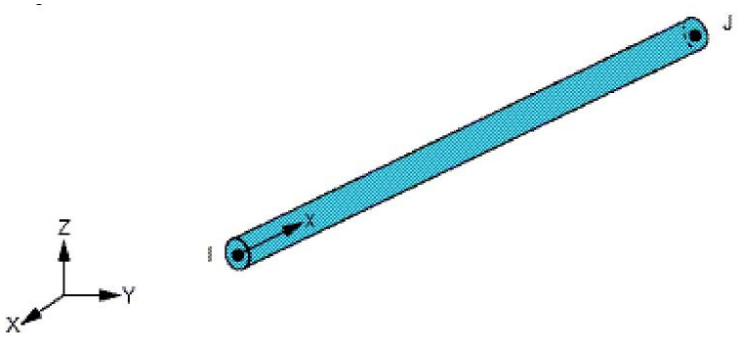

Figure 200
Geometry, node location, and coordinate system for LINK68

This element is defined by two nodes, the cross sectional area and the material properties. LINK68 was used to model the prestressing strands and the hairpin bar in the thermal physics analysis. The element solves for the temperature and gives solution as nodal temperature, which is stored as a results file for being used in the subsequent physics environment.

Elements used in Stress Analyses

SOLID65. The SOLID65 is a 3-D structural solid element especially designed for modeling concrete. This element has eight nodes with three translational degrees of freedom at each node. The element is capable of cracking in tension and crushing under compression. This element is used to model the concrete in structural physics environment. The most important features of this element are that it can handle the nonlinear material properties. Thus, it is capable to model cracking, crushing, plastic deformation and creep. The geometry, nodal locations, and the coordinate system for this element are shown in Figure 201.

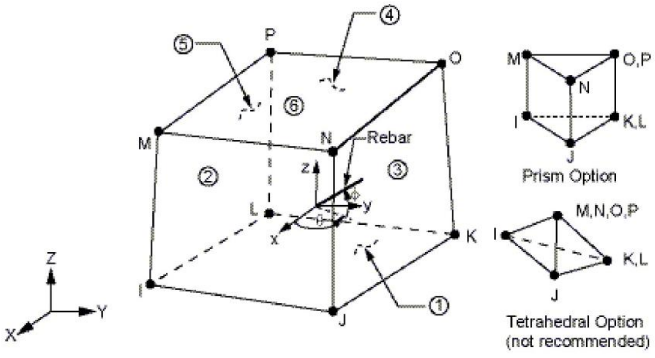

Figure 201
Geometry, node location, and coordinate system for SOLID65

LINK8. LINK8 is a 3-D spar element used to model trusses, cables, links, springs, etc. It has two nodes, and each node has three translational degrees of freedom. It is a uniaxial tension compression element thus no bending is considered. The element is defined by two nodes, a cross sectional area, and other material properties. This element is used to model the prestressing strands and hairpin bars in the structural physics environment. The prestressing is applied by incorporating the initial strain. The geometry, nodal locations, and the coordinate system of this element are shown in Figure 202.

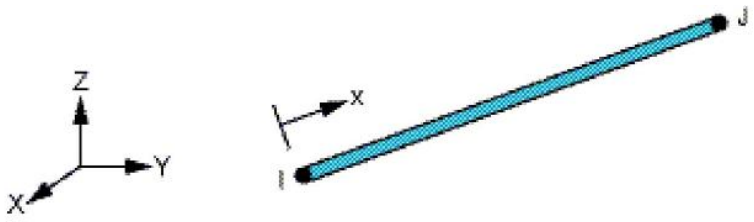

Figure 202
Geometry, node location, and coordinate system for LINK8

SOLID45. SOLID45 is a 3-D structural solid used to model solid structures. This solid has 8-nodes with each node having three translational degrees of freedom in the x, y, and z direction. This element has large deflection and strain capabilities, for which it has been used to model the bearing pads in these analyses. The bearing pad consists of an alternate layer of steel and rubber; the rubber is used for energy dissipation and the steel layer is being used for vertical stiffness. The equivalent stiffness properties are used as an input material parameter to model the bearing pads. The geometry, nodal locations, and the coordinate system for this element are shown in Figure 203.

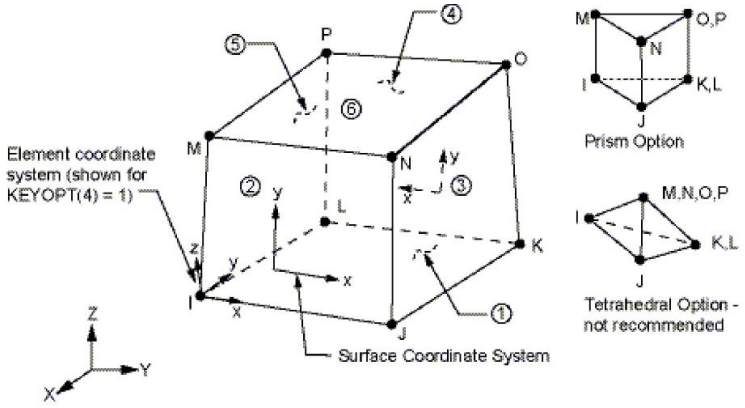

Figure 203
Geometry, node location, and coordinate system for SOLID45

CONTA178. To model the contact and sliding between two nodes of any elements, CONTA178 was used. This is a two-node element with three degrees of freedom at each

node in the x, y, and z directional translation. A 2-D axisymmetric problem can also be modeled with this element by constraining the translation in the z direction. The element is capable of supporting compression in the contact normal direction and Coulomb friction in the tangential direction. The initial gap can also be modeled with this element. The geometry, nodal locations, and the coordinate system for this element are shown in Figure 204.

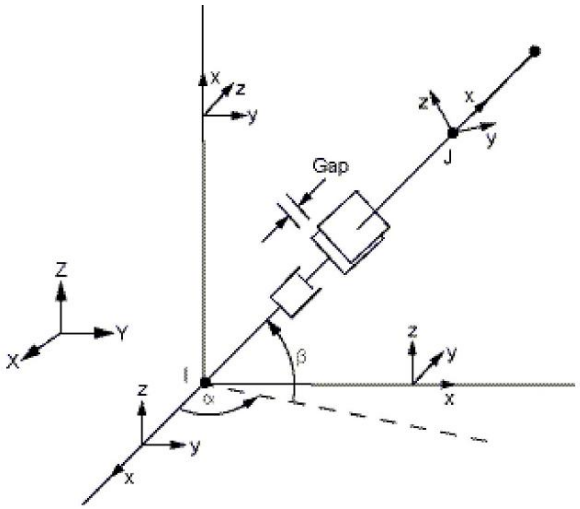

Figure 204
Geometry, node location, and coordinate system for CONTA178

In order to define this element, two nodes, initial gap size or interference, initial element status and two damping coefficients need to be defined. The orientation of the interface is defined by two ways: by the node locations or by the user defined normal direction. The KEYOPT feature is used to define the contact algorithm. A coefficient of friction is used as the only material property for this element. The diaphragm is poured after placing the girder over the bents; therefore, a cold joint developed between the girder and diaphragm interface. To model this contact, CONTA178 element was used in this study.

APPENDIX G

mRESTRAINT Parametric Study Results

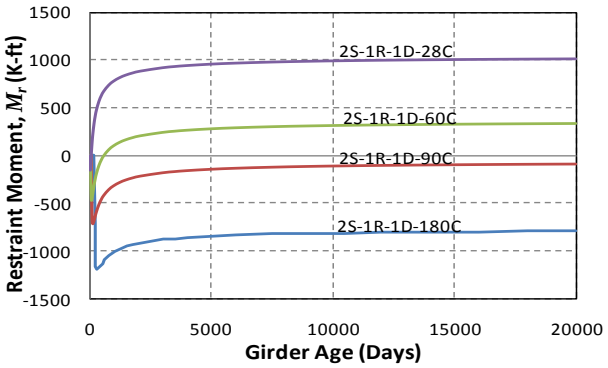

(a) $L_1 = L_2$ and $I_{dia} = I_g$

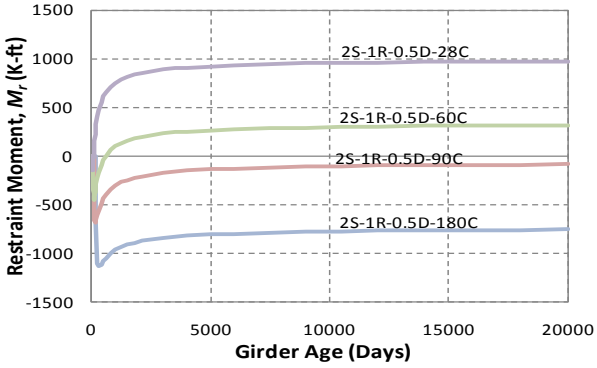

(b) $L_1 = L_2$ and $I_{dia} = 0.5*I_g$

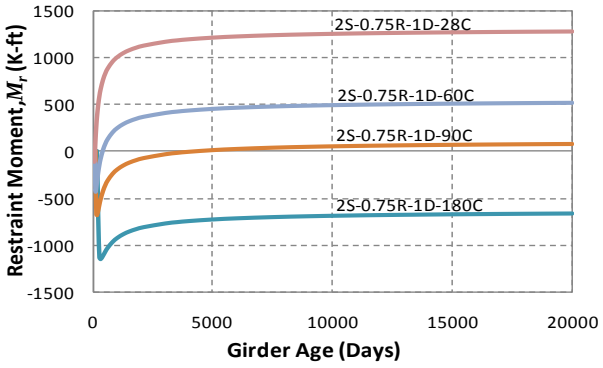

(c) $L_1 = 0.75*L_2$ and $I_{dia} = I_g$

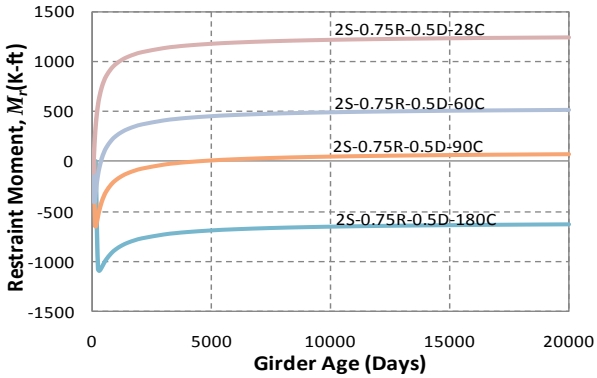

(d) $L_1 = 0.75*L_2$ and $I_{dia} = 0.5*I_g$

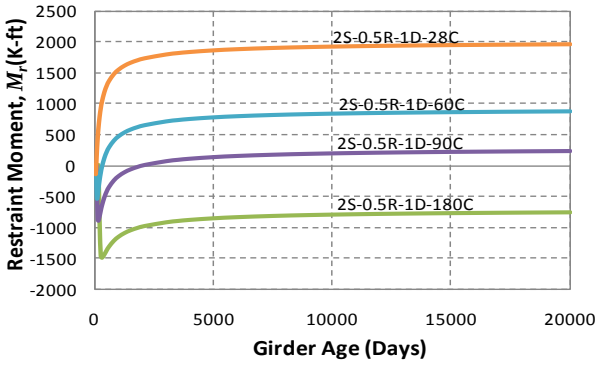

(e) $L_1 = 0.5*L_2$ and $I_{dia} = I_g$

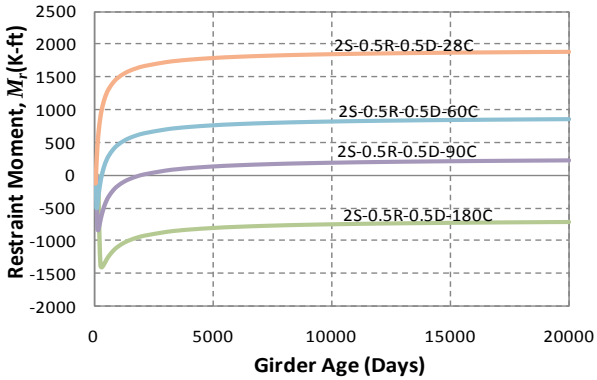

(f) $L_1 = 0.5*L_2$ and $I_{dia} = 0.5*I_g$

Figure 205
***M_r* estimates for two span cases**

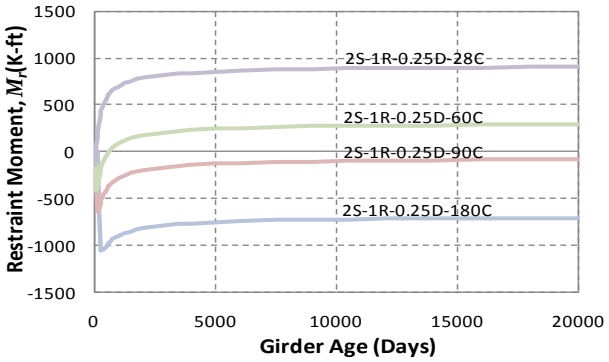

(a) $L_1 = L_2$ and $I_{dia} = 0.25*I_g$

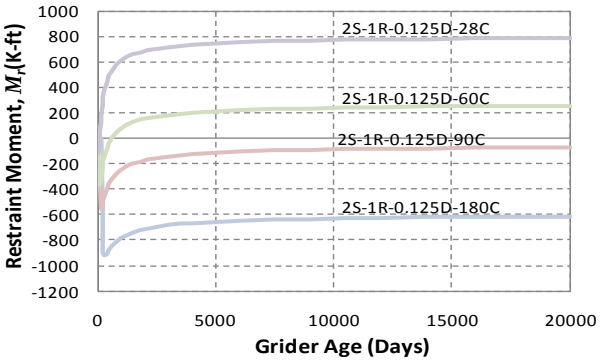

(b) $L_1 = L_2$ and $I_{dia} = 0.125*I_g$

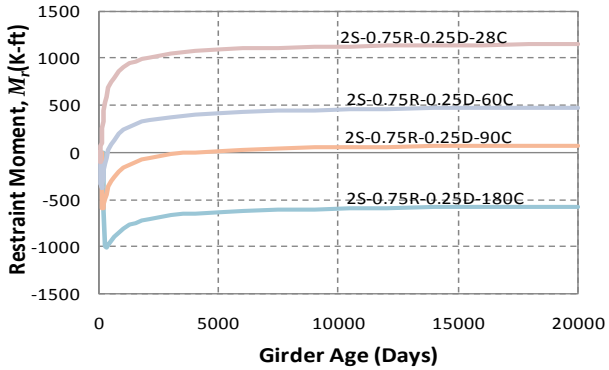

(c) $L_1 = 0.75*L_2$ and $I_{dia} = 0.25*I_g$

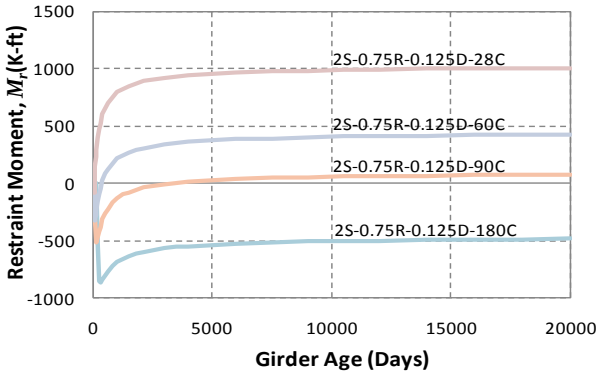

(d) $L_1 = 0.75*L_2$ and $I_{dia} = 0.125*I_g$

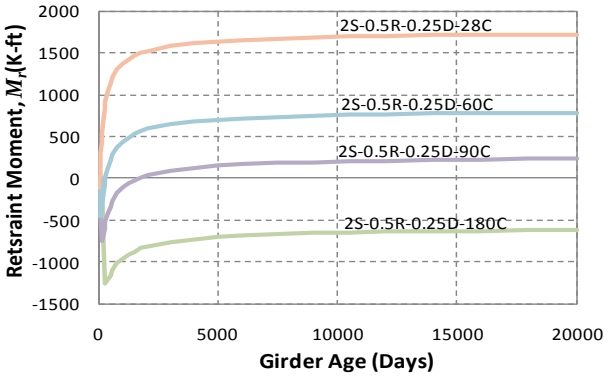

(e) $L_1 = 0.5*L_2$ and $I_{dia} = 0.25*I_g$

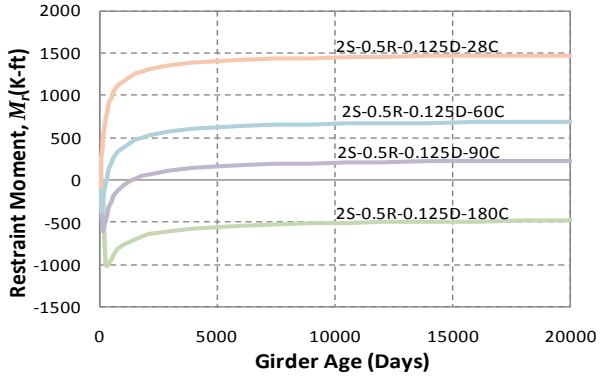

(f) $L_1 = 0.5*L_2$ and $I_{dia} = 0.125*I_g$

Figure 205
***M_r* estimates for two span cases (continued)**

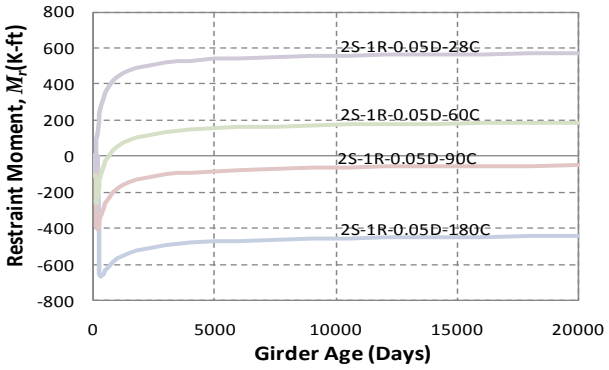

(a) $L_1 = L_2$ and $I_{dia} = 0.05*I_g$

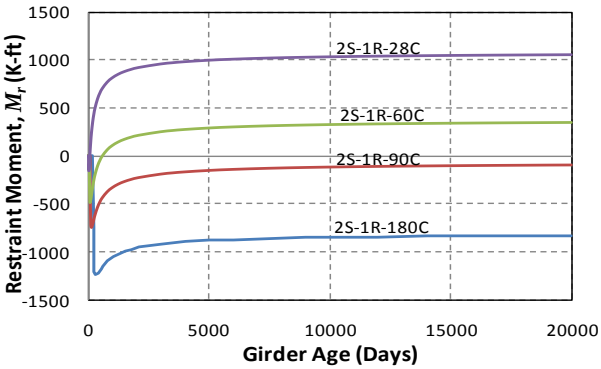

(b) $L_1 = L_2$ and $I_{dia} = 0$

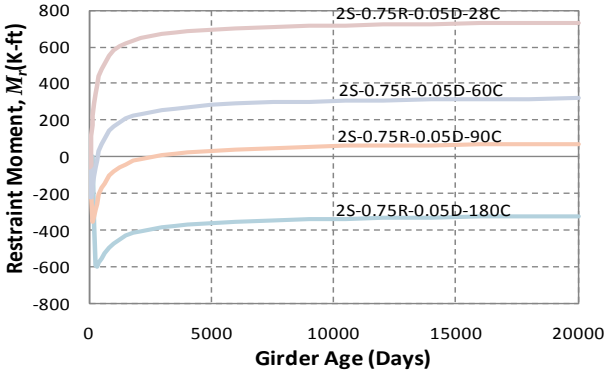

(c) $L_1 = 0.75*L_2$ and $I_{dia} = 0.05*I_g$

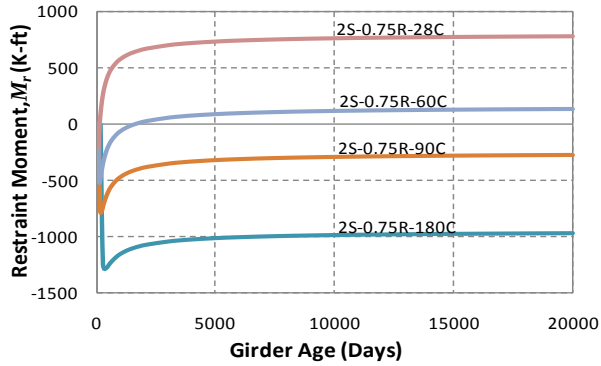

(d) $L_1 = 0.75*L_2$ and $I_{dia} = 0$

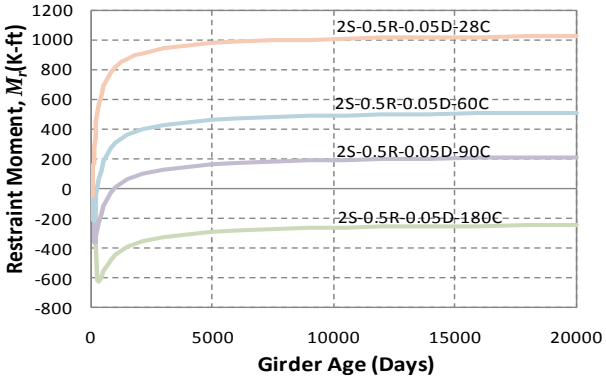

(e) $L_1 = 0.5*L_2$ and $I_{dia} = 0.05*I_g$

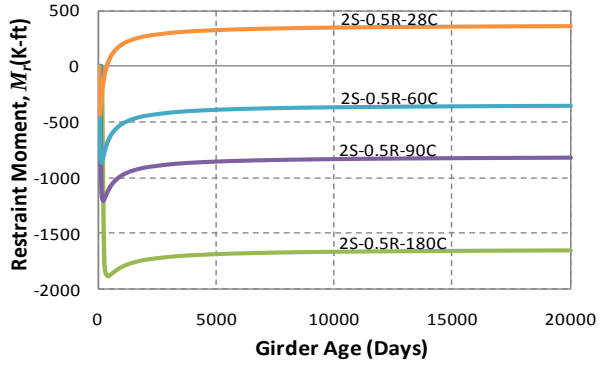

(f) $L_1 = 0.5*L_2$ and $I_{dia} = 0$

Figure 205
***M_r* estimates for two span cases (continued)**

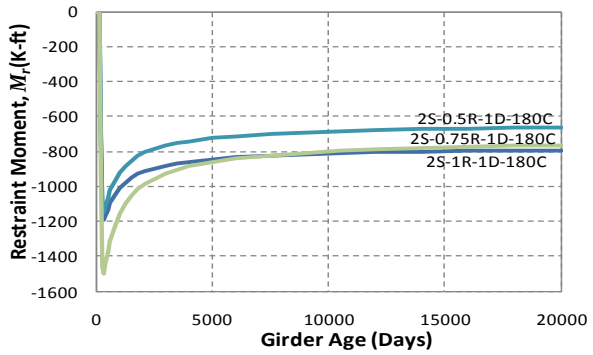

(a) Age = 180 days and $I_{dia} = I_g$

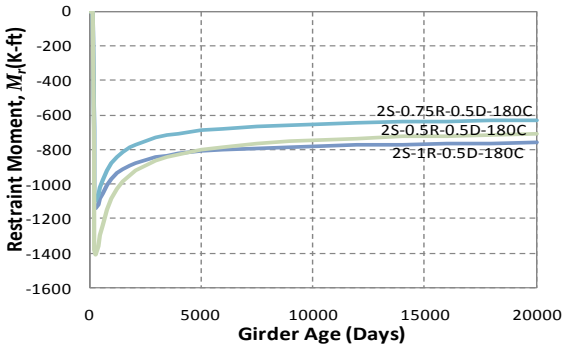

(b) Age = 180 days and $I_{dia} = 0.5*I_g$

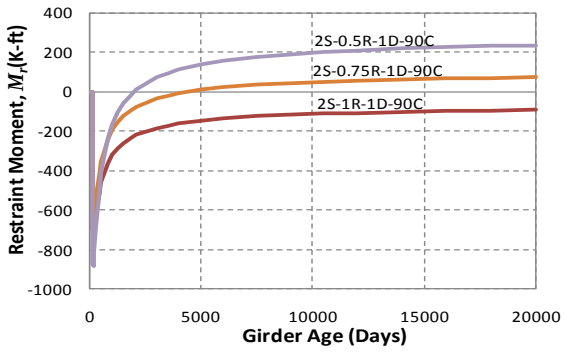

(c) Age = 90 days and $I_{dia} = I_g$

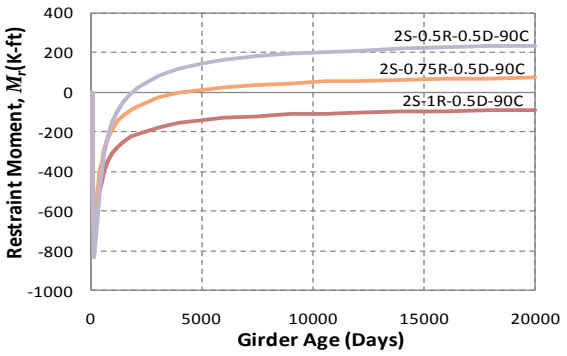

(d) Age = 90 days and $I_{dia} = 0.5*I_g$

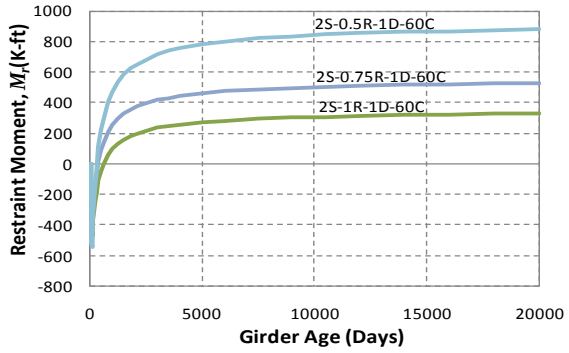

(e) Age = 60 days and $I_{dia} = I_g$

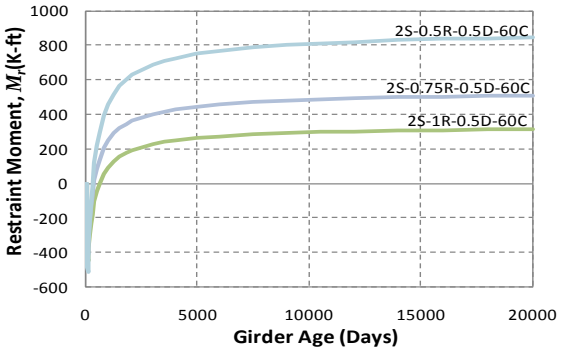

(f) Age = 60 days and $I_{dia} = 0.5*I_g$

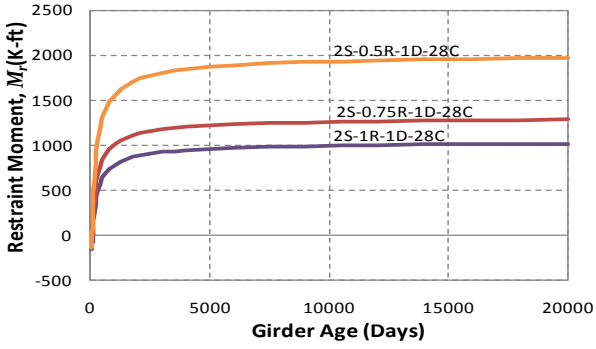

(g) Age = 28 days and $I_{dia} = I_g$

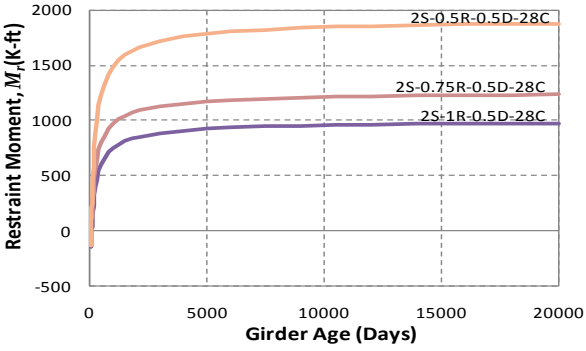

(h) Age = 28 days and $I_{dia} = 0.5*I_g$

Figure 205
***M_r* estimates for two span cases (continued)**

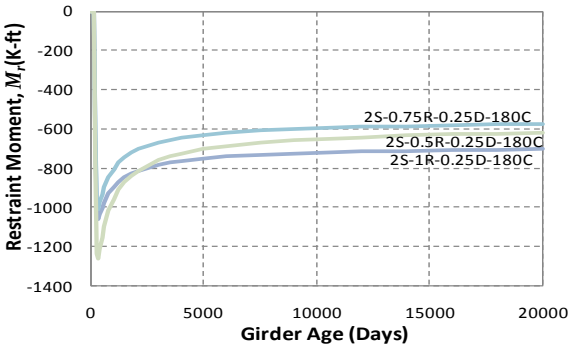

(a) Age = 180 days and $I_{dia} = 0.25*I_g$

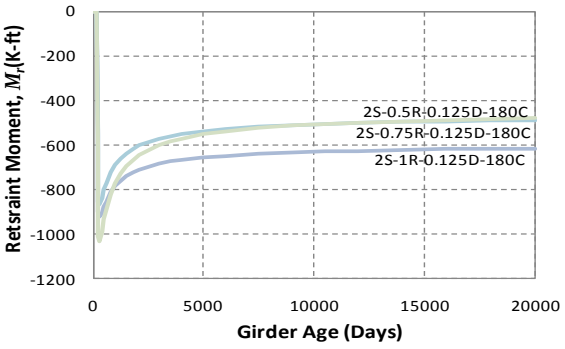

(a) Age = 180 days and $I_{dia} = 0.125*I_g$

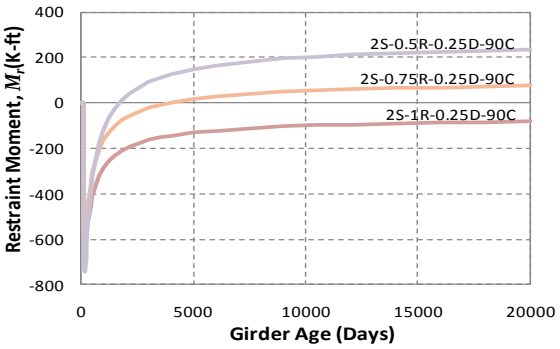

(b) Age = 90 days and $I_{dia} = 0.25*I_g$

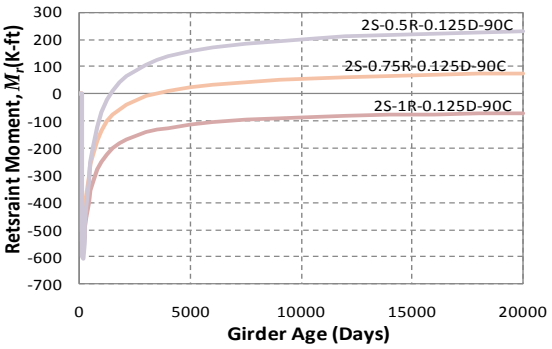

(b) Age = 90 days and $I_{dia} = 0.125*I_g$

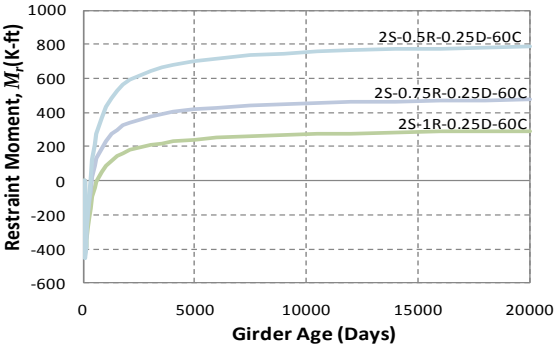

(c) Age = 60 days and $I_{dia} = 0.25*I_g$

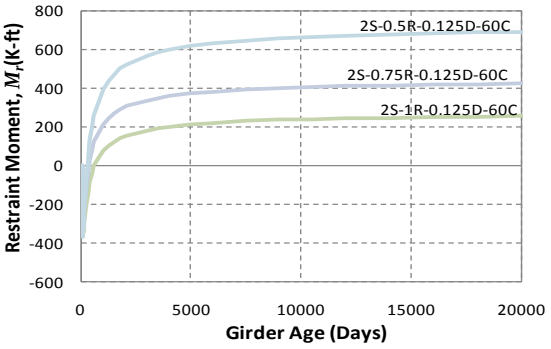

(c) Age = 60 days and $I_{dia} = 0.125*I_g$

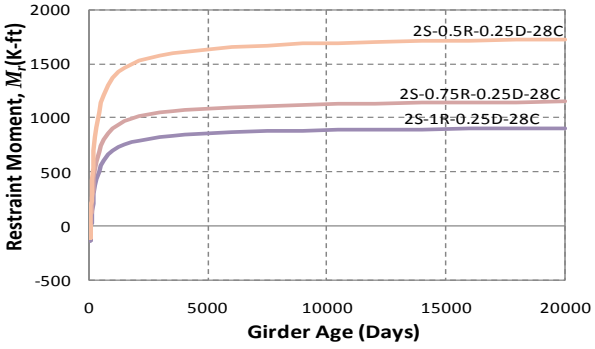

(d) Age = 28 days and $I_{dia} = 0.25*I_g$

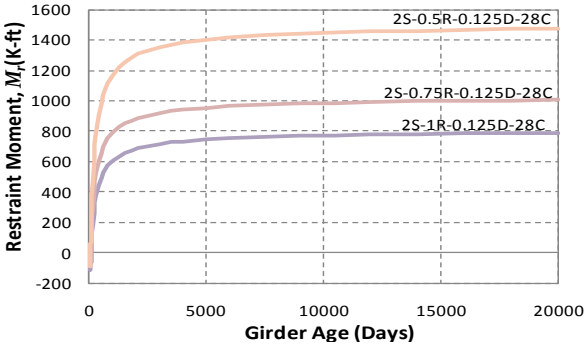

(d) Age = 28 days and $I_{dia} = 0.125*I_g$

Figure 205
***M_r* estimates for two span cases (continued)**

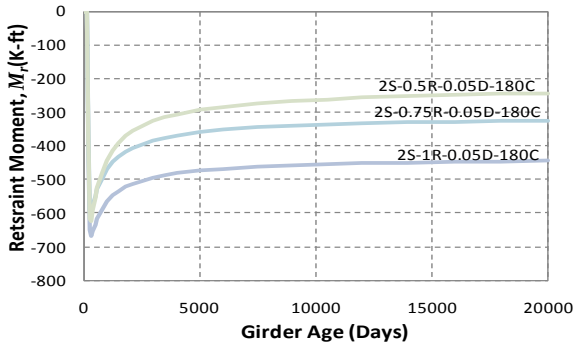

(a) Age = 180 days and $I_{dia} = 0.05I_g$

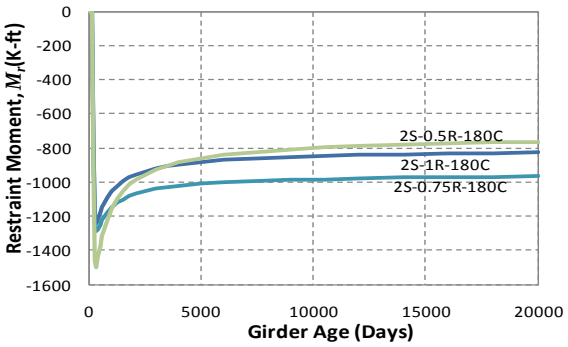

(a) Age = 180 days and $I_{dia} = 0$

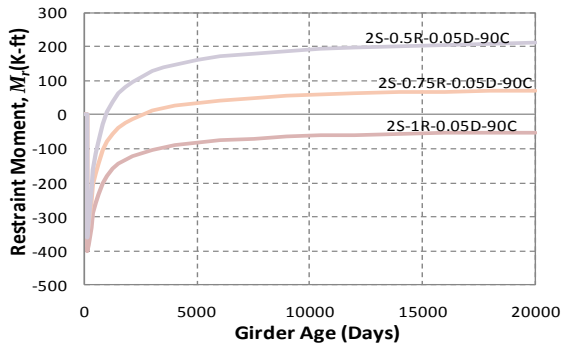

(b) Age = 90 days and $I_{dia} = 0.05I_g$

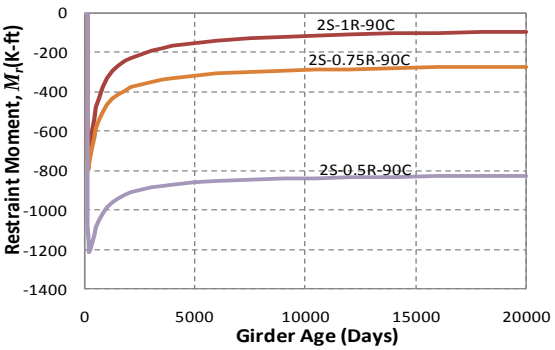

(b) Age = 90 days and $I_{dia} = 0$

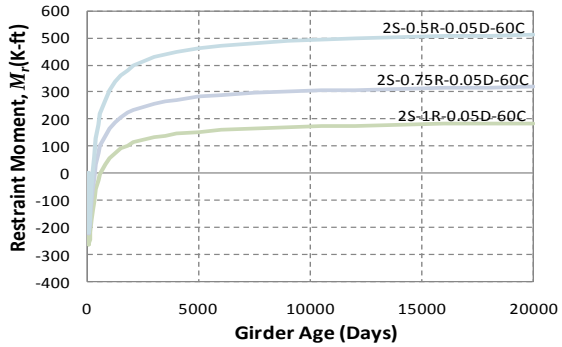

(c) Age = 60 days and $I_{dia} = 0.05I_g$

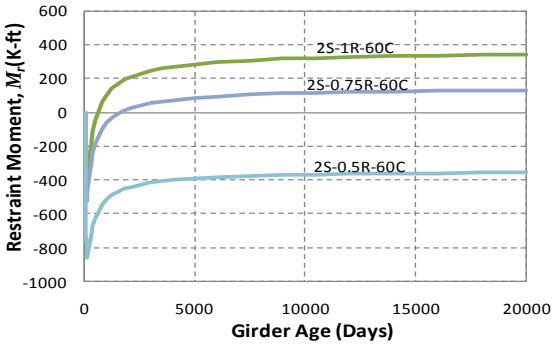

(c) Age = 60 days and $I_{dia} = 0$

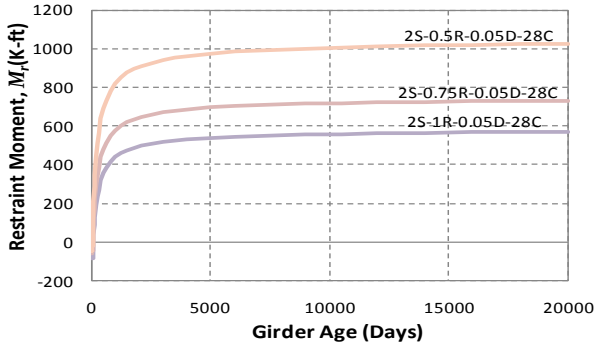

(d) Age = 28 days and $I_{dia} = 0.05I_g$

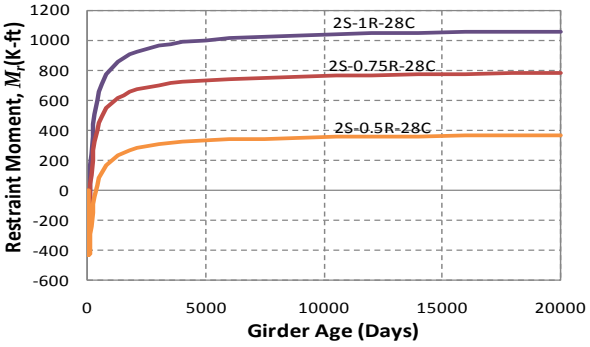

(d) Age = 28 days and $I_{dia} = 0$

Figure 205
***M_r* estimates for two span cases (continued)**

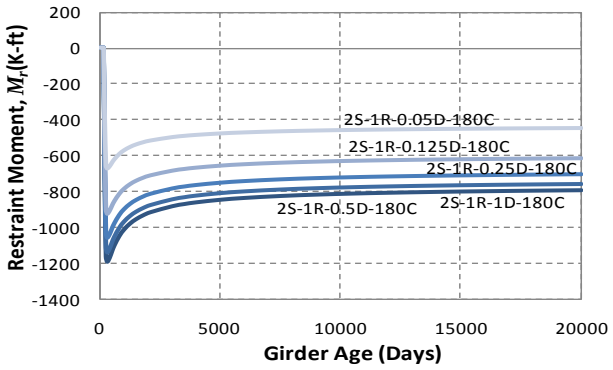

(a) $L_1 = L_2$ and Age = 180 days

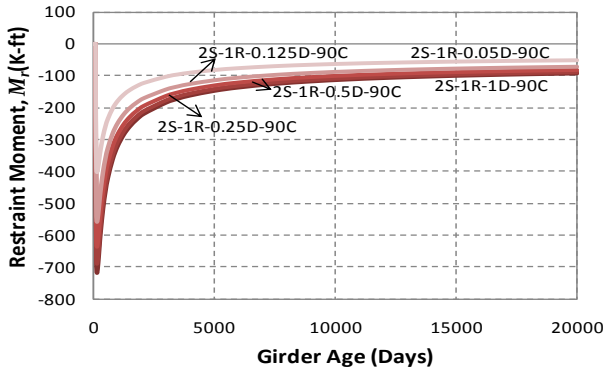

(a) $L_1 = L_2$ and Age = 90 days

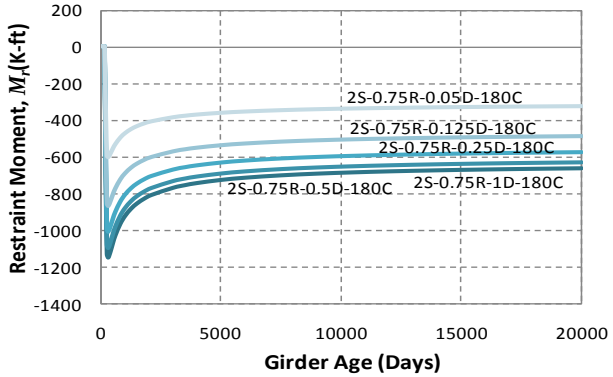

(b) $L_1 = 0.75*L_2$ and Age = 180 days

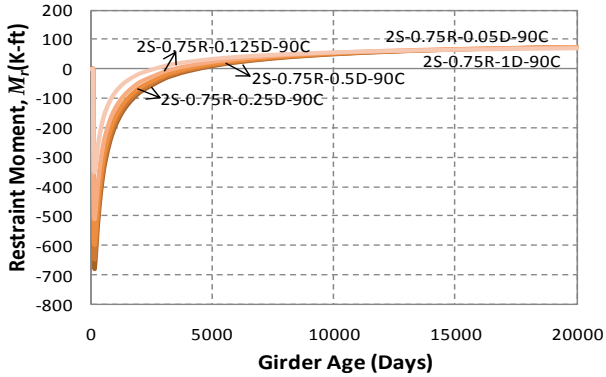

(b) $L_1 = 0.75*L_2$ and Age = 90 days

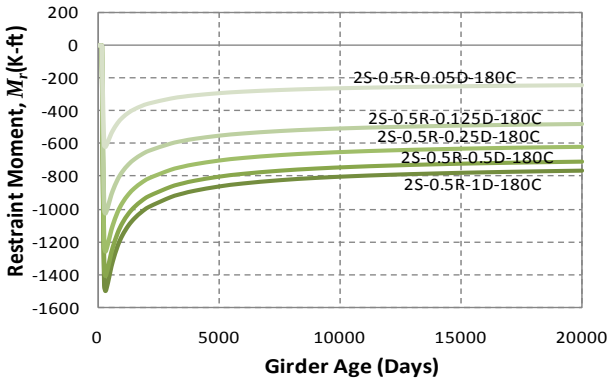

(c) $L_1 = 0.5*L_2$ and Age = 180 days

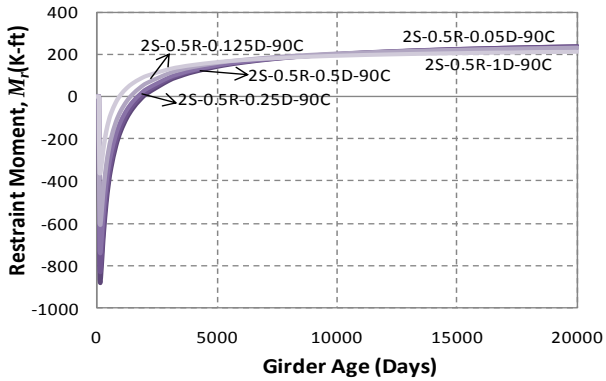

(c) $L_1 = 0.5*L_2$ and Age = 90 days

Figure 205
***M_r* estimates for two span cases (continued)**

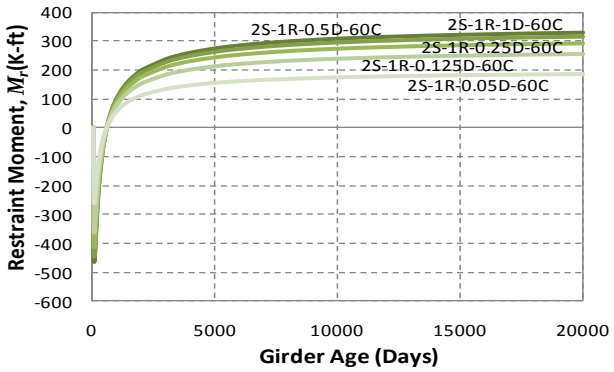

(a) $L_1 = L_2$ and Age = 60 days

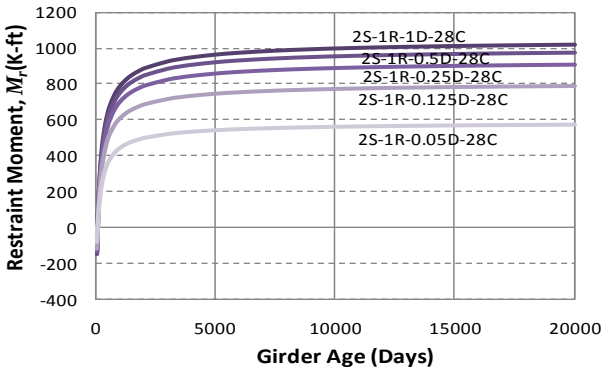

(a) $L_1 = L_2$ and Age = 28 days

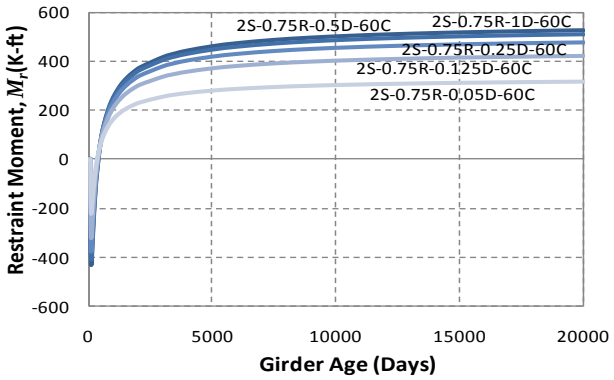

(b) $L_1 = 0.75*L_2$ and Age = 60 days

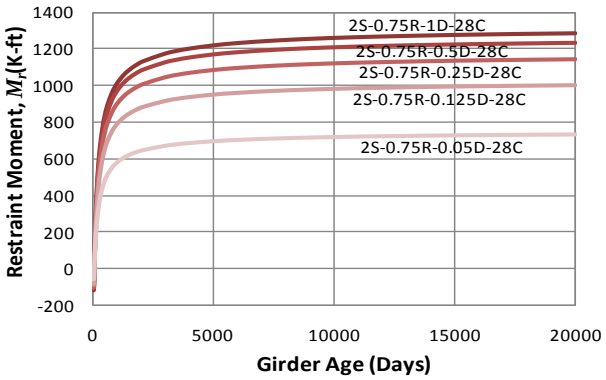

(b) $L_1 = 0.75*L_2$ and Age = 28 days

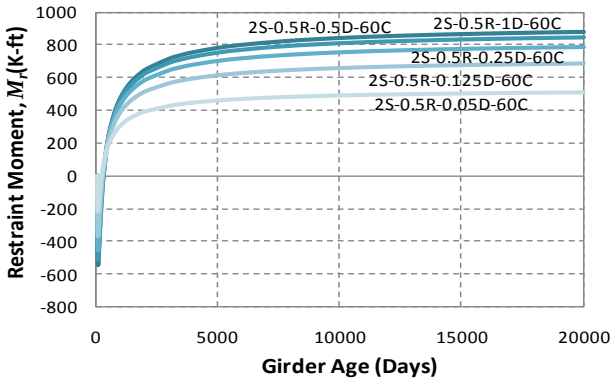

(c) $L_1 = 0.5*L_2$ and Age = 60 days

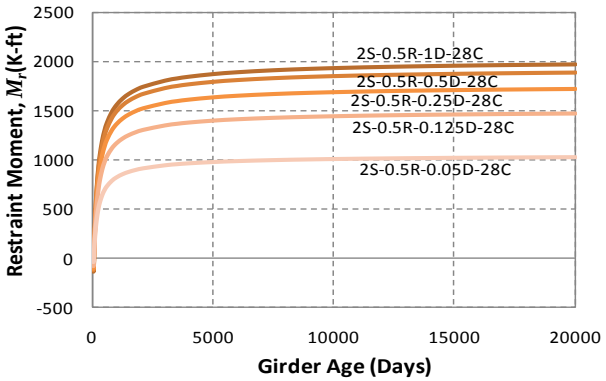

(c) $L_1 = 0.5*L_2$ and Age = 28 days

Figure 205
***M_r* estimates for two span cases (continued)**

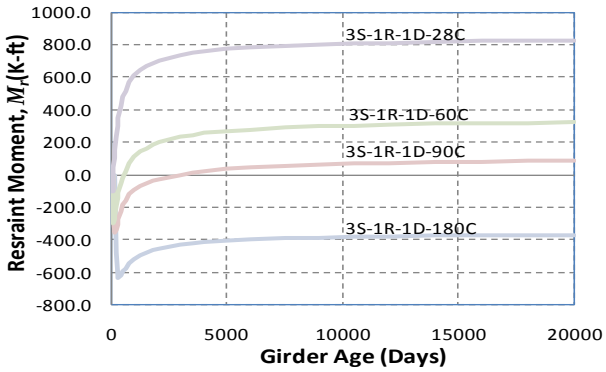

(a) $L_1 = L_2 = L_3$ and $I_{dia} = I_g$

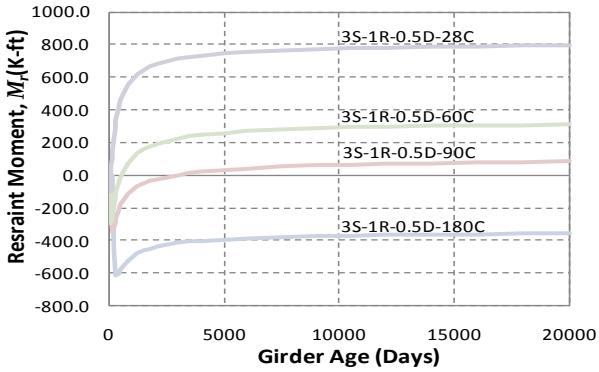

(a) $L_1 = L_2 = L_3$ and $I_{dia} = 0.5*I_g$

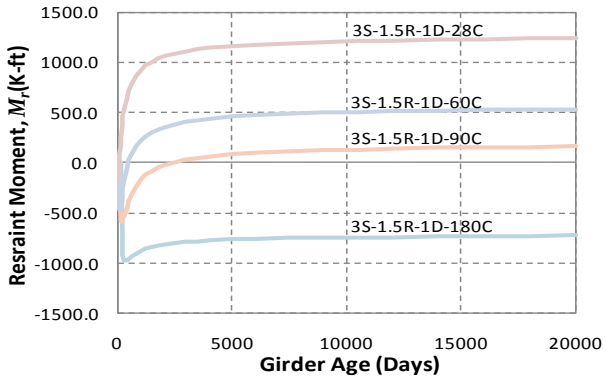

(b) $L_2 = 1.5*L_1 = 1.5*L_3$ and $I_{dia} = I_g$

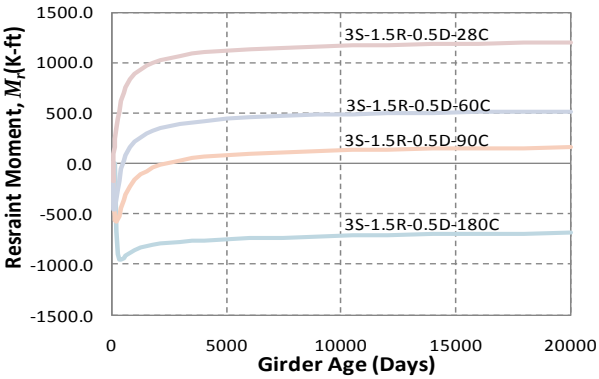

(b) $L_2 = 1.5*L_1 = 1.5*L_3$ and $I_{dia} = 0.5*I_g$

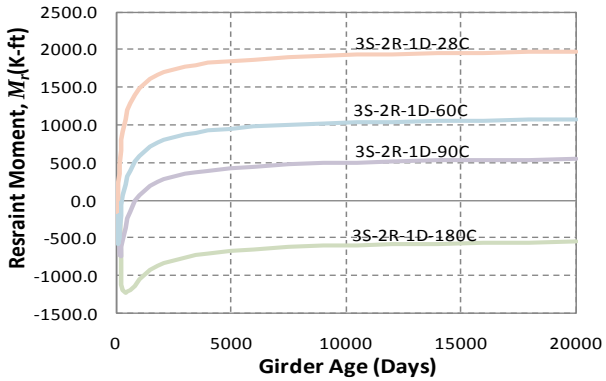

(c) $L_2 = 2*L_1 = 2*L_3$ and $I_{dia} = I_g$

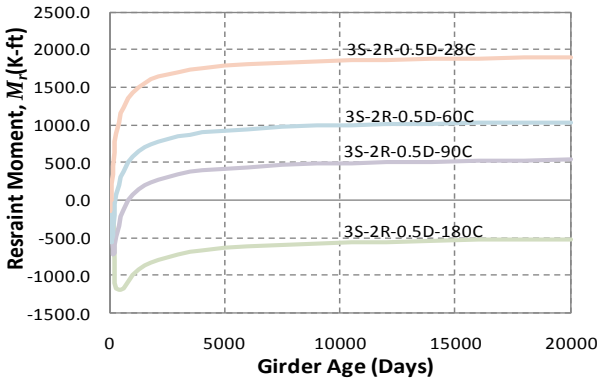

(c) $L_2 = 2*L_1 = 2*L_3$ and $I_{dia} = 0.5*I_g$

Figure 206
***M_r* estimates for three span cases**

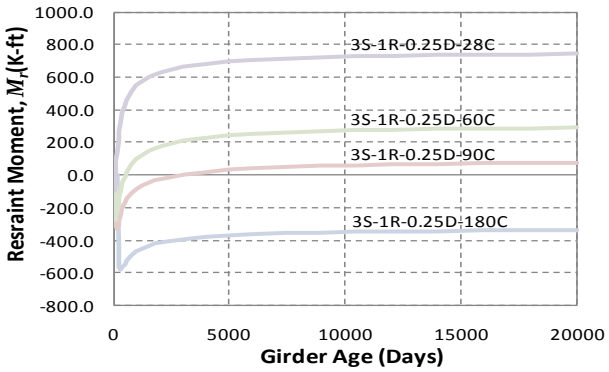

(a) $L_1 = L_2 = L_3$ and $I_{dia} = 0.25*I_g$

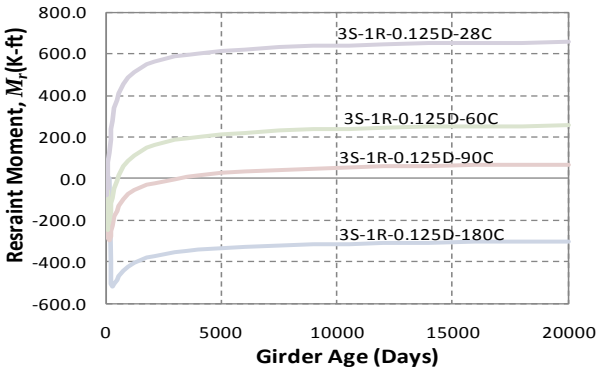

(a) $L_1 = L_2 = L_3$ and $I_{dia} = 0.125*I_g$

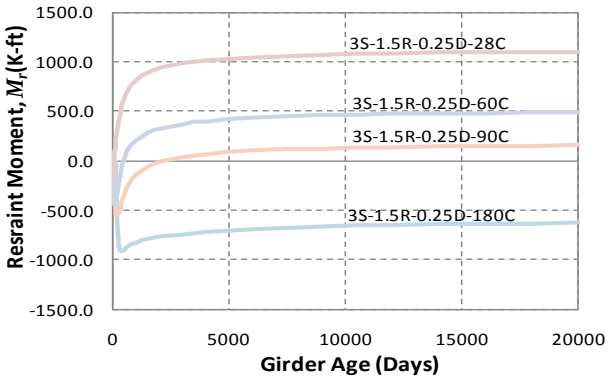

(b) $L_2 = 1.5*L_1 = 1.5*L_3$ and $I_{dia} = 0.25*I_g$

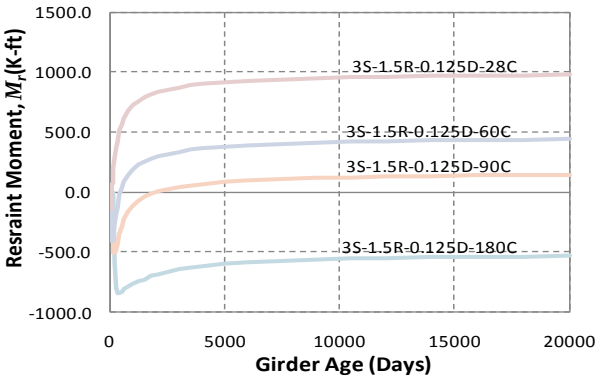

(b) $L_2 = 1.5*L_1 = 1.5*L_3$ and $I_{dia} = 0.125*I_g$

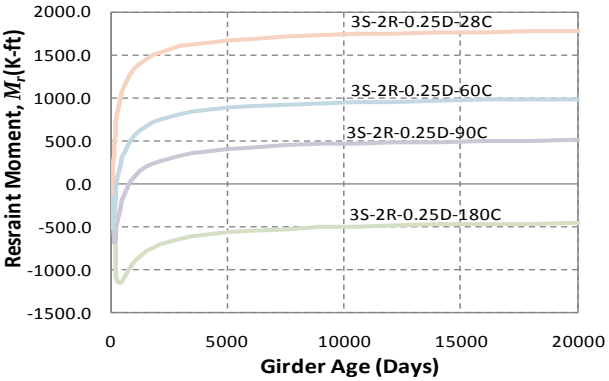

(c) $L_2 = 2*L_1 = 2*L_3$ and $I_{dia} = 0.25*I_g$

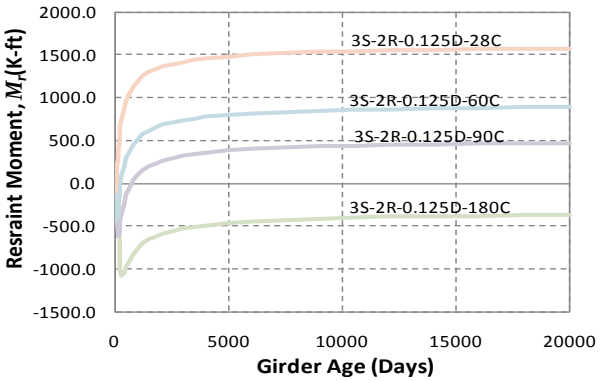

(c) $L_2 = 2*L_1 = 2*L_3$ and $I_{dia} = 0.125*I_g$

Figure 206
***M_r* estimates for three span cases (continued)**

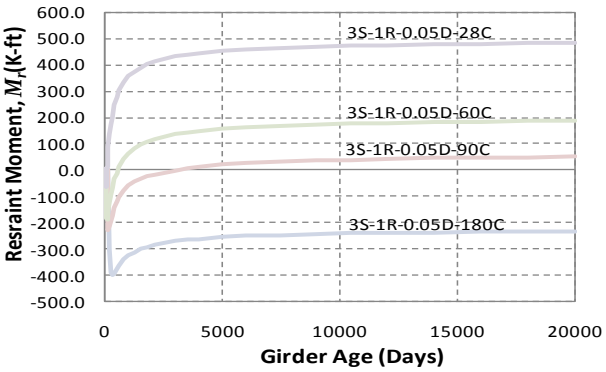

(a) $L_1 = L_2 = L_3$ and $I_{dia} = 0.05*I_g$

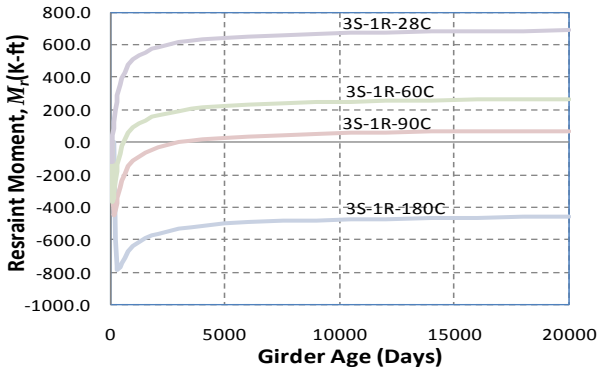

(a) $L_1 = L_2 = L_3$ and $I_{dia} = 0$

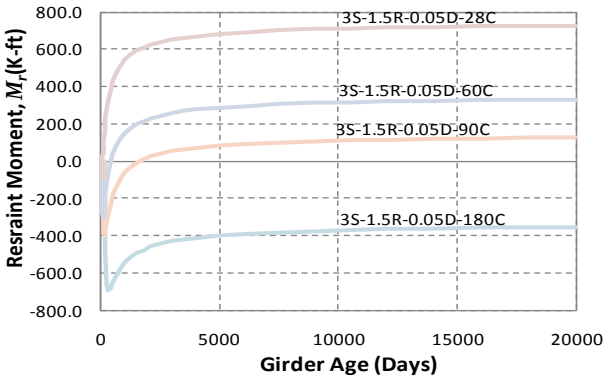

(b) $L_2 = 1.5*L_1 = 1.5*L_3$ and $I_{dia} = 0.05*I_g$

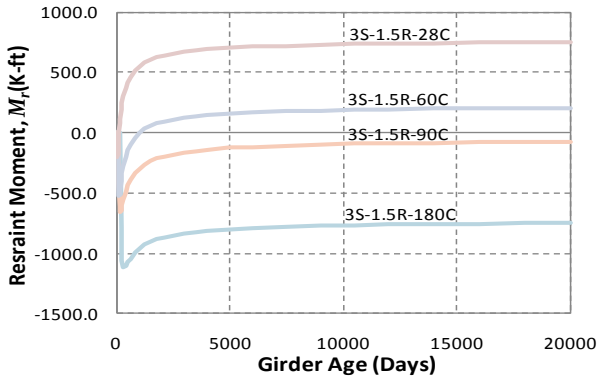

(b) $L_2 = 1.5*L_1 = 1.5*L_3$ and $I_{dia} = 0$

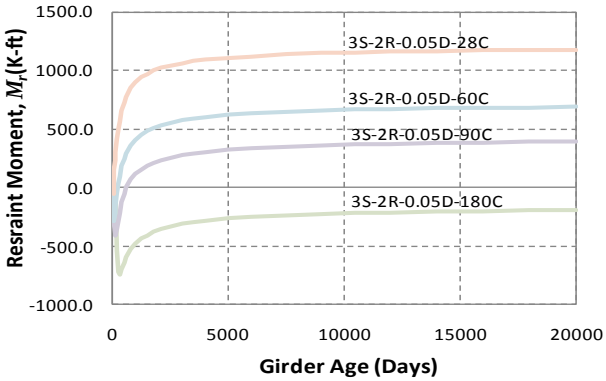

(c) $L_2 = 2*L_1 = 2*L_3$ and $I_{dia} = 0.05*I_g$

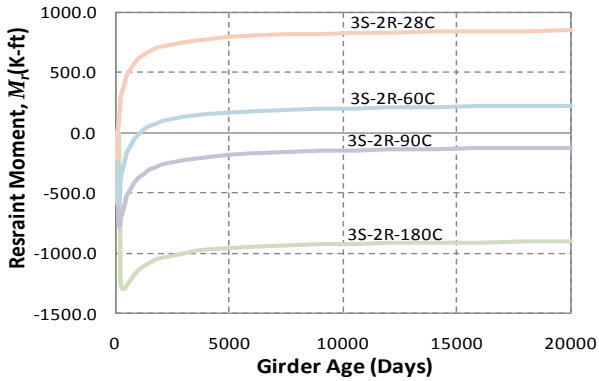

(c) $L_2 = 2*L_1 = 2*L_3$ and $I_{dia} = 0$

Figure 206
***M_r* estimates for three span cases (continued)**

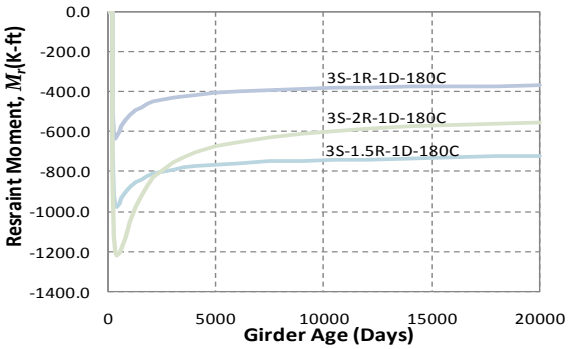

(a) Age = 180 days and $I_{dia} = I_g$

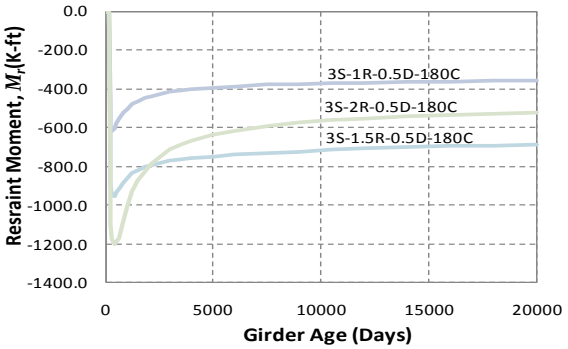

(b) Age = 180 days and $I_{dia} = 0.5*I_g$

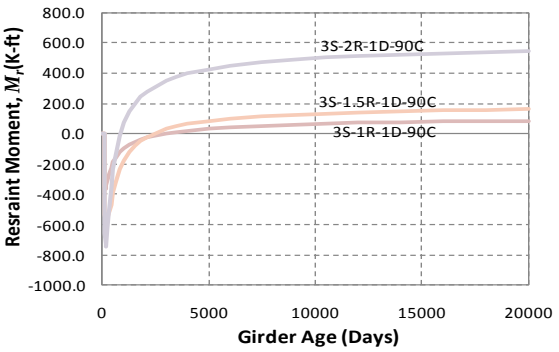

(c) Age = 90 days and $I_{dia} = I_g$

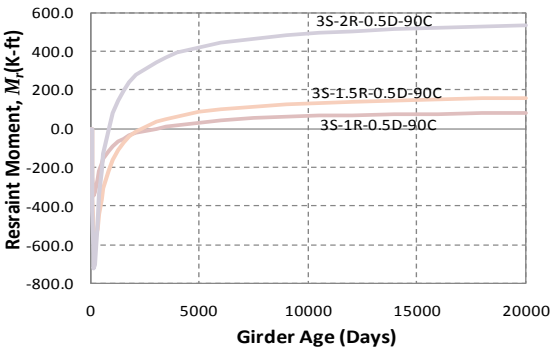

(d) Age = 90 days and $I_{dia} = 0.5*I_g$

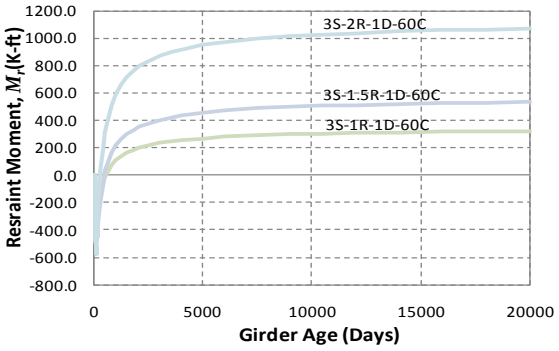

(e) Age = 60 days and $I_{dia} = I_g$

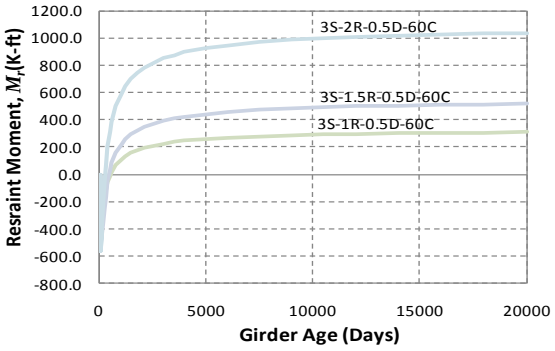

(f) Age = 60 days and $I_{dia} = 0.5*I_g$

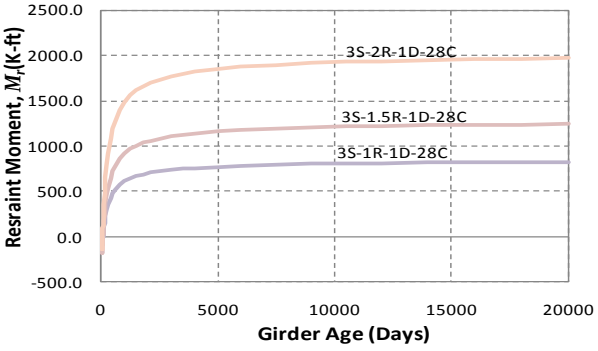

(g) Age = 28 days and $I_{dia} = I_g$

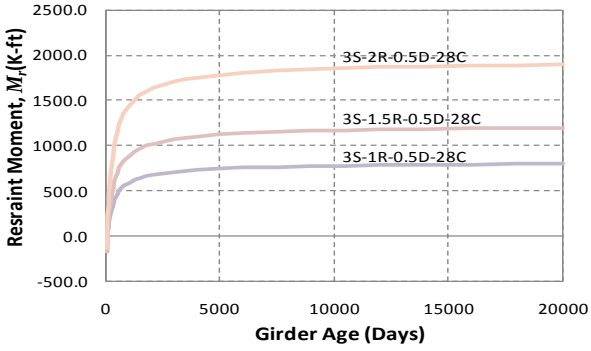

(h) Age = 28 days and $I_{dia} = 0.5*I_g$

Figure 206
***M_r* estimates for three span cases (continued)**

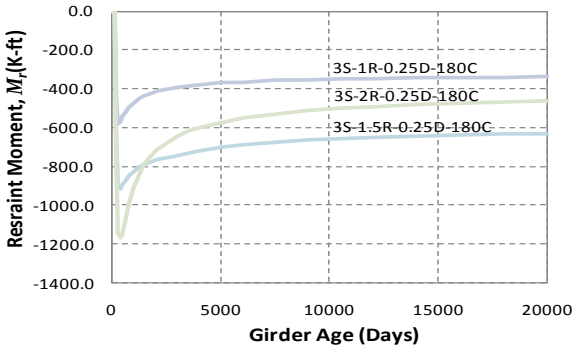

(a) Age = 180 days and I_{dia} = 0.25*I_g

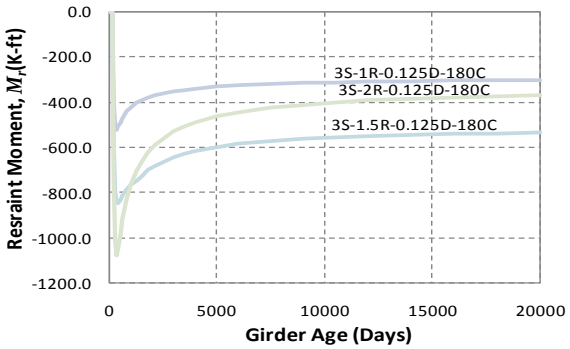

(b) Age = 180 days and I_{dia} = 0.125*I_g

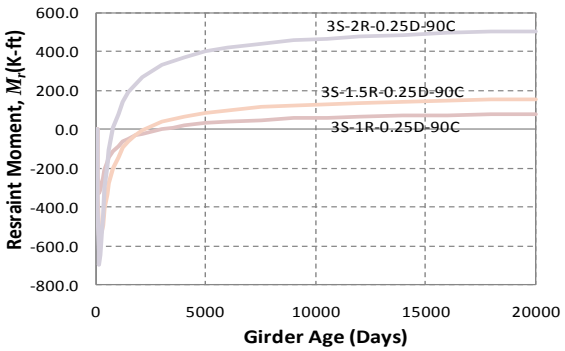

(c) Age = 90 days and I_{dia} = 0.25*I_g

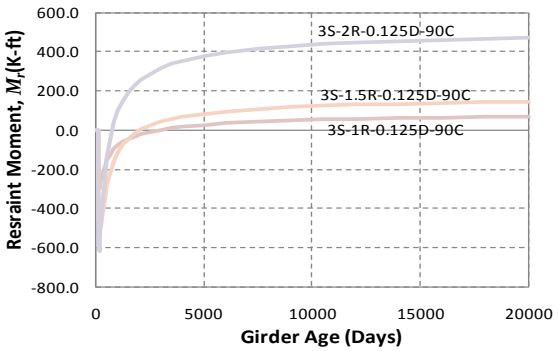

(d) Age = 90 days and I_{dia} = 0.125*I_g

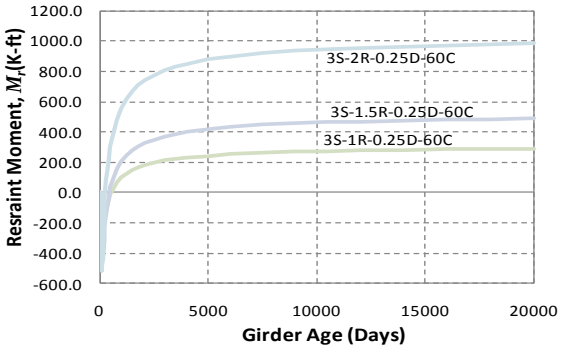

(e) Age = 60 days and I_{dia} = 0.25*I_g

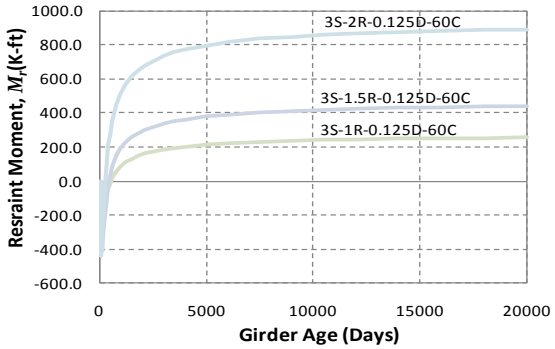

(f) Age = 60 days and I_{dia} = 0.125*I_g

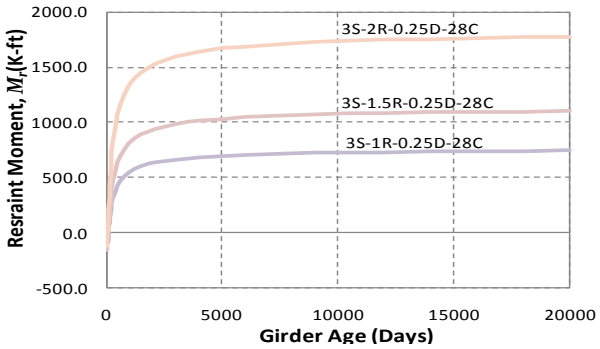

(g) Age = 28 days and I_{dia} = 0.25*I_g

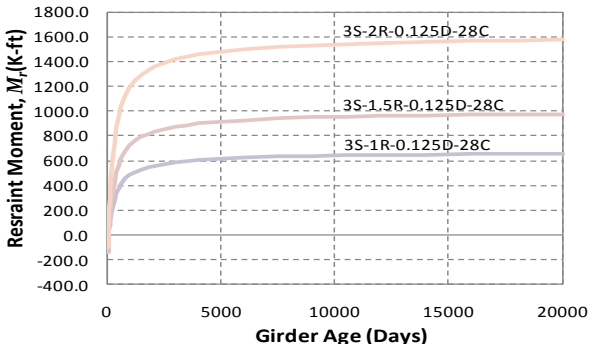

(h) Age = 28 days and I_{dia} = 0.125*I_g

Figure 206
***M_r* estimates for three span cases (continued)**

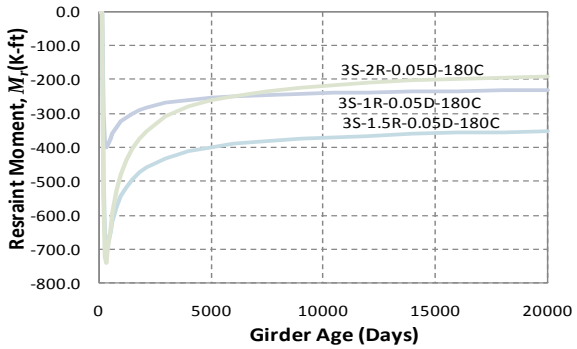

(a) Age = 180 days and $I_{dia} = 0.05I_g$

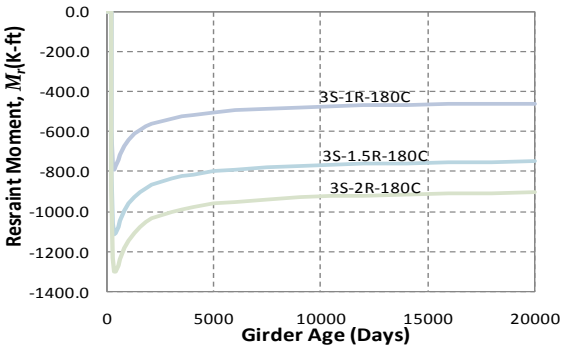

(b) Age = 180 days and $I_{dia} = 0$

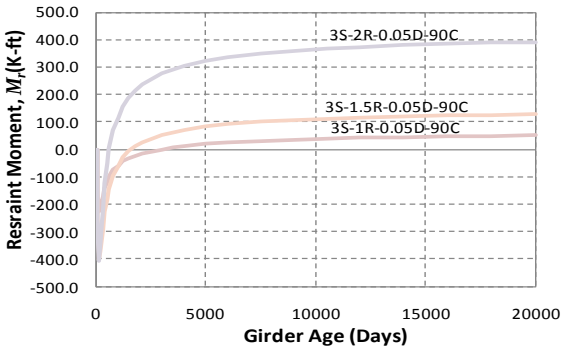

(c) Age = 90 days and $I_{dia} = 0.05I_g$

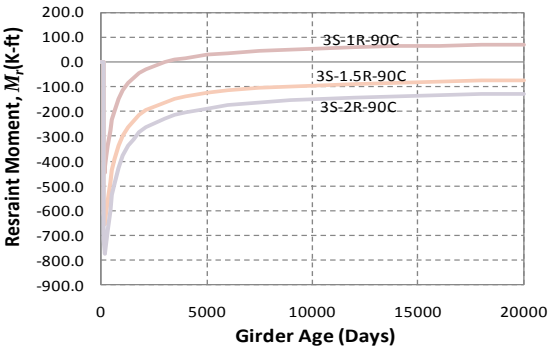

(d) Age = 90 days and $I_{dia} = 0$

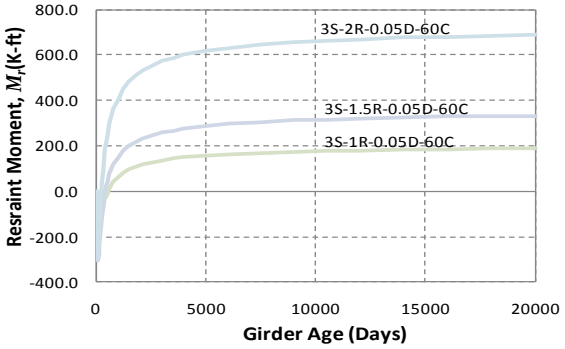

(e) Age = 60 days and $I_{dia} = 0.05I_g$

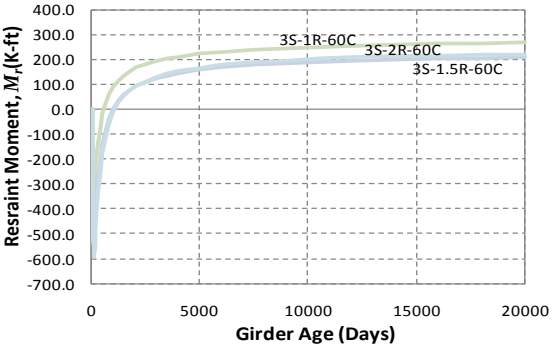

(f) Age = 60 days and $I_{dia} = 0$

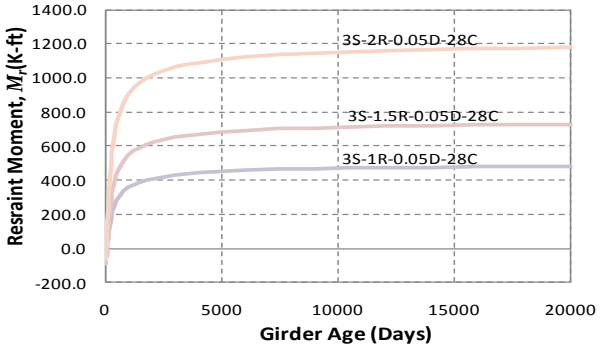

(g) Age = 28 days and $I_{dia} = 0.05I_g$

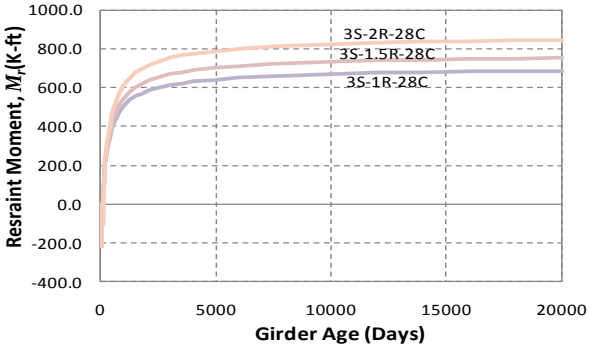

(h) Age = 28 days and $I_{dia} = 0$

Figure 206
***M_r* estimates for three span cases (continued)**

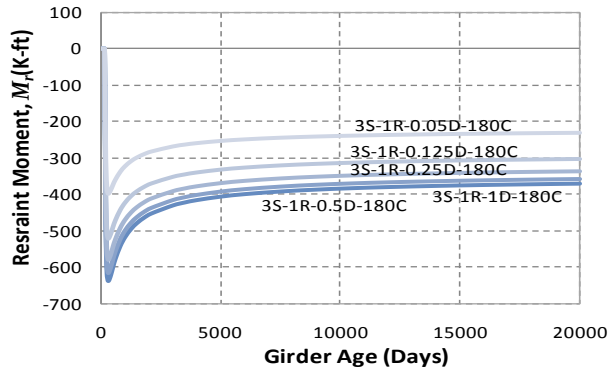

(a) $L_1 = L_2 = L_3$ and Age = 180 days

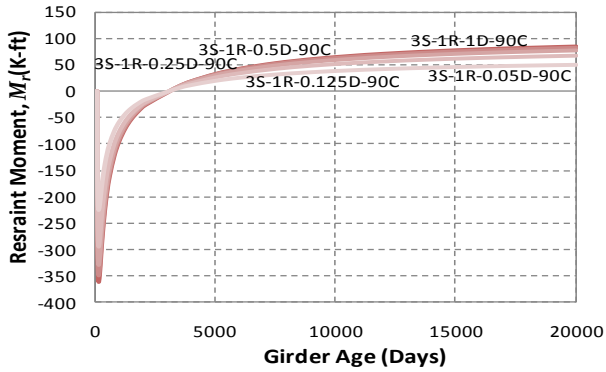

(b) $L_1 = L_2 = L_3$ and Age = 90 days

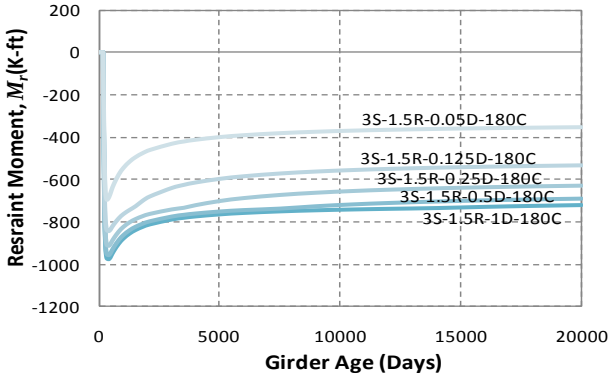

(c) $L_2 = 1.5*L_1 = 1.5*L_3$ and Age = 180 days

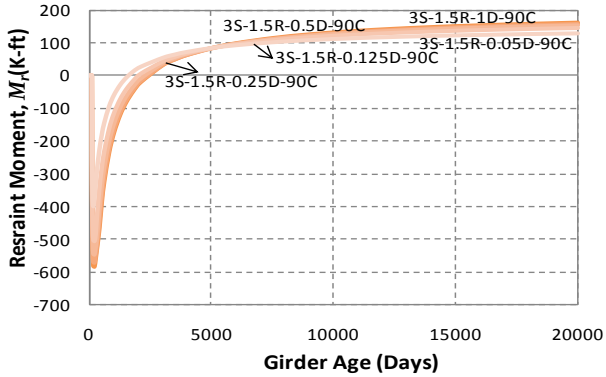

(d) $L_2 = 1.5*L_1 = 1.5*L_3$ and Age = 90 days

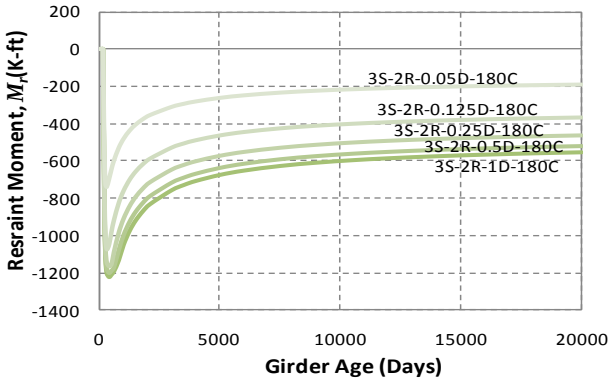

(e) $L_2 = 2*L_1 = 2*L_3$ and Age = 180 days

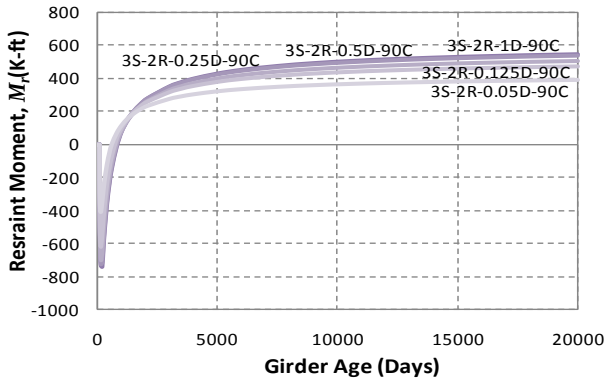

(f) $L_2 = 2*L_1 = 2*L_3$ and Age = 90 days

Figure 206
***M_r* estimates for three span cases (continued)**

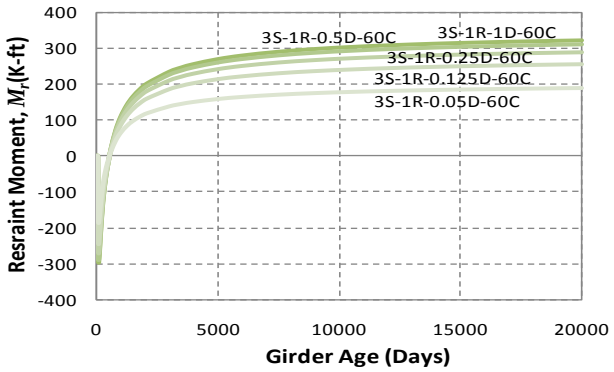

(a) $L_1 = L_2 = L_3$ and Age = 60 days

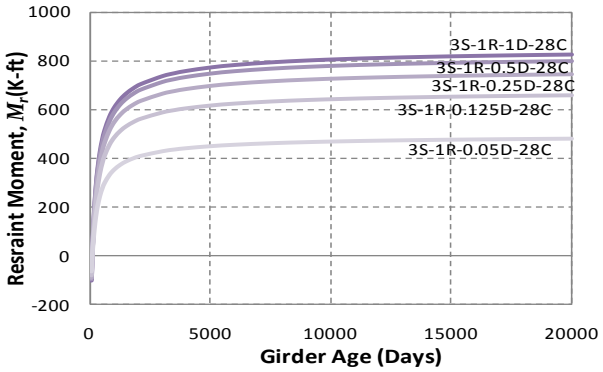

(b) $L_1 = L_2 = L_3$ and Age = 28 days

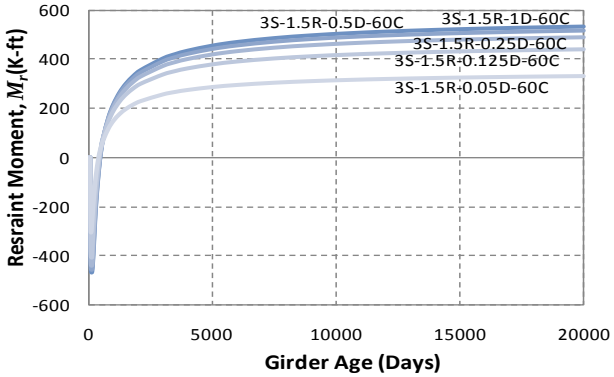

(c) $L_2 = 1.5*L_1 = 1.5*L_3$ and Age = 60 days

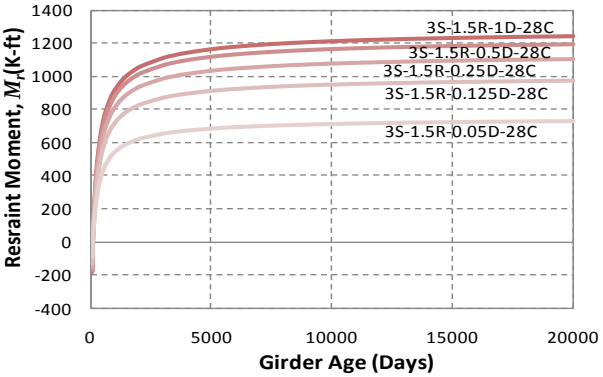

(d) $L_2 = 1.5*L_1 = 1.5*L_3$ and Age = 28 days

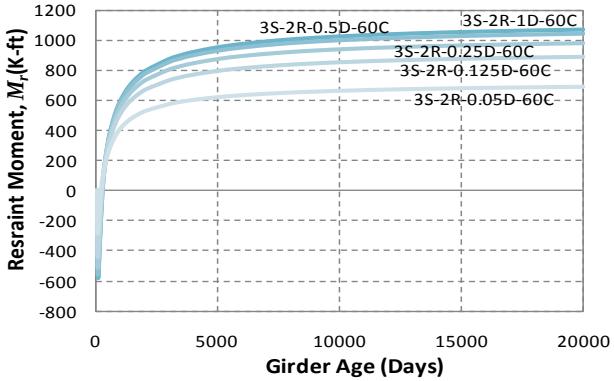

(e) $L_2 = 2*L_1 = 2*L_3$ and Age = 60 days

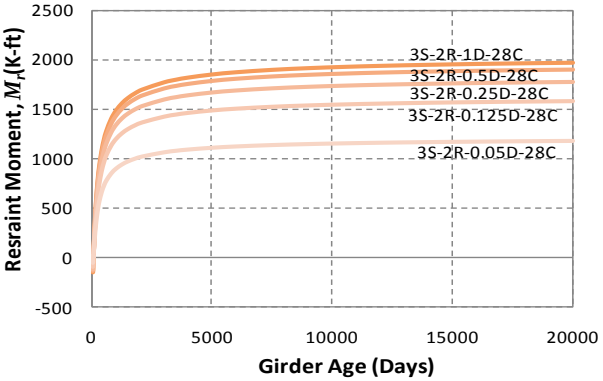

(f) $L_2 = 2*L_1 = 2*L_3$ and Age = 28 days

Figure 206
***M_r* estimates for three span cases (continued)**